Organic/Inorganic Hybrid Nanoparticulate Resonant Contrast Agents



Iris Kramberger

Christ Church

University of Oxford

Thesis submitted for the degree of

Doctor of Philosophy

Trinity, 2016

Abstract

An intriguing frontier for magnetic resonance imaging (MRI) is the development of responsive Gd^{3+}-based contrast agents (CAs) that can report physiological variations in the tissue microenvironment.[1] Heterogeneous biological milieu and quantification of the CA concentration at the site of interest are the major limitations of responsive concentration-dependent protic MRI probes. A ratiometric approach based on dual-mode CAs containing a ^{19}F MRI reporter, in addition to a paramagnetic moiety, is one of the feasible strategies to overcome this drawback.[2]

Since high fluorine content is required for *in vivo* imaging, nanoparticles offer advantageous characteristics over molecular probes due to their large surface area and size, allowing the incorporation of high concentrations of fluorinated probes and paramagnetic CAs. For emerging applications of Gd^{3+} complexes at ultra-high magnetic fields, it was found that not only octadentate ($q = 1$), but also highly kinetically stable nonadentate ($q = 0$) Gd^{3+}-DOTA systems can be incorporated into the mesopores of silica nanoparticles, resulting in an 8-fold increase in proton longitudinal relaxivity from 0.7 mM^{-1} s^{-1} to 6.2 mM^{-1} s^{-1} at 4.7 T compared to their molecular counterparts. A further 7-fold increase in longitudinal relaxivity was achieved when the silica surface of such particles was functionalised with highly acidic propyl sulphonates, enabling faster proton transfer through a hydrogen-bonded hydronium network. pH responsiveness of Gd^{3+} complexes tethered to particles has, on the other hand, been achieved through either local mobility or water access regulated by pH-responsive polymers acting as gating valves on the mesopores.

Moreover, symmetric ^{19}F MRI CAs were accommodated within micron- and nano-sized matrices comprised of polyelectrolytes, quaternary ammonium first generation dendrimers and centrifugable oil-containing silica nanocapsules. For these, the biggest challenge has been posed by restricted local mobility, which notably shortens transverse relaxation time and attenuates the ^{19}F NMR signal. Finally, polymers based on fluorinated quaternary ammonium, pH-sensitive and Gd^{3+}-DOTA methacrylates were prepared, exhibiting a dual $^{19}F/^{1}H$ MRI contrast with reverse pH response.

Declaration and Statement of Collaboration

I, Iris Kramberger, declare that this thesis titled as Organic/Inorganic Hybrid Nanoparticulate Resonant Contrast Agents is written by myself and presented after corrections by Prof. Jason J. Davis. This thesis is based on my own work with the exception of the relevant published work of other researchers, which is always acknowledged by proper citation and referencing within the text, and the following reported experiments:

- Synthesis: The picolinate Ln^{3+}-DOTA, trifluoroethoxy isophthalic acid and α,α'-bis(Ln^{3+}-DO3A)-5-amino-*m*-xylene derivatives were prepared by Dr. Asha Brown (Prof. Paul D. Beer, Inorganic Chemistry Laboratory, University of Oxford).

- Characterisation: The solid-state NMR spectra were acquired by Dr. Nick H. Rees (Inorganic Chemistry Laboratory, University of Oxford), MALDI-TOF spectra were recorded by Dr. Ashley Shepherd and ICP-MS data were obtained by Prof. Kym Jarvis (Viridian Partnership).

- Measurements: All MRI images and most[1] of the ^{1}H and ^{19}F NMR relaxation time measurements presented were obtained by Dr. Alexandr A. Khrapitchev (Prof. Nicola Sibson, Department of Oncology, University of Oxford), whereas fast field cycling ^{1}H NMR relaxometry was conducted by Dr. Carlos Mattea (Prof. Siegfried Stapf, Technische Universität Ilmenau). Plasmid DNA preparation and evaluation of transfection efficiency was performed by Dr. Jing Zhang (Prof. Terence Rabbitts, Weatherall Institute of Molecular Medicine, University of Oxford).

[1] From 2012 to 2014, ^{1}H and ^{19}F NMR relaxation times were obtained by myself in the Department of Physiology, Anatomy and Genetics as well as in the Chemistry Research Laboratory, University of Oxford.

Acknowledgements

I would like to thank my dissertation supervisor, Prof. Jason J. Davis, for his supervision throughout the dissertation process. I am grateful that he has given me the opportunity to explore many of the ideas in detail. I would also like to express my gratitude to Prof. Stephen Faulkner, Prof. Andrew Baldwin, Dr. Daniel Trawny, Dr. Gemma-Louise Davies and Dr. Manuel Tropiano for their advice and support. Special thanks go to Dr. Alexandr A. Khrapitchev, Dr. Carlos Mattea, Dr. Jing Zhang, Dr. Ashley Shepherd and Dr. Nick H. Rees for the measurements as well as Dr. Asha Brown for synthesis and many fruitful discussions. I would especially like to thank Prof. Lothar Helm, who shared with me his strong knowledge on relaxation mechanisms. I have also benefited from stimulating discussion with Prof. Vladimir I. Bakhmutov. I would like to thank Jason Davis group members for all the laughter they provided over the four years.

I am grateful to Christ Church, especially Prof. Dirk G. A. L. Aarts and tutors of graduate studies Prof. Mishtooni Boose and Prof. Edwin Simpson, for their support, both academic and especially personal, for the duration of this course. I am very much indebted to EPSRC, Scatcherd European Scholarship and Christ Church for their financial support.

Finally, I would like to acknowledge the consistent support and encouragement of my parents, grandparents, family and friends. Many thanks go to Keyron Hickman-Lewis for proof-reading most parts of the thesis in a record time. I would especially like to thank my partner Felix Tennie without whom I would not have made it this far. His continuous support, patience, inspiration, motivation and devotion during these years are greatly acknowledged. I am very much looking forward to our lifelong collaboration in science, music, literature, philosophy and politics among many other exciting endeavours.

Abbreviations and Symbols

χ	Volume magnetic susceptibility
Δ	Magnitude of the transient zero-field splitting interaction
τ_C	Correlation time of a molecule
τ_D	Translational diffusion
μ_H	Proton gyromagnetic ratio
τ_M	Water exchange correlation time
τ_{pore}	H_2O exchange correlation time from the interior of the pores to the bulk
τ_R	Rotational correlation time
τ_{RG}	Global rotational correlation time of macromolecules or nanoparticles
τ_{RL}	Local rotational motion of the linker
μ_S	Electron gyromagnetic ratio
τ_v	Correlation time for the modulation of the zero-field splitting interaction
$A/\hbar$	Scalar coupling constant
B_0	Primary magnetic field strength
E_{DGdH}	Translational diffusion activation energy for the diffusion of a water proton away from a Gd^{3+} complex
F^2	Order parameter
q	Number of primary coordination sphere water molecules
r_1	Longitudinal relaxivity
r_2	Transverse relaxivity
T_1	Longitudinal relaxation time
T_2	Transverse relaxation time
AIBN	2,2-azobis(2-methylpropionitrile)
APS	Ammonium persulphate
ATRP	Atom transfer radical polymerisation

BET	Determination of surface area and porosity of a solid by the Brunauer, Emett & Teller method
BMS	Bulk magnetic susceptibility
CA	Contrast agent
CP/MAS	Cross polarisation/magic angle spinning solid-state NMR
CPMG	Carr-Purcell-Meiboom-Gill sequence for measuring T_2 of any nucleus
CTAB	Cetyltrimethylammonium bromide
DAEMA	2-(diethylamino)ethyl methacrylate
DLS	Dynamic light scattering
DMAP	*N,N*-dimethylaminopyridine
DOTA	1,4,7,10-tetraazacyclododecane-1,4,7,10-tetraacetate
DP/MAS	Direct polarisation/magic angle spinning solid-state NMR
DQ MAS	Double-quantum solid-state NMR under fast magic-angle spinning
EDC	1-ethyl-3-(3-dimethylaminopropyl)carbodiimide
EDTA	Ethylenediamine tatraacetic acid
ESI-MS	Electrospray ionisation mass spectrometry
FID	Free induction decay
FOV	Field of view
FTIR	Fourier transform infrared spectroscopy
GEMS	Gradient echo multi slice MRI sequence
HOBt	1-hydroxybenzotriazole hydrate
ICP-MS	Inductively coupled plasma mass spectrometry
lb	Line broadening factor
Ln	Lanthanide
MAA	Methacrylic acid
MALDI	Matrix-assisted laser desorption/ionisation mass spectrometry
MeI	Methyl iodide

MRI	Magnetic resonance imaging
MSN	Mesoporous silica nanoparticle
NHS	*N*-hydroxysuccinimide
NMR	Nuclear magnetic resonance
NMRD	Nuclear magnetic relaxation dispersion
NP	Nanoparticle
nt	Number of scans
PdI	Polydispersity index
PEG	Polyethylene glycol
PFD	Perfluorodecalin
PRE	Paramagnetic relaxation enhancement
QAS	Quaternary ammonium salt
RF	Radio frequency
SAP	Square antiprism
SBM	Solomon-Bloembergen-Morgan theory of relaxation
SEMS	Spin echo multi slice MRI sequence
SNR	Signal-to-noise ratio
sw	Spectral or sweep width
TE	Echo time
TEA	Triethylamine
TEM	Transmission electron microscopy
TEOS	Tetraethyl orthosilicate
TFA	Trifluoroacetic acid
TGA	Thermogravimetric analysis
Thk	Slice thickness in MRI
TR	Repetition time
TSAP	Twisted square antiprism
UV-vis	Ultraviolet-visible spectroscopy
ZFS	Zero-field splitting

Contents

1 Introduction **1**

1.1 An Overview of Relaxation Theory and Paramagnetic Contrast Agents 1

1.2 T_1 Contrast Agents and Solomon-Bloembergen-Morgan Theory 6

1.2.1 Inner-Sphere Relaxation 8

1.2.2 Effect of Water Exchange and its Determination by ^{17}O NMR 12

1.2.3 Second- and Outer-Sphere Relaxation 16

1.3 Macromolecular Effects on Paramagnetic Relaxation Enhancement . . 18

1.3.1 Zeolites and Mesoporous Nanosized Materials as Efficient Nanoparticulate MRI-Reporters 21

1.4 Physiologically Responsive Molecular and Nanoparticulate MRI-Based Sensors 24

1.4.1 q Number and Luminescence Studies 26

1.4.2 Concentration-Independent Responsive MRI Contrast Agents 28

1.5 ^{19}F MRI Contrast Agents 30

1.5.1 Paramagnetically Enhanced ^{19}F NMR Relaxation 33

1.5.2 Environmentally Responsive PRE ^{19}F MRI Contrast Agents . 34

1.6 Objectives of this Work 36

2 Effect of q Number on Ultra-High Field MRI of Gd^{3+} Complexes Appended to MSNs **38**

2.1 Introduction 38

2.2 Results and Discussion 39

2.2.1 Paramagnetic Contrast Agent Functionalisation of MSNs and Their Relaxometric Properties 39

2.2.2 Confirmation of Hydration Numbers by Luminescence Measurements 56

2.2.3 ^{17}O NMR Measurements Reveal Strong Second-Sphere Contribution 57

2.2.4 Further Analysis of the Second/Outer-Sphere Contribution . . 59

2.3 Conclusion 62

3 Enhanced Propagation of the Paramagnetic Effect by Sulphonation of MSNs **63**

3.1 Introduction 63

3.2 Results and Discussion 65

3.2.1 Physicochemical Characterisation of Sulphonated Mesoporous Silica Nanoparticles . . . 65
3.2.2 Detection of Immobile Protons by ^{1}H-^{1}H DQ MAS NMR . . . 69
3.2.3 Relaxometric Properties of Sulphonated Nanoparticulate Contrast Agents . . . 73
3.2.4 Influence of Sulphonation on the Luminescence Properties of Eu^{3+}-Doped MSNs . . . 77
3.2.5 ^{17}O NMR Indicates Faster Water Exchange Rates upon Sulphonation . . . 80
3.2.6 Sulphonation Effects on Water Residence Correlation Times . 82
3.3 Conclusion . . . 84

4 pH-Activatable Polymer-Capped Mesoporous Nanoparticulate MRI Probes 86
4.1 Introduction . . . 86
4.2 Results and Discussion . . . 88
4.2.1 Preparation of Polymer-Coated Mesoporous Silica Nanoparticles . . . 88
4.2.2 Relaxivity Assessment of pH-Responsive Polymer-Functionalised Nanoparticulate Resonant Agents . . . 98
4.2.3 Confirmation of Anion- and pH-Unresponsive Hydration Numbers by Luminescence Measurements . . . 103
4.2.4 ^{17}O NMR Measurements Reveal Variable Water Access with pH . . . 105
4.2.5 Poly(DAEMA)-Capped MSNs as Potential Theranostic Agents . . . 106
4.3 Conclusion . . . 109

5 Effect of Internal Mobility on Molecular and Nanoparticulate ^{19}F MRI CAs 111
5.1 Introduction . . . 111
5.2 Results and Discussion . . . 112
5.2.1 Mobile Fluorine Incorporation into MSNs via Polymers . . . 115
5.2.2 Nanoencapsulated Fluorinated Oil . . . 118
5.2.3 Polyelectrolyte Micelles with Symmetric ^{19}F MRI Probes . . . 121
5.2.4 Quaternary Ammonium Salts as ^{19}F MRI Probes . . . 127
5.3 Conclusion . . . 135

6 Dual ^{19}F/^{1}H Nanoparticulate MRI Contrast Agents 138
6.1 Introduction . . . 138
6.2 Results and Discussion . . . 140
6.2.1 Paramagnetically Enhanced ^{19}F NMR Relaxation in Water-Soluble Mesoporous Silica Nanoparticles . . . 140
6.2.2 Reduced ^{19}F NMR T_1/T_2 Ratios by Dinuclear Lanthanide Complex Conjugation to Polymer-Coated Silica Nanoparticles . . . 144

6.2.3 pH-Responsive PEGylated and non-PEGylated Polymeric Dual $^{19}F/^{1}H$ MRI Contrast Agents 147
6.3 Conclusion 157

7 Experimental Procedures **159**
7.1 Materials and Methods 159
7.2 Syntheses 168
7.3 Nanoparticle and Polymer Sample Preparation Methods 184

Appendix A Appendix to Chapters II, III and IV **197**

Appendix B Appendix to Chapters V and VI **209**

Bibliography **236**

Chapter 1

Introduction

1.1 An Overview of Relaxation Theory and Paramagnetic Contrast Agents

Since the extension of nuclear magnetic resonance (NMR) to magnetic resonance imaging (MRI) in the nineteen seventies,[3] clinical MRI has become a routine diagnostic technique for obtaining anatomical information without any invasiveness or risk of ionising radiation.[4] MRI benefits from high water content in biological systems as the molecule contains protons that are the most NMR sensitive and the most abundant nuclei *in vivo*.[5] Due to its spin, each proton possesses a magnetic dipole moment. In the presence of a stationary magnetic field B_0, only two orientations for $I = 1/2$ along the spin rotation axis are allowed: a lower energy level, which corresponds to the spin of the protons aligned in the direction of the field, and a less favourable higher energy level, wherein the nuclear magnets are oriented antiparallel to the field (Fig. 1.1). The spin system absorbs energy when hydrogen nuclei are excited by a time-varying magnetic field in a plane perpendicular to B_0 known as radio frequency (RF) pulse, which is an electromagnetic wave that is tuned to the Larmor precession frequency ($\omega_0 = \gamma \cdot B_0$) of the protons and to their chemical shift.

This leads to an annihilation of the population difference between the upper and lower levels and consequently to a rotation of the magnetisation vector away from the axial field. When the RF pulse is turned off, the spin system reorientates and regains thermal equilibrium due to two simultaneous processes known as longitudinal T_1 and transverse T_2 relaxation mechanisms.[6, 7, 8]

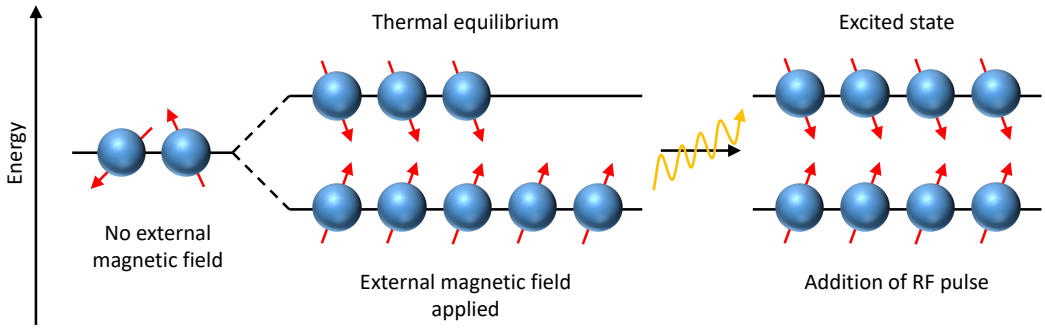
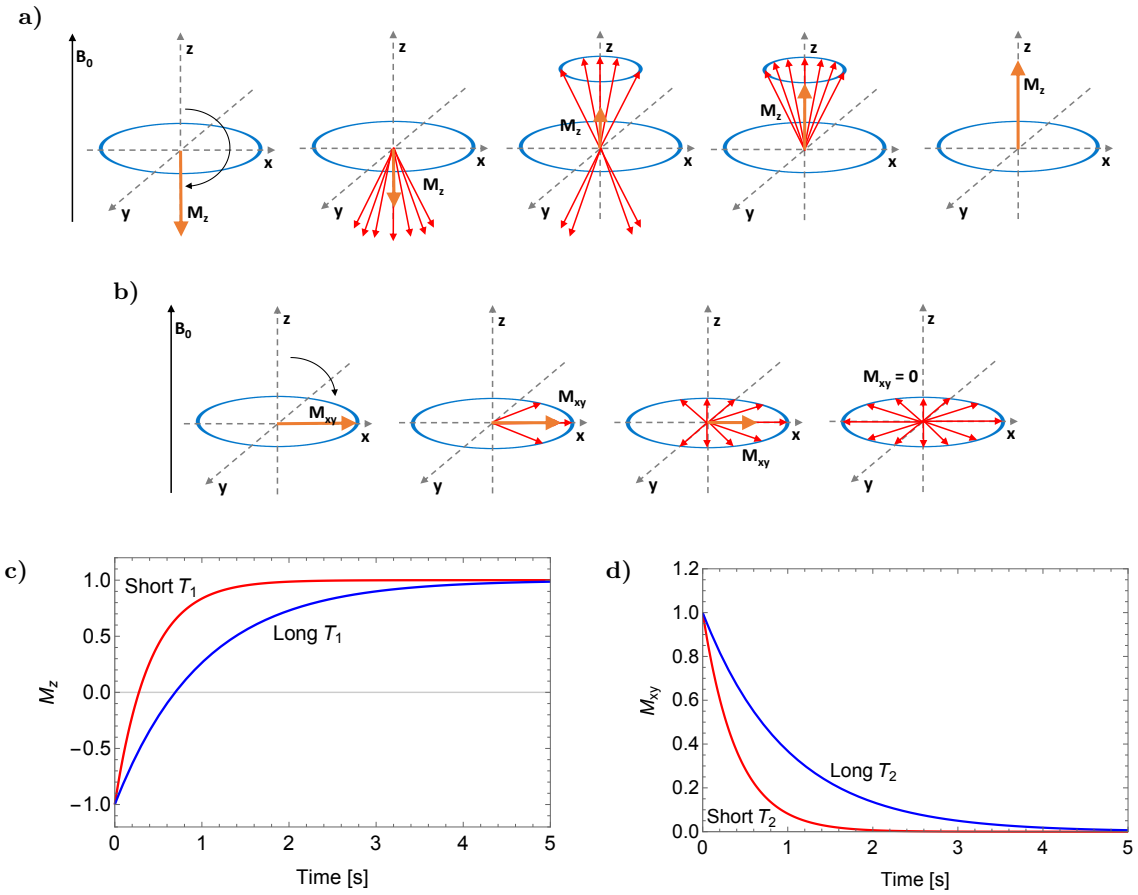


Figure 1.1: Without external magnetic field, the hydrogen nuclear spins are randomly oriented (*i.e.* there is no net magnetisation). When placed in a large magnetic field B_0, the spins align parallel or antiparallel to B_0. As more spins have a lower energy state and are aligned parallel to B_0, the net magnetisation M_0 is in the z-direction. Upon RF excitation pulse rotating in the xy-plane, the energy absorbed can be high enough to equalise the populations of the two energy levels. After the RF pulse is removed, a completely or partially saturated system returns to equilibrium by spin-lattice and spin-spin relaxation.[6, 9]

The spin-lattice relaxation time T_1 is enthalpy driven by the redistribution of the acquired RF energy to the surroundings, *i.e.* to the lattice when the population difference regains thermal equilibrium. The demagnetisation occurs in the direction of the external magnetic field along the z-axis as the proton's dipole moment vector relaxes back to its ground state (Eq. (1.1), Fig. 1.2 a) and c)). T_1 corresponds to the time necessary for the longitudinal magnetisation vector M_z to be restored to 63 % of its original equilibrium value. As a result of transitions from a higher to a lower state, energy dissipates to other nuclei and electrons, which is reflected in the spin-spin relaxation time T_2. T_2 describes the time it takes for spins to exchange energy because of the loss of synchronisation. It signifies the time for transverse component of the magnetisation vector to decay towards its equilibrium, and is thus also referred



$$M_z(t) = 2M_0(1 - e^{\frac{-t}{T_1}}) \qquad (1.1)$$

$$M_{xy}(t) = M_0 \cdot e^{\frac{-t}{T_2}} \qquad (1.2)$$

Figure 1.2: As soon as the RF pulse is removed, the longitudinal magnetisation vector M_z (a) and c)) begins to recover, while its transverse counterpart M_{xy} (b) and d)) starts to disappear.[10]

to as transverse relaxation time (Eq. (1.2), Fig. 1.2 b) and d)). T_2 corresponds to a 37 % reduction of the initial magnetisation vector located in a plane perpendicular to the outer magnetic field. It progresses at a rate either equal to, or faster than, longitudinal relaxation since the return of magnetisation to the z-direction usually triggers a loss of the net magnetisation in the xy-plane. While T_2 depends only on spin-spin interactions, a parameter known as T_2^* is frequently used in MRI. Beside depending on spin-spin interactions, T_2^* also takes into account external as well as sample-related magnetic field inhomogeneities and is thus always faster than T_2.[6, 10]

As a result of random motions of individual molecules within a sample, each spin

experiences a small local magnetic field that is fluctuating in time. Together with the magnetic interactions with either neighbouring nuclear spins or the spins of unpaired electrons, which will be regarded in Sec. 1.2, these mechanisms contribute additively to relaxation rates. The time dependency of such oscillations can be assessed with an autocorrelation function $G(\tau)$ most simply approximated by an exponential decay function with constant τ_C. Therefore, the rate with which $G(\tau)$ decreases depends on the frequency of the field oscillations. Since these fluctuations and their related relaxation parameters are also well understood in terms of probabilities of motions at specific frequencies rather than times, double Fourier transformation of $G(\tau)$ yields a spectral density function $J(\omega)$ that takes the form of a Lorentzian function described by Eq. (1.3) when the molecular reorientations can be estimated by the movement of a simple sphere.[11]

$$J(\omega) = \frac{2\tau_C}{1 + \omega^2 \tau_C^2}, \tag{1.3}$$

$$\frac{1}{T_1} = C \cdot J(\omega), \tag{1.4}$$

$$\frac{1}{T_2} = \frac{C}{2} \cdot \left[J(\omega) + J(0) \right]. \tag{1.5}$$

Therefore, $J(\omega)$ represents the efficiency of random local fields experienced by nuclei at frequency ω and depends on changes of the molecular location and orientation described by the correlation time of a molecule τ_C. Fig. 1.3 shows that for large molecules (long τ_C), the first term of Eq. (1.5), which occurs because of the T_1 relaxation contribution (Eq. (1.4)), becomes insignificant, thus leading to a larger difference between T_1 and T_2, while for smaller molecules (short τ_C), both terms become almost identical resulting in nearly equivalent T_1 and T_2 values.[12, 13]

For MRI image generation, it is necessary to map the spatial arrangement between spin density and the current induced by the transitions of relaxing magnetic moments in the sample. As the protons return to their unexcited state, the spins

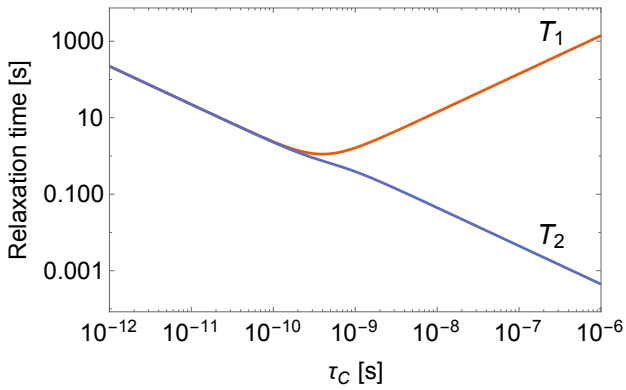


Figure 1.3: Dependency of T_1 and T_2 relaxation times of two protons on the correlation time τ_C at 400 MHz.

develop an oscillating magnetic field that induces a tiny current in the receiver coil in the xy-plane, which records an exponentially decaying sinusoidal signal known as free induction decay (FID). In order to obtain an NMR spectrum, the time domain function is Fourier transformed into the frequency domain spectrum.[10] To produce a 3D MRI image, on the other hand, the FID signal is recorded in each dimension. This is achieved by multiple applications of RF pulses, while varying magnetic field gradients to the B_0 field in the x-, y- and z-directions at different times in the region of interest also known as the field of view (FOV), labelling each voxel within the selected slice by its phase and frequency. Multiple FIDs usually provide enough information to create the image that can be either T_1-, T_2- or T_2^*-weighted depending on the application and timing of the RF pulses. For example, a short repetition time (TR, *i.e.* the time interval between two excitations pulses) increases T_1 weighting as the differences between regions with various values of T_1 will be highlighted, while a long echo time (TE), which is the time interval between the application of an RF pulse and the acquisition of the signal, contributes to increased T_2 weighting. In addition to the TR and TE parameters, the choice of the flip angle of initial or subsequent RF excitation, which may be a small angle ($< 90°$), a 90° or a 180° rotation, also influences the quality of the obtained image as well as the acquisition speed. For instance, after the 90° pulse, a spin echo (SE) sequence uses an additional 180°

pulse in order to flip proton spins and generate an echo as the spins rephase, which neutralises the T_2^* effects. This results in a long signal acquisition time, and hence a better signal. Most gradient echo (GE) sequences, on the other hand, use an initial excitation pulse of $< 90°$, which affects the amount of longitudinal magnetisation being flipped into the xy-plane. Since the 180° rephasing pulse is not applied, the dephasing occurs through T_2^* effects making the sequence faster, but more susceptible to field inhomogeneities.[14]

1.2 T_1 Contrast Agents and Solomon-Bloembergen-Morgan Theory

Sometimes, the MRI contrast generated by the different magnetic and physical properties of water protons in various tissues is insufficient to distinguish between healthy and diseased states. The acceleration of T_1 and T_2 relaxation times of water protons and the resulting enhancement of MR image contrast can be obtained through the introduction of paramagnetic, superparamagnetic or ferromagnetic contrast agents. Their efficiency is expressed in terms of relaxivity r_i ($i = 1$ or 2 with r_1 and r_2 being associated with T_1 and T_2, respectively), which is a measure of the ability to relax protons as a function of the concentration of contrast agents (CAs) and can be obtained by the following equation:

$$\frac{1}{T_{i,obs}} = r_i[M] + \frac{1}{T_{i,dia}}; \qquad i = 1, 2. \tag{1.6}$$

Here, $[M]$ corresponds to the concentration of a metal in mM. The observed relaxation rates $T_{i,obs}^{-1}$ are comprised of paramagnetic and diamagnetic contributions ($T_{i,obs}^{-1} = T_{i,para}^{-1} - T_{i,dia}^{-1}$), which correspond to relaxation rates $T_{i,para}^{-1}$ and $T_{i,dia}^{-1}$ in the presence or absence of the metal, respectively. As only $T_{i,para}^{-1}$ depends on the metal concentration $[M]$, a linear relationship can be obtained with the intercept of $T_{i,dia}^{-1}$

and the slope of r_i in units of mM^{-1} s^{-1} as shown in Eq. (1.6).[10]

Negative contrast agents reduce T_2 more than T_1. As a result, they usually have a r_2/r_1 ratio as high as 6 or more and produce darker images, the most common being superparamagnetic materials with large magnetic susceptibilities, such as iron oxide nanoparticles.[1] Positive T_1 contrast agents, such as paramagnetic metal ions[2] with a large number of unpaired electrons and long electronic relaxation times (*e.g.* Gd^{3+} and Mn^{2+}), on the other hand, have r_2/r_1 ratios of 1-2 and provide brighter T_1-weighted MR images while diminishing any field inhomogeneities that might lead to image artefacts or decreased signal intensities as the magnetic susceptibility change is much smaller than for the T_2 probes.[16, 17, 18] When the concentration of Gd^{3+}-based CAs is very low, the strong T_1 shortening effects dominate over the T_2 ones and are thus not observed. However, depending on the tissue type and pulse sequence parameters, once the Gd^{3+} concentration increases (*e.g.* at concentrations greater than 5-10 mM in the case of Gd^{3+}-DTPA), MRI signal intensity starts to fall possibly due to magnetic susceptibility effects.[19]

The symmetric seven-electron ground state ($^8S_{7/2}$) that results in a slow electronic relaxation rate, which is reduced by six orders of magnitude compared to that of other Ln^{3+} ions, is the reason why gadolinium(III) is the most potent MRI CA.[20] Gd^{3+} itself, however, is toxic with a radius similar to that of Ca^{2+} so that it can easily disrupt physiological Ca^{2+} signalling pathways.[21] In order to omit other toxic effects associated with free Gd^{3+} ions, such as a potential risk of nephrogenic systemic fibrosis,[22, 23] the trivalent lanthanide cations must be bound in a kinetically inert and thermodynamically stable chelate, which is usually a macrocyclic derivative based on 1,4,7,10-tetraazacyclododecane (cyclen). Although the electronic and magnetic properties are not affected considerably by the coordinating ligand due to the $4f$

[1] For example, the commercially available CA Resovist has respective r_1 and r_2 values of 25.4 mM^{-1} s^{-1} and 151.0 mM^{-1} s^{-1} at 0.47 T.[15]

[2] For example, the commercially available CA Magnevist (gadolinium(III) diethylenetriaminepentaacetic acid (Gd^{3+}-DTPA)) has respective r_1 and r_2 values of 3.8 mM^{-1} s^{-1} and 4.2 mM^{-1} s^{-1} at 0.47 T.[15]

electrons being delocalised only partly onto ligand orbitals resulting in mostly ionic bonding, a multidentate chelate decreases the number of water molecules that can directly ligate to Gd^{3+}, thus reducing its efficiency as a CA.[18]

1.2.1 Inner-Sphere Relaxation

The efficiency of Gd^{3+}-based CAs is defined in terms of longitudinal relaxivity r_1, which defines the relaxation rate enhancement per millimolar concentration of the paramagnetic CA, and which depends on numerous parameters based on the electron spin relaxation, dynamics and structural characteristics of Gd^{3+} complexes. Among the latter, the number q of inner-sphere water molecules ligated directly to the Gd^{3+} ion (typically, $r_{Gd-O} < 3$ Å) plays a very important role in relaxivity modulation since the local magnetic field of the paramagnetic centre decays rapidly with distance (Fig. 1.4). Beside short-range interactions, water molecules hydrogen-bonded to the chelate in the second-sphere (3.8 Å $< r_{Gd-O} <$ 5.2 Å) as well as water molecules freely diffusing around the complex in the outer-sphere also contribute appreciably to dipolar coupling between the electron magnetic moment of the Gd^{3+} ion and the nuclear magnetic moment of water protons.[18, 24, 25]

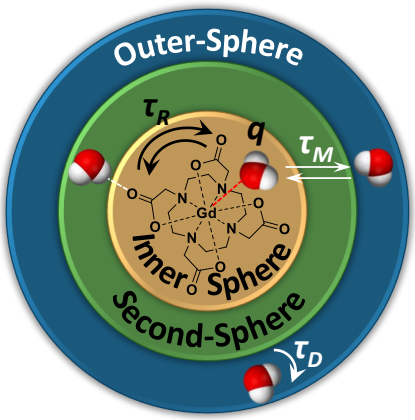


Figure 1.4: Illustration of first-, second- and outer-sphere contribution of a Gd^{3+}-DOTA complex to the observed ^1H relaxivity.

The observed longitudinal and transverse relaxivities r_i are the direct sum of the inner-sphere (IS), second-sphere (SS) and outer-sphere (OS) relaxivities:

$$r_i = r_i^{IS} + r_i^{SS} + r_i^{OS}. \tag{1.7}$$

The inner-sphere contribution r_i^{IS} of the paramagnetic CAs to the observed relaxivity is a function of the residence time of the inner-sphere water molecules ($\tau_m = \frac{1}{k_{ex}}$), which is important for the transmission of the paramagnetic effect to bulk water, the hydration number q and the mole fraction of water molecules bound to the metal P_M, where the subscript M denotes the inner-sphere water molecule.[26]

$$r_i^{IS} = \frac{P_M}{T_{iM} + \tau_M}; \qquad P_M = \frac{q[Gd]}{[H_2O]} = \frac{q[Gd]}{55.6}; \qquad i = 1, 2. \tag{1.8}$$

Here, [Gd] is the concentration of gadolinium, and T_{iM} stands for either longitudinal or transverse relaxation time of the ligated water protons. T_{iM} can be influenced by three mechanisms dependent on magnetic field, nucleus and chemical environment, namely by dipole-dipole (DD) coupling, scalar (SC) interaction and Curie spin (CS) relaxation.

$$T_{iM} = T_i^{DD} + T_i^{SC} + T_i^{CS}. \tag{1.9}$$

The pseudo contact interaction (DD, "through space", *i.e.* homo- or heteronuclear and intra- or intermolecular) depends on hyperfine interactions, in this case magnetic interactions between the nuclear spins of water protons and the electron spins of unpaired electrons in the paramagnetic system. Thus, DD depends on changes in the direction of electron spins (electronic relaxation T_{ie}), on the orientation of a water molecule relative to the unpaired electrons and also on the water exchange rate, which is important for the transmission of the paramagnetic effect to bulk water. Electronic spin relaxation and water exchange also influence the Fermi contact interaction (SC,

"through bonds"), which is independent of the orientation of the complex. CS, on the other hand, depends on the exchange and reorientation, but not on electronic relaxation. It is a result of the change in the magnetic moment caused by the various populations of electron spin energy levels in paramagnetic species. CS thus gains significance in the relaxation enhancements of lanthanides with high magnetic moments and short electronic relaxation times, such as dysprosium(III), as well as in T_{2M} at ultra-high magnetic fields (the CS contribution increases quadratically with the applied field and is proportional to the squared magnetic moment of the complex) or in Gd^{3+} complexes with long rotational correlation times τ_R.[11, 25, 26, 27, 28]

The inner-sphere relaxation times T_{iM} have been described by the modified Solomon-Bloembergen-Morgan theory based on the point-dipole approximation with unpaired electrons positioned at the centre of the paramagnetic metal.[29, 30]

$$\begin{aligned}\frac{1}{T_1^{DD}} + \frac{1}{T_1^{SC}} =& \frac{2}{15}\left(\frac{\mu_0}{4\pi}\right)^2 \frac{\gamma_H^2 g_e^2 \mu_B^2 S(S+1)}{r_H^6}\left[\frac{3\tau_{C_1}}{1+\omega_H^2\tau_{C_1}^2} + \frac{7\tau_{C_2}}{1+\omega_S^2\tau_{C_2}^2}\right] \\ &+ \frac{2}{3}S(S+1)\left(\frac{A}{\hbar}\right)^2\left[\frac{\tau_{e_2}}{1+\omega_S^2\tau_{e_2}^2}\right],\end{aligned} \tag{1.10}$$

$$\begin{aligned}\frac{1}{T_2^{DD}} + \frac{1}{T_2^{SC}} =& \frac{1}{15}\left(\frac{\mu_0}{4\pi}\right)^2 \frac{\gamma_H^2 g_e^2 \mu_B^2 S(S+1)}{r_H^6}\left[4\tau_{C_1} + \frac{3\tau_{C_1}}{1+\omega_H^2\tau_{C_1}^2} + \frac{13\tau_{C_2}}{1+\omega_S^2\tau_{C_2}^2}\right] \\ &+ \frac{2}{3}S(S+1)\left(\frac{A}{\hbar}\right)^2\left[\tau_{e_1} + \frac{\tau_{e_2}}{1+\omega_S^2\tau_{e_2}^2}\right].\end{aligned} \tag{1.11}$$

In Eq. (1.10) and Eq. (1.11), r_H refers to the distance between the electron spin of the metal and a proton of water, S is the spin state that equals 7/2 in the case of Gd^{3+}, γ_H is the nuclear gyromagnetic ratio, ω_H and ω_S are the respective proton and electron Larmor precession frequencies ($\omega = \gamma \cdot B_0$, where B_0 is the external field), g_e is the electron spin g factor, μ_B is the Bohr magneton, $A/\hbar$ is the hyperfine coupling constant between the electron spin of the metal and the proton spin of the ligated water, while τ_{C_i} and τ_{e_i} are the dipole-dipole and scalar correlation times, respec-

tively, which influence the relaxation through parameters describing the dynamics and electron spin relaxation times of the paramagnetic complexes:[31]

$$\frac{1}{\tau_{C_i}} = \frac{1}{T_{ie}} + \frac{1}{\tau_M} + \frac{1}{\tau_R}; \qquad \frac{1}{\tau_{e_i}} = \frac{1}{T_{ie}} + \frac{1}{\tau_M}; \qquad i = 1, 2. \tag{1.12}$$

The efficiency of the CA can be most easily adjusted by the optimisation of the parameters incorporated in the dipole-dipole correlation time τ_{C_i}, especially since the metal-proton distance, which influences the T_i^{DD} as the inverse sixth power, is more or less constant in Gd^{3+} systems (about 3.1 Å for 8- and 9-coordinate Gd^{3+} complexes).

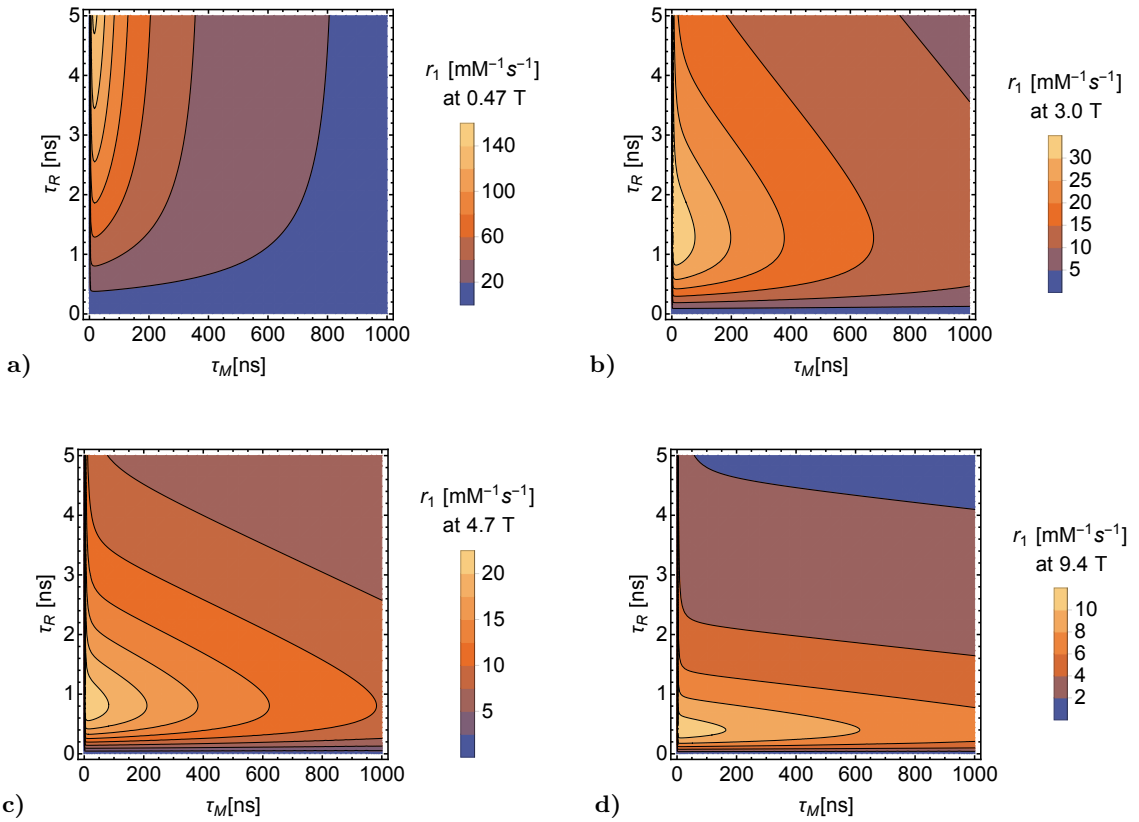


Figure 1.5: Contour plots showing the effect of rotational τ_R and water residency τ_M correlation times on protic longitudinal relaxivities colour coded by the side bars at a) 0.47 T, b) 3.0 T, c) 4.7 T and d) 9.4 T. The relaxivities decrease with higher field and become maximal when τ_M is minimised. The rotational correlation time τ_R of small molecular contrast agents is on the order of 0.01-0.10 ns, which is represented as the blue strip with lowest relaxivity on graphs b) and c). The incorporation of Gd^{3+} complexes into bigger macromolecular moieties slows down the rotation resulting in a drastically enhanced r_1.[27]

On the other hand, increasing the hydration number q can result in a loss of kinetic inertness and displacement of water molecules by endogenous anions such as phosphate, which leads to a substantial reduction of relaxation enhancement.[32] The three parameters of τ_{C_i} must therefore be optimised simultaneously to achieve maximum relaxation enhancement (*cf.* Fig. 1.5) and still comply with the fast exchange condition where inner-sphere relaxivity is not limited by water exchange.

At fields lower than 0.1 T, the electronic relaxation term in the expression for τ_{C_i} (Eq. (1.12)) becomes dominant, *i.e.* $\tau_R \gg T_{1e}$, $\tau_M \gg T_{2e} \Rightarrow \tau_{C_1} \approx T_{1e}$ and $\tau_{C_2} \approx T_{2e}$. The trend in MR imaging, however, is towards fields higher than 1.5 T as both signal-to-noise ratio and resolution increase with applied field. At field strengths most commonly used in clinical applications ($B_0 \geq 1.5$ T), water exchange in small Gd^{3+} complexes is sufficiently fast (about 5-50 ns) to provide an efficient means to transfer the effect to the bulk water. It is also adequately slow compared to the length of τ_R, which is on the picosecond scale (approximately 50-200 ps). Since for Gd^{3+} complexes T_{1e} is in the 1-5 ns range at 0.34 T and increases quadratically with the applied field, T_{1e} is longer than τ_R ($T_{1e}, T_{2e} \gg \tau_R$, $\tau_R \approx \tau_{C_1} \approx \tau_{C_1}$) at $B_0 \geq 1.5$ T. Therefore, the τ_R parameter dominates and determines the $\tau_{C_i}^{-1}$ rate of small molecular CAs.[24, 27, 33, 34]

1.2.2 Effect of Water Exchange and its Determination by ^{17}O NMR

In extreme cases, τ_M can range from 0.1 ns to tens of μs.[33] If it is too fast ($T_{1M} >> \tau_M$), the water molecule is not bound to Gd^{3+} for a sufficiently long time. This limits the relaxation rate of water protons T_{1M}^{-1} and accordingly the relaxivity, too. On the other hand, if the water residency time is too long, the number of exchanges of the relaxed water with the bulk water is heavily reduced resulting in a decreased transmission of paramagnetic enhancement and relaxivity.[34] Beside the

q number and the size of the CA, τ_M can be also optimised by tailoring the coordination chemistry in the immediate vicinity of the Gd^{3+} ion by increasing the steric crowding around the metal and/or exchanging the functional groups. Swapping an acetate oxygen donor arm on the chelate for a different one can drastically influence the water exchange correlation time with τ_M increasing from *phosphonate* $\sim$ *phenolate* $<$ **acetate** $<$ *hydroxamate* $\sim$ *sulphonamide* $<$ *acetamide* $\sim$ *pyridyl* $\sim$ *imidazole*. As can be seen in Fig. 1.6, α-substituted acetates seem to be the most ideal donor groups, which also provide the longest electronic relaxation times.[35]

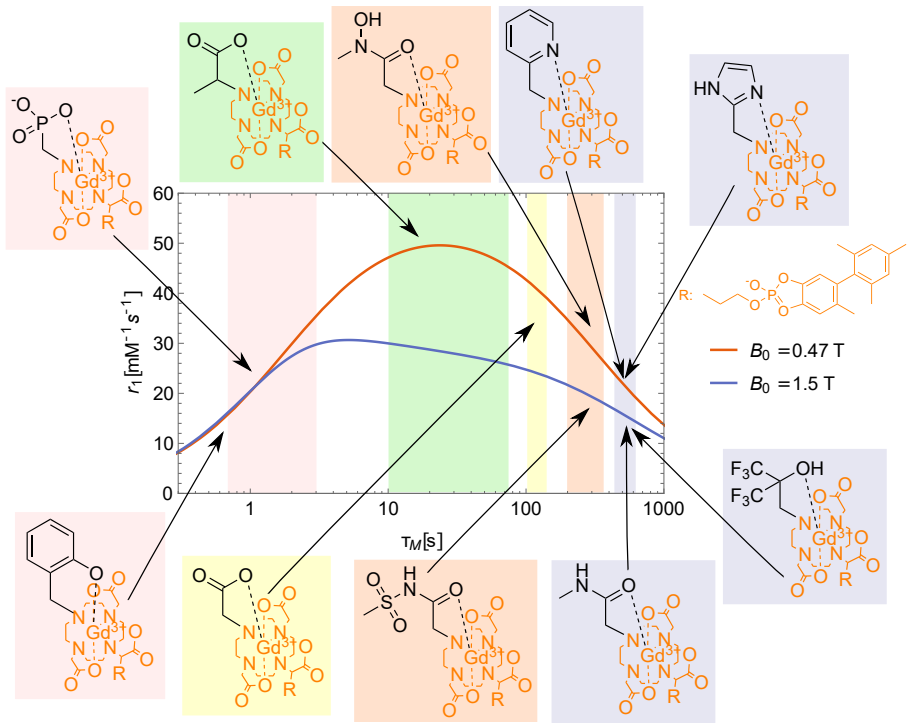


Figure 1.6: Graph showing dependence of longitudinal relaxivity on τ_M at two different magnetic fields has been produced using the parameters given by Ref. [35] R denotes an albumin-binding substituent, which was used for the study in the presence or absence of human serum albumin. Replacing one single donor arm in the DOTA system can have a profound impact on relaxivity, which can be limited if water residency times are either too short (as in the case of phosphinate derivatives) or too long (as in the case of amides).

The water exchange lifetime might not only be dependent on the water molecule exchange, but also on whether the incoming water molecule assists the Gd^{3+}-ligated

water to escape the first coordination sphere (known as associative or dissociative activation mechanism), as well as on the potentially faster prototropic exchange on the ligand itself if any pH-responsive functional groups are present in a 4 Å radius of the coordinated water. The latter process can fortunately be neglected for most chelates if the pH ranges between 2.0 and 8.0.[36] τ_M can thus be determined directly by variable-temperature ^{17}O NMR as the oxygen atom of the coordinated water is closer to Gd^{3+} than the water protons and the chemical shifts of ^{17}O resonances are generally larger than those of ^{1}H.[11] The water exchange rate is temperature-dependent and is considered to comply with the Eyring equation, wherein $\Delta S^{\ddagger}$ and $\Delta H^{\ddagger}$ are the entropy and enthalpy of exchange activation, respectively, while $k_{ex}^{298.15}$ is the exchange rate at 25 °C, R is the gas constant, T is the absolute temperature, k_B is Boltzmann's constant and h is Planck's constant.[37]

$$k_{ex} = \frac{1}{\tau_M} = \frac{k_B T}{h} exp\left\{ \frac{\Delta S^{\ddagger}}{R} - \frac{\Delta H^{\ddagger}}{R \cdot T} \right\} = \frac{k_{ex}^{298.15}}{298.15} exp\left\{ \frac{\Delta H^{\ddagger}}{R} \left(\frac{1}{298.15} - \frac{1}{T} \right) \right\}. \quad (1.13)$$

The equations for ^{17}O NMR relaxation times and chemical shifts have been derived by Swift and Connick.[38] The ^{17}O NMR relaxation times can be determined by subtracting the contribution of the diamagnetic counterpart of the Gd^{3+} complex T_{id}^{o} from the measured paramagnetic enhancement of ^{17}O nuclei (Eq. (1.14)).[39] The ^{17}O longitudinal relaxation time T_{1r} is controlled by dipolar and quadrupolar couplings, both of which are characteristic of the dynamics. The dipolar contribution occurs due to a direct interaction of the oxygen nucleus with the electron spin of the Gd^{3+} ion. Quadrupolar coupling, on the other hand, is a natural result of the ^{17}O nucleus that exhibits a nuclear spin of $I = 5/2$ and thus possesses an electric quadrupole moment. The spectral density of the quadrupolar relaxation depends on the rotational correlation time of the Gd^{3+}-O vector and can thus be used for estimating the τ_R of the molecular monomeric complexes.[40, 37]

The water exchange lifetime τ_M, on the other hand, can be obtained from the reduced transverse relaxation time T_{2r} that is governed by the scalar interaction, which is less important in ^{1}H NMR relaxation since the water protons are farther away from Gd^{3+}.[11, 37]

$$\frac{1}{T_{2r}} = \frac{1}{P_M}\left[\frac{1}{T^o_{2obs}} - \frac{1}{T^o_{2d}}\right] = \frac{1}{\tau_M}\frac{(T^o_{2M})^{-2} + \tau_M^{-1}(T^o_{2M})^{-1} + (\Delta\omega^o_m)^2}{(\tau_M^{-1} + (T^o_{2M})^{-1})^2 + (\Delta\omega^o_m)^2} + \frac{1}{T^o_{2OS}}, \quad (1.14)$$

where $\Delta\omega^o_m$ is the difference in the chemical shift of the inner-sphere and bulk water, T^o_{2M} is the ^{17}O transverse relaxation time of the inner-sphere water and T^o_{2OS} is the T_2 contribution of the outer-sphere water, which is mostly neglected.[37] The intersection of τ_M, $\Delta\omega^o_M$ and T^o_{2OS} in the reduced chemical shift and transverse relaxation time equations can be disentangled by assessing their temperature dependency, whereby four temperature regimes can be distinguished, of which only two are commonly measured by ^{17}O NMR due to vapourising and freezing restrictions of water (Fig. 1.7).[11]

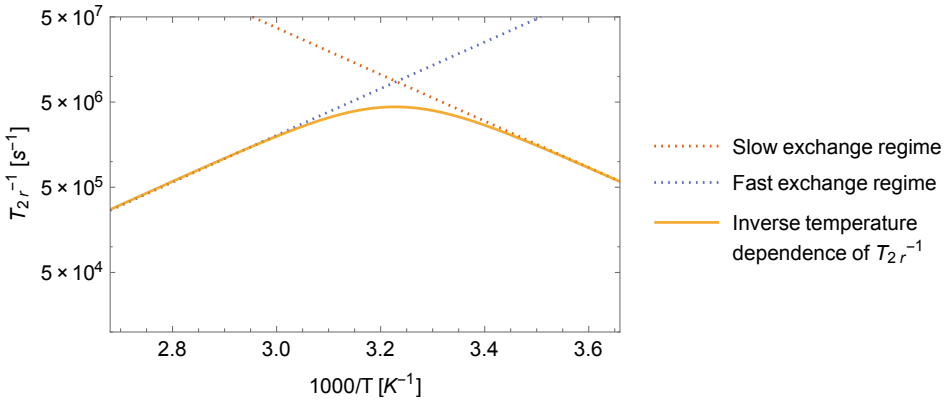


Figure 1.7: Inverse temperature dependence of the reduced ^{17}O relaxation rates of $[Gd(DOTA)(H_2O)]^-$ (depicted in Fig. 1.4) including the fast and slow exchange regimes.[3]

[3] All the parameters and constants were taken from Ref. [37] using Swift/Connick[38] and temperature-dependent electronic relaxation time equations at $B_0 = 14.1$ T:

$$\frac{1}{T_{1e}} = \frac{1}{25}\Delta^2\tau_V(4S(S+1)-3)\left(\frac{1}{1+\omega_S^2\tau_V^2} + \frac{4}{1+4\omega_S\tau_V}\right),$$

$$\frac{1}{T_{2e}} = \Delta^2\tau_V\left(\frac{5.26}{1+0.372\omega_S^2\tau_V^2} + \frac{7.18}{1+1.24\omega_S\tau_V}\right), \qquad \tau_V = \tau_V^{298.15} exp\frac{E_v}{R}\left(\frac{1}{T} - \frac{1}{298.15}\right).$$

At low temperature, a very slow exchange takes place leading to T_{2r}^{-1} and $\Delta\omega_r^o$ being governed by $(T_{2OS}^o)^{-1}$ and $\Delta\omega_{OS}^o$, respectively. If the temperature is increased, which is illustrated by the slow exchange regime in Fig. 1.7, T_{2r}^{-1} becomes faster and proportional to τ_M^{-1}. The maximum of T_{2r}^{-1} represents the transition from slow to fast exchange regime, while the sign of the temperature dependence of T_{2r}^{-1} relies on whether the transverse relaxation is dominated by τ_M or by the relaxation time of the bound water molecule T_{2M}^o. In the fast exchange region, T_{2r}^{-1} is very much influenced by the applied field and proportional to $(\Delta\omega_M^o)^2/k_{ex}$. The fastest exchange is attained at maximum temperatures, where T_{2r}^{-1} and $\Delta\omega_r^o$ are governed by the inner-sphere $(T_{2M}^o)^{-1}$ and $\Delta\omega_M^o$, respectively.[11, 37, 38, 40]

1.2.3 Second- and Outer-Sphere Relaxation

In most cases, the inner-sphere relaxation is the main contributor to the observed relaxivity. However, second- and outer-sphere contributions might also have a non-negligible effect on the relaxivity. The overall contribution to the observed relaxivity of this relaxation mechanism depends on the nature of the chelate's functional groups, hydrogen bond sharing capability of the inner-sphere water as well as on whether water molecules are prevented from binding to the Gd^{3+} centre ($q = 0$).[27] As can be seen in the nuclear magnetic relaxation dispersion (NMRD) profile in Fig. 1.8,[37] the outer-sphere contribution to the longitudinal relaxivity at low fields (0.01-10 MHz) is smaller than that of the inner-sphere, however, at higher magnetic fields, the outer-sphere provides comparable contributions to the overall relaxivity.

The average τ_M' of the second-sphere water can be in the range of picoseconds, which is shorter than τ_R, and needs to be prolonged in order to increase its participation to the overall relaxivity.[39] This can be achieved by replacing, for example, the acetate arms with phosphinates or amides (the latter donor having pendant methylphosphonate or ethyl carboxylate substituents), which result in strengthened

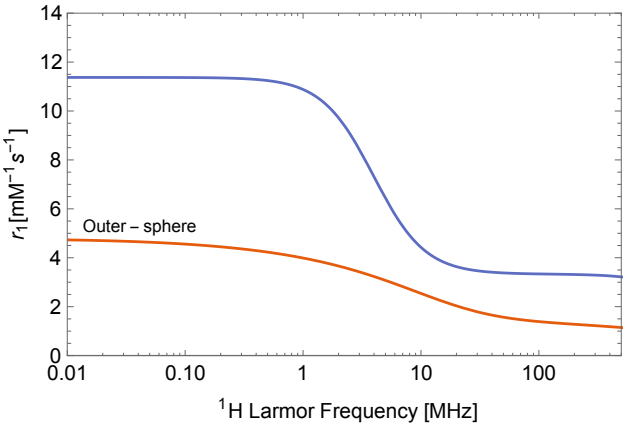


Figure 1.8: Outer-sphere contribution (-) to the overall ^{1}H r_1 (-) of $[Gd(DOTA)(H_2O)]^-$. The graph depicts a modelled NMRD profile that can be practically obtained by measuring relaxation times over a selection of magnetic fields, usually from 0.01 MHz to 20 MHz, while the missing high-field data points are complemented by NMR measurements.

hydrogen bonding interactions with the second-sphere water molecules.[41] If τ'_M or the interaction of the second-sphere water with the organic part of the Gd^{3+} complex takes longer than the translational diffusion time τ_D, *i.e.* the time essential for water molecules to diffuse away from the complex, then the second coordination sphere can be comparable to the inner-sphere relaxation time description (*cf.* Eq. (1.8), q' and τ'_M represent the number of hydrogen-bonded water molecules and their lifetime, respectively). However, if τ'_M becomes shorter than τ_D, the second- and outer-sphere contributions are difficult to be considered separately, especially at imaging fields.[42]

Although difficult to quantify, the outer-sphere relaxation time T_{1p}^{OS} is a result of dipole-dipole coupling between water and the Gd^{3+} ion, and is based on Freed's description of the interaction between free radicals and solvent molecules (Eq. (1.15)).[43] The conventional formulation includes electronic relaxation T_{ie} as well as the diffusion-related effects, such as the distance of closest approach (denoted as a) between the paramagnetic centre and water molecules reflecting the molecular size and charge distribution with τ_D representing the time needed for a solvent molecule to diffuse a distance of $\sqrt{2}a$. τ_D equals a^2/D, wherein D is the sum of the

diffusion coefficients of the Gd^{3+} probe and water.[24, 42, 44, 45]

$$\frac{1}{T_{1p}^{OS}} = \left(\frac{32\pi}{405}\right)\gamma_H^2\gamma_S^2\hbar^2 S(S+1)\frac{N_A[Gd]}{1000aD}\left[3j(\omega_H, T_{1e}) + 7j(\omega_S, T_{2e})\right], \tag{1.15}$$

$$j(\omega, T_{ie}) = Re\left\{\frac{1+\frac{1}{4}\sqrt{i\omega\tau_D + \frac{\tau_D}{T_{ie}}}}{1+\sqrt{i\omega\tau_D + \frac{\tau_D}{T_{ie}}} + \frac{4}{9}\left(i\omega\tau_D + \frac{\tau_D}{T_{ie}}\right) + \frac{1}{9}\sqrt[3]{i\omega\tau_D + \frac{\tau_D}{T_{ie}}}}\right\}. \tag{1.16}$$

Here, N_A represents Avogadro's number, $[Gd]$ is the concentration of the Gd^{3+} complex, Re is the real part of the spectral density expression, while all the other parameters have been described by explaining the Eq. (1.10) and Eq. (1.12) in Sec. 1.2.1.

1.3 Macromolecular Effects on Paramagnetic Relaxation Enhancement

Another strategy to improve the efficiency of CAs is to reduce the local rotational motion by increasing the dimension of a CA. This is achieved when Gd^{3+} probes are incorporated into macromolecular or nanosized carriers, such as dendrimers,[46] zeolites,[47] gadofulerenes[48] and polymers,[40] which may also improve the MRI contrast by delivering a large amount of Gd^{3+} species at the site of interest. The increase in ^1H relaxivity associated with the concurrent elongation of the overall rotational correlation time from the picosecond (50-200 ps for small molecules) to the nanosecond (0.4-50 ns) range is limited by the slow water exchange rate that does not meet the fast exchange condition ($\tau_m << T_{1m}$). Note that this is quite difficult to achieve since the longitudinal relaxation time of the bound water protons T_{1m} can be more than a magnitude shorter than in molecular systems and is thus the main limiting factor of the nanoparticulate water relaxation rate enhancement.[16, 24]

Compared to the slow motion of a nanosized system, fast rotation around the flexible linker through which the Gd^{3+} complex is covalently attached to the surface

of the particle can be another limiting factor in the relaxivity enhancement,[24] while the size of the nanoparticle does not further influence the relaxivity when its radius is larger than about 4 nm (Fig. 1.9).

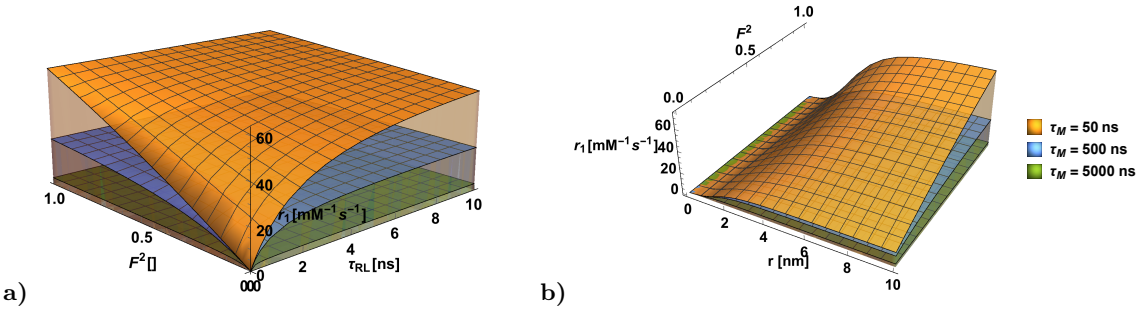


Figure 1.9: 3D graphs showing longitudinal relaxivity dependency on order parameter F^2 as well as on a) τ_{RL} and b) radius of a Gd^{3+} complex-doped nanoparticulate contrast agent[4] with τ_M equalling either 50 ns, 500 ns or 5000 ns at 1.5 T. It is again evident that τ_M can counteract any relaxivity enhancing effects and that these are less dependent on F^2 in the case of τ_{RL} indicating the importance of the local over the global environment. Graph b) also demonstrates that if the radius of a contrast agent is larger than approximately 4 nm, an increase in its size does not further boost r_1, which is more dependent on F^2.

The Lipari-Szabo approach[49] incorporated into the SBM equations (Eq. (1.17) and (Eq. 1.18)) differentiates the contribution of the faster local rotational motion τ_{RL} around the axis of the linker from the slower global rotation of the nanoparticles τ_{RG}. The degree, to which τ_{RL} and τ_{RG} contribute to the overall τ_R, is given by the order parameter F^2 ($0 \leq F^2 \leq 1$). This parameter accounts for numerous states of rotational dynamics (Fig. 1.10). Since its theoretical description is intractable, it can only be obtained from fitted experimental NMRD data (Eq. (1.17), Fig. 1.11). If τ_{RL} is insignificant, as in an absolutely rigid environment, F^2 equals 1. In a more flexible conformation, where F^2 approaches 0, the internal motions become entirely independent of the global motion (Fig. 1.10).[47] These nanoscale effects on the inner-

[4]The τ_{RG} dependency on the particle radius r was determined by the Stokes equation,[11] where k_B represents Boltzmann's constant, η the viscosity of water and T the absolute temperature:

$$\tau_{RG} = \frac{4\pi\eta r^3}{3k_B T}$$

sphere contribution to the longitudinal relaxation time of the bound water T_{1m} are described by the following equation:[24]

$$\frac{1}{T_{1m}^{LS}} = \frac{2}{15}\left(\frac{\mu_0}{4\pi}\right)^2 \frac{\gamma_H^2 g_e^2 \mu_B^2 S(S+1)}{r_H^6}\left[\frac{3F^2\tau_{d_1G}}{1+\omega_H^2\tau_{d_1G}^2} + \frac{3(1-F^2)\tau_{d_1}}{1+\omega_S^2\tau_{d_1}^2} + \frac{7F^2\tau_{d_2G}}{1+\omega_H^2\tau_{d_2G}^2} + \frac{7(1-F^2)\tau_{d_2}}{1+\omega_S^2\tau_{d_2}^2}\right]; \tag{1.17}$$

$$\frac{1}{\tau_{d_iG}} = \frac{1}{T_{ie}} + \frac{1}{\tau_M} + \frac{1}{\tau_{RG}}; \qquad \frac{1}{\tau_{d_i}} = \frac{1}{\tau_{d_iG}} + \frac{1}{\tau_{RL}}; \qquad i = 1, 2. \tag{1.18}$$

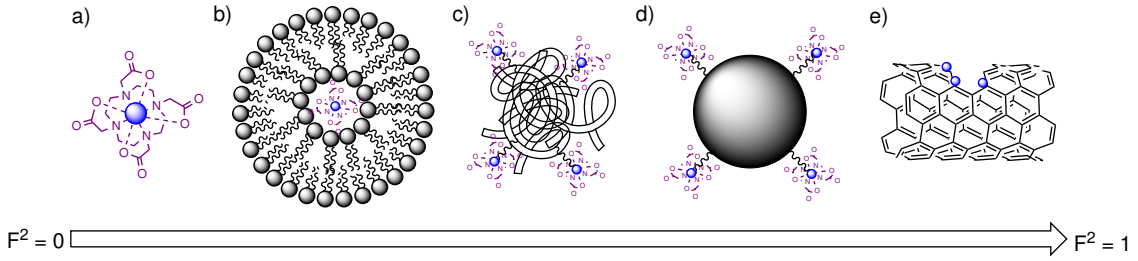


Figure 1.10: Schematic representation of the order parameter F^2 increasing in the following sequence, which corresponds to a more rigid environment and higher relaxivity: a) molecular Gd^{3+} complexes,[37] b) Gd^{3+} complexes incorporated into the lumen of the liposomes,[50] c) Gd^{3+} complexes covalently bound to polymers,[51] d) Gd^{3+} complexes appended to solid nanoparticles[47] and e) Gd^{3+} ion clusters confined within the single-walled carbon nanotubes.[52] This figure also shows that if any residual CAs are physisorbed rather than covalently attached to the surface, much higher relaxivities can be attained similar to those of the example e), where the flexible conjugation linker is missing ($\tau_{RL} \approx \tau_{RG}$) as Gd^{3+} is directly incorporated into the nanoparticulate matrix.

As depicted in Fig. 1.8, the typical NMRD profiles of small molecular CAs contain a characteristic plateau in the lower frequency range (0.01-1 MHz), followed by a decreasing slope due to $\omega_S\tau_C \approx 1$ and the final plateau in the higher frequency range ($>$ 10 MHz). If the molecular Gd^{3+} probes are incorporated into a nanodimensional matrix (Fig. 1.11), a distinctive peak appears after the plateau at approximately 20-50 MHz, which represents the strong influence of rotational correlation time and electronic relaxation time. If the molecular tumbling is reduced, the NMRD peak is not just increased, but also shifted to lower frequencies.[24]

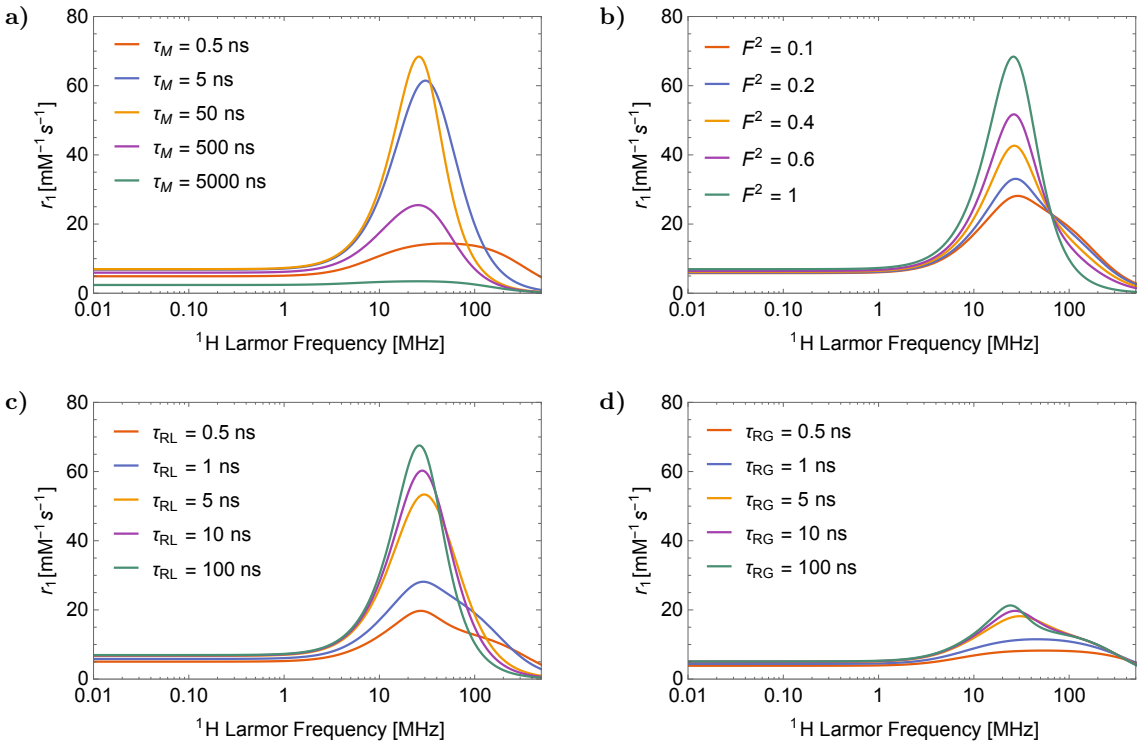


Figure 1.11: NMRD curves demonstrate the importance of the optimal τ_M over τ_R (graph a)) and τ_{RL} over τ_{RG} (graphs b), c) and d)). Graph a) shows that τ_M can outweigh the relaxation-enhancing effects of a slowly tumbling and internally rigid CA (τ_{RG} = 10 ns, τ_{RL} = 5 ns, F^2 = 0.9 ns) if it is smaller than 0.5 ns and larger than 100 ns. Graph c) shows that the contribution of internal motion is also more important than the global tumbling of the particle (τ_{RG} = 10 ns, F^2 = 0.1 ns, τ_M = 50 ns). As a result, b) F^2 has a similar impact on relaxivity (τ_{RG} = 10 ns, τ_{RL} = 1 ns, τ_M = 50 ns). Graph d) illustrates that r_1 cannot be substantially increased when the internal motions are fast (τ_{RL} = 0.5 ns, F^2 = 0.1 ns, τ_M = 50 ns) no matter how elongated τ_{RG} might be. For high field applications, on the other hand, r_1 is highest when τ_{RL} is shortest (in this case 0.5 ns and 1 ns).

1.3.1 Zeolites and Mesoporous Nanosized Materials as Efficient Nanoparticulate MRI-Reporters

Biocompatible and functionalisable nanosized porous materials provide a large surface area and uniform porous space that is suitable for the accommodation of numerous Gd^{3+} species. Regarding the pore size, such materials can be described as microporous (with pore diameters of 2 nm and below), mesoporous (2-50 nm) or macroporous (above 50 nm).[53] Among the microporous materials, crystalline zeolites with Gd^{3+} ions incorporated into the cavities have been intensively studied as MRI CAs,

especially of NaY type with a silicate-to-alumina ratio of greater than 1.5.[54, 55] As the negative charge of anionic AlO_4 tetrahedra are counterbalanced by exchangeable counter cations (*e.g.* K^+ or Na^+), Gd^{3+} or Mn^{2+} can be introduced into the silicate-alumina framework of zeolites through ion exchange. However, small pores and slow diffusion from the interior of the zeolite proved to be one of the limiting factors of the theoretically attainable relaxivity.[47]

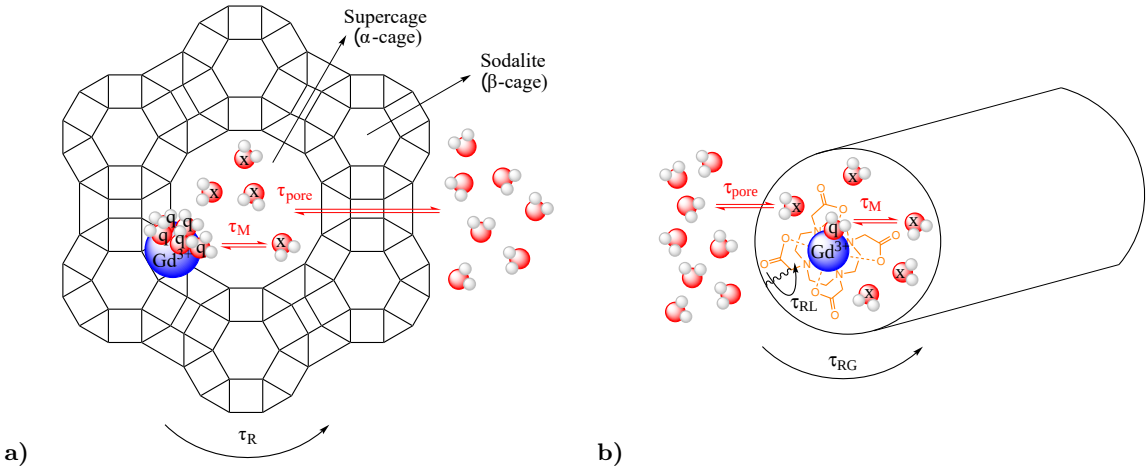


Figure 1.12: Schematic representation of a) NaY zeolite framework with incorporated Gd^{3+} species in a sodalite cage protruding into the supercage[55], while b) represents a mesopore of mesoporous silica with a Gd^{3+} chelate appended to the wall of the pore.[56]

Although GdNaY ($q = 7$) is resistant to low pH and re-exchange with alkali cations, bulky Gd^{3+} chelates would be too big to enter the cages (1.18 nm in diameter) and could be introduced into the pore system only by a ship-in-a-bottle type synthesis or onto the silanol groups of the outer surface by grafting chlorosilanes or alkoxysilanes that act as linkers (Fig. 1.12). For the latter type of synthesis, amorphous mesoporous silica nanoparticles (MSNs) are more suitable as they can accommodate Gd^{3+} complexes inside the channels (2-50 nm, of which 2-8 nm are used for MRI CAs) that can either run in a parallel arrangement as 2D hexagonal arrays of cylindrical mesopores (*e.g.* MCM-41 (2-6 nm pore size), SBA-15 (5-10 nm)) or can build up a 3D porous geometry (*e.g.* MCM-48 (2-4 nm pore size)).[47] The desired porous structures and sizes

can be attained by implementing suitable surfactant templates (*e.g.* cetyltrimethylammonium bromide (CTAB) for MCM-41, Pluronic P103 (EO_{17}-PO_{55}-EO_{17}, where EO = poly(ethylene oxide) and PO = poly(propylene oxide)) for SBA-15,[57] or a mixture of CTAB and Pluronic F127 (EO_{106}-PO_{70}-EO_{106}) for MCM-48).[58] For MRI applications, Gd^{3+} chelates such as DOTA-monoamide derivatives have been incorporated into the mesopores of SBA-15 and MCM-41 MSNs, which exhibited respective relaxivities of 7 mM^{-1} s^{-1} and 27 mM^{-1} s^{-1} at 20 MHz,[56] while higher relaxivities have been shown to correlate with bigger pores due to an increased number of free water molecules (denoted as x) per Gd^{3+} ion and due to a reduced residence time of water molecules within the pores τ_{pore}.[59]

In the porous systems, it is the diffusion of water from the interior of the pores to the bulk that limits the relaxivity. Therefore, Peters *et al.* [55] developed a "two-step" model for NMRD analysis, whereby in the first step, only the relaxivity inside the cavity is considered, in which water molecules in the first coordination sphere of Gd^{3+} ions exchange with free water molecules inside the zeolite. Eq. (1.19), derived from the Bloch equations, gives the ^1H longitudinal relaxation rate of water inside the pore $T_{1,pore}^{-1}$ at high Gd^{3+} concentration.[55]

$$\frac{1}{T_{1,pore}} = \frac{\frac{q}{x}}{\tau_{pore} + T_{1,m}\left(1 + \frac{q}{x}\right)}, \tag{1.19}$$

where $T_{1,m}$ is the longitudinal relaxation time of the inner-sphere water protons, which is given either by the SBM or by the Lipari-Szabo-modified SBM theory depending on whether Gd^{3+} is fixed into the matrix as in the case of zeolites or if it is appended within the pore via a linker as in the case of MSNs (Fig. 1.12). Hereby, the overall global rotation of the nanosized system τ_{RG} must be considered separately from the contribution of the faster local motion τ_{RL}.[24, 49]

In the second step, the exchange of water is considered between the inside of the

pore and the bulk by diffusion through the pore channels. This step enables the propagation of the relaxation enhancement from the interior of the material to the bulk water outside. If the chemical exchange between protons in two magnetically distinct environments (*i.e.* inside and outside the zeolite) takes place under highly dilute conditions of the paramagnetic entities, the proton longitudinal relaxivity reads:

$$r_1^{IS} = \frac{P_{pore}}{\tau_{pore} + T_{1,pore}} = \frac{x+q}{55.6 \cdot 10^3} \frac{1}{\tau_{pore} + T_{1,pore}}. \tag{1.20}$$

For zeolite-immobilised Gd^{3+}, the contribution of water molecules diffusing past the paramagnetic centre can be neglected for both the exterior and the interior, particularly at Larmor frequencies higher than 0.1 MHz.[55, 59] In the case of Gd^{3+} chelated into an organic ligand appended to mesoporous silica nanoparticles, second- and outer-sphere water interactions may become very important contributing mechanisms, which will be investigated in Ch. 2 and 3.

1.4 Physiologically Responsive Molecular and Nanoparticulate MRI-Based Sensors

In addition to the role of concentration, MR frequency, temperature and electronic properties of CAs, several other physicochemical parameters, such as τ_m, τ_R, water accessibility to the probe as well as the number of inner- and second-sphere water molecules can be manipulated to produce changes in relaxivity.[4] Upon tuning these parameters, stimuli-responsive contrast agents can be designed so that MRI contrast is either triggered or diminished in a specific microenvironment in response to various physiological triggers, such as a change in pH,[60] the presence of specific biomolecules (*e.g.* human carboxypeptidase B),[61] certain cations (*e.g.* Cu^{2+})[62] and a reducing environment.[63] The former two examples are depicted in Fig. 1.13, with a) showing copper sensing through modulation in the coordination environment of a Gd^{3+} CA

that results in increased q and thus larger r_1 values,[62] while b) illustrates the dissolution of perthiolated β-cyclodextrin-based nanocapsules with incorporated Gd^{3+} complexes by reduction of the disulphide bonds connecting the cyclodextrin units with tris(2-carboxyethyl)phosphine (TCEP) resulting in decreased τ_R and r_1 values.[63]

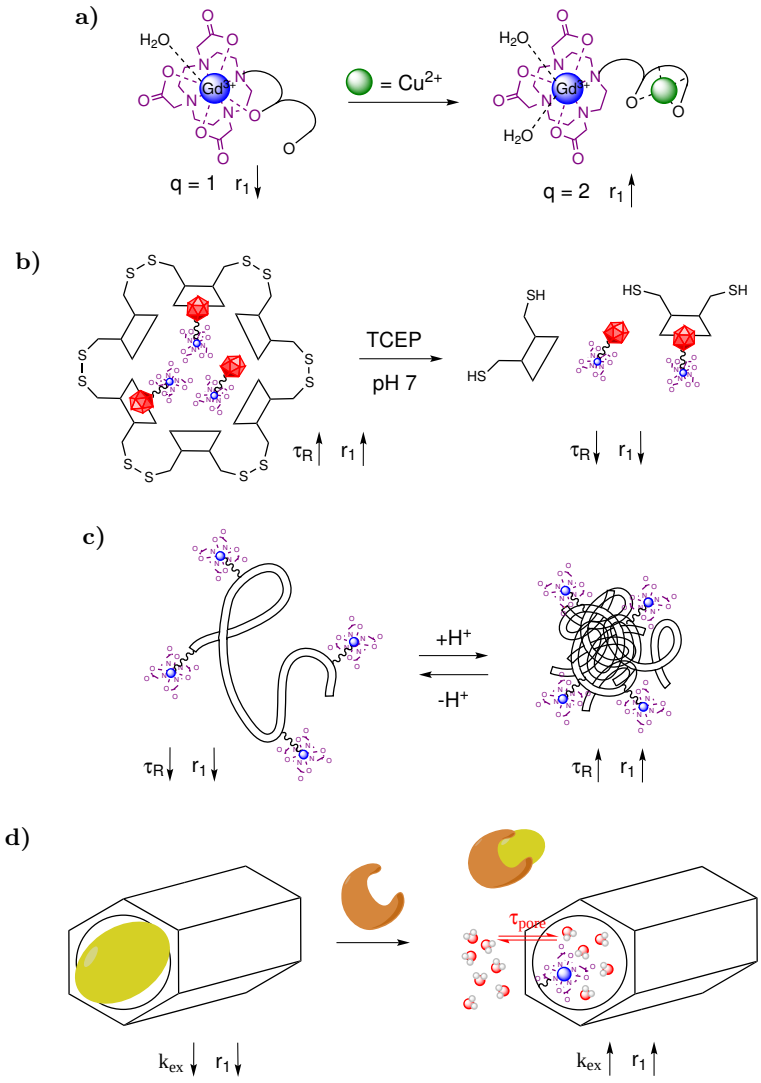


Figure 1.13: Schematic drawing of molecular and nanoparticulate contrast agents responsive to a) metal cations,[62] b) reducing environment,[63] c) pH[51] and d) presence of specific proteins.[64] The corresponding MRI contrast responsiveness occurs due to a change in a) q value, b-c) rotational correlation time and d) water exchange rate.

The physicochemical parameters were also utilised in nanoparticulate MRI probes to reveal variations in pH in the region of interest,[65] which are useful in the

detection of a pathological microenvironment, such as malignant tissue with pH ranging from 5.8 to 7.0, while the physiological pH is around 7.4.[66] pH-triggered changes in T_1 contrast are frequently accomplished via alternations in F^2,[67] q,[68] τ_R[69] or τ_M[70] through the incorporation of pH-responsive Gd^{3+} chelates that possess pKa values around physiological pH by employing functional groups, such as arylsulphonamide,[71] imidazole,[65] nitrophenol,[72] ketal[73] and phosphonate,[74] which affect the q value as a result of a change in pH. For instance, Aime *et al.* [75] loaded large unilamellar vesicles with an amphiphilic Gd^{3+}-DO3A derivative bearing a sulphonamide moiety that was protonated at low pH. This caused a removal of the arm from the coordination cage of the Gd^{3+} ion (change in q from 0 to 2) as well as the Gd^{3+} complex intercalation into the liposomal membrane. This in turn led to an increased τ_R with respect to the free complex, a higher membrane permeability to water and, consequently, an enhanced longitudinal relaxation rate, which was recorded at two different magnetic fields in order to obtain a ratiometric map.[75]

On the other hand, a pH-triggered response across a nanoparticle scaffold could be achieved by gating water accessibility to the mesopores (Fig. 1.13 d)),[64] by conformational conversion between a compact globular and less rigid extended form of the polymeric nanoparticles (Fig. 1.13 c)),[51] through the incorporation of either cleavable linkers[76] or monomers with responsive functional groups,[77] and by switching between hydrophobic interactions and electrostatic repulsions of the polymer chains.[67] The latter approach will be tested as a water-gating mechanism at the mesopores of mesoporous silica nanoparticles loaded with Gd^{3+} chelates in Ch. 4.

1.4.1 q Number and Luminescence Studies

The determination of hydration states of Gd^{3+} complexes in aqueous solution is of significant interest to the design of thermodynamically stable, kinetically inert and q-activatable MRI CAs. Studying the luminescence properties of Gd^{3+} chelates directly

is challenging due to their unfavourable molar absorptivity and weak luminescence in solution.[78] As Gd^{3+} possesses excited states lying higher in energy than the triplet state of a ligand, analogous Eu^{3+}, Tb^{3+} and Yb^{3+} complexes having excited states below the triplet state energies (Fig. 1.14) are usually prepared and a huge laser-induced photon flux is deployed as the excitation source.[79]

The first assessment of the hydration state by measuring the luminescence decay rates of Eu^{3+} and Tb^{3+} complexes in H_2O and D_2O was reported by Horrocks and Sudnick.[79] The deactivation of the luminescence of excited Ln(III) ions is a result of a vibrational energy transfer involving the oscillators of the bound ligand or solvent molecules. The OH oscillators of coordinated or closely diffusing H_2O trigger the deactivation of the $^5D_0$ excited state in the case of Eu^{3+}, while its deuterium-based counterparts are ineffective quenchers of the excited state. This is because the corresponding OD oscillators possess lower stretching frequencies, thus providing a difference between luminescence decay rates in H_2O ($\tau^{-1}_{H_2O}$) and D_2O ($\tau^{-1}_{D_2O}$), which is directly proportional to the q value.[79, 80, 81]

$$q = A(\tau^{-1}_{H_2O} - \tau^{-1}_{D_2O} - k_{XH}), \tag{1.21}$$

$$k_{XH} = \alpha + \beta n_{OH} + \gamma n_{NH} + \delta n_{O=CNH}, \tag{1.22}$$

where A denotes the proportionality constant for lanthanide susceptibility to non-radiative deactivation by OH oscillators, k_{XH} is the sum of various weaker quenching contributions (defined by β, γ and δ constants) from n number of alcoholic (OH), secondary amine (NH) and amide (O=CNH) oscillators located on the chelating ligands, while α represents the $^5D_0$ deactivation constant of the second-sphere and closely diffusing water molecules.[80, 82]

The information on the inner-sphere water displacement by anion binding and ternary complex formation can be provided either by prolonged Eu^{3+} excited state

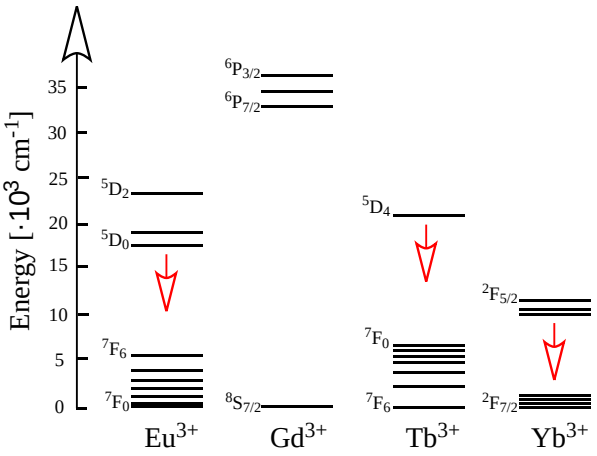


Figure 1.14: Electronic energy level scheme for Eu^{3+}, Gd^{3+}, Tb^{3+} or Yb^{3+}, wherein the downward pointing red arrows show the lanthanide luminescent state. For example, in the case of Eu^{3+}, excitation of the $^5D_2$ state is succeeded by swift non-radiative relaxation to the luminescent $^5D_0$ state and emission to the ground ^7F states, resulting in typical peaks in the luminescence emission spectra.

lifetimes[82] or by changes in the intensity of Eu^{3+} emission bands.[83] In the latter case, the binding affinities can be investigated by plotting the intensities of emission peaks as a function of added water-displacing substrate, followed by non-linear regression fitting and association constant determination. The strongest emissions emerge from $^5D_0 \rightarrow {}^7F_1$, $^5D_0 \rightarrow {}^7F_2$ and $^5D_0 \rightarrow {}^7F_4$ transitions (Fig. 1.14), while others are mostly very weak or absent. The $^5D_0 \rightarrow {}^7F_1$ one around 590 nm has a strong magnetic dipole character, which is not influenced by the ligand environment, while the electric-dipole-allowed $^5D_0 \rightarrow {}^7F_2$ and $^5D_0 \rightarrow {}^7F_4$ transitions are very sensitive to the coordination environment.[83, 84] Luminescence measurements will therefore be implemented to reveal both the number of bound inner-sphere water molecules and the change in coordination environment at the lanthanide in the presence of oxy-anions.

1.4.2 Concentration-Independent Responsive MRI Contrast Agents

The responsive Gd^{3+}-based CAs have a common limitation attributed to the inability to quantify the concentration of a contrast agent present *in vivo* at the

site of interest. Because of the heterogeneous endogenous tissue signals, it is impossible to determine the magnitude of the response, while in the *in vitro* studies the metal concentration can be straightforwardly confirmed.[2] There are several alternative approaches available that circumvent this problem including chemical exchange saturation transfer (CEST) contrast agents carrying multiple exchangeable protons with distinct chemical shifts,[85] dual MRI-PET agents with an additional $^{18/19}$F functionality,[86] ligand-field-induced chemical shifts of nearby protons generated by certain Ln^{3+}-containing complexes,[87] ratiometric MRI contrast agents with a ratio between transverse and longitudinal paramagnetic relaxation rates depending on the parameter of interest, but not on the concentration, and dual ^{19}F/^{1}H MRI contrast agents.[68]

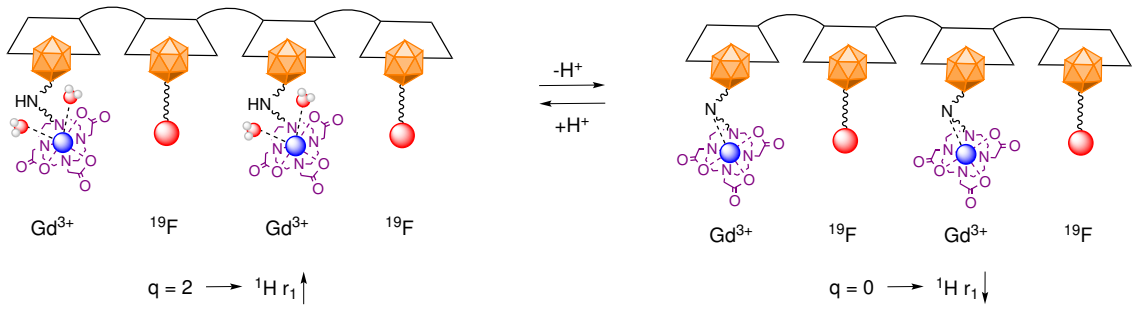


Figure 1.15: Illustration showing potential ratiometric pH mapping probe for dual ^{19}F/^{1}H MRI, wherein diamonds represent an adamantane moiety binding to poly-β-cyclodextrins represented by connected trapezoids.[68]

In the latter case, a ratiometric ^{19}F/^{1}H mapping of pH (Fig. 1.15) was examined *in vitro* with a Gd^{3+} chelate based on a pH-sensitive sulphonamide group and a fluorinated reporter, the latter serving as a concentration reporting moiety. Both were bearing an adamantane group that was non-covalently hosted by a macromolecular carrier consisting of poly-β-cyclodextrin units, thus preventing the ^{19}F MRI probe to be too close to the fast relaxing Gd^{3+} that would have otherwise caused broadening and consequently inaccuracies in the determination of the concentration. Upon depro-

tonation at high pH, the sulphonamide arm of DO3A entered the coordination cage of Gd^{3+} replacing the two inner-sphere H_2O molecules ($q = 0$), thus decreasing the relaxivity.[68] In Ch. 6, Gd^{3+} and ^{19}F MRI probes will both be covalently incorporated into a pH-responsive polymeric scaffold in order to prepare concentration-independent MRI CAs having an easily exchangeable stimuli-responsive matrix.

1.5 ^{19}F MRI Contrast Agents

The high concentration of protons distributed throughout the body also makes it difficult to detect targeted contrast agents with ^1H MRI.[88] Fluorinated agents offer great specificity since ^{19}F MRI measurements do not suffer any interference from a background signal. This is because the negligible ^{19}F NMR signal stems from immobilised fluorine in the bone matrix and teeth, which exhibits very short relaxation times and is thus undetectable, while the detectable mobile fluorine is essentially absent in the human body (less than 10^{-3} μmol/g wet tissue weight).[89] Fluorine naturally constitutes 100 % of the NMR-active isotope ^{19}F with a nuclear spin of 1/2 and resonates at a frequency that is 94 % of that of ^1H, potentially allowing for the use of existing ^1H MRI scanner infrastructure for ^{19}F MRI measurements. Therefore, fluorine also possesses a high intrinsic sensitivity, which almost matches the one for ^1H at 83 % at constant field for an equal number of nuclei so that the ^{19}F NMR peaks in fluorine-containing compounds can nearly be as easily detected as the ^1H ones.[90]

Although a background ^{19}F NMR signal is absent in the human body, the acquisition of sufficient signal intensity in a reasonable time remains the foremost disadvantage of the ^{19}F MRI. Thus, ^{19}F MRI contrast agents have to be administered in high dosage to give signals of sufficient intensity.[89, 91] Increasing the concentration of a ^{19}F MRI probe results in reduced solubility[92] and molecular mobility, which shortens the transverse relaxation time and diminishes the MRI signal.[93] To overcome

this problem, nanoparticles such as amphiphilic diblock copolymeric micelles,[94] dendrimers,[95] emulsions or core-shell silica nanoparticles[96] have been designed, which contain the fluorinated moiety within a fluid environment (Fig. 1.16).[92]

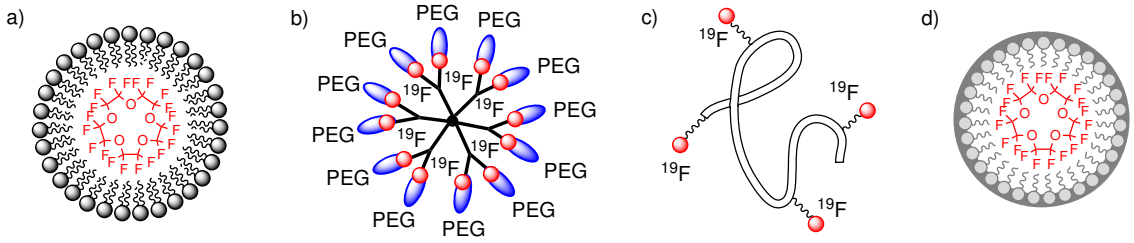


Figure 1.16: Depiction of typical nanoparticulate and macromolecular ^{19}F MRI CAs in the form of: a) liposomes,[97] b) dendrimers,[98] c) polymers[94] and d) core-shell silica nanoparticles.[96]

The relaxation of ^{19}F nuclei is mediated by inter-nuclear dipole-dipole interactions (DD) when fluorine is within van der Waals contact of hydrogen nuclei and by chemical shift anisotropy (CSA) that occurs due to the Zeeman interaction with the external magnetic field.[99, 100] The most simplified T_1 and T_2 relaxation of ^{19}F nuclei in macromolecular species incorporating the Bloch-Redfield-Wangsness theory[101] and the Lipari-Szabo restricted motion model for the spectral density $J(\omega)$ can be described in the following expressions:[99, 100]

$$\begin{aligned}\frac{1}{T_1^{19F}} =& \frac{1}{T_1^{DD}} + \frac{1}{T_1^{CSA}} = \frac{1}{4}\left(\frac{\gamma_H\gamma_F\hbar\mu_0}{4\pi r_{HF}^3}\right)^2 (3J(\omega_F) + 6J(\omega_H+\omega_F) \\ &+ J(\omega_H-\omega_F)) + \frac{\Delta\sigma^2 B_0^2\gamma_F^2}{3}J(\omega_F),\end{aligned} \tag{1.23}$$

$$\begin{aligned}\frac{1}{T_2^{19F}} =& \frac{1}{T_2^{DD}} + \frac{1}{T_2^{CSA}} = \frac{1}{4}\left(\frac{\gamma_H\gamma_F\hbar\mu_0}{4\pi r_{HF}^3}\right)^2 (4J(0) + J(\omega_H-\omega_F) \\ &+ 3J(\omega_F) + 6J(\omega_H) + 6J(\omega_H+\omega_F)) + \frac{\Delta\sigma^2 B_0^2\gamma_F^2}{18}(4J(0) + 3J(\omega_F)),\end{aligned} \tag{1.24}$$

$$J(\omega) = \frac{2}{5}\left(\frac{F^2\tau_{RG}}{1+\omega^2\tau_{RG}^2} + \frac{(1-F^2)\tau_C}{1+\omega^2\tau_C^2}\right), \qquad \frac{1}{\tau_C} = \frac{1}{\tau_{RG}} + \frac{1}{\tau_I}. \tag{1.25}$$

Here, r_{HF} is the distance of F-H dipolar interaction,[5] $\Delta\sigma$ is the chemical shift tensor anisotropy parameter, τ_c is the overall correlation time, τ_I is the internal motional correlation time, γ_F and γ_H are the respective gyromagnetic ratios of fluorine and hydrogen, ω_F and ω_H are the respective Larmor frequencies of fluorine and proton, $\hbar$ is the reduced Planck constant and μ_0 is the vacuum permeability.[100] The graph modelled after these functional relations (Fig. 1.17) demonstrates the effects of reduced mobility and rigidity on diminishing ^{19}F T_2 relaxation times.

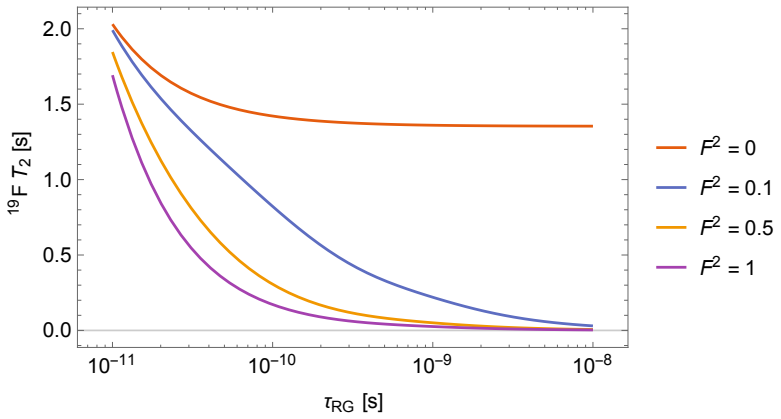


Figure 1.17: Graph of ^{19}F transverse relaxation time dependency on global rotational time τ_{RG} and order parameter F^2 at 7.0 T and $\tau_I = 5 \cdot 10^{-12}$ s by considering contributions from CSA and dipole-dipole relaxation ($r_{FH} = 2.4$ Å and $\Delta\sigma = 5 \cdot 10^5$ rad s^{-1}).[102]

If the internal and global motions are slightly restricted, the ^{19}F relaxation times will become increasingly short and the ^{19}F NMR signal will merge with the baseline and become undetectable. These effects are fundamentally different from the ones observed in ^{1}H MRI because the presence of fluorine is not detected indirectly, such as for the proton of exchangeable water ligated to the paramagnetic CA, but is rather directly contained with the system under inspection, for which reason both CSA as well as global and internal motions contribute substantially to the observed relaxation times and linewidths of the ^{19}F NMR spectra. This can thus quickly lead to an

[5] In the presence of a -CF_3 group, the dipole-dipole contribution becomes more complex and fluorine-fluorine interaction must also be included in the DD term.

attenuation of the ^{19}F NMR signal, which will be investigated in Ch. 5.

1.5.1 Paramagnetically Enhanced ^{19}F NMR Relaxation

Aside from improving the delivery of fluorinated probes, the sensitivity of ^{19}F MRI can be further enhanced with the introduction of a proximate paramagnetic centre, such as a lanthanide chelate that enhances the ^{19}F relaxation rates, thus improving the signal-to-noise ratio and allowing for more rapid data acquisition per unit time.[103] The so called paramagnetic relaxation enhancement (PRE) effect requires Ln^{3+}-based probes to be positioned in the 4.5-7.5 Å range.[104] This is because the abrupt distance dependence (*i.e.* r_{FLn}^{-6}) of the electron-nuclear dipolar interaction defines the nuclear spin relaxation rates and makes the PRE inefficient if the ^{19}F-Ln^{3+} distance is too large. However, at very short distances, severe line-broadening results in the loss of the MRI signal. The diamagnetic inter-nuclear DD and CSA contributions as described in Eq. (1.23) and Eq. (1.24) are insignificant in contrast to the dominant paramagnetic DD contribution. The scalar mechanism is also negligible in comparison because of its strong distance reliance, while the electronic relaxation time and magnetic dipole moment of the lanthanides play an important role in the PRE ^{19}F NMR relaxation. This is expressed through Curie relaxation in the following equations:[103]

$$\begin{aligned}\frac{1}{T_1^{19F-PRE}} =& \frac{1}{T_1^{DD}} + \frac{1}{T_1^{C}} = \frac{2}{15}\left(\frac{\mu_0}{4\pi}\right)^2 \frac{\gamma_F^2 g_e^2 \mu_B^2 S(S+1)}{r_{FLn}^6}\left[\frac{7\tau_{PRE}}{1+\omega_S^2\tau_{PRE}^2}\right. \\ &\left. + \frac{3\tau_{PRE}}{1+\omega_F^2\tau_{PRE}^2}\right] + \frac{2}{5}\left(\frac{\mu_0}{4\pi}\right)^2 \frac{\omega_F^2 (g_e^2\mu_B^2 S(S+1))^2}{(3k_BT)^2 r_{FLn}^6}\frac{3\tau_R}{1+\omega_F^2\tau_R^2},\end{aligned} \tag{1.26}$$

$$\begin{aligned}\frac{1}{T_2^{19F-PRE}} &= \frac{1}{T_2^{DD}} + \frac{1}{T_2^{C}} = \frac{1}{15}\left(\frac{\mu_0}{4\pi}\right)^2 \frac{\gamma_F^2 g_e^2 \mu_B^2 S(S+1)}{r_{FLn}^6}\left[4\tau_{PRE} + \frac{3\tau_{PRE}}{1+\omega_F^2\tau_{PRE}^2}\right. \\ &\left. + \frac{13\tau_{PRE}}{1+\omega_S^2\tau_{PRE}^2}\right] + \frac{1}{5}\left(\frac{\mu_0}{4\pi}\right)^2 \frac{\omega_F^2 (g_e^2\mu_B^2 S(S+1))^2}{(3k_BT)^2 r_{FLn}^6}\left[4\tau_R + \frac{3\tau_R}{1+\omega_F^2\tau_R^2}\right],\end{aligned} \tag{1.27}$$

where γ_F is the gyromagnetic ratio of the ^{19}F nucleus, r_{FLn} is the distance between fluoride and Ln^{3+}, ω_S and ω_F are the electron and ^{19}F Larmor frequencies, T is the absolute temperature and k_B is Boltzmann's constant, while all the other parameters have been described on P. 10. τ_{PRE} is a correlation time that depends on the rotational correlation time τ_R and longitudinal electronic relaxation time T_{1e}.[103]

$$\frac{1}{\tau_{PRE}} = \frac{1}{\tau_R} + \frac{1}{T_{1e}}. \tag{1.28}$$

The PRE ^{19}F relaxation rates thus strongly depend on the electronic relaxation times and the magnetic moment of the lanthanide, on the rotational correlation time of the complex, and on the electron-nuclear separation as illustrated in Fig. 1.18, in which case the ^{19}F NMR relaxation rates are paramagnetically enhanced by Gd^{3+}. The influence of the rotational correlation time on ternary complex formation between a carboxylated ^{19}F MRI probe and a Gd^{3+} complex will be investigated in Ch. 6.

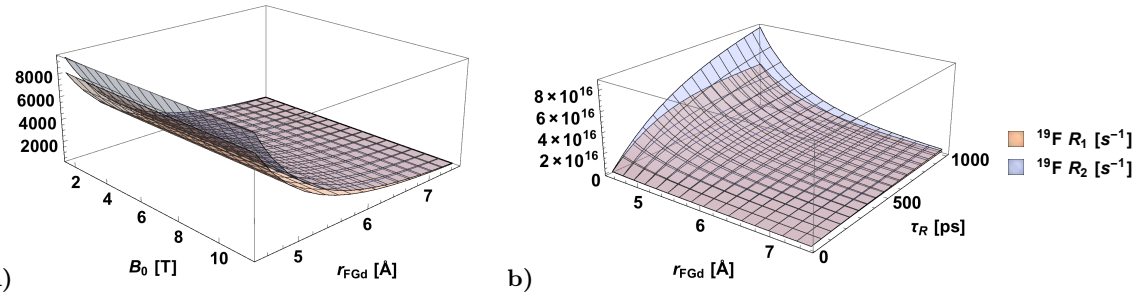


Figure 1.18: 3D graphs show an effect of fluorine-Gd^{3+} separation r_{FGd}, rotational-correlation time τ_R and magnetic field B_0 on paramagnetically enhanced ^{19}F relaxation rates at 298 K. The 3D graphs were obtained either with fixed a) τ_R at 50 ps or b) B_0 at 7.0 T. T_{1e} was set to 1.4 ns.

1.5.2 Environmentally Responsive PRE ^{19}F MRI Contrast Agents

Owing to the distance-dependent relaxation enhancement, the covalent incorporation of a fluorinated group into a lanthanide chelate has enabled the development of

functional ^{19}F MRI probes that can report the presence of enzymes,[105, 106] endogenous alkali metal cations,[107] metabolites[108] and changes in pH[68] by altering the lanthanide coordination environment.

Two approaches of PRE probe design have been reported. In the first instance, irreversible transformation within a probe takes place. Mizukami *et al.* [106] developed a probe consisting of a Gd^{3+}-DO3A complex (Fig. 1.19 a)) coupled to a reporting fluorine moiety via an enzyme peptide sequence that was specifically recognised and cleaved by caspase-3, thus releasing the fluorinated probe and negating the intramolecular PRE. This led to T_2 lengthening and ^{19}F NMR signal recovery.[106]

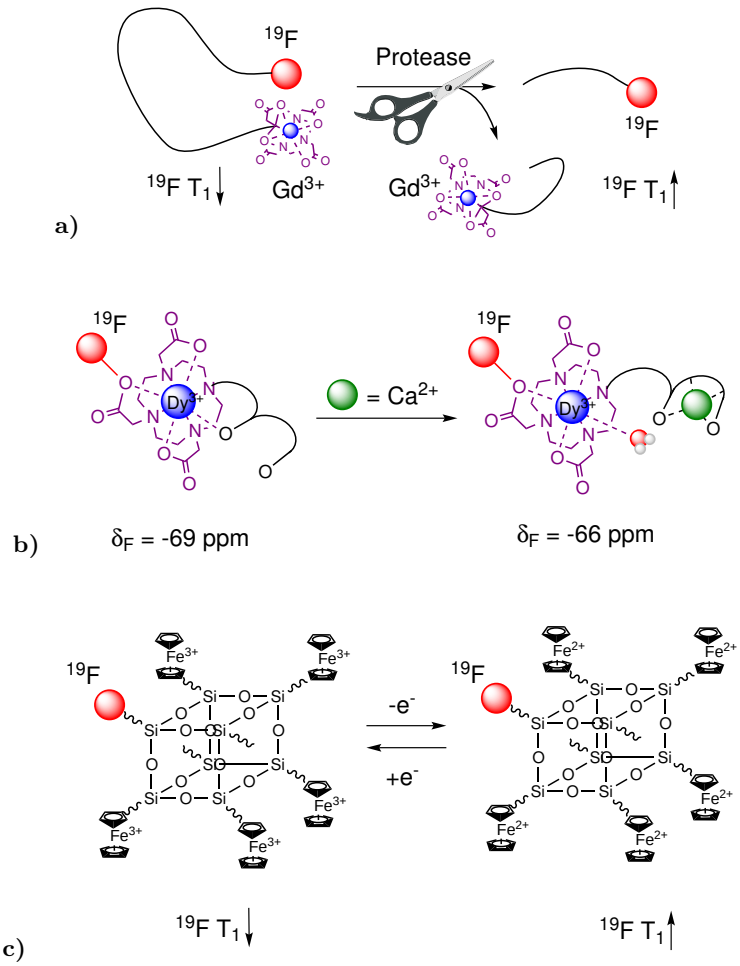


Figure 1.19: Schematic representation showing PRE ^{19}F MRI CAs responsive to a) proteolysis-capable enzymes (*e.g.* caspase),[106] b) metal cations[107] and c) presence of redox-active species.[109]

Further examples of smart ^{19}F MRI CAs include a paramagnetic ^{19}F NMR chemical shift probe (Fig. 1.19 b)) that responds selectively to calcium. Calcium affects the coordination geometry of Ln^{3+} and thus changes the ^{19}F NMR chemical shift.[107] A redox-responsive multimodal PRE ^{19}F MRI probe (Fig. 1.19 c)) has also been prepared by conjugating only one trifluoroacetyl amide group, 3-5 ferrocenes and 2-4 rhodamines to cubic octameric polyhedral oligomeric silsesquioxanes measuring 1.5 nm in diameter. Upon ferrocene oxidation with ammonium persulphate, the probe exhibited decreased fluorescence intensity and accelerated ^{19}F relaxation rates resulting in the loss of ^{19}F NMR signal due to interaction with an unpaired electron of Fe^{3+}. The ^{19}F NMR signal (T_1 = 0.67 s and T_2 = 0.66 s, 7.0 T) could be recovered by reduction to Fe^{2+} with ascorbic acid.[109] While such systems have been successfully applied *in vitro*, major modifications would be necessary for *in vivo* application, requiring highly fluorinated probes due to low NMR sensitivity.

Reversible PRE NMR interaction can occur either at the complex or at the metal, wherein a weakly bound ligand or solvent molecule can be displaced. The PRE has been, for example, used to switch on the ^{19}F NMR signal in an indicator displacement assay. For this, a ^{19}F-labelled phosphate indicator enabled the detection of phosphorylated analytes that switched on the ^{19}F NMR signal after displacing the fluorinated reporter from a zinc(II)-bis(dipicolylamine) receptor with a covalently attached paramagnetic relaxation agent.[110] The properties of the anionic and macrocylic ligands can thus be tuned to provide either excellent or destructive PRE ^{19}F NMR signal.

1.6 Objectives of this Work

The current status of the field of responsive MRI contrast agents points both to excellent advances, but also to significant limitations. In most cases, the interaction with inorganic salts and biological components (*e.g.* proteins) as well as the depen-

dence of relaxation times on the concentration of the CA at the site of interest results in difficulties with the quantification of a stimuli-triggered change in MRI contrast. This in particular still presents a major challenge in developing clinically applicable stimuli-responsive contrast agents.

The main objective of the present work is to synthesise a kinetically stable dual-mode nanoparticulate magnetic resonance imaging agent with high fluorine content, a single ^{19}F resonance and an environmentally responsive moiety that will embed a protic Gd^{3+}-DOTA complex. While the ^{19}F NMR signal will report on the concentration, the ^{1}H relaxation times will provide insight into the stimuli responsiveness of the MRI CA.

In the first research chapter, $q = 0$ and $q = 1$ Gd^{3+}-DOTA complexes will be incorporated into mesoporous silica nanoparticles in order to probe the second- and outer-sphere contributions as well as their applicability at ultra-high MRI fields following the ongoing trend towards ultra-high fields in modern clinical MRI.

The next chapter will investigate the surface effects on MRI contrast of Gd^{3+}-DOTA complexes incorporated into mesoporous silica nanoparticles to obtain even higher paramagnetically enhanced relaxivities by rectifying the water exchange limit exhibited by the mesopores.

The third research chapter aims to achieve a pH-triggered on-off switching capability in MRI contrast across Gd^{3+}-doped MSNs by two mechanisms, by either local mobility or water access regulated by pH-responsive polymer chains that can switch between hydrophobic interactions and electrostatic repulsions upon pH change.

The fourth chapter focuses on the preparation of molecular, macromolecular and nanoparticulate ^{19}F MRI contrast agents, while the last chapter concentrates on the design and synthesis of dual ^{19}F/^{1}H MRI CAs based on Gd^{3+}-doped mesoporous silica nanoparticles and polymers in order to either improve ^{19}F MRI sensitivity or investigate potential concentration-independent pH-responsive bimodal probes, respectively.

Chapter 2

Effect of Hydration Number on Ultra-High Field MRI Efficiency of Gd^{3+} Complexes Appended to Mesoporous Silica Nanoparticles

2.1 Introduction

Higher spatial resolution, sensitivity and signal-to-noise ratios as well as shorter signal acquisition times provided at high (3.0 T) and ultra-high (> 3.0 T) magnetic field MRI scanners have stimulated a surge in number of clinically accessible ultra-high field MRI.[111] Since commercial molecular Gd^{3+}-based CAs and their slow tumbling counterparts become less powerful at such field strengths compared to lower magnetic fields, it is necessary to optimise CAs to be effective at high fields.[112, 111] Simulations presented in Ch. 1 (Fig. 1.5 on P. 11) have illustrated that only a suitable interplay between short water residence time and sufficiently (but not overly) long rotational correlation times (best around 0.5-2.0 ns) can meet such requirements.

Larger relaxation time enhancements can be achieved with a higher second-sphere contribution or inner-sphere hydration number.[27] In the latter case, $q \geq 2$ Gd^{3+} complexes, such as heptadentate Gd^{3+}-DO3A derivatives are prone to ternary com-

plex formation with physiologically relevant oxy-anions that can drastically reduce the ^{1}H NMR relaxivity,[82] while only sterically protected $q = 2$ Gd^{3+} complexes can still feature high thermodynamic stability and inertness, such as a heptadentate ligand stabilised by a bis(aquated) picolinate derivative ($[Gd(CyPic3A)(H_2O)_2]^-$).[113] Many other macrocylic and linear polydentate ligands containing picolinate moieties have also been reported to exhibit high thermodynamic stability and inertness to metal ion dissociation, especially in the form of the nonadentate Gd^{3+} complexes.[114, 115, 116]

In this chapter, the inner-, second- and outer-sphere contribution to ultra-high field MRI applications will be probed by incorporation of either $q = 0$ or $q = 1$ Gd^{3+} complexes into MCM-41 type mesoporous silica nanoparticles (MSNs), which offer a highly chemically tuneable, high surface area and biocompatible platform capable of supporting great enhancements in relaxivity.[117, 118, 119] As a pure second/outer-sphere MRI CA, a nonadentate Gd^{3+} chelate ($q = 0$) based on a DOTA-platform with a picolinate side chain has been chosen, whereas an octadentate Gd^{3+}-DOTA chelate with a monoamide pendant arm ($q = 1$) is evaluated as the inner- and second/outer-sphere MRI CA.

2.2 Results and Discussion

2.2.1 Paramagnetic Contrast Agent Functionalisation of MSNs and Their Relaxometric Properties

If the Gd^{3+} chelates are incorporated too deeply into the pores of MSNs, the paramagnetic transmission to the bulk water outside the pores is strongly suppressed and can only be slightly improved with increased temperature as the exchange rate between water molecules located inside and outside of the pores increases.[56] Thus, MSNs containing an amine anchor at the pore entrance were loaded with DOTA-NHS-ester and post-metallated with $GdCl_3$ (particles denoted as **MSN-Gd·L**$_{NHS}$) prepared af-

ter the protocol in Ref. [119], which yielded a very high r_1 in water (33.7 mM^{-1} s^{-1} at 7.0 T) that was drastically reduced in the presence of oxy-anions (3.7 mM^{-1} s^{-1} and 9.2 mM^{-1} s^{-1} in phosphate (pH 7.4) and formate (pH 4.0), respectively). Although such particles were probed as pH-responsive MRI CAs by capping their pores with poly(2-(diethylamino)ethyl methacrylate) via free radical polymerisation (Ch. 3, P. 87) and exhibited a remarkably high 2.5-fold increase in r_1 at pH 4.0 compared to pH 7.4 (from 16.3 mM^{-1} s^{-1} to 40.9 mM^{-1} s^{-1}) due to electrostatic repulsions of the protonated polymer chains, these results were unreliable as the control was also responsive to both oxy-anions and pH. It was thus necessary to identify the following weaknesses of the Gd^{3+} post-metallation protocol: the NHS-ester of the DOTA chelate can readily hydrolyse before reacting with amines on the silica surface, purification of the particles by centrifugation does not remove excess of Gd^{3+} ions associated with MSNs, and arsenazo(III) testing of the supernatant after washings does not reveal if there are any free Gd^{3+} ions on the nanoparticulate surface present.

It can be assumed that beside uncomplexed Gd^{3+}, the chelated Gd^{3+} is in a form of hydrolysed DOTA physisorbed onto the silica surface of **MSN-Gd·L**$_{NHS}$ (Fig. 2.1). This would confirm the high longitudinal relaxivity in water since there is no flexible organic linker present between Gd^{3+} complex and the silica surface and since oxy-anions most likely replace the physisorbed **Gd·L**$_{NHS}$ yielding reduced relaxivities similar to their molecular counterparts. Indeed, dialysing **MSN-Gd·L**$_{NHS}$ against EDTA reduced the Gd content in the sample from $10.2 \cdot 10^3$ μg/g to $8.7 \cdot 10^2$ μg/g.[1] The efficiency of EDTA analysis was probed when $GdCl_3$ was incubated with MSNs (particles denoted as **MSN-Gd**) and washed by centrifugation under the same conditions as **MSN-Gd·L**$_{NHS}$. Before EDTA dialysis, Gd content was still present at $2.5 \cdot 10^2$ μg/g exhibiting r_1 relaxivities as high as 64.9 mM^{-1} s^{-1} at 7.0 T, while after EDTA analysis, the presence of free Gd was completely exterminated (1.1 μg/g),

[1] μg/g stands for microgram of gadolinium per gram of nanoparticles.

indicating the efficiency of the removal of unchelated gadolinium by EDTA.

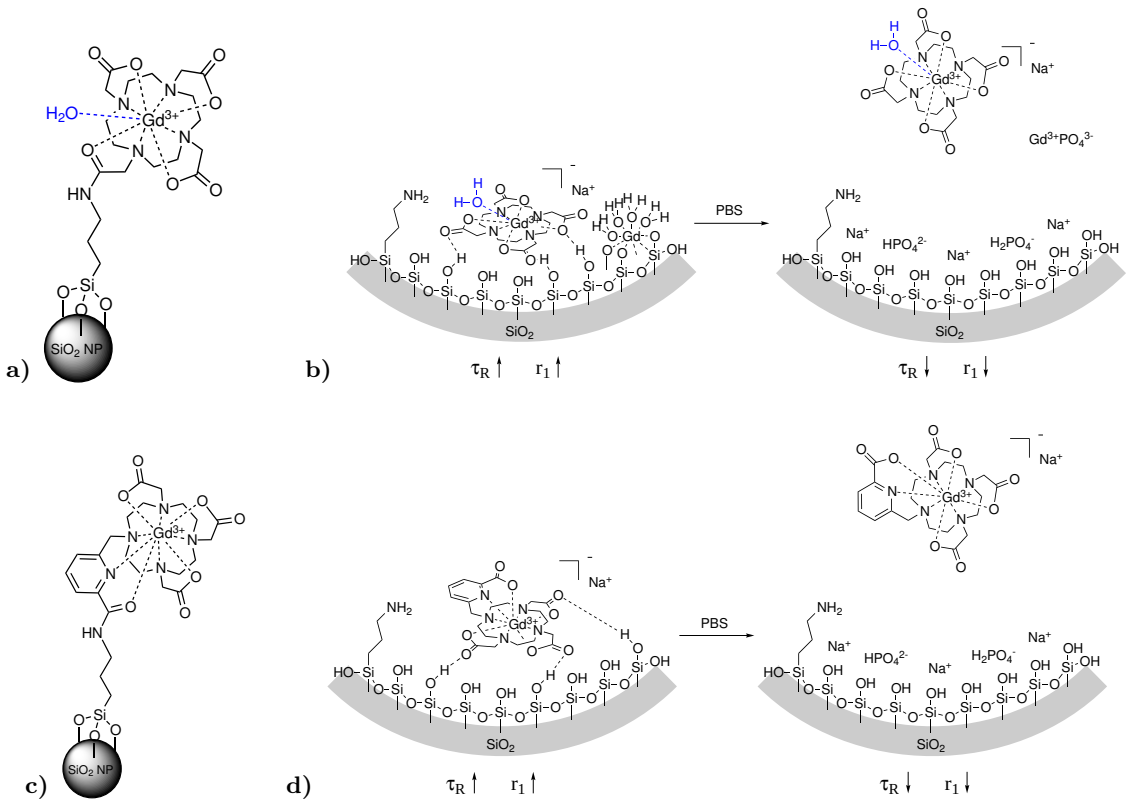


Figure 2.1: Illustrations above depict the expected conjugation of a) **Gd·L**$_{NHS}$ and c) **Gd·L**$_0$ onto the silica surface of the mesopores, while b) and d) illustrate the physisorption of respective Gd^{3+} complexes that leads to enhanced protic relaxivity. This is heavily reduced in the presence of competing oxy-anions that probably replace physisorbed Gd^{3+} complexes on the silica surface. The small amount of uncomplexed Gd^{3+} ions, on the other hand, reacts with PO_4^{3-} ions in order to form $GdPO_4$,[120] which has a reduced solubility in water, thus reducing the observed r_1.

To confirm that the reduction in relaxivity is a result of physisorption of Gd^{3+} chelate onto silica, a coordinatively saturated $q = 0$ premetallated Gd^{3+} chelate of nonadentate ligand bearing a picolinate pendant **Gd·L**$_0$ was doped into MSNs (**MSN-Gd·L**$_0$, Fig. 2.2) by carbodiimide chemistry. Luminescence lifetime measurements and binding titrations of **Gd·L**$_0$ with phosphate (pH 7.4) indicated that no oxy-anion ligation on the lanthanide took place. Steric blocking of the picolinate thus prevents water displacement and formation of ternary adducts with oxy-anions as

there are no inner-sphere water molecules present. As expected, the relaxivity of the purely second/outer-sphere molecular CA in H_2O ($r_1 = 0.69 \pm 0.09$ mM^{-1} s^{-1}, which was also retained in the presence of phosphate ($r_1 = 0.73 \pm 0.05$ mM^{-1} s^{-1})), was significantly reduced compared to commercial $q = 1$ and $q = 2$ Gd^{3+} chelates.[116]

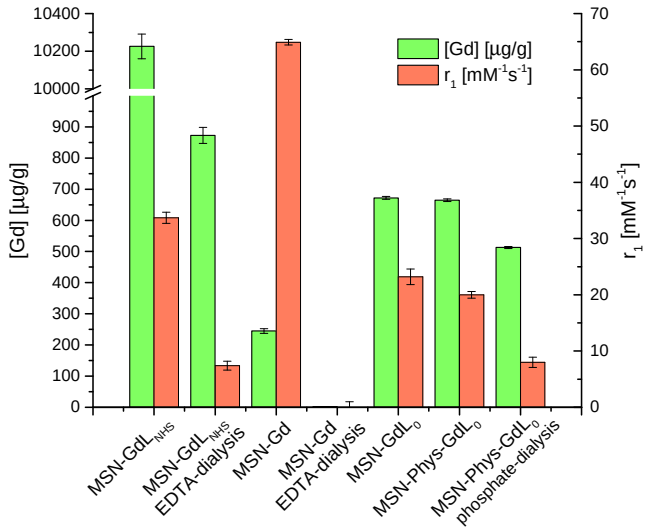


Figure 2.2: The graph represents comparison between Gd content and r_1 relaxivity at 7.0 T before (**MSN-Gd·L_{NHS}, MSN-Gd, MSN-Gd·L_0, MSN-Phys-Gd·L_0**) and after 24 h dialysis period against either EDTA solution (**MSN-Gd·L_{NHS}-EDTA-dialysis, MSN-Gd-EDTA-dialysis**) or phosphate buffer solution (**MSN-Gd·L_0-phosphate-dialysis**). It shows that **Gd·L_0** content in **MSN-Gd·L_0** was very similar when the complex was coupled to the surface through carbodiimide-mediated amidation or physisorbed onto the particles indicating that coupling was unsuccessful, which was also the case in **MSN-Gd·L_{NHS}**, wherein the Gd content was drastically reduced after EDTA dialysis.

Although the luminescence properties of **MSN-Gd·L_0** were comparable to its molecular counterpart,[2] the longitudinal relaxivity was enhanced to 23.2 ± 1.4 mM^{-1} s^{-1} in H_2O, whereas r_1 in phosphate dropped to 3.9 ± 1.9 mM^{-1} s^{-1}. The 34-fold increase in r_1 arises from the increased τ_R value of the paramagnetic complex, whereas the reduced relaxivity in phosphate can be again attributed to the predominantly failed conjugation of the **Gd·L_0** complex to the aminated MSNs (Fig. 2.1) as the picolinic acid group coordinates to the

[2] $q = 0.2$, luminescence titrations with phosphate indicated no water-displacement by oxy-anions.

lanthanide, and thus might not be reactive enough or sterically available to be fully conjugated to the particles. The proof for this hypothesis is given by the r_1 relaxivity and the total gadolinium content, which are very similar in both physisorbed and carbodiimde coupled complexes (20.9 mM^{-1} s^{-1} (665 μg/g of Gd) and 23.2 mM^{-1} s^{-1} (672 μg/g of Gd), respectively). As a consequence, phosphate is likely to replace $\mathbf{Gd{\cdot}L_0}$ adsorbed onto the silica walls leading to a reduced τ_R and consequently a decreased relaxivity (Fig. 2.2).

In order to solve the issues associated with free Gd^{3+} and unsuccessful conjugation, premetallated Gd^{3+}-DOTA complexes bearing either an aminopropoxy picolinate pendant arm (denoted as $\mathbf{Gd{\cdot}L_1}$) or a propargyl monoamide side arm (denoted as $\mathbf{Gd{\cdot}L_2$) were implemented as $q = 0$ and $q = 1$ contrast agents, respectively.

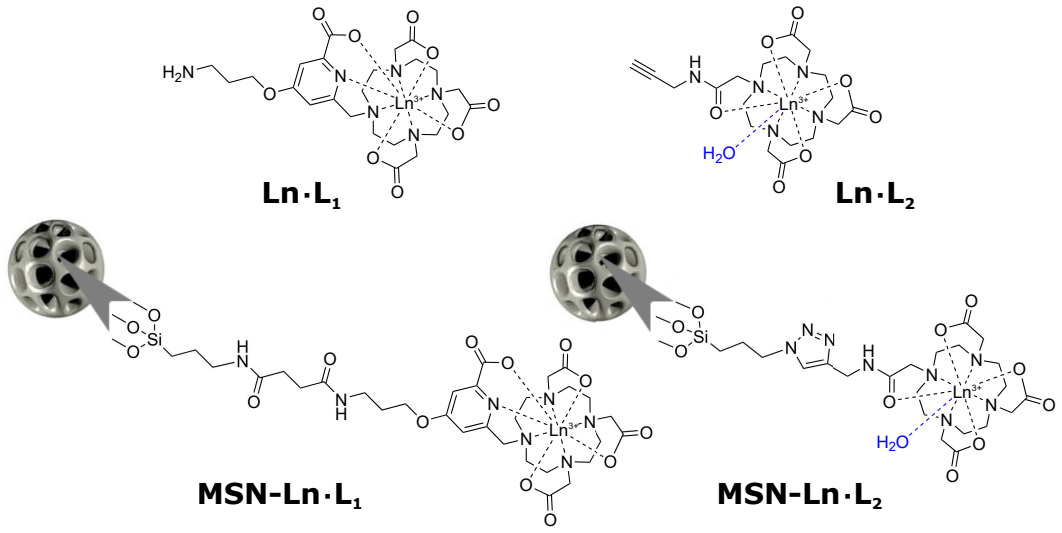


Figure 2.3: Schematic representation of molecular Ln^{3+} complexes $\mathbf{Ln{\cdot}L_1}$ and $\mathbf{Ln{\cdot}L_2}$ incorporated into $\mathbf{MSN\text{-}Ln{\cdot}L_1}$ and $\mathbf{MSN\text{-}Ln{\cdot}L_2}$, respectively.

As a result of missing inner-sphere contribution, the longitudinal relaxivity of molecular $\mathbf{Gd{\cdot}L_1}$ could only reach 0.7 ± 0.2 mM^{-1} s^{-1} at 4.7 T, which was retained at pH 4.0-7.4 as well as in the presence of various oxy-anions. Since it was anticipated that the relaxivity of the outer-sphere CA could be enhanced by tethering to MSNs due to an elongated local rotational correlation time τ_{RL}, the $\mathbf{Gd{\cdot}L_1}$ deriva-

tive was appended to the edge of the mesopores because of an improved water access. For this purpose, aminated MSNs (hydrodynamic diameter = 153.2 ± 1.3 nm, PdI = 0.1)[3] were prepared by an aqueous Stöber technique[121] via a 10 μmol % co-condensation of (3-aminopropyl)triethoxysilane,[122] which was delayed by one hour into the particle synthesis in order to incorporate amine anchoring groups as close to the periphery inside the pore walls as possible, although a few were also located on the external surfaces of the particles.[4] This peripheral effect is reflected in similar, but slightly increased zeta-potentials (ζ-potential = -20.6 ± 2.1 mV) compared to those of non-functionalised MSNs (ζ-potential = -23.7 ± 1.6 mV) dispersed in water (Fig. 2.4). The thermogravimetric analysis (TGA) of the latter also shows the complete removal of cetyltrimethylammonium bromide (CTAB) surfactant used as a template for the mesoporous network of MSNs. This was also confirmed by ^{1}H-^{1}H double-quantum solid-state NMR as described in Fig. 3.6 on P. 71.

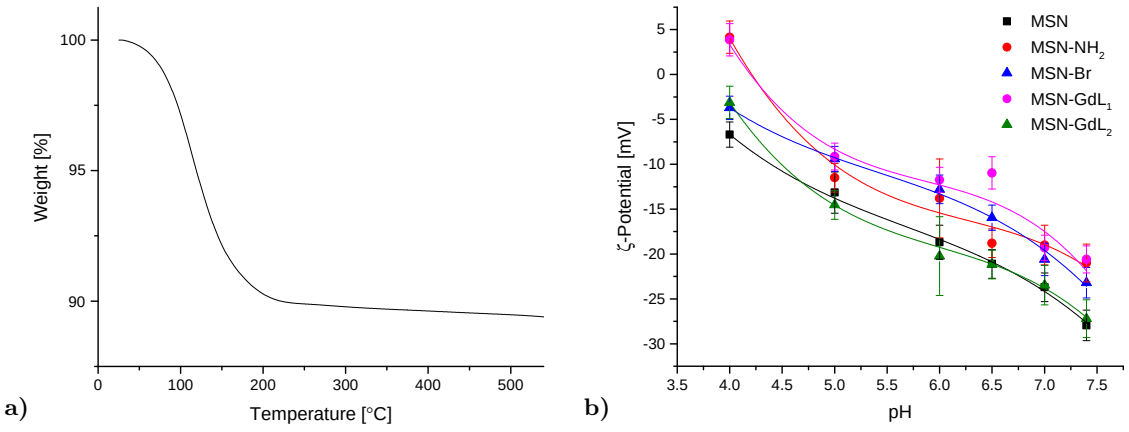


Figure 2.4: a) Thermogravimetric analysis of bare MSNs shows the weight loss at 100 °C, which indicates the removal of residual water, while CTAB surfactant, which is usually removed around 260 °C, could not be detected. b) pH dependency of zeta-potentials of mesoporous silica nanoparticles (■ **MSN**), amine-functionalised MSNs (● **MSN-NH$_2$**), bromide-functionalised MSNs (▲ **MSN-Br**), as well as **Gd·L$_1$**- and **Gd·L$_2$**-functionalised MSNs (● **MSN-Gd·L$_1$** and ▲ **MSN-Gd·L$_2$**, respectively) demonstrate the change in zeta-potentials upon Gd^{3+} complex loading into MSNs.

[3]The size and surface charge properties of MSNs were characterised by dynamic light scattering (DLS) measurements as described on P. 160 in Experimental Procedures.

[4]Further experimental details can be found on P. 184.

The aminated MSNs were subsequently carboxylated by succinic anhydride, which was confirmed by solid-state NMR and FTIR (Fig. 2.6). As 0.16 wt % amination and carboxylation would not be detected by these two techniques, the characterisations were performed by a 100-fold increased degree of functionalisation and implementation of small non-lanthanide adducts bearing the same functional groups only to confirm that all involved surface reactions were successful. The efficient carboxylation of free amines by succinic anhydrides was confirmed by ^{13}C and ^{29}Si MAS NMR (App. A.1 on P. 197). The latter typically exhibits two sets of chemical shift ranges of -120 ppm to -90 ppm and -70 ppm to -50 ppm, which correspond to Q^n and T^m sites, respectively. Q^n designates $[SiO_n(OH)_{4-n}]$ silicates with n = 0-4, which equals the number of Si-O-Si bridging oxygens, while T^m denotes $[RSiO_m(OH)_{3-m}]$ organosiloxanes with m = 1-3. Because of the amplified electronic shielding of the silicon, the chemical shift moves upfield with each further Si-O-Si bridge.[123] Fig. 2.5 shows the ^{29}Si MAS NMR spectra of unmodified MSNs that exhibit only Q^2, Q^3 and Q^4 sites as well as of propylsuccinamide-functionalised MSNs, which possess two additional chemical shifts at -58.6 ppm and -57.7 ppm assigned to T^2 and T^3, respectively. The ^{13}C MAS NMR spectrum of propylsuccinamide-functionalised MSNs, on the other hand, is especially characterised by an amide peak located at 174.3 ppm (Fig. 2.6).

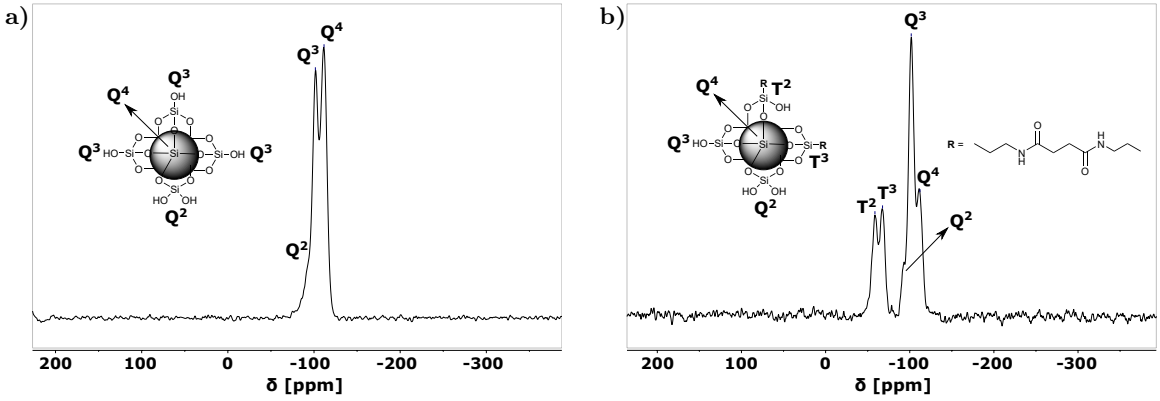


Figure 2.5: ^{29}Si DP/MAS NMR spectra showing a) non-functionalised and b) propylsuccinamide-functionalised MSNs with additional organosiloxane T^2 and T^3 sites.

FTIR spectra of MSNs (Fig. 2.6) are represented by siloxane ring vibrations at 690 cm^{-1}, siloxane bridge vibrations at 790 cm^{-1}, surface silanol groups at 960 cm^{-1}, asymmetric Si-O-Si stretchings in SiO_4 tetrahedra at 1060 cm^{-1} and OH-bendings of molecular water at 1640 cm^{-1}, while a broad band visible around 3500 cm^{-1} occurs due to OH-stretching, adsorbed water and hydrogen-bonded silanols. A small bump can also be seen around 3700 cm^{-1}, which can be ascribed to terminal or isolated silanols (Q^3).[124] Successful propylsuccinamide-functionalisation was again confirmed by the presence of the amide -NH stretching band at 1550 cm^{-1}.

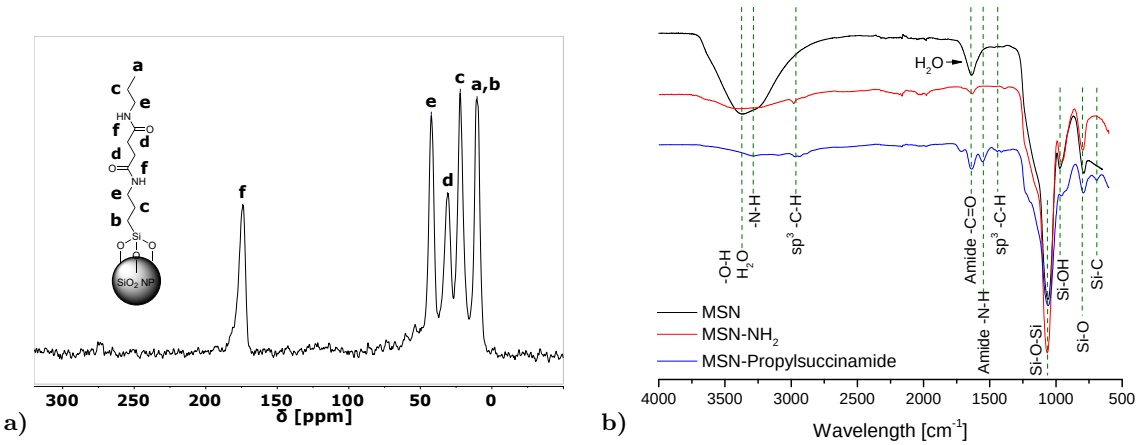


Figure 2.6: a) ^{13}C CP/MAS NMR spectrum showing a successful carbodiimide reaction onto carboxyl-functionalised MSNs. FTIR spectra of a) native (**- MSN**), amine-functionalised MSNs (**- MSN-NH_2**) and propylsuccinamide-functionalised MSNs (**- MSN-Propylsuccinamide**).

The enneadentate ligand was then doped into MSNs by carbodiimide chemistry[5] using 1-ethyl-3-(3-dimethylaminopropyl)carbodiimide and 1-hydroxybenzotriazole hydrate in dry DMF under N_2 yielding particles[6] denoted as **MSN-Gd·L_1**. After conjugation to the particles, several centrifugation/redispersion cycles with EDTA as well as Soxhlet-dialysis extraction were required to remove free metals and physosorbed complexes. Arsenazo(III) tests indicated that only chelated Gd^{3+} ions were present in

[5]Further experimental details can be found on P. 184.

[6]Hydrodynamic diameter = 165.4 ± 5.8 nm, PdI = 0.2, ζ-potential = -21.1 ± 2.6 mV. The microstructure was investigated by TEM as depicted in Fig. 2.11.

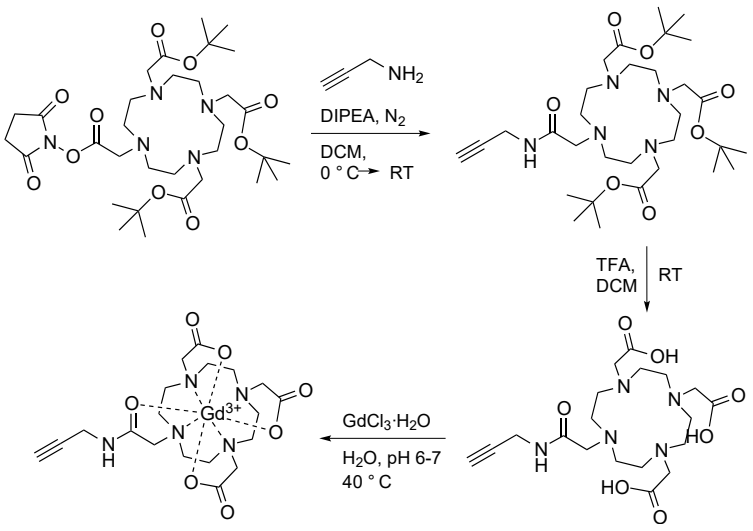


Figure 2.7: Synthesis of the alkyne-derivative of Gd^{3+}-DOTA monoamide complex $\mathbf{Gd{\cdot}L_2}$.

the particle suspension (Fig. 3.8 on P. 74), while transmetallation tests with zinc chloride implied that no leaching of Gd^{3+} occurred after 48 hours (App. A.3 on P. 198).[7] Furthermore, ICP-MS results showed that 3323 ± 9 μg/g of Gd were present in the sample when carbodiimide coupling route was chosen, while only 70.5 ± 0.7 μg/g of Gd were found, when $\mathbf{Gd{\cdot}L_1}$ was physosorbed onto the particles.

$\mathbf{Gd{\cdot}L_2}$, a premetallated Gd^{3+}-DOTA complex with a propargyl amide pendant arm (Fig. 2.7),[8] was synthesised after a modified procedure described by Mindt and others.[125] Since the functional group of the chelate is in this case an alkyne, $\mathbf{Gd{\cdot}L_2}$ was conjugated to azide-functionalised mesopores by click chemistry. Azide-terminated MSNs were prepared in two steps,[9] first by co-condensation with (3-bromopropyl)trimethoxysilane (BPTMS, 1 mmol % for NMR/FTIR characterisation and 10 μmol % for all other characterisations including $\mathbf{Ln{\cdot}L_2}$ doping), followed by conversion into -N_3 by nucleophilic substitution with sodium azide (Fig. 2.8). The reaction was optimised by performing the Huisgen 1,3-dipolar cycloaddition of propargyl amine as well as by characterisation with FTIR and solid-state NMR (Fig. 2.9,

[7] The analytical procedures of arsenazo(III) and zinc transmetallation tests are described on P. 167.
[8] Further experimental details can be found on P. 168.
[9] Further experimental details can be found on P. 185.

App. A.4 on P. 198). The ^{13}C CP/MAS NMR spectrum in App. A.2 on P. 198 shows that upon azide substitution, the resonance of the carbon adjacent to the bromide group was shifted from 35.9 ppm to 53.5 ppm, while an azide stretching band appeared at 2100 cm^{-1} in the FTIR spectrum, which decreased in intensity when the click reaction was performed. The presence of the triazole ring was also confirmed by ^{13}C CP/MAS NMR that exhibited characteristic triazole ring carbon signals at 122.4 ppm and 143.3 ppm.

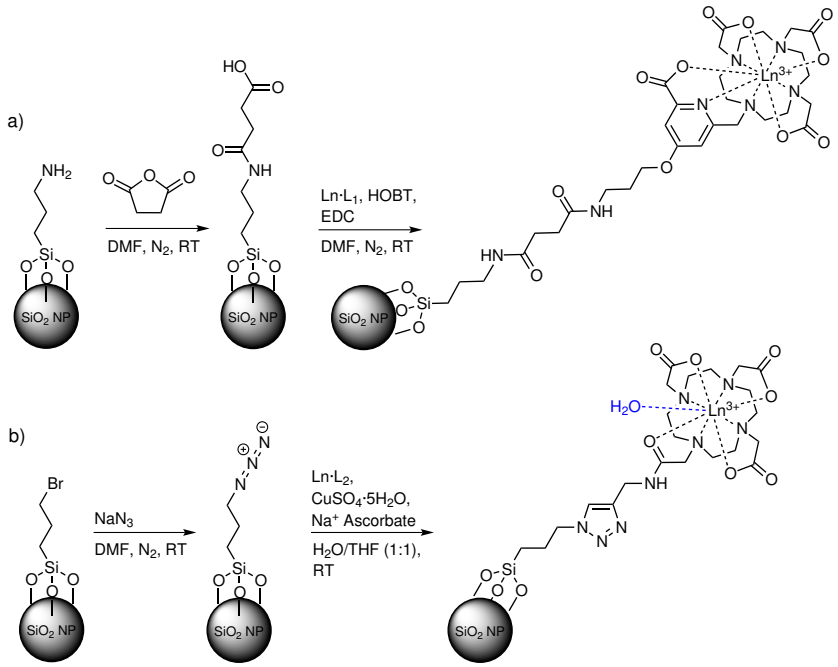


Figure 2.8: Synthetic pathway for a) $q = 0$ and b) $q = 1$ Ln^{3+}-DOTA complexes loaded into MSNs a) **MSN-Ln·L$_1$** and b) **MSN-Ln·L$_2$**.

The click reactions of **Gd·L$_2$** onto azide-functionalised MSNs were then performed in the presence of $CuSO_4$ and sodium ascorbate (Fig. 2.8). Besides free Gd^{3+}, the removal of residual paramagnetic Cu^{2+} is also crucial for accurate relaxivity determination. When such particles were purified only by multiple centrifugation/redispersion cycles, 198.9 ± 3.3 μg/g of excess copper could be detected in the sample. The copper content was further reduced when the sample was incubated with either EDTA or EDTA and sodium diethylthio carbamate yielding a total copper

amount of either 71.3 ± 1.6 μg/g or 9.9 ± 0.5 μg/g, respectively. Thus, after **Gd·L$_2$** conjugation to the particles, several centrifugation/redispersion cycles with sodium diethylthio carbamate and EDTA followed by Soxhlet-dialysis extraction were required to remove free metals and physosorbed complexes. The resulting **MSN-Gd·L$_2$** particles (ζ-potential = -24.3 ± 1.9 mV, hydrodynamic diameter = 151.8 ± 1.2 nm, PdI = 0.1) incorporated 4904.7 ± 1.3 μg/g of Gd, whereas the control particles stirred with **Gd·L$_2$**, but without the presence of catalysing $CuSO_4$ and sodium ascorbate, contained only 70.7 ± 0.8 μg/g of Gd and 4.9 ± 0.5 μg/g of Cu, implying that the combined EDTA and sodium diethlythio carbamate purification procedures were successful in removing both Gd and Cu.

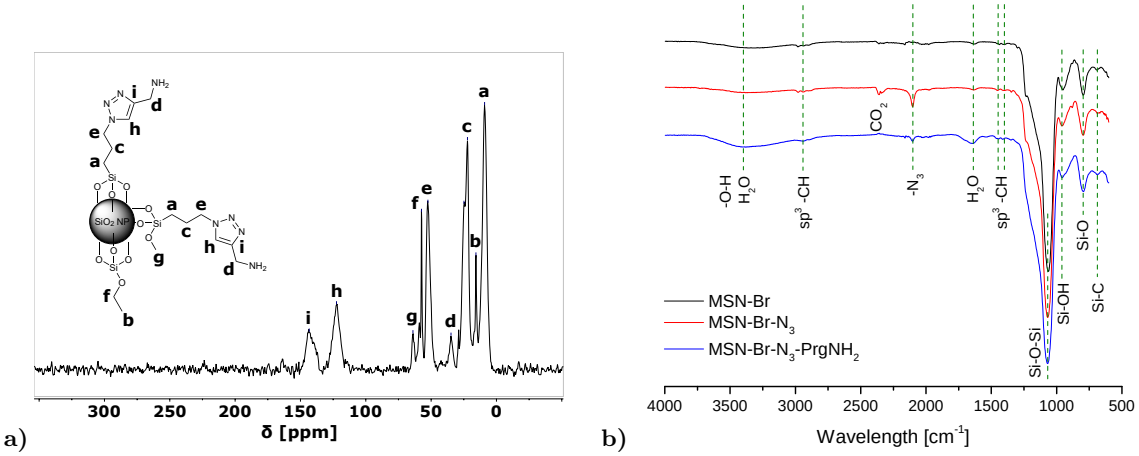


Figure 2.9: a) ^{13}C CP/MAS NMR spectrum showing the successful click reaction of propargyl amine onto azide-functionalised MSNs. b) FTIR spectra of bromide-functionalised MSNs (**- MSN-Br**), azide-functionalised MSNs (**- MSN-Br-N$_3$**) and triazolylmethyl amine-functionalised MSNs (**- MSN-Br-N$_3$-PrgNH$_2$**).

The relaxation time measurements[10] of **MSN-Gd·L$_1$** yielded ^{1}H longitudinal relaxivities increased by 8-fold compared to their molecular counterpart **Gd·L$_1$** (Tab. 2.1 and Tab. 2.2). The ^{1}H r_1 relaxivity in water increased from 0.7 ± 0.2 mM^{-1} s^{-1} to 6.2 ± 0.9 mM^{-1} s^{-1}. This was held constant over the physiological pH range, when

[10]The detailed description of the relaxation time measurements and the determination of relaxivities can be found on P. 162-163, while accompanying linear fits can be found in App. A.5-A.7 on P. 199-201.

the particles were dissolved in 10 mM buffer solutions of phosphate (pH 6.5, 6.8 and 7.4), HEPES (pH 6.8 and 7.4), MES (pH 6.0), acetate (pH 5.0) and formate (pH 4.0) at 4.7 T indicating that the particles are stable at such conditions and that the presence of oxy-anions does not affect the relaxivity (Fig. 2.10).

Table 2.1: Table showing details of ^{1}H longitudinal and transverse relaxivities in water (at 20 °C at 4.7 T). Error margins represent cumulative errors arising from duplicate repetitions of relaxivity assessment.

	r_1 [$\mathbf{mM^{-1}\ s^{-1}}$] **at 4.7 T**	r_2 [$\mathbf{mM^{-1}\ s^{-1}}$] **at 4.7 T**	r_2/r_1 **ratio at 4.7 T**
Gd·L$_1$	0.7 ± 0.2	0.9 ± 0.6	4.3
NS-Gd·L$_1$	3.9 ± 0.9	38.3 ± 6.2	9.8
MSN-Gd·L$_1$	6.2 ± 0.9	49.6 ± 9.4	8.0
Gd·L$_2$	4.2 ± 0.5	5.5 ± 0.9	1.3
NS-Gd·L$_2$	14.5 ± 0.9	107.9 ± 28.5	7.4
MSN-Gd·L$_2$	16.0 ± 0.8	135.5 ± 19.2	8.5

In comparison to **Gd·L$_2$**, **MSN-Gd·L$_2$** particles exhibited a 4-fold increase in ^{1}H NMR longitudinal relaxivity from 4.2 ± 0.5 $mM^{-1}\ s^{-1}$ to 16.0 ± 0.8 $mM^{-1}\ s^{-1}$ at 4.7 T in H_2O. This value was also stable across the physiological pH range (Fig. 2.10) as well as in the presence of zinc chloride over 48 hours (App. A.3 on P. 198). The observed elevated relaxivities are assignable to the Gd^{3+} chelate being confined within the restricted global movement of the solid particle τ_{RG}, while the less rigid covalent linker brings certain flexibility to the system as the additional local rotational motions τ_{RL} are faster than the global rotation of the particle. They therefore present a limiting factor of the theoretically achievable longitudinal relaxivities through shortening the effective τ_R.

Another possible consequence of restricted global and local motions are greater r_2

values (Tab. 2.1), which increased from 0.9 ± 0.6 mM^{-1} s^{-1} to 49.6 ± 14.5 mM^{-1} s^{-1} in **MSN-Gd·L$_1$** and from 5.5 ± 0.9 mM^{-1} s^{-1} to 135.5 ± 19.2 mM^{-1} s^{-1} in **MSN-Gd·L$_2$** NPs compared to their respective molecular counterparts, thus affecting the efficiency of the particles as positive CAs. Indeed, Peters *et al.* [126] reported on r_2 values of Gd^{3+}-doped zeolite particles that were similar to the longitudinal ones up to a magnetic field of 60 MHz. They observed a pronounced enhancement of r_2 values attributed to microscopic field gradients that dephase the water protons, which diffuse past the weakly magnetised zeolites.[126] Among other possible mechanisms, these local susceptibility effects might also explain, why further increments of Gd^{3+} amounts in mesoporous silica nanoparticles led to reduced r_1 values.

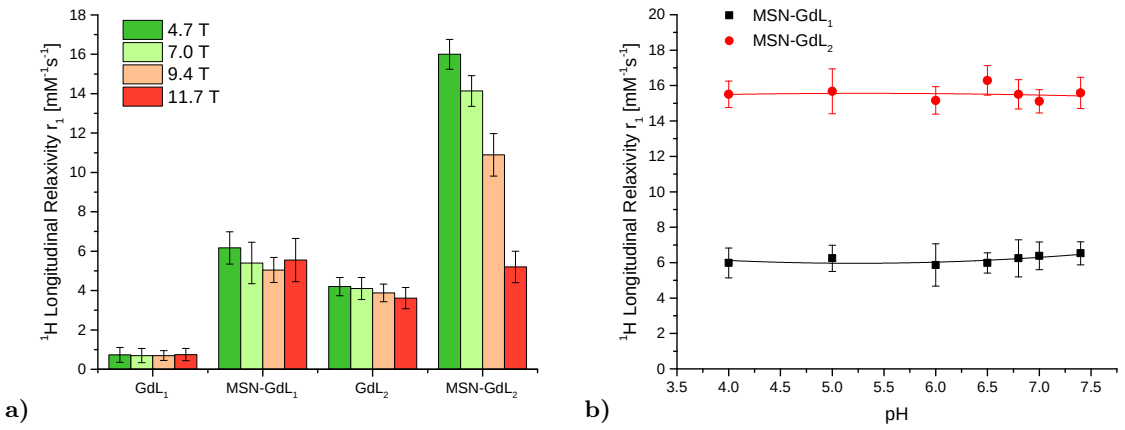


Figure 2.10: a) Graph showing field dependence of protic longitudinal relaxivity of $q = 0$ and $q = 1$ molecular and nanoparticulate contrast agents. b) Graph depicting the dependence of longitudinal relaxivities of ■ **MSN-Gd·L$_1$** and ● **MSN-Gd·L$_2$** on pH. 10 mM acetate, MES, formate and phosphate buffer solutions were used to fix the pH over three different concentrations of nanoparticles.

The larger increase in the r_1 value of $q = 0$ CAs appended to MSNs compared to $q = 1$ CAs tethered to MSNs, on the other hand, demonstrates the importance of the second- and outer-sphere contribution in Gd^{3+}-grafted MSNs although the overall relaxivity of the latter was still 3-fold higher than of the former pointing to a bigger contribution of the inner-sphere relaxivity at 4.7 T. However, as seen in Fig. 2.10, the difference decreases rapidly with higher field and the second/outer-sphere con-

Table 2.2: Table showing details of ^1H longitudinal relaxivities in water (at 20 °C at 4.7 T, 7.0 T and 9.4 T) as well as q values of the Eu^{3+} counterparts. Error margins represent cumulative errors arising from duplicate repetitions of relaxivity assessment.

	r_1 [mM^{-1} s^{-1}] at 4.7 T	r_1 [mM^{-1} s^{-1}] at 7.0 T	r_1 [mM^{-1} s^{-1}] at 9.4 T	k_{ex}^{310} [$\cdot 10^6$ s^{-1}]	q value	Gd [$\mu g/g$]
Gd·L$_1$	0.7 ± 0.2	0.7 ± 0.4	0.7 ± 0.3	0.5	0.20	$201 \cdot 10^3$
NS-Gd·L$_1$	3.9 ± 0.9	3.9 ± 1.0	3.5 ± 0.7	NM	0.04	2071 ± 14
MSN-Gd·L$_1$	6.2 ± 0.9	5.4 ± 1.1	5.0 ± 0.6	27.6	0.02	3323 ± 9
Gd·L$_2$	4.2 ± 0.5	4.1 ± 0.6	3.9 ± 0.5	NM	1.04	$250 \cdot 10^3$
NS-Gd·L$_2$	14.5 ± 0.9	13.3 ± 0.9	9.7 ± 0.7	NM	1.05	1427 ± 16
MSN-Gd·L$_2$	16.0 ± 0.8	14.1 ± 0.8	10.9 ± 1.1	6.3	1.07	4905 ± 62

tribution soon becomes the dominating term as the relaxivities of $q = 0$ and $q = 1$ CAs tethered to MSNs become almost equal. From 4.7 T to 11.7 T, the longitudinal relaxivities of **MSN-Gd·L$_1$** and **MSN-Gd·L$_2$** decreased by 10 % and 67 %, respectively. The decrease of longitudinal relaxivity with increasing field was accompanied by a slight increase in r_2 values from 49.6 ± 9.4 mM^{-1} s^{-1} to 50.7 ± 8.6 mM^{-1} s^{-1} in **MSN-Gd·L$_1$** and from 135.5 ± 19.2 mM^{-1} s^{-1} to 181.8 ± 24.8 mM^{-1} s^{-1} in **MSN-Gd·L$_2$** upon an increase in the magnetic field from 4.7 T to 9.4 T (App. A.5 on P. 199 and App. A.6 on P. 200).

Beside greater magnetic dipole-dipole interactions, the reduced r_1 values upon heavier Gd^{3+} doping into MSNs might also be a result of an increased number of relaxometrically silent species located deeper within the pores, which experience a limited water exchange rate from the interior of the pores to the bulk. Botta *et al.* [56] reported almost 4-fold lower relaxivities when Gd^{3+} was grafted into SBA-15 type MSNs compared to those loaded in MCM-41 type MSNs due to different accessibility of water molecules to Gd^{3+} complexes predominantly positioned either within the mesopores or on the surface, respectively. On the other hand, Davis *et al.* [119] observed a 4-fold decrease in relaxivity when Gd^{3+} complexes were doped into non-porous silica compared to Gd^{3+} chelates loaded into mesoporous silica nanoparticles

quoting internal wall restraint and prolonged diffusional rate as the main reasons.

In order to probe the impact of Gd^{3+} complex incorporation into the mesopores on the second/outer-sphere contribution, non-porous silica nanoparticles measuring 60 nm in diameter were prepared by a protocol adapted and up-scaled from Ref. [127].[11] The surface was post-grafted with either 10 μmol % APTES or BPTMS and converted to either carboxyl or azide functional groups for the attachment of **Gd·L$_1$** or **Gd·L$_2$** to yield either **NS-Gd·L$_1$** or **NS-Gd·L$_2$**, respectively. While the longitudinal relaxivity of the latter decreased only by approximately 10 % (from 16.0 mM^{-1} s^{-1} to 14.5 mM^{-1} s^{-1}) compared to **MSN-Gd·L$_2$**, the r_1 value of **NS-Gd·L$_1$** was reduced by 37 % (from 6.2 mM^{-1} s^{-1} to 3.9 mM^{-1} s^{-1}) compared to **MSN-Gd·L$_1$** (Tab. 2.2 and Fig. 2.13). These results thus suggest that the contribution of the second/outer-sphere is less pronounced in non-porous than in mesoporous particles. The beneficial role of the pores in longitudinal relaxation enhancement becomes consequently more important for $q = 0$ contrast agents, whereas r_2 values decreased in both cases (*i.e.* **NS-Gd·L$_1$** and **NS-Gd·L$_2$**) by about 20 % compared to their mesoporous nanoparticulate counterparts.

In addition to the hydration number, the relaxometric dissimilarities between $q = 0$ and $q = 1$ CAs incorporated into silica NPs might be influenced by the charge and linker of the Gd^{3+} complexes as well as by the residual surface functional groups. For example, **Gd·L$_1$** bears a negative charge, while **Gd·L$_2$** carries a neutral one. The linker chemistry and length also makes **Gd·L$_1$** appended to the silica surface via a 2 nm long dipropyl butanediamide linker slightly more flexible compared to **Gd·L$_2$**, which is conjugated to silica via a rigid triazole ring (approx. 1 nm). The possibility, however, remains that the former is more likely to collapse onto the surface, which would also increase local rigidity.

Lastly, residual surface groups of silica particles supporting **Gd·L$_1$** consist of

[11] Further experimental details can be found on P. 186.

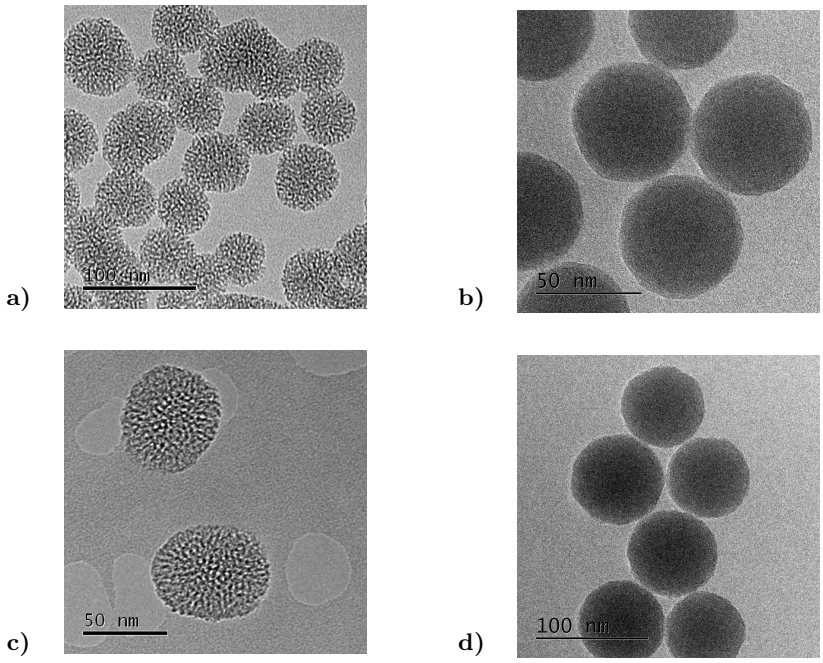


Figure 2.11: TEM images of a), c) mesoporous and b), d) non-porous silica nanoparticles a), b) before and c), d) after **Gd·L**$_1$-loading. Scales correspond to a) 100 nm, b) 50 nm, c) 50 nm and d) 100 nm.

amines and carboxyls, while those in **MSN-Gd·L**$_2$ contain mostly azides. The influence of residual ionic groups in **MSN-Gd·L**$_1$ and **MSN-Gd·L**$_2$ on the respective relaxivities was thus probed by acetylation.[12] **MSN-Gd·L**$_1$**-Est** particles were obtained by esterification of amines with acetic anhydride and acidic methylation of carboxyls with methanol, while **MSN-Gd·L**$_2$**-Est** particles were prepared by reduction of residual azides with triphenylphosphine and subsequent acetylation with acetic anhydride. The group and charge conversion were confirmed by both ζ-potentials and solid-state ^{13}C NMR, respectively (Fig. 2.13, App. A.1 on P. 197). Upon acetylation, the surface charge loses its steep dependency on pH, and instead varies in a parabolic fashion in the range from -20 mV to -10 mV from pH 4.0 to 7.4. Despite noticeable zeta-potential changes, the observed r_1 at 4.7 T, 7.0 T and 9.4 T were within error of the non-acetylated MSNs. As MSNs were functionalised with only 0.2 wt % of the

[12] Further experimental details can be found on P. 186.

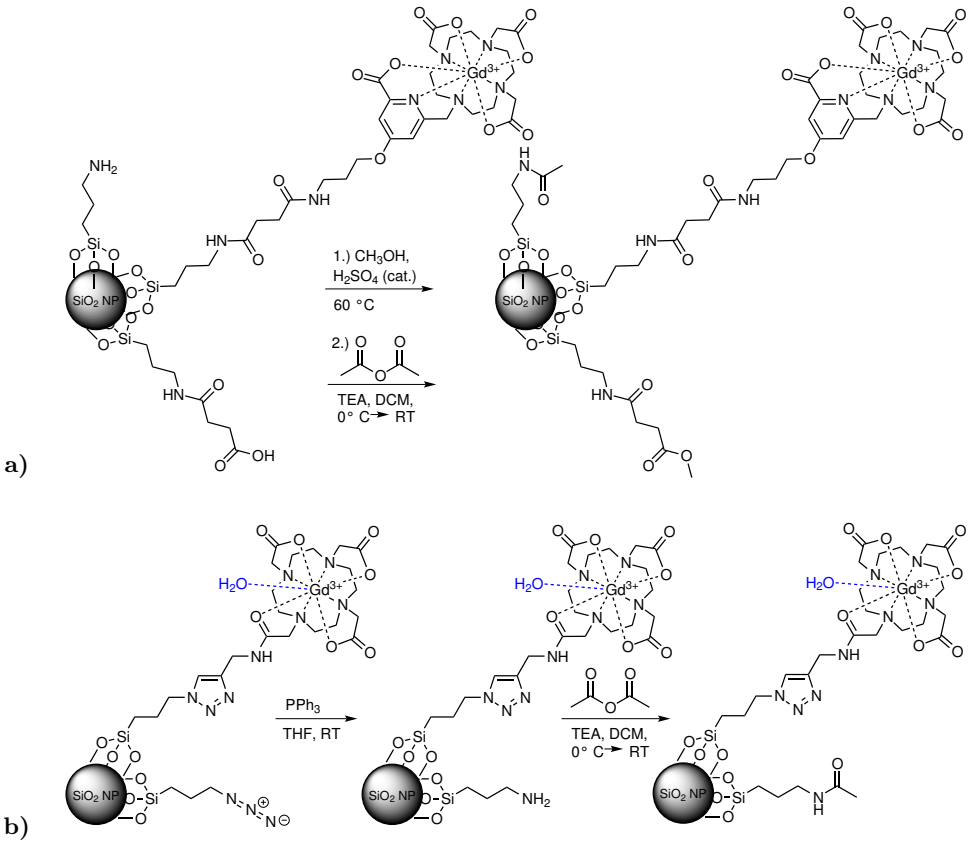


Figure 2.12: Preparation of a) **MSN-Gd·L$_1$-Est** and b) **MSN-Gd·L$_2$-Est** by reduction of residual azide groups as well as esterification of residual amine and carboxyl groups in **MSN-Gd·L$_1$** and **MSN-Gd·L$_2$**, respectively.

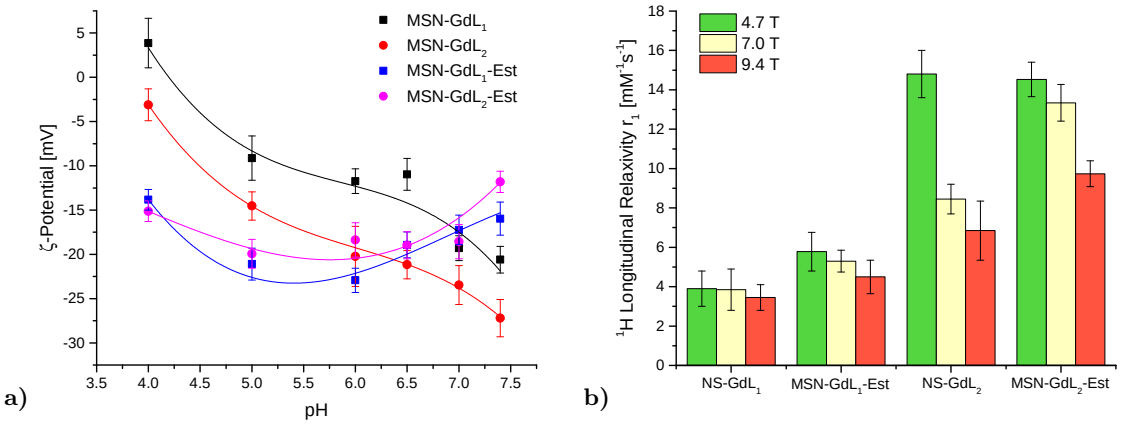


Figure 2.13: a) pH dependence of ζ-potentials of ■ **MSN-Gd·L$_1$-Est** and • **MSN-Gd·L$_2$-Est** compared to ■ **MSN-Gd·L$_1$** and • **MSN-Gd·L$_2$** demonstrating the successful esterification. b) Graph on the right shows field dependence of protic longitudinal relaxivity of $q = 0$ and $q = 1$ nanoparticulate contrast agents.

functional groups capable of reacting with Gd^{3+} chelates, it can be concluded that the residual functional groups on the particles are so minuscule in concentration that the presence and charge of such groups do not influence neither local rotation, nor accessibility of the solvent to the metal centre, nor relaxivity.

2.2.2 Confirmation of Hydration Numbers by Luminescence Measurements

The number of inner-sphere water molecules in the Eu^{3+} complexes in an aqueous solution was determined by measuring the luminescence lifetimes[13] of the complexes in H_2O and D_2O.[79] As the silica nanoparticles are colloidally stable and transparent to light and photophysically inert,[128] their presence did not influence the luminescence measurements. Following excitation at 393 nm, the first order rate constant of the emission intensity decay at 616 nm was measured. With the empirical relationship between luminescence decay rates in H_2O and D_2O as described in the Introduction (Sec. 1.4.1 on P. 26), it was possible to determine the q values of 0.02 and 1.07 for **MSN-Eu·L$_1$** and **MSN-Eu·L$_2$**, respectively.

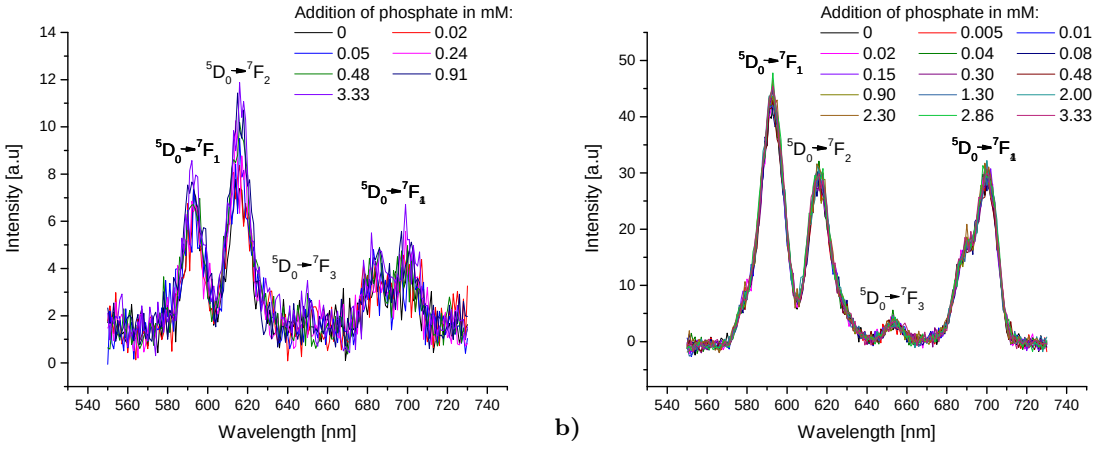


Figure 2.14: Comparison of the emission spectra (293 K, $\lambda_{ex} = 393$ nm) of a) **MSN-Eu·L$_1$** and b) **MSN-Eu·L$_2$** as a function of added phosphate (10 mM, pH 7.4).

[13]Further details on luminescence measurements are given on P. 166.

In the case of the picolinate derivative, the data pointed to a hydration number of almost zero, which indicates that there are no inner-sphere water molecules present as the cooridnation sphere is saturated by nine heteroatoms of the ligand. Picolinate's steric blocking in **Eu·L**$_1$, which is a $q = 0$ CA, and monoamide ligation to the lanthanide in **Eu·L**$_2$, which is a $q = 1$ CA with one inner-sphere water molecule, thus prevent water displacement and formation of ternary adducts with anions. Titrations of **Eu·L**$_1$ and **Eu·L**$_2$ with phosphate (pH 7.4) also confirmed that there was indeed no oxy-anion interference with the lanthanides, while lifetime measurements at different pH values in H_2O and D_2O confirmed that within experimental error there was no change in q value with pH.

2.2.3 ^{17}O NMR Measurements Reveal Strong Second-Sphere Contribution

In the slow exchange limit (Fig. 2.15), where ^{17}O NMR $R_{2r} \approx k_{ex}$ as explained in detail in Sec. 1.2.2 on P. 12, it was possible to estimate τ_M $(= 1/k_{ex})$.[14] Although luminescence studies of $q = 0$ complexes showed that there is no water ligand bound to the lanthanide centre, τ_M values as low as 3.5 μs and 36.2 ns were obtained at 310 K for **Gd·L**$_1$ and **MSN-Gd·L**$_1$, respectively. Since the outer-sphere contribution to the ^{17}O relaxation rates is reported to be negligible due to the dominant scalar coupling contribution to T_{2r} with the oxygen nucleus of water being directly ligated to the paramagnetic centre[129] and since the lifetimes of the coordinated water in the first-sphere in this case must equal zero, τ_M might be mostly affected by the water exchange lifetimes in the second-sphere $\tau_{M'}$. This might be possible if the nonadentate complex adopts a coordination geometry similar to octadentate's twisted-square antiprismatic isomer (TSAP), which is known to affect the distance between both the 1^{st}- and the 2^{nd}-sphere water molecules, whereby the former is elongated and the latter shortened

[14] Further details can be found in Experimental Procedures on P. 164.

when compared to regular square antiprismatic geometry (SAP).[130, 131]

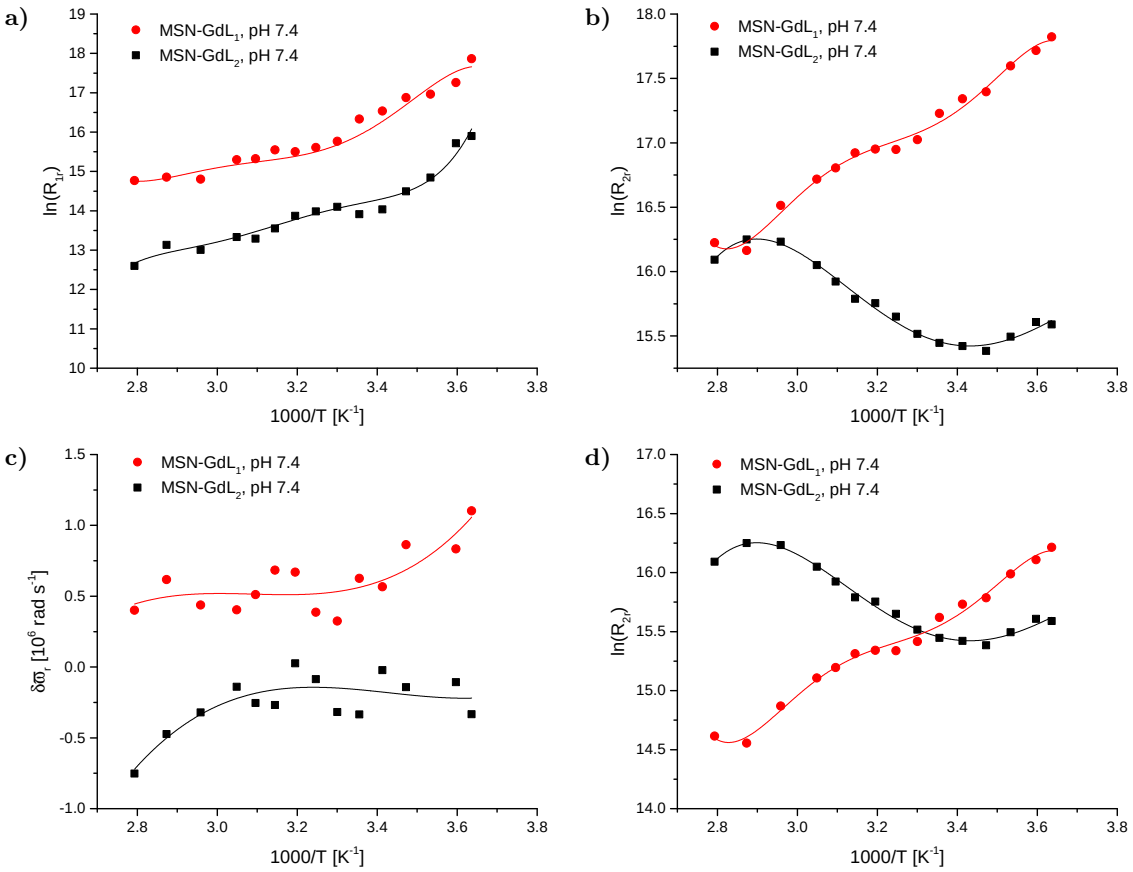


Figure 2.15: Temperature dependence of the paramagnetic contribution to the ^{17}O nucleus of water showing reduced a) longitudinal R_{1r} (q of **MSN-Gd·L$_1$** was set to 0.02) and b), d) transverse R_{2r} relaxation rates as well as c) ^{17}O chemical shifts $\delta\omega_r$ of ● **MSN-Gd·L$_1$** and ■ **MSN-Gd·L$_2$**. The reduced longitudinal and transverse relaxation rates represent the difference in $H_2{}^{17}O$ relaxation rates measured in the presence of MSNs and in the presence or absence of Gd^{3+} as a function of reciprocal temperature. The rates are normalised to the molar fraction of coordinated water (*e.g.* $q = 0.02$ and 1.00 were taken into consideration for $q = 0$ CAs in graphs b) and d), respectively).

MSN-Gd·L$_2$, which possesses one inner-sphere water molecule, was found to be in a slower exchange regime than **MSN-Gd·L$_1$**. Its τ_M (218.1 ns, Tab. 2.2) was 6-times longer than the water residence lifetime of the $q = 0$ nanoparticulate counterpart. However, such τ_M is still slightly faster than the values of about 440-480 ns that have previously been reported by Carniato *et al.* [132] for monoamide $q = 1$ CAs incorporated into MSNs. In fact, even molecular Gd^{3+} chelates having one carboxylate

group swapped for an amide exhibit exchange rates a factor of 3-4 times lower than their tetra-carboxylate counterparts. The slower water exchange rate in the presence of a ligating monoamide is a result of weaker binding to Gd^{3+} since the free space available to a water molecule is increased. As a consequence, a water molecule can ligate nearer to the lanthanide.[40]

If the q value of Eq. (1.14) in the case of **MSN-Gd·L$_1$** is set to 1, it is possible to analyse the combined second/outer-sphere contribution to **MSN-Gd·L$_2$** (Fig. 2.15 d)). This contribution decreases from $10.9 \cdot 10^6$ s^{-1} to $1.9 \cdot 10^6$ s^{-1} affecting the ^{17}O R_{2r} rates at high temperature. The $ln(R_{2r})$ dispersion at high temperature starting from 293 K is due to the inner-sphere water, *i.e.* due to water exchange, which is quite slow as it increases with temperature. At 298 K, the inner- and second/outer-sphere contribution are quite similar as τ_M can be estimated at 164 ns and 196 ns, respectively. With higher temperature, the inner-sphere contribution dominates ever more, leading to the inner-sphere rate of $6.3 \cdot 10^6$ s^{-1} compared to the second/outer-sphere rate of about $4.6 \cdot 10^6$ s^{-1} at 310 K. The peak is reached at 348 K, when the water exchange rate of the second/outer-sphere is reduced to $2.1 \cdot 10^6$ s^{-1} and the k_{ex} of the inner-sphere is increased to $11.4 \cdot 10^6$ s^{-1}. The higher outer-sphere contribution effect at lower temperatures is also reflected in the trend of the chemical shift. These results suggest that the combined second- and outer-sphere contributions in **MSN-Gd·L$_1$** and **MSN-Gd·L$_2$** are quite similar.

2.2.4 Further Analysis of the Second/Outer-Sphere Contribution

To strengthen our understanding of the second/outer-sphere contribution to the relaxometric properties of $q = 0$ and $q = 1$ Gd^{3+}-DOTA complexes loaded into mesoporous silica nanoparticles, the NMRD profiles obtained at 293 K were fitted to the standard SBM theory extended by the Lipari-Szabo restricted motion model for the spectral

density $J(\omega)$ as well as by the mesopore contribution as discussed in Sec. 1.3.1 on P. 21. The effects of the mean-square zero-field splitting energy Δ^2 and the correlation time for the distortion of the metal polyhedron τ_v were similar in both **MSN-Gd·L**$_1$ and **MSN-Gd·L**$_2$ samples (Tab. 2.3). These parameters are implemented as empirical NMRD fitting parameters that were useful for bringing the maxima of fitted NMRD curves (Fig. 2.16, performed with a home-written Mathematica program) towards higher frequencies as also determined by Decuzzi *et al.*,[52] while their physical relevance can be examined by complementing electron paramagnetic resonance spectroscopy (EPR).

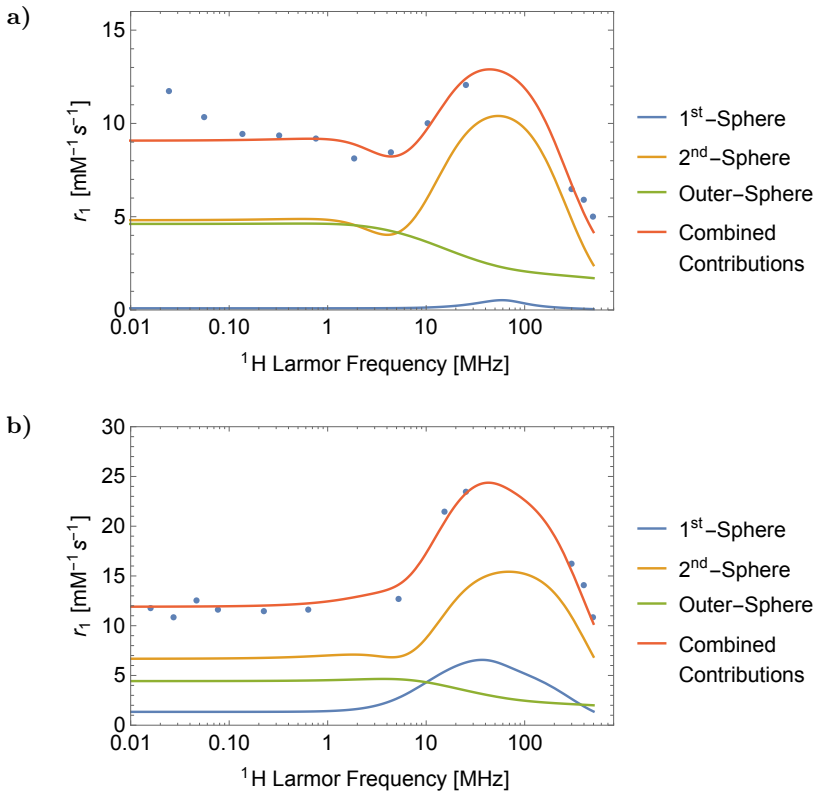


Figure 2.16: NMRD profiles of a) **MSN-Gd·L**$_1$ and b) **MSN-Gd·L**$_2$. Relaxation times were recorded at 293 K.

The fitting of the structural Lipari-Szabo parameters, such as τ_{RG}, can be quite accurate for smaller macromolecules, *e.g.* dendrimers, while in the range higher than

10 ns, which is the case for global rotational time of the silica nanoparticles, the results of the NMRD fits become insensitive to the actual τ_{RG} values, while the τ_{RL} values of the Gd^{3+}-appended CA are in the lower than 10 ns range because of the flexible organic linker that limits the theoretically achievable relaxivity. As expected, such values still signify restricted mobility compared to their molecular counterparts with rotational correlation times in the picosecond range.

Table 2.3: Roughly approximated parameters resulting from fits of the longitudinal NMRD profiles.[15]

	MSN-Gd·L$_1$	**MSN-Gd·L$_2$**
τ_v^{293} $[ps]$	30.1	31.2
Δ^2 $[\cdot 10^{19} s^{-2}]$	3.2	4.4
τ_{RG}^{293} $[ns]^{[b]}$	$\approx 20.2^{[a]}$	21.6
τ_{RL}^{293} $[ns]$	$\approx 0.8^{[a]}$	1.1
F^2	$\approx 0.4^{[a]}$	0.5
τ_{pore}^{293} $[\mu s]$	$\approx 10.0^{[a]}$	23.6
τ_D^{293} $[ps]$	44.7	39.7
q'	1	1
$\tau_{R'}^{293}$ $[ns]$	0.7	0.4
$\tau_{M'}^{293}$ $[ns]$	68.0	86.4

The absence of the inner-sphere contribution in **MSN-Gd·L$_1$** as depicted in Fig. 2.16 can only be explained by the dominant second/outer-sphere contribution. The best fit revealed slightly shorter residence times of the second-sphere water $\tau_{M'}$ in **MSN-Gd·L$_1$** (68 ns) compared to **MSN-Gd·L$_2$** (86 ns), while the diffusion correlation times τ_D were about the same. Due to the absence of the inner-sphere water

[15] [a] Estimation of these parameters is unreliable due to missing inner-sphere contribution. [b] The NMRD fits were insensitive to the real value of τ_{RG}^{293} $[ns]$ in the range higher than 10 ns.

in **MSN-Gd·L**$_1$, the residence time of water molecules located inside the pores τ_{pore} could be estimated only in **MSN-Gd·L**$_2$ to be 24 μs, which is similar to those reported for Gd^{3+}-loaded SBA-15 mesoporous silica nanoparticles,[133] where the τ_{pore} values of 6-37 μs increasing with smaller pore size were observed.

2.3 Conclusion

Herein, it has been shown that kinetically stable Gd^{3+} complexes lacking inner-sphere water can also be implemented as clinically-applicable contrast agents when incorporated into mesoporous silica nanoparticles. An 8-fold increase in longitudinal relaxivity from 0.7 mM^{-1} s^{-1} to 6.2 mM^{-1} s^{-1} was observed when such particles were employed to accommodate nonadentate Gd^{3+} chelates with an aminopropoxy picolinate side arm within their mesopores. A similar 4-fold increase in r_1 from 4.2 mM^{-1} s^{-1} to 16.0 mM^{-1} s^{-1} was observed when octadentate $q = 1$ Gd^{3+} complexes bearing a monoamide side arm were incorporated into the mesopores. The relaxivities of both particles were retained in the presence of a wide range of oxy-anions and zinc ions. The relaxivities were also unresponsive to a change in pH. The increase in relaxivity was attributed to elongated local rotational correlation time and strong second- and outer-sphere contributions as supported by ^{17}O NMR and ^{1}H NMRD analysis most likely due to their favourable peripheral position within the mesopores. Less favourable magnetic susceptibility effects at ultra-high fields, on the other hand, also shortened water proton relaxation times, particularly the T_2 values. Since the relaxivities of $q = 0$ CAs doped into mesoporous silica nanoparticles decreased only slightly with higher field (4.7 T to 11.7 T) and since the trend in NMR imaging, like in spectroscopy, is toward higher fields, such nanoparticulate contrast agents would be able to provide a greater signal-to-noise ratio and increased resolution at such fields, when appropriate pulse sequence parameters would be implemented.

Chapter 3

Enhanced Propagation of the Paramagnetic Effect by Sulphonation of Mesoporous Silica

3.1 Introduction

The efficient transmission of the paramagnetic effect from the inner-sphere of Gd^{3+} through the confined space of MSNs to the bulk water outside of the particle is at least as important as an optimised water exchange rate. When Djanashvili *et al.* [134] exchanged the cations of LTL (Linde Type L) zeolites with Gd^{3+} ($q = 6$), the high relaxivity was shown to be a result of water cluster formation in the main channels allowing for the very rapid hops of water protons (via Grotthuss mechanism) from the inner-sphere of the paramagnetic centre through clusters of hydronium ions bridged by hydrogen bonds to the bulk water outside the zeolite. The water proton mobility in the LTL zeolites was therefore fast enough ($\tau_{zeo} \leq 10^{-8}$ s), such that τ_M was not restricting r_1. Only at pH values above 8.0, a slow water exchange between the interior and exterior of the cavities became the limiting factor as the hydrogen-bonded water network was disrupted by low concentrations of hydronium as well as by ionisation of Gd^{3+}-bound water molecules.[134]

Although proton conductivity is also intrinsic to hydrated silica systems, it never attains high values,[135] especially because of the out-of-plane silanols that form strong hydrogen bonds with the absorbed water molecules creating a network that resembles ice, rather than the liquid phase.[136] Zeolites, on the other hand, possess a very strong Brønsted acidity and are good ionic conductors very much depending on the SiO_2/Al_2O_3 ratio. The migration of protons is limited to the AlO_4 position where the protons can jump between the oxygen atoms enclosing aluminium.[137] In dried zeolites, the Brønsted acid protons are located on hydroxyl groups extending over Si and Al. In the presence of water, a proton leaves the hydroxyl group, thus forming a hydronium cation that becomes attached to AlO_4 and can hop to neighbouring water molecules.[138]

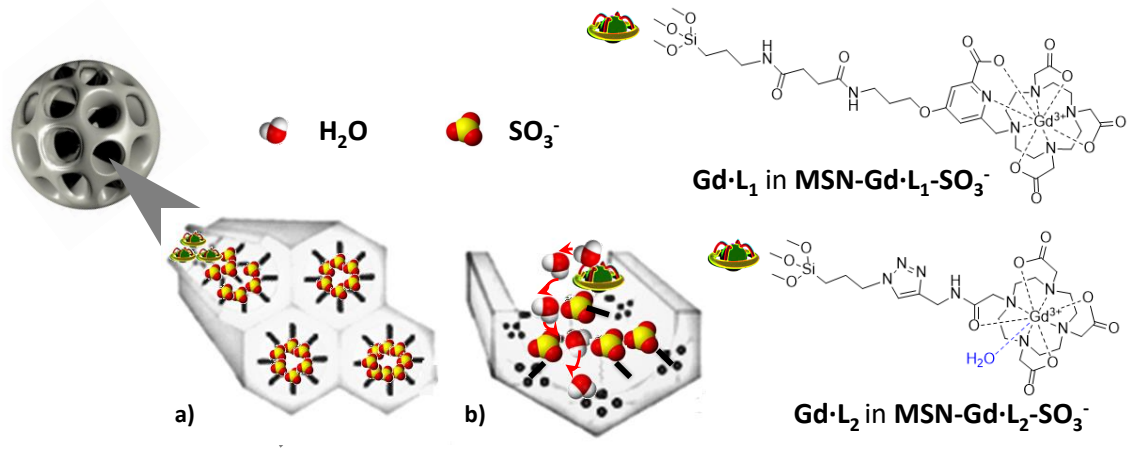


Figure 3.1: a) Schematic representation of **MSN-Gd·L$_i$-SO$_3^-$** incorporating either **Gd·L$_1$** or **Gd·L$_2$**, which are depicted as green complexes inside the mesopores.[1] b) Illustration of the proton conducting mechanism in sulphonic acid-functionalised silica via Grotthuss mechanism. Due to the presence of sulphonates, the excessive proton diffuses through the hydrogen-bonded network of hydronium ions.

When mesoporous silica is functionalised with sulphonate groups, a higher proton conductivity in the range of 10^{-2}-10^{-1} S/cm can be achieved.[139] Hydration thus

[1]Here, **Ln** stands for the incorporated lanthanide centre and subscript $i = \mathbf{1}$ or **2** in ligand **L** stands for either a $q = 0$ or $q = 1$ Ln^{3+} chelate, respectively, as described in Ch. 2.

bridges the acid sites and proton hopping can occur at the sulphonic groups grafted within the pores, while water dissociation also arises more readily due to the presence of surface silanols.[140] It was assumed that upon sulphonation of the silica surface it would be possible to increase the relaxivities of $q = 0$ and $q = 1$ CAs doped into MCM-41 type mesoporous silica nanoparticles (Ch. 2) due to faster transfer of the paramagnetically enhanced first-, second- and outer-sphere water to the bulk water as protons would be allowed to hop more easily between the SO_3^- groups (Fig. 3.1). Indeed, in this chapter, surprisingly high longitudinal relaxivites are presented upon alkyl sulphonate functionalisation of MSNs loaded with Gd^{3+} complexes.

3.2 Results and Discussion

3.2.1 Physicochemical Characterisation of Sulphonated Mesoporous Silica Nanoparticles

In order to functionalise the mesopores with alkyl sulphonates that would enable the proton hopping Grotthuss mechanism through an array of H_3O^+ ions connected by hydrogen bonds, **MSN-Gd·L$_1$** and **MSN-Gd·L$_2$** were post-grafted with (3-mercaptopropyl)trimethoxysilane silane (MPTS, 0.1 mmol per 25 mg MSNs) in dry toluene.[2] Although MPTS was used in excess, no extra particles were observed after several centrifugation/redispersion cycles as demonstrated by hydrodynamic diameter measurements (Fig. 3.5) and TEM images (App. A.4 on P. 198). The grafting procedure was chosen over co-condensation in order to prevent any cross-reactions and possible formation of S-S bridges as thiols are quite nucleophilic and easily oxidisable.[141] The mercapto groups were converted to Brønsted acids bearing -SO_3H groups by acid-catalysed oxidation with H_2O_2 to yield **MSN-Ln·L$_1$-SO$_3^-$** and **MSN-Ln·L$_2$-SO$_3^-$** particles. Sulphonic acid bears the highest oxidation number of

[2]Further experimental details are presented in Experimental Procedures on P. 187.

the sulphur species, and is mostly present in the deprotonated form at physiological pH (pKa = -6 for CH_3SO_3H).[142]

The first indication of successful sulphonate oxidation was provided by solid-state ^{13}C NMR (Fig. 3.2). Sulphide-functionalised MSNs denoted as **MSN-SH** were recognised by an intense resonance signal at 26.6 ppm ascribed to the carbon attached to the thiol group, while a very weak peak at 41.8 ppm points to the faint presence of contaminating disulphide S-S bridges. This disappeared upon acid-catalysed oxidative transformation of thiol into sulphonic groups as the carbon next to the SO_3^- group was visible around 59.5 ppm, while the mercaptopropyl peak at 26.6 ppm disappeared completely. Oxidation was thus considered to be complete.

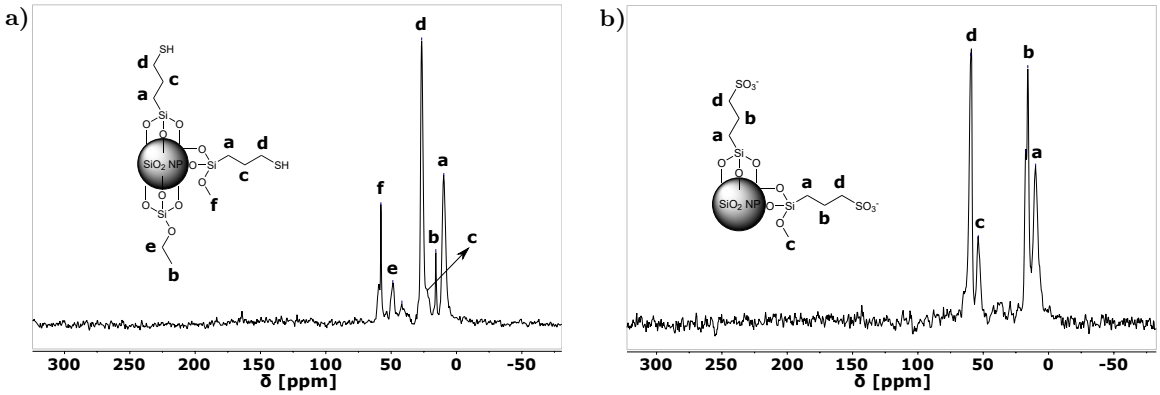


Figure 3.2: ^{13}C CP/MAS NMR spectra showing mercapto-functionalised mesoporous silica nanoparticles before a) **MSN-SH** and after b) **MN-SO$_3^-$** oxidation.

Full oxidation was also confirmed by FTIR spectra (Fig. 3.3). Both **MSN-SH** and **MSN-SO$_3^-$** displayed the typical functional group region associated with silica particles as well as the stretching bands of the propyl chain in the region of 2950 cm^{-1} and 1350-1450 cm^{-1}, while the disulphide absorption bands would be difficult to detect as they constitute the fingerprint portion of the FTIR spectra (500-540 cm^{-1}). The weak thiol peak of **MSN-SH** can be found around 2550 cm^{-1}, which disappears completely upon oxidation. Instead, the new peak around 1040 cm^{-1} that is characteristic of the stretching vibration of the sulphonate group appears in the FTIR

spectrum of the oxidised **MSN-SO$_3^-$** sample.

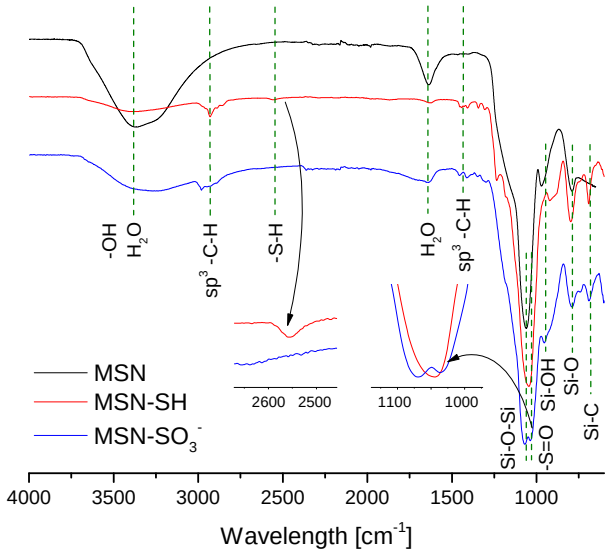


Figure 3.3: FTIR spectrum of bare MSNs (**- MSN**), (3-mercaptopropyl)trimethoxysilane-grafted MSNs (**- MSN-SH**) and sulphonate-functionalised MSNs (**- MSN-SO$_3^-$**). The zoomed-in graph insets show the thiol peak at 2550 cm^{-1} and, next to the silanol peak, a peak around 1070 cm^{-1} attributed to the sulphonate species.

The mesoporous characteristics of sulphonated and non-sulphonated MSNs were quantitatively evaluated by nitrogen physisorption (BET).[3] All three types of unmodified MSNs, aminated MSNs (**MSN-NH$_2$**)[4] and aminated/sulphonated MSNs (**MSN-NH$_2$-SO$_3^-$**) exhibited a similar type IV BET sorption isotherm, while only unmodified MSNs exhibited a hysteresis loop of type H1 in the high relative pressure range, wherein adsorption/desorption branches were nearly parallel and vertical (Fig. 3.4). This is typical for MCM-41 type materials and MCM-41 type MSNs.[143, 144] **MSN-NH$_2$** and **MSN-NH$_2$-SO$_3^-$** particles, on the other hand, exhibited a type H4 adsorption hysteresis. A hysteresis loop is related to blocking and vacating the mesopores and is affected by the deviation of the pore diameter along channels.[144, 145]

[3] Further details are presented on P. 161.

[4] **MSN-NH$_2$** were aminated by co-condensation. Instead of further functionalisation and **Gd·L$_i$** incorporation, such particles were post-grafted with (3-mercaptopropyl)trimethoxysilane and oxidised to sulphonated MSNs (**MSN-NH$_2$-SO$_3^-$**) in order to be subjected to BET analysis.

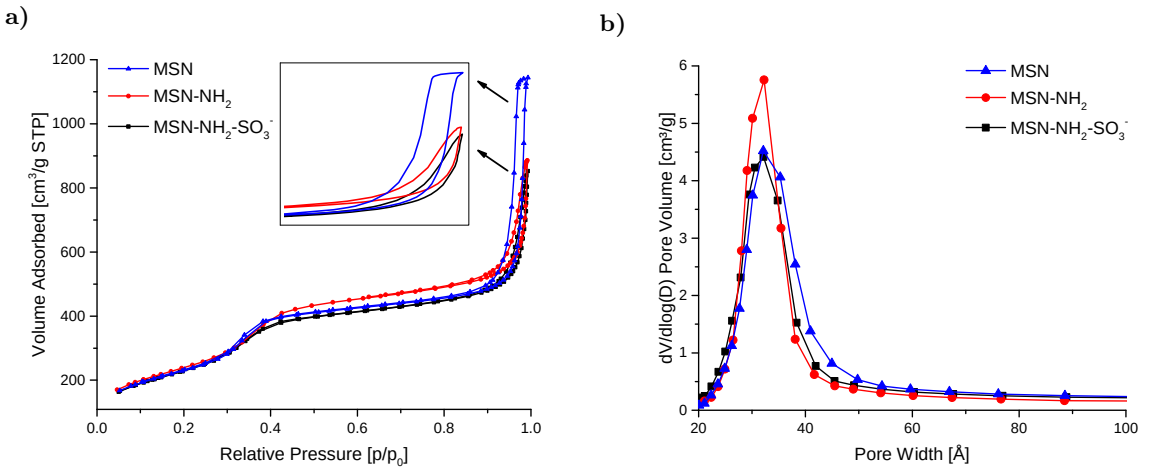


Figure 3.4: a) Nitrogen adsorption/desorption isotherms of bare MSNs (▲ **MSN**), aminated MSNs (● **MSN-NH$_2$**) as well as after (3-mercaptopropyl)trimethoxysilane grafting and thiol oxidation (■ **MSN-NH$_2$-SO$_3^-$**). b) Graph shows the respective BJH pore size distributions obtained on the basis of nitrogen adsorption.

Since the hysteresis loops and BJH pore size distributions of the samples under study are both clearly visible and quite narrow, it can be assumed that the mesopores are highly monodisperse, while the presence of the characteristic step in the 0.1-0.3 p/p_0 range indicates a well-ordered mesoporous lattice. Bare MSNs, aminated MSNs and aminated/sulphonated MSNs all exhibited a BET surface area and BJH pore size of approximately 870 m^2/g and 3.2 nm, respectively, indicating that neither the co-condensed amination nor the post-grafted sulphonation blocked the pores, although a reduction of the total pore volume was detected by about 20 % upon functionalisation with either amine or sulphonate.

Table 3.1: Pore and surface characteristics of bare MSNs (**MSN**), aminated MSNs (**MSN-NH$_2$**) and aminated/sulphonated MSNs (**MSN-NH$_2$-SO$_3^-$**).

	BET Surface Area [m^2/g]	**Pore Volume [cm^3/g]**	**Pore Size BJH [nm]**	**ζ-Potential at pH 7.4 [mV]**	**ζ-Potential at pH 4.0 [mV]**
MSN	871.9	1.9	3.2	-28.0	-6.7
MSN-NH$_2$	882.8	1.5	3.3	-21.0	4.2
MSN-NH$_2$-SO$_3^-$	865.1	1.4	3.2	-25.6	-24.5

The successful oxidation of sulphides to sulphonates was further confirmed by reduced ζ-potentials. Upon oxidation, the ζ-potentials of thiol-functionalised **MSN-Gd·L$_1$-SH** decreased from 10.9 ± 1.8 mV to -38.2 ± 1.9 mV in water, while the ζ-potentials of thiolated **MSN-Gd·L$_2$-SH** decreased from -15.3 ± 1.2 mV to -42.6 ± 0.7 mV. The ζ-potentials of **MSN-Gd·L$_i$-SO$_3^-$** were also reduced compared to **MSN-Gd·L$_i$** especially at low pH (Fig. 3.5), when silanols and other residual organic groups are protonated, while acidic sulphonate groups remain negatively charged. As the trend and magnitude of the zeta-potentials of **MSN-Gd·L$_1$-SO$_3^-$** and **MSN-Gd·L$_2$-SO$_3^-$** samples are very much alike, a similar degree of sulphonate functionalisation can be assumed.

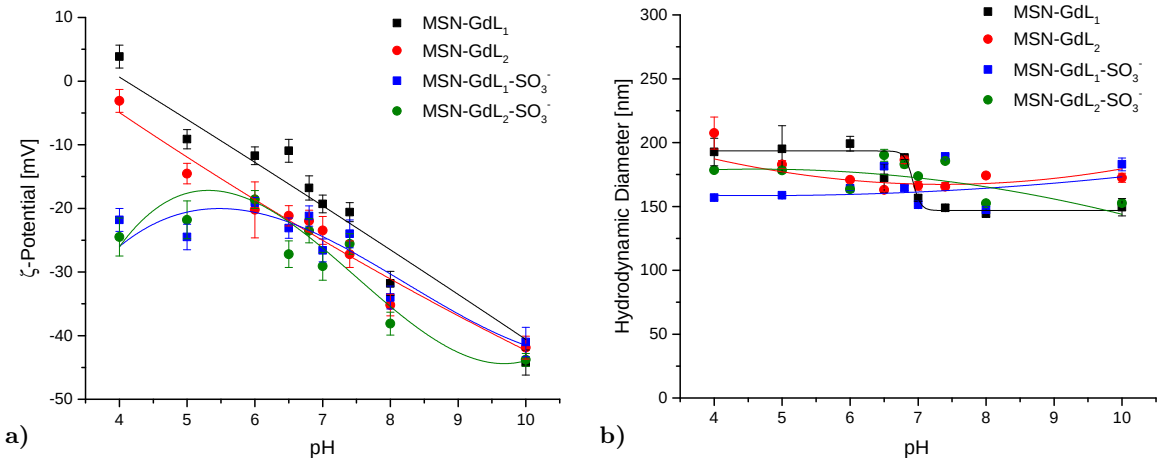


Figure 3.5: Graphs showing the pH dependence of a) ζ-potentials and b) hydrodynamic diameters of ■ $q = 0$ and ● $q = 1$ sulphonated MSNs. The heavily reduced ζ-potentials at low pH occur due to negatively charged sulphonate groups, while peripheral silanols in ■ **MSN-Gd·L$_1$** and ● **MSN-Gd·L$_2$** are gradually protonated as the pH decreases resulting in higher ζ-potentials.

3.2.2 Detection of Immobile Protons by ^{1}H-^{1}H DQ MAS NMR

Compared to the regular NMR in solids under magic-angle spinning (MAS), the 2D double-quantum ^{1}H-^{1}H NMR under fast MAS (DQ MAS) can detect solely the strong dipole-dipole coupling of the spin pairs, while those that vanish from the DQ

MAS spectrum correspond to the protons with very weak dipolar couplings.[146] The latter phenomenon is ideal to show that the water protons associated with the sulphonated silica surface are highly mobile.

If two kinds of dipolar-coupled spins with different chemical shifts are examined, either separated or closely lying spin pairs can be detected. In the former case, DQ signals appear at two different frequencies on the diagonal of a 2D graph exhibiting the dipole-dipole couplings, which are proportional to the intensities of the DQ signals. If the spin pairs are, on the other hand, intermingled, the signals appear at the geometric average of the two frequencies in the DQ dimension and are also detected at both respective frequencies in the single-quantum (SQ) dimension, *i.e.* symmetrically on each side of the diagonal. The SQ dimension thus represents the regular solid-state MAS NMR, while the DQ signals contain information on the dipole-dipole coupling constant and the proximity of the coupled spin pairs.[146, 147]

The large area and the presence of silanol groups on the surface of MSNs provide plenty of surface-water molecule interactions that can be investigated by DQ MAS NMR.[148] When the MSNs are vacuum-dried at room temperature and exposed to moist air for several weeks before the measurements begin, the surface seems to be well-covered with water, which is connected into a hydrogen-bonded network with a resonance peak at 5.2 ppm. The non-hydrogen bonded surface silanol groups are absent from the SQ dimension of the ^{1}H-^{1}H DQ MAS NMR spectra in Fig. 3.6, which would have been represented by the 1.7 ppm peak. The hydrogen-bonded silanols, on the other hand, can be found at 2.7 ppm, and strong DQ coherence between cluster water molecules and silanols occurs at a weighted average of around 4.3 ppm, which indicates a strong coupling and prototropic exchange. No CTAB-related peaks, which are typically shifted to 0.8 ppm, 1.2 ppm, 1.8 ppm, 3.0 ppm and 3.5 ppm,[149] were observed in the NMR spectra, implying that there was no residual surfactant from the synthesis present on the surface as already confirmed by the TGA in Sec. 2.2.1.

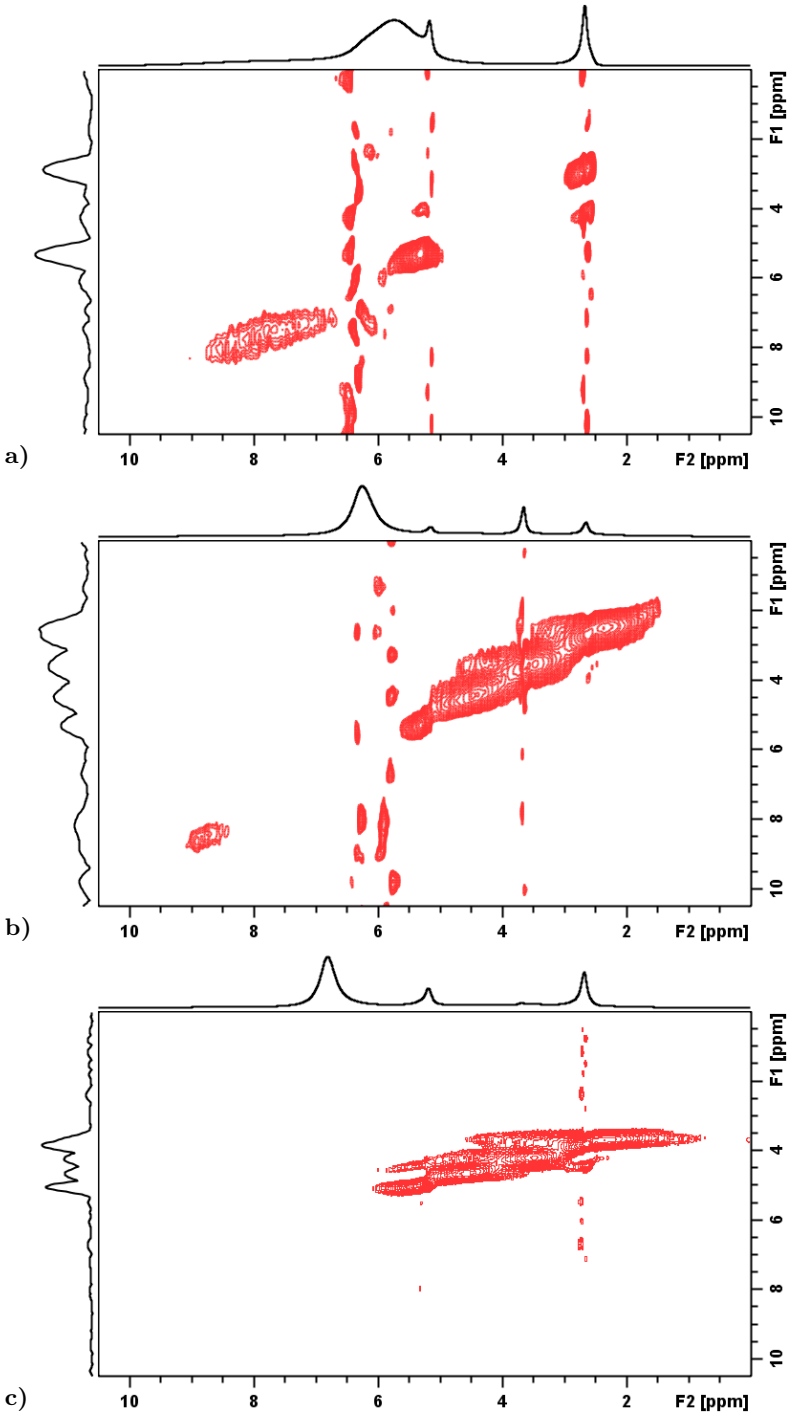


Figure 3.6: ^{1}H-^{1}H DQ MAS NMR spectra of a) unmodified **MSN**, b) thiolated **MSN-SH** and c) sulphonated **MSN-SO$_3^-$**. With each functionalisation step, the water-surface resonance in the SQ spectrum (*horizontal F2*) moves downfield from a) 5.9 ppm over b) 6.4 ppm to c) 6.9 ppm. The peaks at 2.7 ppm, 3.7 ppm, 5.2 ppm and 6.0-7.0 ppm in the SQ dimension can be attributed to the following situations: hydrogen bonding between adjacent surface silanols, water physisorbed onto the silica surface, protons in hydrogen-bonded bulk water and H_2O hydrogen-bonded to the surface silanols. While SQ-axis shows all the protons on the silica surface, the DQ-axis (*vertical F1*) shows only the protons and their intermixed counterparts with strong dipolar couplings.

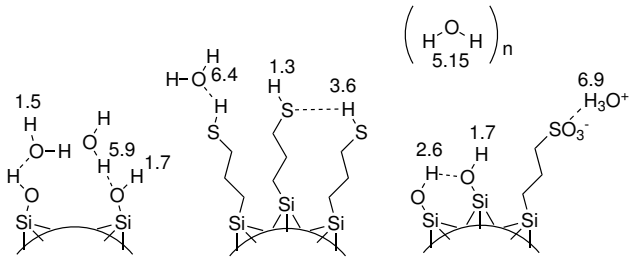


Figure 3.7: Scheme of involved interactions of functional groups and water arrangements, whereby water is hydrogen-bonded to the surface of unmodified and sulphur-containing MSNs. The first silanol on the left is an out-of-plane one, which is acting as the hydrogen bond donor, while the in-plane silanol is a hydrogen bond acceptor. The numbers indicate the observed chemical shifts likely to be associated with such configurations.[148]

Besides unmodified **MSN**s, ^{1}H-^{1}H DQ MAS NMR spectra in Fig. 3.6 also represent MSNs bearing mercaptopropyl groups (**MSN-SH**) as well as MSNs with mercaptopropyl groups oxidised into corresponding sulphonates (**MSN-SO$_3^-$**). These two samples exhibit an additional peak at 3.6 ppm, which is heavily reduced in the **MSN-SO$_3^-$** spectrum suggesting that it might be a result of hydrogen bonding between thiol groups as the absence of the intermixed signal points towards dipolar coupling within the group, which is absent in bare MSNs. The protons of water hydrogen-bonded to the surface silanols in MSNs can be observed as a broadened resonance around 5.9 ppm due to many chemical and physical environments of water hydrogen-bonded to silanol groups, thus contributing to a wide distribution of isotropic chemical shifts since NMR is an integral method. For example, the in-plane silanol groups pictured in Fig. 3.6 exhibit weak acidity (pKa = 8.5) and weak hydrogen bonds with water, while the out-of-plane silanol groups have higher acidity (pKa = 5.6) and thus form strong hydrogen bonds with water.[136] One diagonal and many off-diagonal vertical cross-peaks attributed to water hydrogen-bonded to the surface silanols in MSNs hint at strong hydrogen bonding as well as at an involvement of spins that are not close in space to each other. Such strong dipolar interactions can also be observed in thiolated **MSN-SH** with a narrower resonance of water hydrogen-bonded to silanol groups shifted downfield to 6.4 ppm, whereas in the case

of sulphonated **MSN-SO$_3^-$** the cross-peaks of the signal that shifted further downfield to 6.9 ppm completely disappear, thus confirming weak dipolar couplings related to fast water exchange, which are a consequence of very mobile protons. The sulphonic group protons in a dry sample would contribute to a resonance signal at 9 ppm,[150] but since the sulphonates are highly acidic, their interaction with water produces hydronium species, thus bringing chemical shifts closer to the hydrogen-bonded water network. A similar observation of the fast proton exchange was reported in humidified Nafion, a sulphonated fluoropolymer, in which case sulphonates were present in a form of sulphonic acid at around 9 ppm.[150] The downfield chemical shift and disappearance of the DQ cross-peak of water hydrogen-bonded to a silanol group in the case of **MSN-SO$_3^-$** sample therefore confirms the occurrence of highly mobile water molecules present on the sulphonated silica surface.

3.2.3 Relaxometric Properties of Sulphonated Nanoparticulate Contrast Agents

Before examining the effect of sulphonation on the relaxivity of **MSN-Gd·L$_1$** and **MSN-Gd·L$_2$**, it was necessary to determine if any Gd^{3+} leaching occurred during sulphonation when harsh oxidation conditions of H_2O_2 and catalytic amount of H_2SO_4 were applied. The aqueous arsenazo(III) tests of **MSN-Gd·L$_1$-SO$_3^-$** and **MSN-Gd·L$_2$-SO$_3^-$** were followed by UV-vis absorption spectrometry. Both tests proved to be negative (Fig. 3.8) meaning that there was no uncomplexed Gd^{3+} present in the particle suspension to which arsenazo(III) could bind.

As indicated in Tab. 3.2 and Fig. 3.9, the relaxivities of $q = 0$ CAs loaded into MSNs increased substantially from 6.2 ± 0.9 mM^{-1} s^{-1} to 45.6 ± 4.9 mM^{-1} s^{-1} upon sulphonation, while the r_1 values of $q = 1$ CAs tethered to MSNs rose only from 16.0 ± 0.8 mM^{-1} s^{-1} to 21.9 ± 2.4 mM^{-1} s^{-1} at 4.7 T.[5] The respective 8-fold and

[5]Linear fits corresponding to the data can be found in App. A.7-A.9 on P. 201-203.

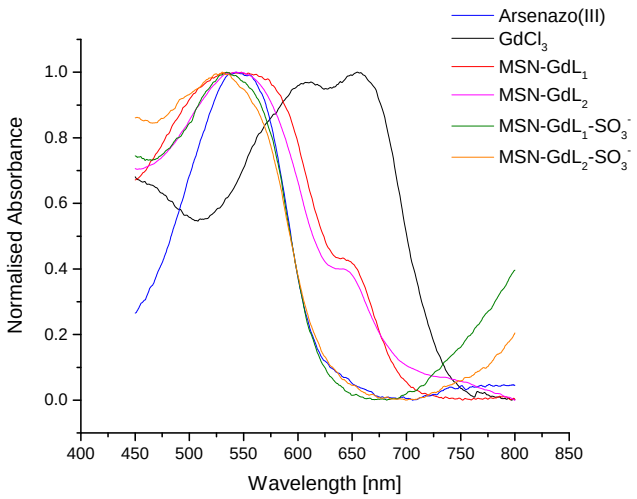


Figure 3.8: Colorimetric studies with arsenazo(III) were performed in water in 1:1 ratio to gadolinium as determined by ICP-MS. The absorbance peak at 560 nm denotes that there is no free Gd^{3+} present, whereas the peaks shifted to 605 nm and 680 nm indicate the presence of Gd^{3+} in solution. As shown by the arsenazo(III) tests of unmodified and sulphonated **MSN-Gd·L$_i$**, all lanthanides were fully chelated.

27 % increases in relaxivities of **MSN-Gd·L$_1$-SO$_3^-$** and **MSN-Gd·L$_2$-SO$_3^-$** compared to their non-sulphonated counterparts are most likely due to an improved propagation of the paramagnetically enhanced water relaxation rates from the interior of the mesopores to the bulk water via the proton hopping Grotthuss mechanism.[151]

Table 3.2: Table showing details of ^{1}H longitudinal relaxivities in water (at 20 °C at 4.7 T, 7.0 T and 9.4 T), water exchange rates determined by ^{17}O NMR and Gd^{3+} content measured by ICP-MS. Error margins represent cumulative errors arising from duplicate repetitions of relaxivity assessment.

	^{1}H r_1 [mM^{-1} s^{-1}], H$_2$O at 4.7 T	**^{1}H r_1 [mM^{-1} s^{-1}], H$_2$O at 7.0 T**	**^{1}H r_1 [mM^{-1} s^{-1}], H$_2$O at 9.4 T**	**k_{ex}^{310} [·10^6 s^{-1}]**	**Gd [μg/g NP]**
MSN-Gd·L$_1$-SO$_3^-$	45.6 ± 4.9	35.4 ± 6.1	29.6 ± 6.5	489.3	1024 ± 7
MSN-Gd·L$_1$	6.2 ± 0.8	5.9 ± 1.1	5.0 ± 0.6	27.6	3323 ± 10
MSN-Gd·L$_2$-SO$_3^-$	21.9 ± 2.4	18.8 ± 2.2	16.4 ± 3.6	9.8	1303 ± 19
MSN-Gd·L$_2$	16.0 ± 0.9	14.1 ± 0.8	10.9 ± 1.1	6.3	1648 ± 73

Since the sulphonated particles exhibited higher proton mobilities and weaker hydrogen bonds with the surface than unmodified or mercaptopropyl-functionalised

MSNs (Section 3.2.2), it can be assumed that faster proton transfer and higher relaxivity are associated with the highly acidic sulphonate groups grafted within the pores and edges of MSNs. These sites act as charge carriers and enable fast proton hopping over hydrogen bond bridged culsters of hydronium ions leading to a decrease in τ_{pore} (*i.e.* the residence time of water molecules located inside the pores). However, a possibility remains that τ_m is still the limiting factor in the case of **MSN-Gd·L$_2$-SO$_3^-$** as the water exchange rate in **MSN-Gd·L$_1$-SO$_3^-$** only depends on the second/outer-sphere contribution possibly explaining the lower increase in r_1 in the case of **MSN-Gd·L$_2$** upon sulphonation.

The transverse relaxivities of **MSN-Gd·L$_2$-SO$_3^-$** (Tab. 3.3), on the other hand, even decreased in comparison to **MSN-Gd·L$_2$** from 135.5 ± 19.2 mM^{-1} s^{-1} to 105.5 ± 34.8 mM^{-1} s^{-1} at 4.7 T leading to a reduction of the r_2/r_1 ratio from 8.5 to 4.8. Although the transverse relaxivities of **MSN-Gd·L$_1$** increased from 49.6 ± 9.4 mM^{-1} s^{-1} to 210.0 ± 29.3 mM^{-1} s^{-1} at 4.7 T upon sulphonation, the r_2/r_1 ratio also decreased from 8.0 to 4.6. The reduced r_2/r_1 ratios might be a result of diminished magnetic susceptibility effects due to highly mobile water molecules inside the mesopores.

Table 3.3: Table showing details of ^{1}H transverse relaxivities of Gd^{3+}-loaded MSNs in water (at 20 °C at), phosphate binding constants K_a and q values at pH 7.4 determined by luminescence measurements of the respective Eu^{3+} counterparts. Error margins represent cumulative errors arising from duplicate repetitions of relaxivity assessment.

	^{1}H r_2 [mM^{-1} s^{-1}], H$_2$O at 4.7 T	**^{1}H r_2 [mM^{-1} s^{-1}], H$_2$O at 7.0 T**	**^{1}H r_2 [mM^{-1} s^{-1}], H$_2$O at 9.4 T**	**K_a [M^{-1}] of phosphate**	**q value**
MSN-Ln·L$_1$-SO$_3^-$	210.0 ± 29.3	226.9 ± 33.2	291.8 ± 40.6	280 ± 150	0.22
MSN-Ln·L$_1$	49.6 ± 9.4	49.7 ± 7.3	50.7 ± 8.6	No binding	0.02
MSN-Ln·L$_2$-SO$_3^-$	105.5 ± 34.8	111.2 ± 36.2	154.9 ± 39.5	720 ± 110	1.16
MSN-Ln·L$_2$	135.5 ± 19.2	176.8 ± 22.6	181.8 ± 24.8	No binding	1.07

The pH dependencies of r_1 (Fig. 3.9) and ζ-potentials (Fig. 3.5) of **MSN-Gd·L$_1$-**

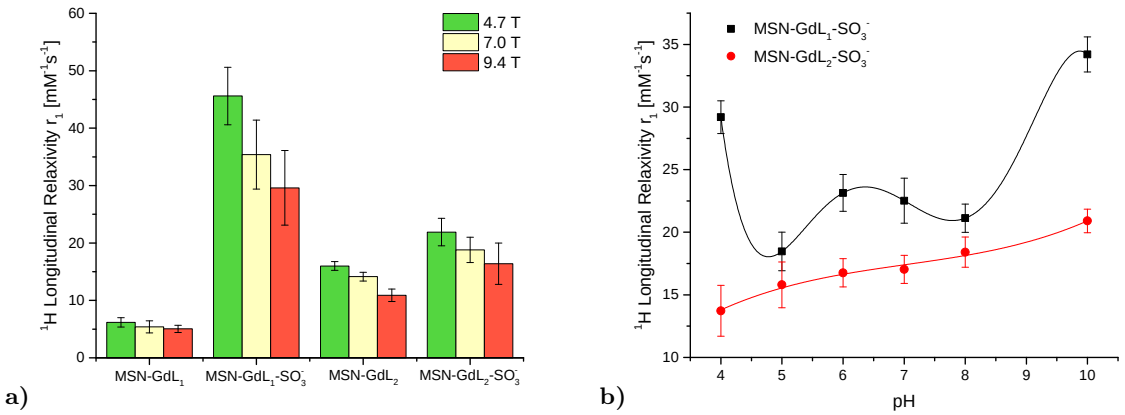


Figure 3.9: Graph showing a) magnetic field and b) pH dependence of protic longitudinal relaxivities of sulphonated MSNs with incorporated $q = 0$ or $q = 1$ contrast agents dispersed in a) ultrapure water (pH ∼7) and b) buffer solutions with the pH range from 4.0-10.0.

SO$_3^-$ and **MSN-Gd·L$_2$-SO$_3^-$** were examined in 10 mM formate (pH 4.0, pKa 3.8), acetate (pH 5.0, pKa 4.8), 2-(*N*-morpholino)ethanesulphonic acid (MES, pH 6.0, pKa 6.1), phosphate (pH 7.0 and 8.0, pKa 7.2) and ethanolamine (pH 10.0, pKa 9.5) buffer solutions in order to ensure the same pH over a whole range of different concentrations (Fig. 3.9 and Fig. 3.10). While the r_1 relaxivities of **MSN-Gd·L$_2$-SO$_3^-$** were reduced only marginally (3-36 % reduction increasing with lower pH) when dissolved in buffer solutions, the r_1 values of **MSN-Gd·L$_1$-SO$_3^-$** decreased by 35-65 % depending on the pH possibly because of the predominantly negatively charged oxy-ions (beside oxy-cations and dissociated NaCl) present in buffer solutions, which have most likely interrupted the hydrogen-bonded water network by adsorbing onto silanols or interacting with hydronium ions. On the other hand, this was also beneficial with regard to the reduction in r_2/r_1 ratios. In **MSN-Gd·L$_1$-SO$_3^-$**, for example, this ratio decreased to 1.4 ($r_1 = 29.2 \pm 5.3$ mM^{-1} s^{-1}, $r_2 = 41.4 \pm 19.8$ mM^{-1} s^{-1}) at pH 4.0. Interestingly, in both cases the highest longitudinal relaxivities were measured at pH 10.0, while the corresponding r_2 values in **MSN-Gd·L$_1$-SO$_3^-$** ($r_1 = 34.2 \pm 9.6$ mM^{-1} s^{-1}, $r_2 = 105.3 \pm 24.1$ mM^{-1} s^{-1}) and **MSN-Gd·L$_2$-SO$_3^-$** ($r_1 = 20.9 \pm 6.2$ mM^{-1} s^{-1}, $r_2 = 102 \pm 27.3$ mM^{-1} s^{-1}) were also relatively low,

thus contributing to reduced r_2/r_1 ratios of 3.0 and 4.9, respectively.

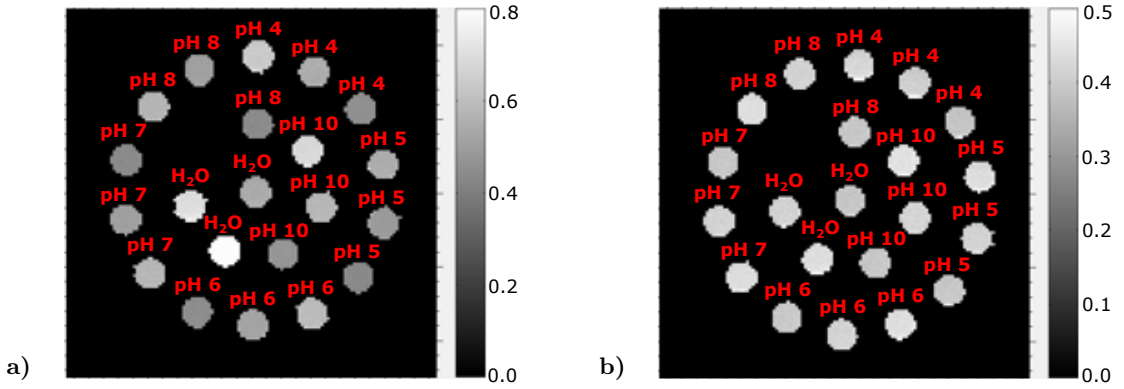


Figure 3.10: T_1-weighted MRI phantoms taken at 4.7 T showing the pH dependence of a) **MSN-Gd·L$_1$-SO$_3^-$** and b) **MSN-Gd·L$_2$-SO$_3^-$**. MRI parameters: SEMS, Thk = 2 mm, matrix = 64 x 64, FOV = 32 mm x 32 mm. Further information can be found on P. 162.

The increased r_1 values at pH 10.0 might be related either to the prototropic exchange catalysed by [OH$^-$] ions or to the increased cooperativity between the sulphonic acid sites and the residual framework composed of deprotonated silanols as shown by the lowest ζ-potentials at highest pH in the case of both sulphonated and non-sulphonated MSNs. This would also confirm the repelling effect of progressively deprotonated surface silanols towards oxy-anions with increasing pH. Therefore, the formation of the hydrogen-bonded network seems to be more important than the enhanced concentration of hydronium ions at lower pH. This observation is also supported by the MD simulations recently conducted by Parrinello *et al.* [152] on the extremely rapid recombination of hydronium and hydroxide ions resulting in formation of a hydrogen-bonded system taking place on a subpicosecond time scale.[152]

3.2.4 Influence of Sulphonation on the Luminescence Properties of Eu^{3+}-Doped MSNs

The pH/pD dependency of the luminescence lifetimes and subsequent determination of the number of bound water molecules at a pH range from 4.0 to 10.0 (Fig. 3.11)

were examined when Eu^{3+} complexes were loaded into MSNs. No significant effect was observed on the q values of **MSN-Eu·L$_1$** and **MSN-Eu·L$_2$**. Sulphonation did, on the other hand, cause a slight decrease in lifetimes with subsequent growth in q values (App. Tab. A.1 on P. 204), however, these changes were still within the error margins. To illustrate, the q values of **MSN-Eu·L$_1$-SO$_3^-$** compared to **MSN-Eu·L$_1$** increased on average from 0.05 to 0.35, while the q values of **MSN-Eu·L$_2$-SO$_3^-$** compared to **MSN-Eu·L$_2$** increased from 1.10 to 1.26. The decrease in τ_{D_2O} lifetimes (20 % on average) is most likely related to residual water present in the sample, whereas the 27 % and 16 % reduction of τ_{H_2O} lifetimes upon sulphonation, when MSNs were doped with $q = 0$ and $q = 1$ CAs, respectively, might be attributed to the increased presence of water molecules in the second-coordination sphere. This is the most probable explanation since both XH oscillators and water molecules beyond the first-sphere have been reported to lower the luminescence lifetimes resulting in non-integral q values.[80, 153]

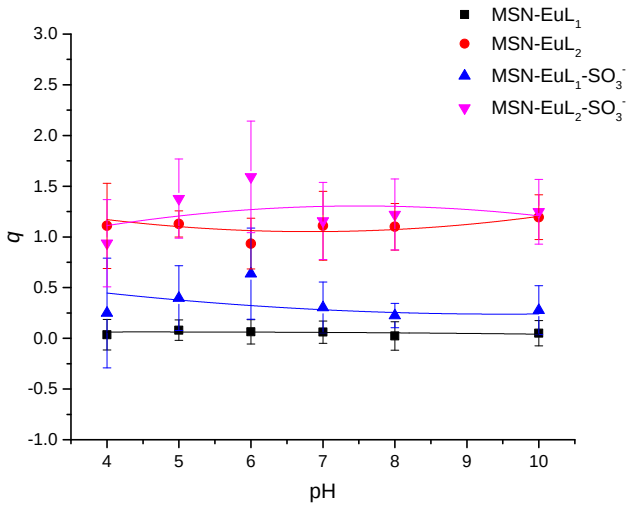


Figure 3.11: pH dependence of q values of ■ **MSN-Eu·L$_1$** and ● **MSN-Eu·L$_2$** as well as their sulphonated counterparts (▲ **MSN-Eu·L$_1$-SO$_3^-$** and ▼ **MSN-Eu·L$_2$-SO$_3^-$**) show that the hydration number does not change considerably with pH. The error bars were obtained from duplicate luminescence lifetime measurements in H_2O and D_2O at two closest pH or pD values being within ± 0.1 error.

The luminescence emission intensities were also perturbed upon addition of oxy-anions such as phosphate, a phenomenon that was not observed in either **MSN-Eu·L**$_1$ or **MSN-Eu·L**$_2$ (Section 2.2.2 on P. 56). The observation is also consistent with the reduced relaxivities in the presence of oxy-ion-containing buffer solutions (Sec. 3.2.3). The dissociation constants of phosphate to europium were determined by phosphate titration and non-linear regression fitting to normalised emission intensities at 590 nm, 615 nm and 700 nm (Fig. 3.12 and App. A.10 on P. 203). The resulting approximated anion dissociation constants for the ternary phosphate-Eu^{3+} complex accounted for 3.6 mM and 1.4 mM for **MSN-Eu·L**$_1$**-SO**$_3^-$ and **MSN-Eu·L**$_2$**-SO**$_3^-$, respectively. The association constant K_a is weaker in **MSN-Eu·L**$_1$**-SO**$_3^-$ possibly due to already negatively charged Eu^{3+} chelate and missing inner-sphere water. Despite the lower K_a, the relaxivity of **MSN-Gd·L**$_1$**-SO**$_3^-$ was decreased by 42 % in the presence of phosphate compared to the 21 % reduction in the r_1 values of **MSN-Gd·L**$_2$**-SO**$_3^-$, however, these were still higher than those of **MSN-Gd·L**$_1$ and **MSN-Gd·L**$_2$. It is plausible to assume that the second/outer-sphere contribution is higher in **MSN-Ln·L**$_1$**-SO**$_3^-$ and **MSN-Ln·L**$_2$**-SO**$_3^-$ as the relaxivity and luminescence emission intensities became more susceptible to the presence of oxy-anions.

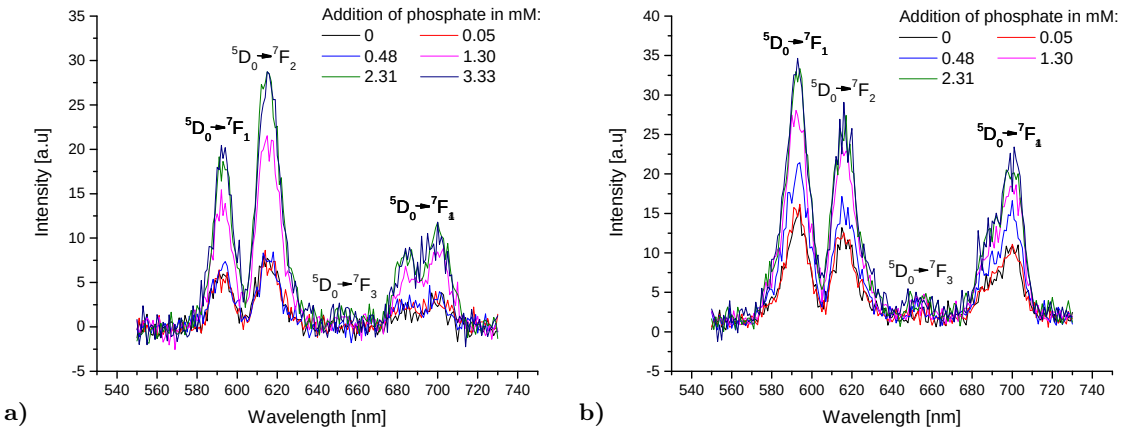


Figure 3.12: Comparison of the normalised emission spectra of a) **MSN-Eu·L**$_1$**-SO**$_3^-$ and b) **MSN-Eu·L**$_2$**-SO**$_3^-$ as a function of added phosphate (10 mM, pH 7.4). Conditions: λ_{ex} = 393 nm, 293 K.

3.2.5 ^{17}O NMR Indicates Faster Water Exchange Rates upon Sulphonation

Since both fast proton mobility and proton relaxivities were shown to increase upon sulphonation, it is expected that the latter might also be a result of the faster water exchange rates. These were indeed confirmed by the temperature-dependent measurements of ^{17}O NMR transverse relaxation rates corrected for diamagnetic contributions (Fig. 3.13). Beyond the intermediate water exchange regime noticeable at low temperatures, fast exchange dominates the temperature range higher than 303 K as the ^{17}O transverse relaxation rates in both sulphonated MSNs decrease with temperature. While non- and sulphonated **MSN-Gd·L$_1$** can both be found in a fast exchange regime, **MSN-Gd·L$_2$** changed from the slow to fast exchange regime upon sulphonation. This transition is a result of second- and outer-sphere domination not only at low, but also at high temperature. Consequently, at 310 K the water exchange rates of **MSN-Gd·L$_2$-SO$_3^-$** are 36 % faster compared to **MSN-Gd·L$_2$** with τ_M decreasing from 158.7 ns to 102.2 ns upon sulphonation, whereas the k_{ex} values of **MSN-Gd·L$_1$-SO$_3^-$** are 38 % higher in contrast to **MSN-Gd·L$_1$** (τ_M decreases from 36.2 ns to 22.5 ns). The latter results were obtained when q values of 0.02 and 0.22 were considered for the calculation of ^{17}O $ln(R_{2r})$ values for **MSN-Gd·L$_1$** and **MSN-Gd·L$_1$-SO$_3^-$**, respectively, as determined by luminescence lifetimes (Sec. 3.2.4). However, if these were both set to $q = 0.02$, an 18-fold increase in k_{ex} was achieved with τ_M decreasing from 36.2 ns to 2.0 ns upon sulphonation. These increments in k_{ex} are consistent with the observed relaxivities as these increased by 65- and 5-fold upon sulphonation of **MSN-Gd·L$_1$** and **MSN-Gd·L$_2$**, respectively.

The absolute reduced chemical shifts at low temperature ($|\Delta\omega_r^o| \cong \Delta\omega_{OS}^o = C_{OS}\Delta\omega_M^o$)[37] also suggest that the second/outer-sphere contributions are similar, but only slightly higher in **MSN-Gd·L$_1$-SO$_3^-$** than in **MSN-Gd·L$_2$-SO$_3^-$**. The ^{17}O longitudinal relaxation rates, on the other hand, are dominated by dipolar-dipolar

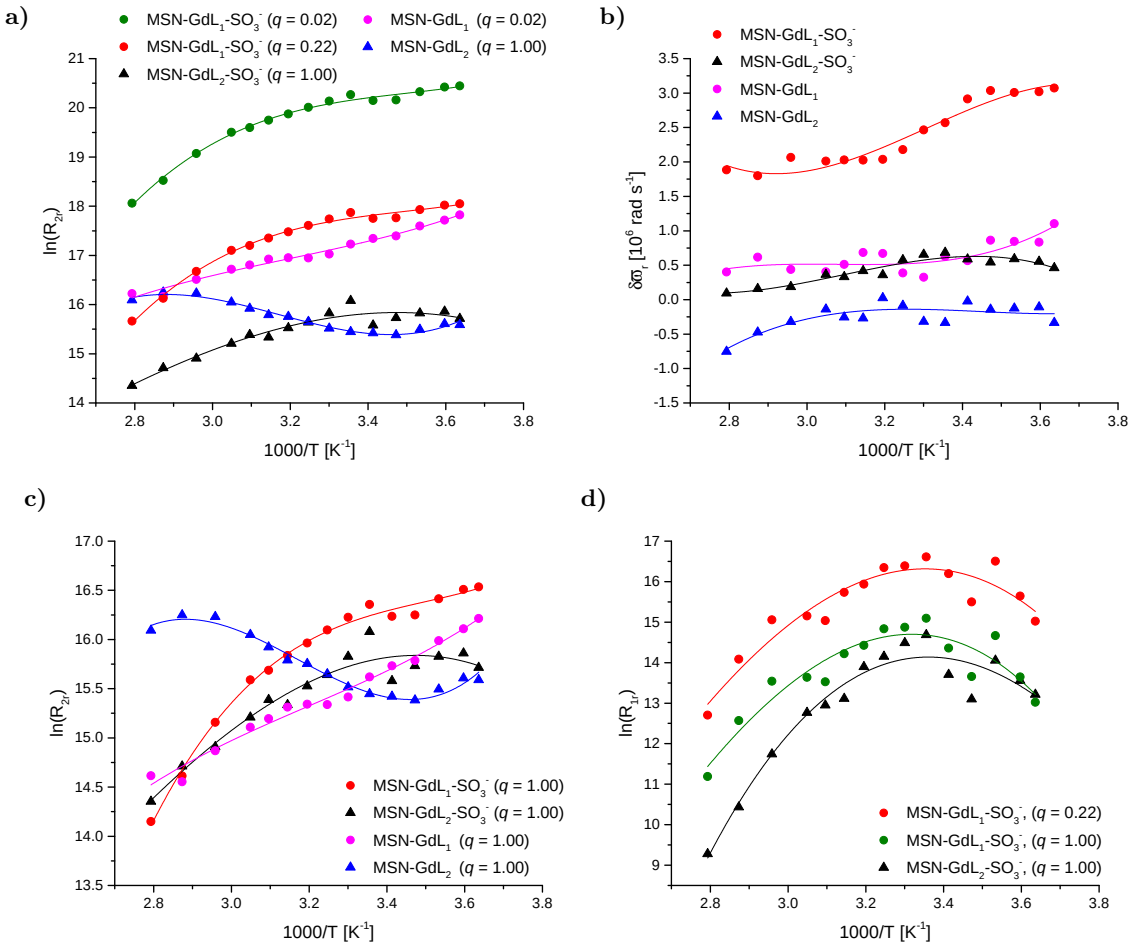


Figure 3.13: Temperature dependence of the paramagnetic contribution to ^{17}O NMR relaxation of water showing reduced d) longitudinal rates R_{1r} and b) chemical shifts $\delta\omega_r$ in ●/● **MSN-Gd·L$_1$-SO$_3^-$** and ▲ **MSN-Gd·L$_2$-SO$_3^-$**. Their ^{17}O reduced transverse R_{2r} relaxation rates (a) and c)) are compared to their non-sulphonated counterparts ● **MSN-Gd·L$_1$** and ▲ **MSN-Gd·L$_2$**. Graph c) assumes a value of $q = 1$ for **MSN-Gd·L$_1$** and **MSN-Gd·L$_1$-SO$_3^-$** instead of the q values determined by luminescence analysis.

and quadrupolar relaxation rates and are thus sensitive to the rotation of the complex through the Gd^{3+}-O vector.[37] Since **MSN-Gd·L$_1$-SO$_3^-$** lacks the inner-sphere water, it cannot be deduced that its local rotational correlation times are shorter due to faster R_{1r}, particularly, when q is set to 1.0, the $ln(R_{1r})$ values can be considered to be within experimental error of each other. These results suggest that the local rotational correlation times are similar, a trend also observed in their unsulphonated counterparts (Fig. 2.15 on P. 58). While rotational dynamics seemed to

be unchanged, the ^{17}O NMR results hint at increased 2^{nd}- and outer-sphere contribution upon sulphonation partially overcoming the slow water exchange limitation of the weakly associated monoamide side arm of the **Gd·L$_2$** complex loaded into MSNs.

3.2.6 Sulphonation Effects on Water Residence Correlation Times

Due to broad maxima shifted towards higher frequencies, the NMRD profiles of **MSN-Gd·L$_1$-SO$_3^-$** and **MSN-Gd·L$_2$-SO$_3^-$** could be best fitted by the combined contributions with an increased second-sphere involvement (Fig. 3.14) similarly to their non-sulphonated counterparts. As in detail discussed in Ch. 2 on P. 60, electronic parameters and nanoparticulate rotational dynamics can only be roughly estimated so that the fitted results must be taken with caution.

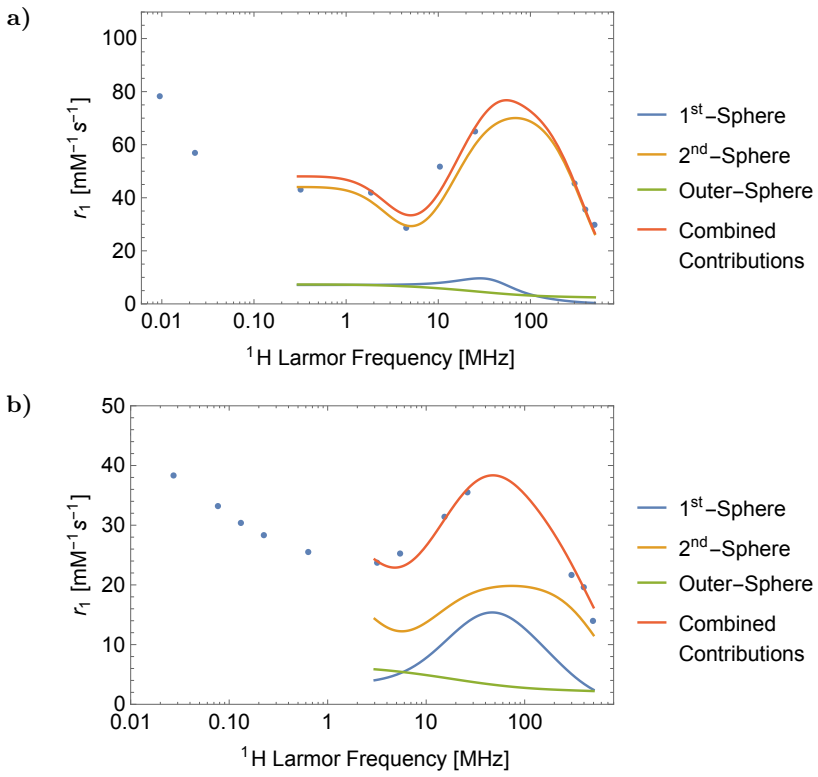


Figure 3.14: NMRD profiles of a) **MSN-Gd·L$_1$-SO$_3^-$** and b) **MSN-Gd·L$_2$-SO$_3^-$**. The relaxation times were measured at 293 K. Relaxivities at lower fields are dominated by T_{1e}, and thus these data points were excluded in the fitting of the NMRD curves.

Upon sulphonation, the second-sphere water residence times $\tau_{M'}$ decreased from 68 ns to 6 ns and from 86 ns to 16 ns in **MSN-Gd·L$_1$-SO$_3^-$** and **MSN-Gd·L$_2$-SO$_3^-$**, respectively (Tab. 3.4). The diffusion correlation times τ_D were also reduced from 45 ps to 23 ps in **MSN-Gd·L$_1$-SO$_3^-$** and from 40 ps to 29 ps in **MSN-Gd·L$_2$-SO$_3^-$**. The exchange of water between the inside and outside of the channels expressed through the residence time of the water molecules located inside the pores τ_{pore} also became faster in sulphonated MSNs decreasing from 24 μs to 10 μs in **MSN-Gd·L$_2$-SO$_3^-$**, while the rotational parameters could be kept approximately the same as already suggested by the variable-temperature ^{17}O NMR measurements.

Table 3.4: Rough approximation of parameters resulting from fits of the longitudinal NMRD profiles.[6]

	MSN-Gd·L$_1$	**MSN-Gd·L$_1$-SO$_3^-$**	**MSN-Gd·L$_2$**	**MSN-Gd·L$_2$-SO$_3^-$**
τ_v^{293} $[ps]$	30.1	29.2	31.2	22.5
Δ^2 $[\cdot 10^{19} s^{-2}]$	3.2	3.5	4.4	2.8
τ_{RG}^{293} $[ns]^{[b]}$	$\approx 20.2^{[a]}$	$\approx 20.0^{[a]}$	21.6	21.8
τ_{RL}^{293} $[ns]$	$\approx 0.8^{[a]}$	≈ 0.9 $^{[a]}$	1.1	1.0
F^2	$\approx 0.4^{[a]}$	$\approx 0.4^{[a]}$	0.5	0.5
τ_{pore}^{293} $[\mu s]$	$\approx 10.0^{[a]}$	$\approx 5.0^{[a]}$	23.6	9.3
τ_D^{293} $[ps]$	44.7	23.1	39.7	28.5
q'	1	1	1	1
$\tau_{R'}^{293}$ $[ns]$	0.7	0.5	0.4	0.3
$\tau_{M'}^{293}$ $[ns]$	68.0	6.3	86.4	15.8
τ_M^{293} $[ns]^{[c]}$	$29.4^{[a]}$	$1.8^{[a]}$	200.8	104.0

The results thus suggest that the propagation of relaxation enhancement from the interior of the pores to the bulk water outside is accelerated by the presence

[6] [*a*] Estimation of these parameters is unreliable due to missing inner-sphere contribution. [*b*] The NMRD fits were relatively insensitive to the real value of τ_{RG}^{293} $[ns]$ in the range higher than 10 ns. [*c*] The first sphere water residence times were taken from ^{17}O NMR results at 293 K.

of sulphonate groups on the silica surface that induce proton hopping and not by rotational restriction. In addition, the second-sphere water exchange seems to be enhanced leading to higher relaxivities at ultra-high fields, which is evident from the difference between the first- and second-sphere contribution in Fig 3.14 b). Whereas the shape of the NMRD curve is independent of the number of second-sphere water molecules, the amplitude of the curve is heavily affected by it suggesting that the higher relaxivity in $q = 0$ compared to $q = 1$ Gd^{3+} complexes doped into MSNs might also be a result of increased second/outer-sphere contribution upon sulphonation possibly due to a much longer and flexible linker of the former. This might allow the picolinate Gd^{3+}-DOTA derivative to bend easily and interact with the sulphonate-functionalised surface.

3.3 Conclusion

While sulphonates remain deprotonated throughout the physiologically relevant pH range, free Gd^{3+}-loaded LTL zeolites rely only on Brønsted acidic hydroxyl groups bridging Al and Si, wherein a decreased protic relaxivity with higher pH (pH $\geq$ 7.0) was observed by Djanashvili *et al.* [134] due to a reduced concentration of hydronium ions and consequently distorted hydrogen-bonded system. Furthermore, such pH was only adjusted by small amounts of HCl or NaOH as addition of any oxy-ion-based buffers would have most likely diminished the r_1 values since Gd^{3+} incorporated into zeolites bears not one but six inner-sphere water molecules that can be easily replaced by anionic species, such as phosphate. Consequently, a better choice might be to incorporate already chelated Gd^{3+} species into the nanoparticle matrix by conjugation, and increase the proton transfer within the channels by sulphonation.

Herein, a 65- and 5-fold increase in longitudinal relaxivity has been observed when mesoporous silica nanoparticles were employed to accommodate nonadentate[7] and octadentate[8] Gd^{3+} complexes, respectively, and subsequently functionalised by mercaptopropyl groups that could be easily oxidated into sulphonates. The relaxivities were increased due to higher second/outer-sphere contribution and faster proton transfer associated with highly acidic sulphonate groups, which were confirmed by ^{1}H NMRD/^{17}O NMR and ^{1}H-^{1}H DQ MAS NMR, respectively. The importance of the unperturbed hydrogen-bonded hydronium network responsible for proton hopping was also demonstrated by the pH responsiveness of longitudinal and transverse relaxivities in the presence of various oxy-anions, especially when negatively charged $q = 0$ Gd^{3+}-DOTA CAs with a picolinate side arm were incorporated into mesoporous silica nanoparticles. MSNs covalently coupled to neutral $q = 1$ CAs through a monoamide pendant arm ligated to Gd^{3+} species and a smaller organic linker consisting of a rigid triazole ring, on the other hand, exhibited a 13-fold lower longitudinal relaxivity enhancement as well as a weaker pH dependence. The highest pH-responsive decrease was 2-fold lower than in $q = 0$ Gd^{3+} complex-loaded sulphonated MSNs. It can thus be reasoned that the local ionic environment, the number of second-sphere water molecules, the first- and second-sphere water exchange rates as well as the length/flexibility of the linker all either contribute or limit the proton relaxivity enhancements achieved through faster proton hopping as a result of sulphonate functionalisation of the silica surface.

[7]Longitudinal relaxivity increased from 0.7 mM^{-1} s^{-1} to 45.6 mM^{-1} s^{-1}.
[8]Longitudinal relaxivity increased from 4.2 mM^{-1} s^{-1} to 21.9 mM^{-1} s^{-1}.

Chapter 4

pH-Activatable Polymer-Capped Mesoporous Nanoparticulate MRI Probes

4.1 Introduction

The large, uniform and easily modifiable porous scaffold of mesoporous silica nanoparticles (MSNs) provides an interesting platform for responsive ^{1}H MRI CAs. Davis *et al.* [122], for example, investigated a practically irreversible MRI contrast switching by blocking water access with proteins to Gd^{3+} species internalised in MSNs and recovering the MRI contrast through pore unblocking triggered by protein-protein recognition.[122] Polymers, on the other hand, offer a chemically controllable, reversible, stimuli-responsive switch based on molecular motion. Okada *et al.* [67] explored pH-responsive polymeric CAs based on *n*-octylamine-modified poly(sodium maleate-alt-ethyl vinyl ether) that could convert between the globular and extended forms. This resulted in reversible switching between high contrast at low pH caused by intramolecular hydrophobic interactions among the *n*-octyl groups and low contrast at high pH due to repulsions among deprotonated carboxyl groups.[67] Sometimes the resulting changes in relaxivity can also stem from the involvement of combined factors.

For example, Sherry *et al.* [154] reported on a G5-PAMAM-based dendrimer with incorporated Gd^{3+} complexes accommodating phosphonate pendant arms. These pendants became progressively protonated at pH lower than 8.5, thus catalysing the proton exchange of inner-sphere water with bulk H_2O, while the protonation of tertiary amines within the dendrimer was assumed to cause internal rigidity indicating that both τ_M and τ_R contributed to the pH responsiveness.[154]

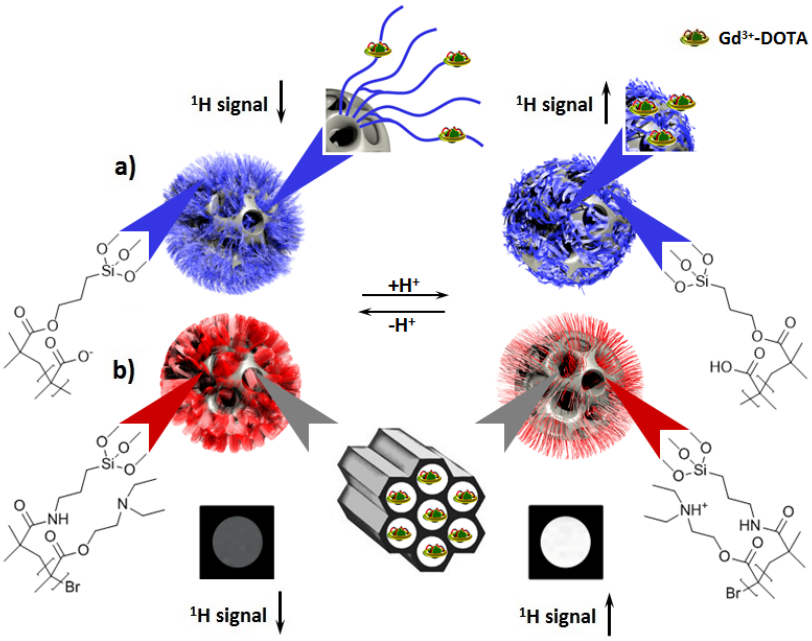


Figure 4.1: Schematic representation of MSNs coated by a) poly(methacrylic acid) or b) poly(2-(diethylamino)ethyl methacrylate)) that increase the ^{1}H relaxivity of incorporated CAs at low pH due to a) slower local rotational tumbling rate or b) improved water access. The arrows denote an increase in the ^{1}H MRI signal at low pH as shown in the T_1-weighted MRI images taken from and further explained in Fig. 4.11 on P. 99.

In this chapter, a pH-triggered response of Gd^{3+} chelates tethered to MSNs was probed through either local mobility or water access regulated by a pH-responsive polymer, which can switch between hydrophobic interactions and electrostatic repulsions upon pH change (Fig. 4.1). The absence of inner-sphere contribution on pH responsiveness was probed by implementation of $q = 1$ or $q = 0$ CAs as outlined in Ch. 2. Polymers were chosen as water flow control valves since monomers conforma-

tionally responsive to temperature, pH and redox triggers can be easily incorporated once a working system has been established.

To investigate the "on-off" switching capability of the nanoparticle-based contrast agent through pH tuning, MSNs were functionalised with pH-responsive polymers. There are several different approaches, which can be employed in the generation of polymer-MSN nanocomposites in order to apply MSNs as containers and pH-responsive polymers as nanovalves that could be opened and closed reversibly by the change in pH. For example, in the so-called pre-polymerisation method, polymerisation takes place in solution followed by grafting of the polymer onto the surface of nanoparticles.[155] In other cases, an *in situ* polymerisation technique involving polymerisation that is initiated on the surface is utilised. This yielded easily controllable and densely populated polymer brushes. To illustrate this method, an ATRP initiator was grafted onto MSNs in order to trigger surface polymerisation of pH-responsive 2-(diethylamino)ethyl methacrylate.[156] Here, ATRP denotes atom transfer radical polymerisation, which is a metal-catalysed polymerisation approach that involves the reversible activation and deactivation between a growing polymer chain and metal species.[157]

4.2 Results and Discussion

4.2.1 Preparation of Polymer-Coated Mesoporous Silica Nanoparticles

In order to determine the best possible stimuli-responsive water accessibility to the pores, two approaches based on "grafting from" and "grafting onto" methods have been investigated (Fig. 4.2).[1] In the former case, the surface-initiated ATRP was chosen to grow polymer chains only on the surface of MSNs, while further control could

[1]Further experimental details are presented in Experimental Procedures on P. 187.

be achieved by the addition of small amounts of a deactivator such as $CuBr_2$[158] and peripheral positioning of the initiator sites. This was attained by a short post-grafting period with (3-aminopropyl)triethoxysilane followed by the acylation of amines with 2-bromoisobutyryl bromide to ensure that the initiators were located as close to the periphery of the mesopores as possible in order to prevent pore jamming. For example, internalised polymer chains would have an opposite effect to pores gated by polymers as swelling of polymers inside the pores would result in a restricted water access, while collapsed polymers would increase the lumen of the pores.

The bromoisobutyryl amide peripherally functionalised MSNs or **MSN-Ln·L**$_i$ particles[2] were subsequently polymerised with 2-(diethylamino)ethyl methacrylate (DAEMA) by surface-initiated ATRP. The reaction was performed at 70 °C in the presence of CuBr and *N,N,N',N",N"*-pentamethyldiethylenetriamine (PMDETA) as a catalyst and reducing agent, respectively, to initiate polymerisation.[159] The removal of residual copper was accomplished by sodium diethylthio carbamate and Soxhlet-dialysis extraction in methanol at 110 °C. The resulting particles denoted as **MSN-Poly(DAEMA)**$_a$ were used only for characterisation purposes, while lanthanide-doped **MSN-Ln·L**$_i$**-Poly(DAEMA)**$_a$ were employed in both relaxometric and characterisation studies.

The successful ATRP initiator grafting and subsequent formation of polymeric brushes were confirmed by FTIR (Fig. 4.7) and solid-state NMR (Fig. 4.3, App. A.11 and App. A.12 on P. 204). The ^{13}C CP/MAS NMR of **MSN-Poly(DAEMA)**$_a$ exhibited two characteristic chemical shifts of the initiator's amide and polymer's ester groups at 172 ppm and 177 ppm, respectively, while in solid-state ^{29}Si NMR two sets of chemical shift ranges of -111 ppm to -100 ppm and -68 ppm to -59 ppm were detected, which correspond to Q and T sites denoting silanols/siloxanes and organosiloxanes,

[2]Here, **Ln** stands for incorporated lanthanide centre and subscript $i = \mathbf{1}$ or $\mathbf{2}$ in ligand **L** stands for either a $q = 0$ or $q = 1$ Ln^{3+} chelate, respectively, as described in Ch. 2.

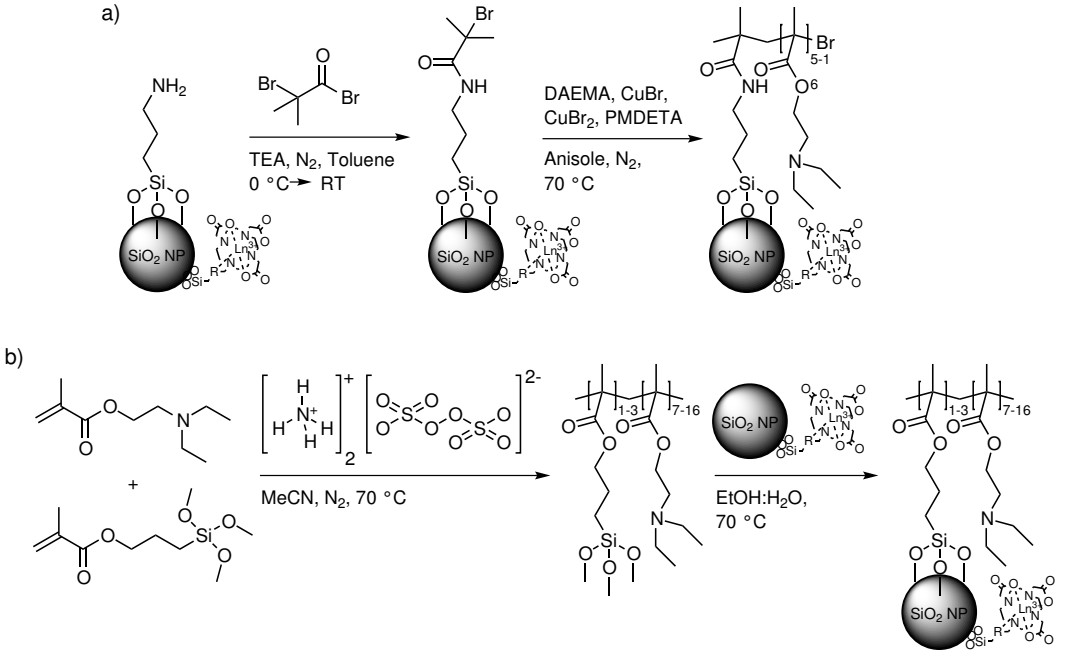


Figure 4.2: Synthetic pathway for pH-responsive polymer chain grafted nanoparticulate resonant contrast agents via a) surface-initiated atom-transfer radical and b) free radical pre-polymerisation.

respectively. When compared to the $\mathbf{Ln{\cdot}L}_1$-doped MSNs, the phosphotungstic acid stained poly(DAEMA) coating was also visible in the TEM images (Fig. 4.8).

In order to also investigate how the "grafting onto" approach affected the MRI contrast upon a change in pH, $\mathbf{MSN\text{-}Poly(DAEMA)}_b$ and $\mathbf{MSN\text{-}Ln{\cdot}L}_i\mathbf{\text{-}Poly(DAEMA)}_b$ were prepared by the pre-polymerisation method (denoted by subscript b),[3] followed by capping of the surface through sticky monomers consisting of 3-(trimethoxysilyl)propyl methacrylate (MPS), which has been previously utilised for polymer functionalisation of silica nanoparticles.[160] DAEMA and MPS were thus first polymerised by free-radical polymerisation with ammonium persulphate as an initiator at 70 °C and then post-grafted onto the nanoparticle surface by condensation. Both ^{29}Si and ^{13}C MAS NMR[4] (Fig. 4.3 and App. A.12 on P. 204) showed efficient grafting and polymerisation by exhibiting typical organosiloxane ^{29}Si and

[3]Further experimental details are given on P. 188.

[4]For solid-state NMR characterisations, the reactions were performed by a 10-fold increased degree of initator and monomer functionalisation.

MPS-poly(DAEMA)-related ^{13}C NMR chemical shifts, respectively. The TEM images also revealed tighter pores compared to **Gd·L$_1$**-loaded MSNs (Fig. 4.8) and thermogravimetric analysis revealed a 13 % weight loss due to the presence of the polymer (App. A.20 on P. 208).

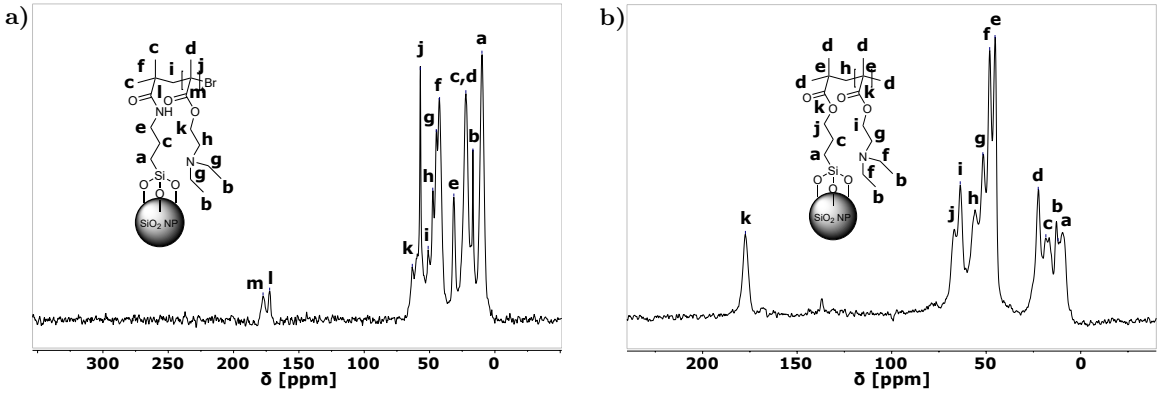


Figure 4.3: ^{13}C CP/MAS NMR spectra showing a) **MSN-Poly(DAEMA)$_a$** by surface-induced ATRP and b) **MSN-Poly(DAEMA)$_b$** functionalised by pre-polymerisation.

To compare the lengths of the polymer brushes of **MSN-Poly(DAEMA)$_a$** and **MSN-Poly(DAEMA)$_b$**, the samples were dissolved in a water/toluene mixture and carefully treated with HF (48 % aq) in order to etch the polymers from the silicon surface, which were subsequently analysed by MALDI-TOF.[5] The resulting molecular weight distributions of the grafted polymer were about 520-1266 g/mol and 1152-2399 g/mol for **MSN-Poly(DAEMA)$_a$** and **MSN-Poly(DAEMA)$_b$**, respectively (Fig. 4.4). Since the polymers were scraped off the silica surface, the results should be taken with caution. If reliable, they would indicate that only 5-16 monomeric units are present in the organosiloxane brushes of **MSN-Poly(DAEMA)$_a$** and 7-16 DAEMA units with 1-3 MPS units in **MSN-Poly(DAEMA)$_b$** indicating that the brushes are composed of smaller oligomers rather than polymers.

Beside probing the water access gating, a pH-triggered change in local mobility was

[5]Further details can be found in Experimental Procedures on P. 166. Instead of MALDI-TOF, molecular weight determination by GPC would have been preferable if available.

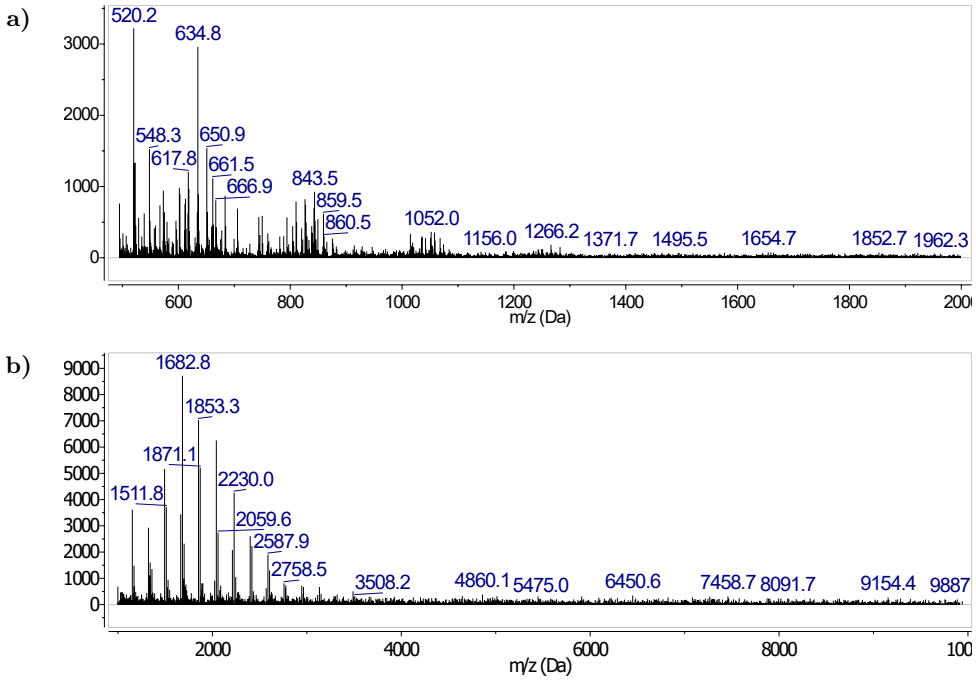


Figure 4.4: MALDI-TOF spectra of a) **MSN-Poly(DAEMA)**$_a$ and b) **MSN-Poly(DAEMA)**$_b$ using 2,5-dihydroxy benzoic acid as the matrix.

also tested by incorporating $q = 0$ and $q = 1$ **Ln**·**L**$_i$ complexes into poly(methacrylic acid)-coated mesoporous silica nanoparticles (denoted as **MSN-Poly(MAA)-Ln**·**L**$_i$, Fig. 4.5). Poly(methacrylic acid) (poly(MAA)) was chosen because of its swelling properties, which occurred at higher pH (pKa is around 5.0) and which are reverse to the pH response provided by poly(DAEMA), since the collapsed polymeric chains at low pH should also increase the MRI contrast. This is similar to the improved water access due to swollen polymer chains in **MSN-Poly(DAEMA)-Ln**·**L**$_i$ at low pH.

For this purpose, MSNs were post-grafted with MPS at RT, which was confirmed by solid-state ^{13}C NMR (App. A.11 on P. 204), and polymerised with methacrylic acid.[6] A small amount of ethylene glycol dimethacrylate (EGDMA) was also added in order to create a cross-linked shell on the mesopores (visible as a cloudy coating on MSNs in Fig. 4.8 d)). This in turn also increases the rigid surface effect of MSNs

[6]Further experimental details can be found on P. 188. For solid-state NMR characterisations, the reactions were performed by a 10-fold increased degree of initator and monomer functionalisation.

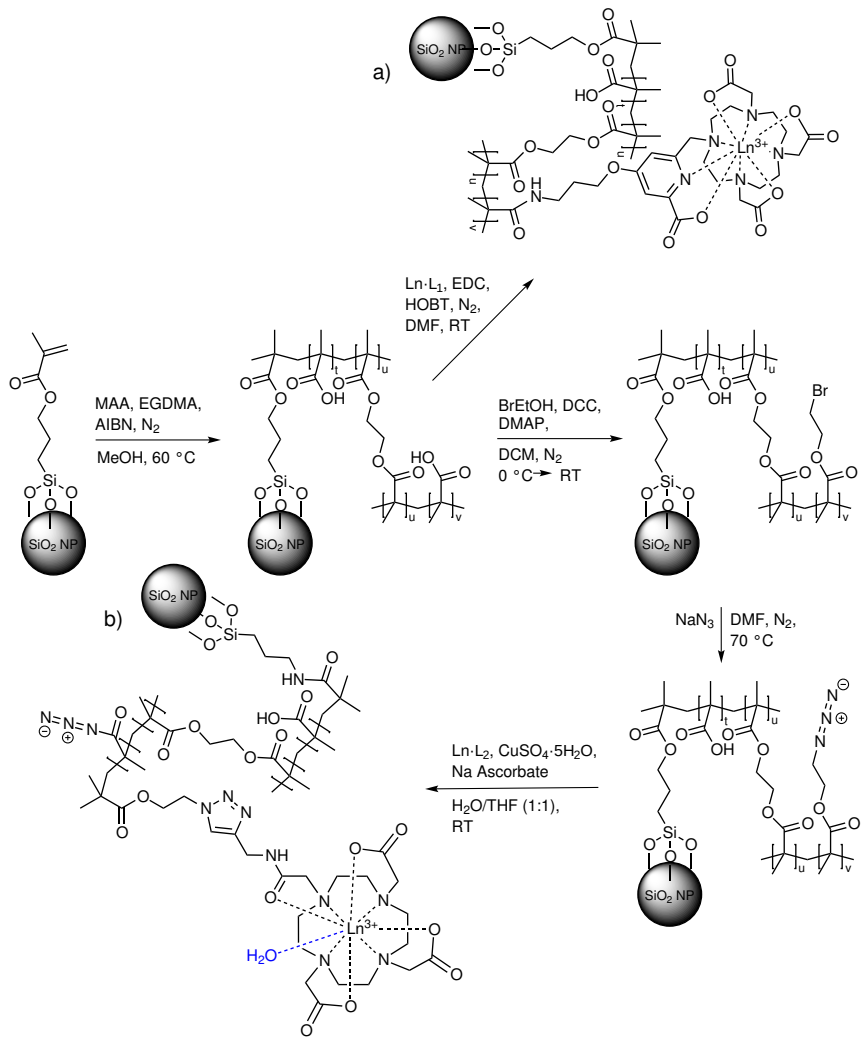


Figure 4.5: Synthesis of pH-responsive poly(methacrylic acid)-coated nanoparticulate resonant contrast agents via free radical polymerisation to yield a) **MSN-Ln·L$_1$-Poly(MAA)** and b) **MSN-Ln·L$_2$-Poly(MAA)**.

when poly(MAA) is in a protonated collapsed state. The surface-initiated ATRP, on the other hand, proved to be inefficient due to the complexation of copper to methacrylic acid and difficulties with the removal of residual copper, which was still visible as a blue suspension even after applying the washing procedures described in Ch. 2 on P. 49. Before appending either **Ln·L$_1$** or **Ln·L$_2$** to **MSN-Poly(MAA)**, the conjugation was optimised with inexpensive alternatives containing the same reacting groups, such as propylamine and propargyl amine. The straightforward carbodiimide reaction of propylamine to **MSN-Poly(MAA)** was confirmed by the appearance of

the amide chemical shift at 172 ppm in the ^{13}C CP/MAS NMR spectrum (Fig. 4.6). For the click reaction, the carboxylic groups were first esterified by bromoethanol and the bromide functional groups converted into azides by nucleophilic substitution with sodium azide before being reacted with propargyl amine, which was verified by the ^{13}C NMR chemical shifts typical for triazole at 126 ppm and 137 ppm (Fig. 4.6 b)).

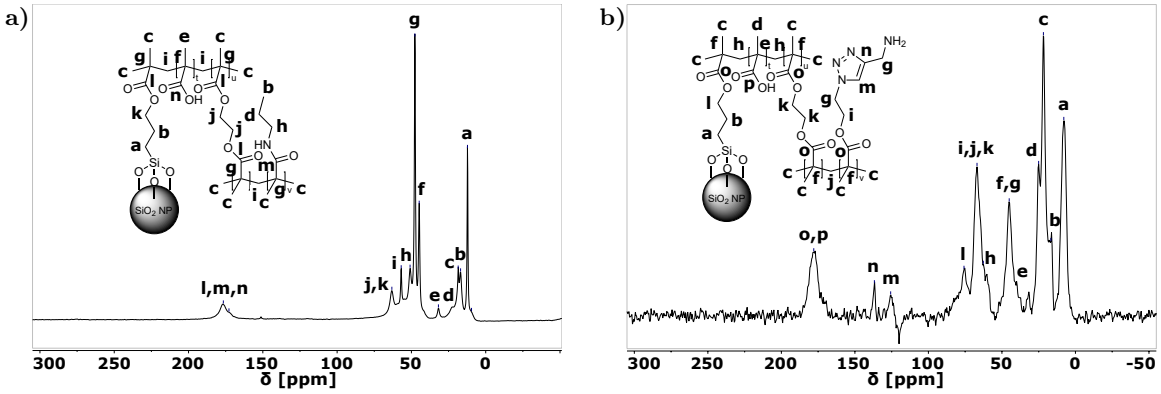


Figure 4.6: ^{13}C CP/MAS NMR spectra of a) **MSN-Poly(MAA)-Propyl amide** and b) **MSN-Poly(MAA)-Triazolylmethyl amine**.

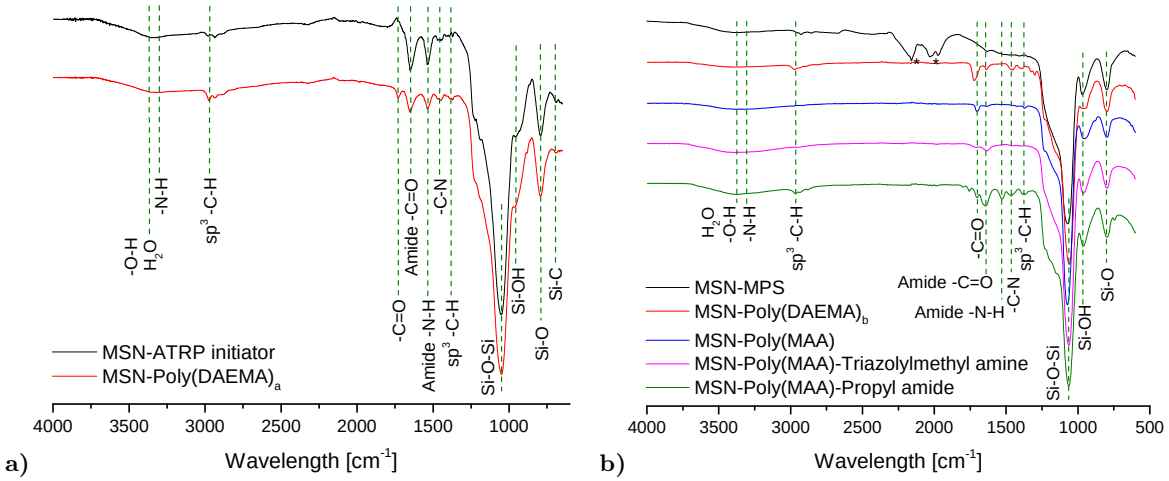


Figure 4.7: FTIR spectra showing a) **MSN-Poly(DAEMA)**$_a$ as well as b) **MSN-Poly(DAEMA)**$_b$ and **MSN-Poly(MAA)** particles.

The ζ-potentials measured over the physiological pH range either increased or decreased upon respective poly(DAEMA) or poly(MAA) functionalisation compared to unmodified MSNs due to additional positive or negative charge provided by ter-

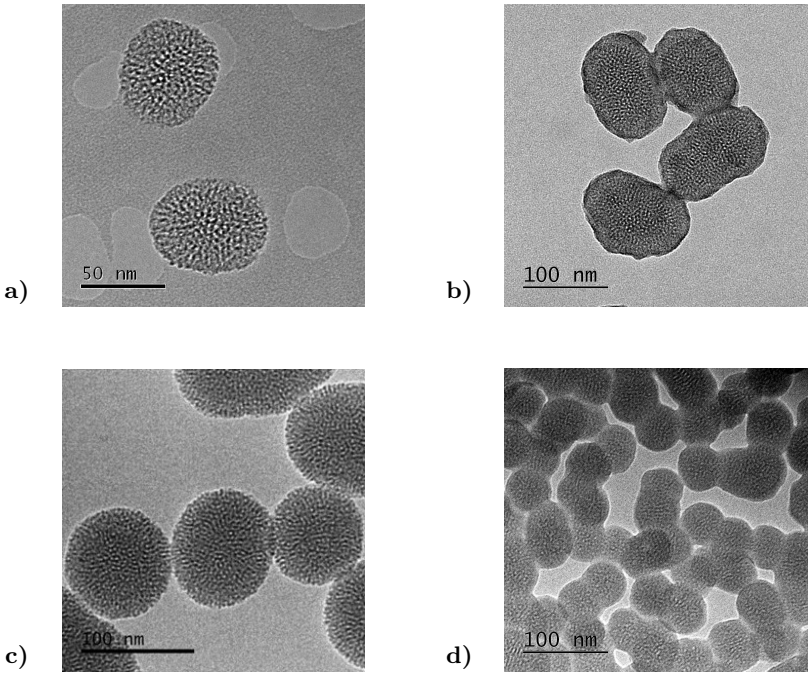


Figure 4.8: TEM images showing a) **MSN-Gd·L$_1$** without a polymer coating, b) **MSN-Gd·L$_1$-Poly(DAEMA)$_a$**, c) **MSN-Gd·L$_1$-Poly(DAEMA)$_b$** and d) **MSN-Gd·L$_1$-Poly(MAA)**. Samples b) and c) were stained with phosphotungstic acid. All scale bars correspond to 100 nm with exception of a), which is set to 50 nm.

tiary amines and carboxyl groups (Fig. 4.9). The isoelectric point of poly(DAEMA)-functionalised MSNs can be found around pH 6.5. At pH 6.8, the ζ-potentials of **MSN-Gd·L$_i$-Poly(DAEMA)$_a$** and **MSN-Gd·L$_i$-Poly(DAEMA)$_b$** were enhanced by 2.4- and 1.8-fold, respectively, indicating that the polymer chains of the former are more densely grafted on the silica surface, which is also visible in the form of a black 2-3 nm thick coating in the TEM image (Fig. 4.8 b)). The hydrodynamic size, on the other hand, did not increase with lower pH and remained unchanged in comparison to unmodified MSNs probably due to the small size of polymeric brushes, which caused aggregation at pH 6.5 and higher because of the absence of electrostatic repulsive forces (App. A.20 on P. 208). The aggregation could not be prevented by grafting of smaller amounts of polymer on the surface, or by replacing the monomer for a monomer with a higher pKa (*i.e.* *N*-(3-imidazol-yl)propyl-methacrylamide, pKa 7.0, App. A.13 on P. 205) nor by the presence of PEGylated chains. However, the stability

was only slightly improved when xanthan gum was added to the suspension as a stabiliser. Despite being negatively charged, **MSN-Poly(MAA)-Gd·L**$_i$ particles also exhibited aggregation at higher pH (App. A.20 on P. 208), which occurred regardless of the 1.5-fold lower ζ-potential compared to unmodified MSNs. The isoelectric point of poly(MAA)-functionalised MSNs can be found either around pH 5.0 or pH 5.5 in **MSN-Poly(MAA)-Gd·L**$_1$ and **MSN-Poly(MAA)-Gd·L**$_2$, respectively. In the former case, the **Gd·L**$_1$ species bearing an amine side arm were directly conjugated to poly(MAA).

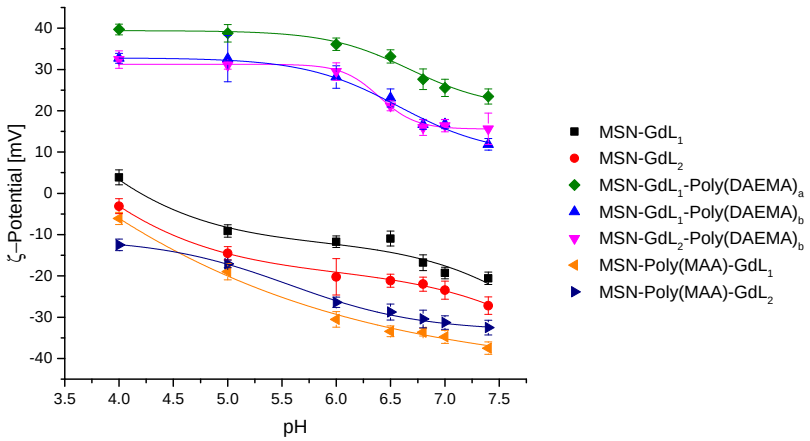


Figure 4.9: The pH dependence of ζ-potentials of either $q = 0$ or $q = 1$ contrast agents loaded into mesoporous silica nanoparticles (■ **MSN-Gd·L**$_1$ and ● **MSN-Gd·L**$_2$), poly(DAEMA)-functionalised MSNs (♦ **MSN-Gd·L**$_1$**-Poly(DAEMA)**$_a$, ▲ **MSN-Gd·L**$_1$**-Poly(DAEMA)**$_b$ and ▼ **MSN-Gd·L**$_2$**-Poly(DAEMA)**$_b$) as well as poly(MAA)-functionalised MSNs (◀ **MSN-Poly(MAA)-Gd·L**$_1$ and ▶ **MSN-Poly(MAA)-Gd·L**$_2$).

The structural properties of the pores in polymer-coated MSNs were analysed by nitrogen adsorption-desorption isotherms, whereby significant decreases in pore volume, surface area and pore size were observed compared to unmodified MSNs as a result of successful polymer grafting (Tab. 4.1 and Fig. 4.10). All polymer-functionalised samples exhibited typical type IV BET isotherms with nearly vertical capillary condensation loops[143] on their adsorption isotherms indicating a narrow pore size distribution. In contrast to bare MSNs, **MSN-Poly(DAEMA)**$_b$ exhibited the most notable decrease in pore volume, surface area and pore size by 67.0 %,

51.6 % and 31.3 %, respectively. The same pore size reduction to 2.3 nm was also achieved in **MSN-Poly(DAEMA)**$_a$, while the reduction of pore volume and surface area in these particles decreased by 50.8 % and 35.3 %, respectively. This result suggests that in **MSN-Poly(DAEMA)**$_b$ polymers cap the pores directly at the edge of the mesopores, while in **MSN-Poly(DAEMA)**$_a$ polymeric chains are not just grafted into the outermost peripheral interior region, but also onto the exterior of the mesopores creating a polymeric shell, which is visible in the phosphotungstic acid stained TEM images. These particles thus exhibit slightly higher surface area and pore volume compared to **MSN-Poly(DAEMA)**$_b$.

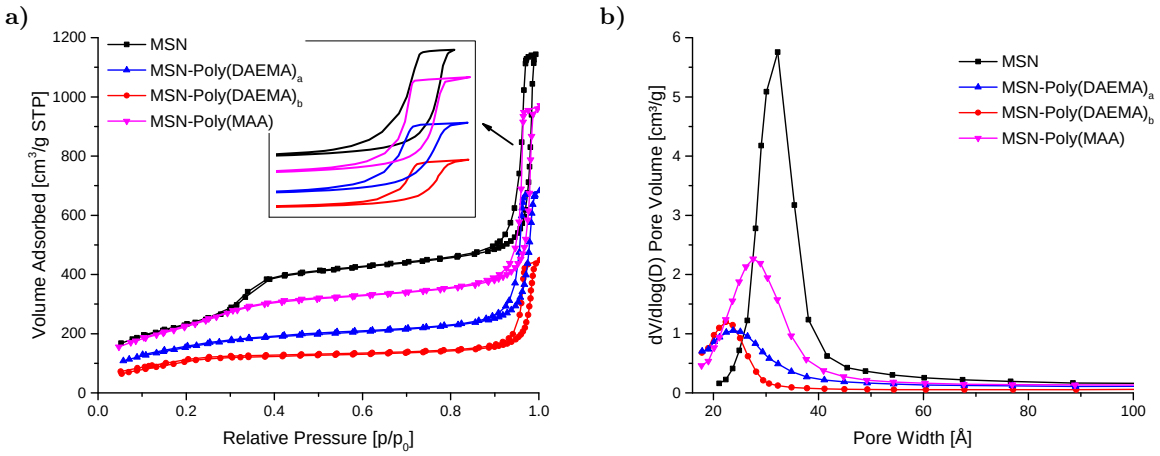


Figure 4.10: a) Nitrogen adsorption/desorption isotherms and b) BJH pore size distributions (from adsorption) of ■ bare MSNs, ▲ **MSN-Poly(DAEMA)**$_a$, ● **MSN-Poly(DAEMA)**$_b$ and ▼ **MSN-Poly(MAA)**.

Table 4.1: Structural properties of MSNs before and after polymer coating.

	BET Surface Area [m^2/g]	**Pore Volume [cm^3/g]**	**Pore Size BJH [nm]**	**ζ-Potential at pH 7.4 [mV]**	**ζ-Potential at pH 4.0 [mV]**
MSN	871.92	1.91	3.2	-28.0	-6.7
MSN-Poly(DAEMA)$_a$	564.34	0.94	2.3	23.4	39.7
MSN-Poly(DAEMA)$_b$	421.93	0.63	2.2	13.8	32.6
MSN-Poly(MAA)	828.34	1.43	3.0	-35.0	-10.5

Both "grafting onto" and "grafting from" procedures thus blocked the pores efficiently. Upon poly(MAA) grafting, on the other hand, the pore volume, surface area

and pore size were reduced by only 5.0 %, 25.1 % and 6.3 %, respectively. This is due to the cross-linked shell made of methacrylic acid monomeric units, which are less bulky than the monomers in poly(DAEMA).

4.2.2 Relaxivity Assessment of pH-Responsive Polymer-Functionalised Nanoparticulate Resonant Agents

As discussed in Ch. 2, the incorporation of octa- and nonadentate lanthanide chelates within the mesopores provided protic r_1 and q values (*cf.* Sec. 2.2.2 on P. 56) unresponsive to endogenous anions and pH. This simplifies the evaluation of the pH responsiveness, which is therefore triggered only by the design of the nanoparticulate scaffold. DAEMA possesses a tertiary amine with a pKa of 7.0-7.3,[161] which implies that at physiological pH (*i.e.* pH 7.4), the polymer chains should be in their uncharged compact form and thus collapsed blocking the pores, while at a pH lower than the pKa, the protonated chains should adopt an extended conformation allowing for ready access of solvent to the mesopores. It turned out that the pores of resulting **MSN-Gd·L$_1$-Poly(DAEMA)**$_a$ and **MSN-Gd·L$_2$-Poly(DAEMA)**$_a$ particles prepared by the surface-induced ATRP polymerisation method were blocked at any pH as indicated by the very long relaxation times (Fig. 4.11) and polymer coating observed in the TEM images (Fig. 4.8). About 8-fold lower Gd content (420 ± 4 μg/g and 560 ± 7 μg/g for **MSN-Gd·L$_1$-Poly(DAEMA)**$_a$ and **MSN-Gd·L$_2$-Poly(DAEMA)**$_a$, respectively) also indicated higher nanoparticulate weight due to the increased amount of polymers compared to unmodified particles (Ch. 2, Tab. 2.2).

For MRI imaging, the samples were dried and redissolved in either formate, MES, acetate or phosphate buffer solutions at pH 4.0-7.4.[7] Since a relatively thick polymer

[7]The relaxation time measurements and relaxivity determination procedure are described on P. 162. The corresponding linear fits can be found in App. A.16 on P. 206.

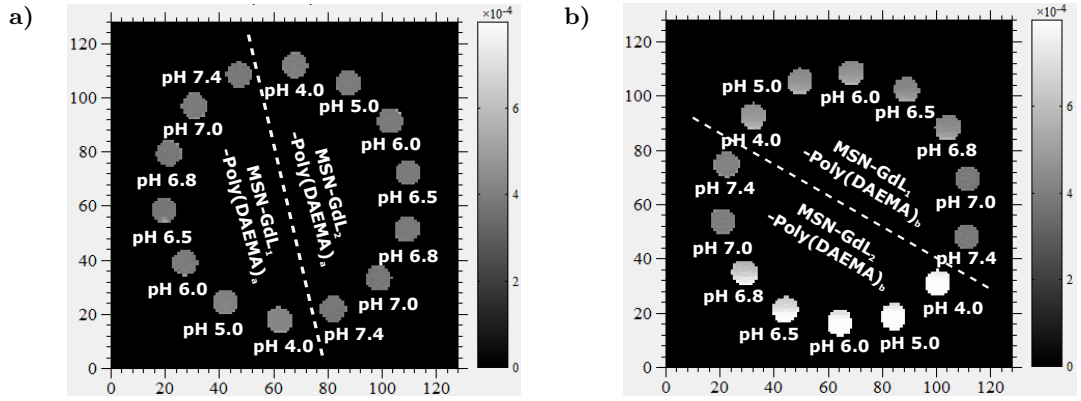


Figure 4.11: pH-dependent MRI contrast of a) **MSN-Gd·L$_2$-Poly(DAEMA)**$_a$ and b) **MSN-Gd·L$_1$-Poly(DAEMA)**$_b$ at 4.7 T. MRI parameters: SEMS, matrix = 64 x 64, FOV = 32 mm x 32 mm, Thk = 2 mm. Further information can be found on P. 162.

coating forms the exterior of such particles, the relaxivities were almost completely impeded. To illustrate, for **MSN-Gd·L$_1$-Poly(DAEMA)**$_a$, the longitudinal proton relaxivities of 3.1 mM^{-1} s^{-1} and 2.5 mM^{-1} s^{-1} were determined at pH 4.0 and pH 5.0, respectively. For **MSN-Gd·L$_2$-Poly(DAEMA)**$_a$, the respective r_1 values of 5.9 mM^{-1} s^{-1} and 3.7 mM^{-1} s^{-1} at pH 4.0 and pH 5.0 were confirmed due to a slightly improved water access. Relaxivities at pH 6.0 and higher could not be resolved because of the prolonged relaxation times and concentration independence indicating a completely diminished relaxivity enhancement due to a collapsed polymer shell and subsequent attenuation of the water exchange rate (Fig. 4.11 a), App. A.16 on P. 206). The samples were also not stable enough to measure any reasonable T_2 values. Even when attempts were made to reduce either the density or length of the polymer chains by decreasing the amount of initiators or monomers grafted onto the surface in order to reduce steric crowding that also drives the chains to stretch away from the surface, r_1 did not seem to improve. Alternatively, impure MSNs with pores blocked by the CTAB surfactant could be used for initiator grafting and polymer growth to ensure that no polymer chains are grafted internally, however, post-grafting of the lanthanide complexes into either initiator- or polymer-functionalised MSNs would be difficult to achieve due to reactivity of the former and small pore size of the latter.

For such purpose, the pre-polymerisation technique seemed to be more suitable. The polymer chains of **MSN-Gd·L$_2$-Poly(DAEMA)$_b$** (946 ± 9 μg/g of Gd^{3+}) with incorporated $q = 1$ CAs and prepared by the "grafting onto" procedure exhibited an increase in r_1 from 0.3 ± 0.1 mM^{-1} s^{-1} at pH 7.4 to 11.4 ± 0.8 mM^{-1} s^{-1} at pH 4.0. The 40-fold enhancement in longitudinal relaxivity can be ascribed to the highly ionised and electrostatic repulsions of the peripheral polymer chains at low pH, which provide a better water access. The r_2 values of **MSN-Gd·L$_2$-Poly(DAEMA)$_b$** also increased correspondingly with lower pH from 5.6 ± 2.1 mM^{-1} s^{-1} at pH 6.8 to 81.6 ± 12.9 mM^{-1} s^{-1} at pH 4.0 (Tab. 4.2, Fig. 4.12).

Table 4.2: Table showing details of ^{1}H longitudinal and transverse relaxivities of **MSN-Gd·L$_i$-Poly(DAEMA)$_b$** at 20 °C at 4.7 T.

	r_1 [mM^{-1} s^{-1}] at pH 7.4	r_1 [mM^{-1} s^{-1}] at pH 6.5	r_1 [mM^{-1} s^{-1}] at pH 4.0	r_2 [mM^{-1} s^{-1}] at pH 7.4	r_2 [mM^{-1} s^{-1}] at pH 6.5	r_2 [mM^{-1} s^{-1}] at pH 4.0
MSN-Gd·L$_1$-Poly(DAEMA)$_b$	0.1 ± 0.5	3.0 ± 0.8	4.1 ± 0.8	0	14.0 ± 0.6	16.4 ± 9.5
MSN-Gd·L$_2$-Poly(DAEMA)$_b$	0.3 ± 0.1	6.8 ± 1.1	11.4 ± 0.8	0	47.3 ± 4.9	81.6 ± 12.9

When $q = 0$ Gd^{3+} complexes were incorporated into such MSNs named as **MSN-Gd·L$_1$-Poly(DAEMA)$_b$** (831 ± 5 μg/g of Gd^{3+}), r_1 increased from 0.1 ± 0.5 mM^{-1} s^{-1} at pH 7.4 to 4.1 ± 0.8 mM^{-1} s^{-1} at pH 4.0, however, only a marginal improvement of the MRI signal intensity was observed upon pH change due to low intrinsic relaxivity and thus lower pH-responsive r_1-related amplitude by a factor of three (Fig. 4.11 and Fig. 4.12). The magnitude of pH responsivness of r_2 values, on the other hand, was larger with r_2 increasing from 5.6 ± 3.2 mM^{-1} s^{-1} at pH 7.4 to 16.4 ± 9.5 mM^{-1} s^{-1} at pH 4.0. In both cases of **MSN-Gd·L$_i$-Poly(DAEMA)$_b$**, the pH response was reversible and the highest longitudinal relaxivity at pH 4.0 was reduced by about 30 % compared to their unmodified counterparts **MSN-Gd·L$_i$** (Tab. 2.2 on P. 52). This is an expected result of polymer gating on the edge of the

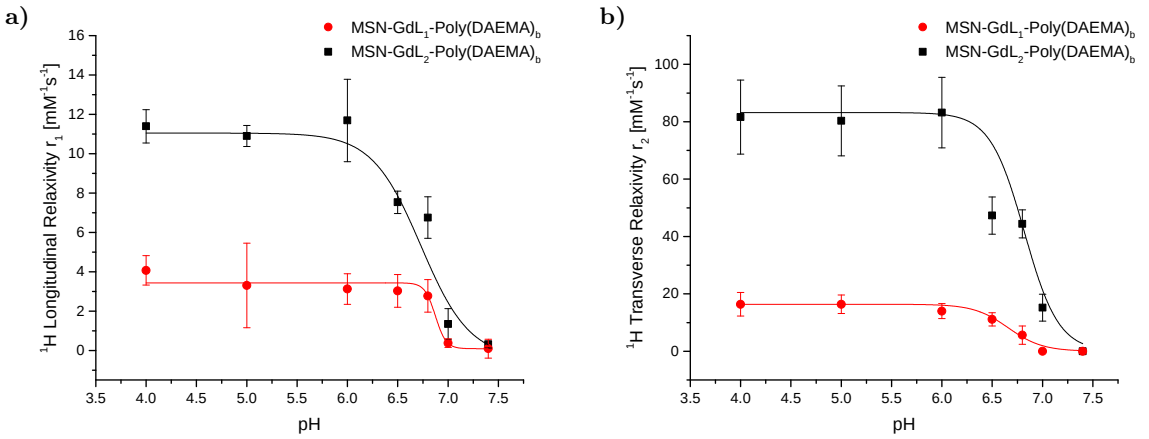


Figure 4.12: pH dependence of a) longitudinal and b) transverse relaxivities of polymer-coated ● **MSN-Gd·L$_1$-Poly(DAEMA)$_b$** and ■ **MSN-Gd·L$_2$-Poly(DAEMA)$_b$** at 4.7 T.

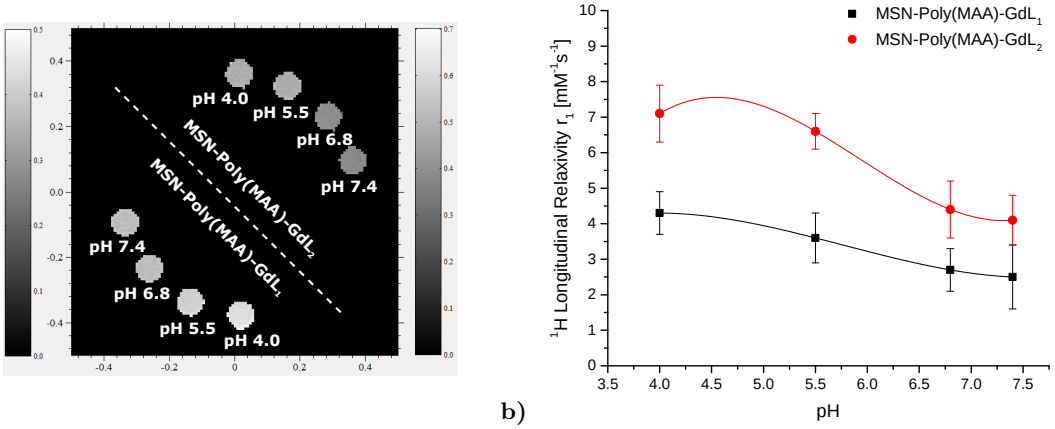
mesopores, which partially restricts water access. The lower MRI signal intensity of $q = 0$ in comparison to $q = 1$ Gd^{3+}-loaded polymer-coated MSNs is, on the other hand, a consequence of the absent inner-sphere water, while pKa, which is seemingly shifted to higher pH, indicates a lesser relaxation enhancement susceptibility of the second/outer-sphere compared to the inner-sphere contribution at partially restricted water access, especially since the sigmoidal curve of the relaxivities plotted against pH is slightly shifted to higher pH when compared to the plot of ζ-potentials versus pH. In contrast, the pH-dependent sigmoidal curves of relaxivities and ζ-potentials of **MSN-Gd·L$_2$-Poly(DAEMA)$_b$** comply with each other.

The pH responsiveness of octa- and nonadentate Gd^{3+} complexes, which were incorporated into poly(methacrylic acid)-coated **MSN-Poly(MAA)-Gd·L$_i$**, was also evaluated (Fig. 4.13 and Tab. 4.3). This time, the pH responsiveness of grafted polymers is reversed. At high pH, the ionised and swollen polymer chains were envisioned to lead to a faster tumbling rate and lower relaxivity, whereas the collapsed protonated polymers at low pH were expected to provide a more rigid environment of higher order parameter and longer local rotational correlation times resulting in increased protic relaxivity. As assumed hitherto, the relaxivity of both **MSN-Poly(MAA)-Gd·L$_1$** and **MSN-Poly(MAA)-Gd·L$_2$** was the highest when the pH of the suspen-

Table 4.3: Table showing details of ^{1}H longitudinal relaxivities of **MSN-Gd·L$_i$-Poly(DAEMA)$_b$** and **MSN-Poly(MAA)-Gd·L$_i$** at 20 °C at 4.7 T as well as q values of the Eu^{3+} counterparts. Error margins represent cumulative errors arising from duplicate repetitions of relaxivity assessment.

	r_1 [mM^{-1} s^{-1}] at pH 7.4	r_1 [mM^{-1} s^{-1}] at pH 6.8	r_1 [mM^{-1} s^{-1}] at pH 5.5 or pH 6.0	r_1 [mM^{-1} s^{-1}] at pH 4.0	k_{ex} [·10^6 s^{-1}] at pH 7.4 → pH 4.0	q value	Gd [μg/g NP]
MSN-Poly (MAA)-Gd·L$_1$	2.5 ± 0.9	2.7 ± 0.6	3.6 ± 0.7	4.3 ± 0.6	NM	0.06	1227 ± 11
MSN-Gd·L$_1$-Poly(DAEMA)$_b$	0.1 ± 0.5	2.8 ± 0.9	3.1 ± 0.8	4.1 ± 0.8	25.6 → 57.0	0.09	831 ± 5
MSN-Poly (MAA)-Gd·L$_2$	4.1 ± 0.7	4.4 ± 0.8	6.6 ± 0.5	7.1 ± 0.8	NM	0.7	1560 ± 8
MSN-Gd·L$_2$-Poly(DAEMA)$_b$	0.3 ± 0.1	6.8 ± 1.1	11.7 ± 2.1	11.4 ± 0.8	6.0 → 10.1	1.18	946 ± 9

sion was the lowest (r_1 = 4.3 ± 0.6 mM^{-1} s^{-1} and 7.1 ± 0.8 mM^{-1} s^{-1} at pH 4.0 for q = 0 and q = 1 systems, respectively) most likely due to protonated and collapsed polymers. By contrast, at high pH, lower relaxivity (r_1 = 2.5 ± 0.9 mM^{-1} s^{-1} and 4.1 ± 0.7 mM^{-1} s^{-1} at pH 7.4 for q = 0 and q = 1, respectively) was most likely triggered by ionised and swollen polymers leading to a faster local tumbling rate of Gd^{3+} complexes.



a) b)

Figure 4.13: pH-dependent a) MRI contrast (at 4.7 T) and b) protic relaxivities of • **MSN-Poly(MAA)-Gd·L$_1$** and ■ **MSN-Poly(MAA)-Gd·L$_2$**.

A change in τ_M most likely also plays a role, however, its contribution is probably inferior to the leading role of τ_{RL} and q, especially since an increase in r_1 at

high pH would have been observed when the polymer chains are swollen and water access is improved. In addition, the impact of τ_M would be further diminished if the ionised methacrylic acid group displaced the water molecule bound to the $q = 1$ Gd^{3+} complex of **MSN-Poly(MAA)-Gd·L$_2$**. Compared to their molecular counterparts (*i.e.* **Gd·L$_1$** and **Gd·L$_2$**), the relaxivities of **MSN-Poly(MAA)-Gd·L$_1$** and **MSN-Poly(MAA)-Gd·L$_2$** increased by 6.1- and 1.7-fold, respectively. As the distances of the appended **Gd·L$_1$** and **Gd·L$_2$** chelates to a polymer chain are very much alike (10 Å and 12 Å, respectively), it is most likely that a slow water exchange rate due to the monoamide side arm and slightly reduced q value limits the relaxivity of **MSN-Poly(MAA)-Gd·L$_2$** as discussed in the next section.

4.2.3 Confirmation of Anion- and pH-Unresponsive Hydration Numbers by Luminescence Measurements

By measuring the luminescence lifetimes in H_2O and D_2O at various pH and pD,[8] it was possible to determine the pH dependency of the q values. As depicted in Fig. 4.14, the hydration numbers of all polymer-functionalised MSNs bearing either a $q = 0$ or $q = 1$ Eu^{3+} complex varied within error indicating that any observed pH responsiveness of relaxivity would not have been associated with a change in the hydration number. All except **MSN-Poly(MAA)-Eu·L$_2$** exhibited similar q values to their non-polymerised counterparts **MSN-Eu·L$_1$** and **MSN-Eu·L$_2$**.

MSN-Poly(MAA)-Eu·L$_2$, on the other hand, displayed slightly lower q values of 0.6-0.7 instead of 1.0. This is because of the partial inner-sphere water displacement by methacrylic acid, which is less effective at vibronic quenching than a water molecule. Therefore, increased τ_{H_2O} were accompanied by decreased τ_{D_2O} lifetimes, which are consistent with the decrease in hydration number. Although the q values are

[8] For measurements in D_2O, pD values were calculated from the relation: $pD = pH_{reading} + 0.41$, where $pH_{reading}$ is the pH value measured with a glass electrode.[162]

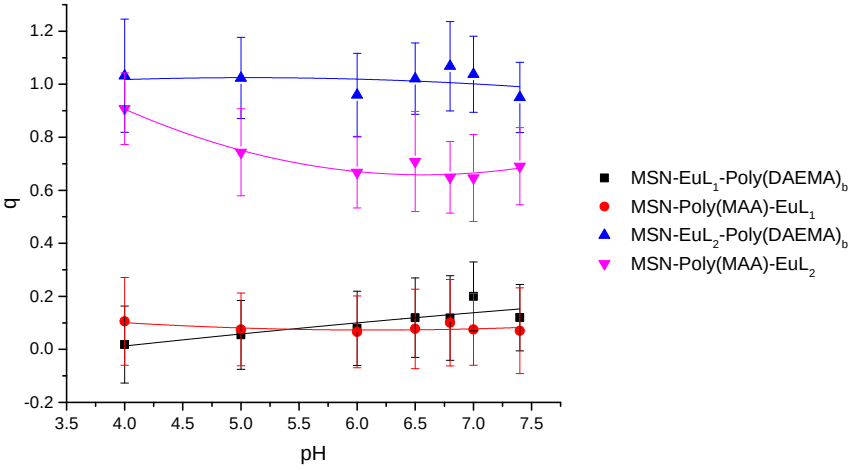


Figure 4.14: pH dependence of q values of ■ **MSN-Eu·L$_1$-Poly(DAEMA)**$_b$, ● **MSN-Poly(MAA)-Eu·L$_1$** and ▲ **MSN-Eu·L$_2$-Poly(DAEMA)**$_b$ show that the hydration numbers do not change significantly with pH except in ▼ **MSN-Poly(MAA)-Eu·L$_2$**. These particles exhibited slightly increased q values at pH lower than 5.0. The error bars were obtained from duplicate luminescence lifetime measurements in H_2O and D_2O.

relatively stable at pH above 5.0, those at pH 4.0 are within error of the **Eu·L$_2$**-loaded non-polymerised MSNs (App. A.1 on P. 204) most likely due to the protonation of poly(methacrylic acid) (pKa is around 4.7-5.0). At higher pH, the incomplete inner-sphere water displacement in **MSN-Poly(MAA)-Eu·L$_2$** causes a perturbation of the Eu^{3+} complexation environment, which can be detected in luminescence emission spectra, wherein the intensities of $^5D_0 \rightarrow {}^7F_0$ and $^5D_0 \rightarrow {}^7F_2$ transitions slightly decrease and notably increase, respectively, compared to **MSN-Eu·L$_2$** (Fig. 2.14 on P. 56) and **MSN-Eu·L$_2$-Poly(DAEMA)**$_b$ (App. A.18 on P. 207). Upon addition of oxy-anions, such as phosphate, these luminescence emission intensities remained stable. The same observation was made in **MSN-Poly(MAA)-Eu·L$_1$**, **MSN-Eu·L$_1$-Poly(DAEMA)**$_b$ and **MSN-Eu·L$_2$-Poly(DAEMA)**$_b$ (App. A.17 and App. A.18 on P. 207) suggesting that the hydration numbers of all polymer-functionalised MSNs, with the exception of **MSN-Poly(MAA)-Eu·L$_2$** below pH 5.0, are independent of variable pH and that all observed pH-responsive relaxivities are independent of the presence of oxy-anions.

4.2.4 ^{17}O NMR Measurements Reveal Variable Water Access with pH

The water exchange rates in **MSN-Gd·L$_1$-Poly(DAEMA)**$_b$ and **MSN-Gd·L$_2$-Poly(DAEMA)**$_b$ were examined by variable-temperature ^{17}O NMR. In this case, lanthanide-free poly(DAEMA)-capped MSNs were taken as a reference at respective pH in order to subtract any potential interference between ^{17}O-enriched water and polymer-functionalised MSNs, while Gd^{3+}-doped non-polymerised MSNs were used as a pH-unresponsive control (Fig. 4.15).

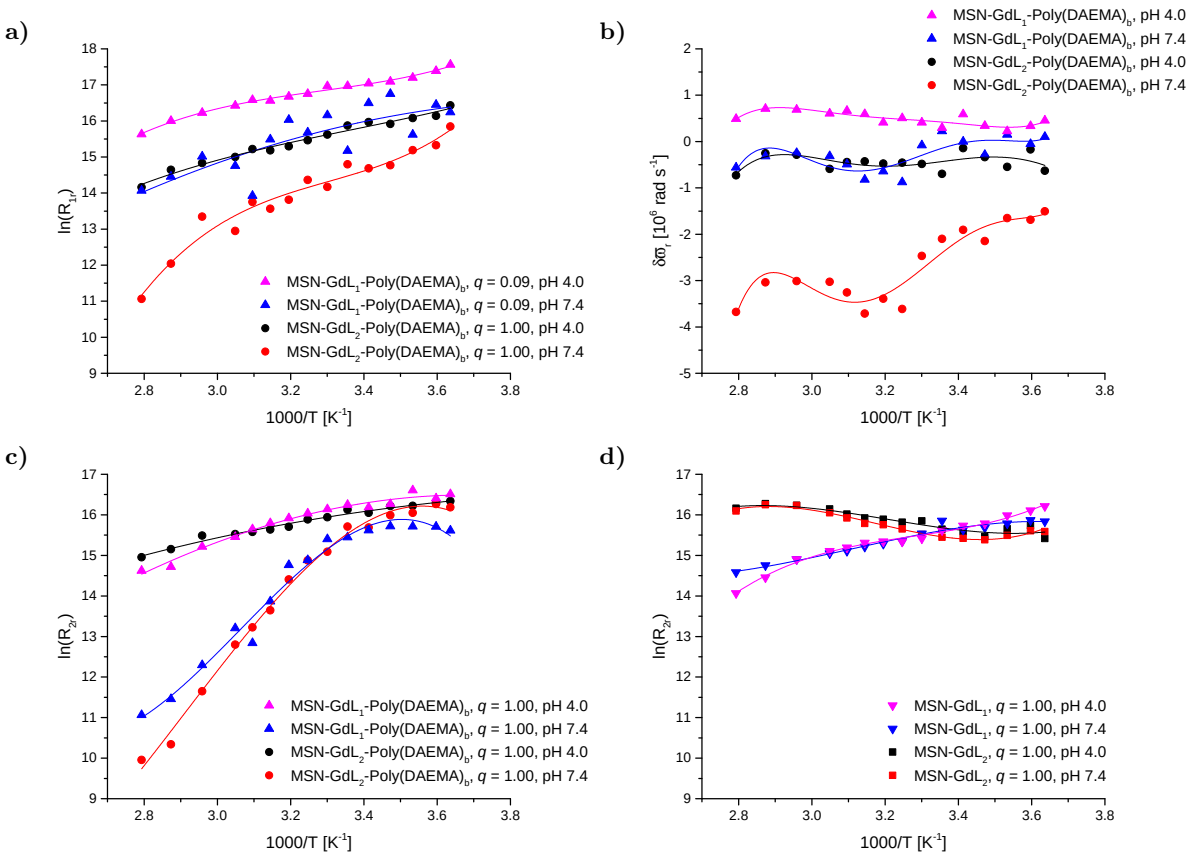


Figure 4.15: Temperature dependence of the paramagnetic contribution to reduced a) longitudinal R_{1r} and c) transverse R_{2r} relaxation rates of ^{17}O-enriched water as well as b) reduced ^{17}O NMR chemical shifts $\delta\omega_r$ in the presence of **MSN-Gd·L$_1$-Poly(DAEMA)**$_b$ and **MSN-Gd·L$_2$-Poly(DAEMA)**$_b$ at low and high pH. Graph d) represents R_{2r} rates of **MSN-Gd·L$_1$** and **MSN-Gd·L$_2$** at pH 4.0 and 7.4 in order to show that the water exchange rates of Gd^{3+}-doped non-polymerised MSNs are not responsive to pH. Large discrepancies in the chemical shifts occur due to low Gd^{3+} concentrations (0.2 mM) used for the measurements as higher concentration of particles would result in increased aggregation.

When respective $q = 1$ and $q = 0$ CAs were incorporated into poly(DAEMA)-coated MSNs, τ_M decreased from 167.2 ns to 99.0 ns and from 39.0 ns to 17.5 ns upon pH change from pH 7.4 to 4.0 (Tab. 4.3 and Fig. 4.15). In both cases, the water exchange rates thus increased by a factor of two when exposed to low pH. The reduced τ_M values at low pH are expected since water influx is increased due to swollen polymer chains. Although the water exchange rates at high pH are relatively fast since ^{17}O lnR_2 values decrease with temperature, it seems that an even faster exchange regime prevails when particles are dispersed at low pH with the lnR_2 values decreasing even steeper with temperature. It can be further noted that both $q = 0$ and $q = 1$ Gd^{3+}-loaded polymer-capped MSNs follow the same trend indicating the dominance of a strong second/outer-sphere over the inner-sphere contribution. This might be due to water confined within the pores as a result of polymeric chains gating the mesopores. The ^{17}O NMR results thus support the conjecture that reversible pH-triggered changes in the relaxivities of **MSN-Gd·L$_1$-Poly(DAEMA)$_b$** and **MSN-Gd·L$_2$-Poly(DAEMA)$_b$** are related to changes in the water exchange rates, which are influenced by the bulk water influx regulated by pH-responsive polymers.

4.2.5 Poly(DAEMA)-Capped MSNs as Potential Theranostic Agents

Gene delivery to the nucleus is often quoted as a major limiting factor of gene therapy. Aside from viral vectors and common manmade lipidic and polymeric polyplexes (such as lipofectamine and polyethylenimine), poly(2-(dimethylamino)ethyl methacrylate)[163] and organically functionalised MSNs[164] have also been investigated as gene delivery agents, which are based on the electrostatic interactions of amine functionalities with negatively charged DNA. To investigate whether **MSN-Ln·L$_i$-Poly(DAEMA)$_b$** could be implemented as potential gene vehicles, **Ln·L$_i$** was swapped for fluorescein (FITC) so that the particles could be tracked by fluores-

cence microscopy.[9] This was achieved by a reaction of 5-carboxyfluorescein succinimidyl ester with pre-dried amine-grafted MSNs dispersed in dry DMF and subsequent poly(DAEMA) coating to yield **MSN-FITC-Poly(DAEMA)**$_b$. Their cytotoxicity was first evaluated using HeLa cells to measure cell viability using AlamarBlue. After 24 h, 100 μg/mL of **MSN-FITC-Poly(DAEMA)**$_b$ exhibited 70.6 $\pm$ 5.2 % viability compared to FITC-functionalised non-polymerised **MSN-FITC**, which showed 80.4 $\pm$ 2.9 % viability.

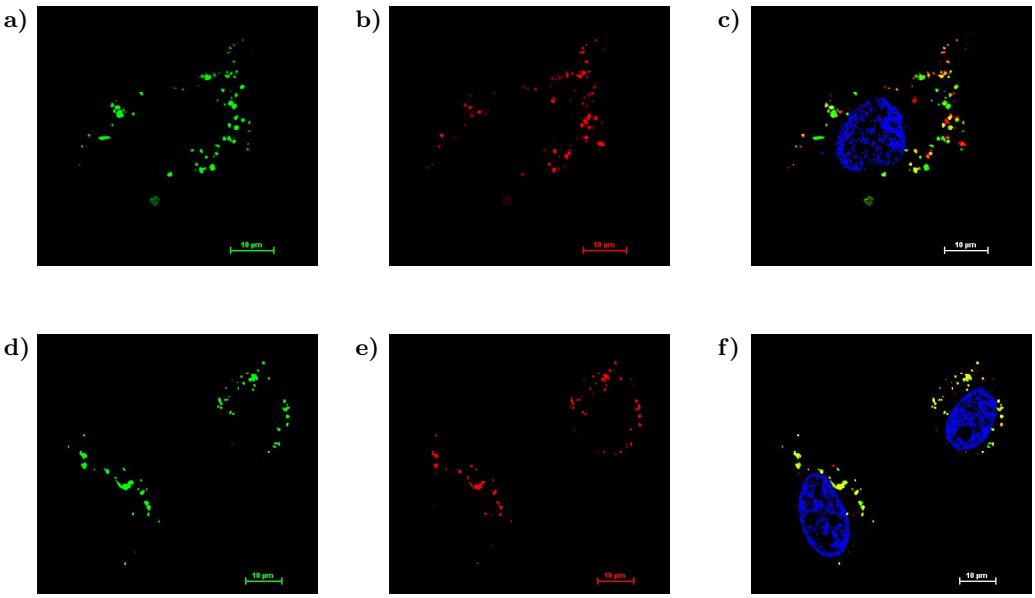


Figure 4.16: Confocal images showing a-c) **MSN-FITC-Poly(DAEMA)**$_b$ and d-f) non-polymerised **MSN-FITC**, whereby endo-lysosomal escape and entrapment can be easily identified. Images a) and d) show FITC-labelled particles, red channels b) and e) denote endo-lysosomes stained by LysoTracker Red, while images c) and f) are a result of merged channels including blue, which shows the nucleus of a cell. Image f) shows **MSN-FITC** particles being trapped within endo-lysosomes resulting in yellow blobs due to the overlap of green (MSNs) and red (endo-lysosomes) channels, while image c) shows that **MSN-FITC-Poly(DAEMA)**$_b$ (green spots) managed to escape the endo-lysosomes as green and red spots can both be clearly distinguished.

As the plasmid DNA (pDNA) must be released into cytoplasm in order to be transported into the nucleus, transcribed into mRNA and translated into proteins, it was

[9] Further experimental details to the respective sample preparation and confocal imaging can be found on P. 189 and P. 167.

necessary to test the particles for their escapability from the endo-lysosomal pathway, which was conducted by confocal microscopy after a protocol described in Ref. [165], wherein the lysosomes were stained red with LysoTracker Red and nucleus blue with a Hoechst fluorescent dye. Thus, when particles were trapped inside the lysosomes, a yellow colour could be observed in confocal images, while separate green and red colours indicated the successful escape of particles into the cytoplasm (Fig. 4.16). The co-localisation was quantified by determining Manders' overlap coefficients M1 and M2[166] using the co-localisation feature of the BioImageXD software.[167] The overlap coefficients vary between 0, designating no correlation, and 1, denoting total co-localisation, thus characterising the degree of overlap between the images. This is divided into two channels, in this case green and red, wherein M1 represents the ratio of intensities in the green image for which the intensity in the red image is above zero compared to the full intensity, whereas M2 denotes the same for the red channel. While 0.42 and 0.55 could be defined for M1 and M2 of the **MSN-FITC** particles (App. A.19 on P. 207), the overlap coefficients were reduced to 0.21 and 0.30, respectively, when poly(DAEMA) was coated onto **MSN-FITC**, thus statistically indicating higher endosomal escape of **MSN-FITC-Poly(DAEMA)**$_b$ particles due to the endo-lysosomalytic proton sponge effect associated with the increased pH buffering capability of the tertiary ammonium groups in DAEMA-based polymers.

In collaboration with Prof Terence Rabbitts at the Weatherall Institute of Molecular Medicine, the gene transfection efficiency of **MSN-Poly(DAEMA)**$_a$ and **MSN-Poly(DAEMA)**$_b$ was investigated using fluorescence microscopy and flow cytometry (Fig. 4.17). Particles were mixed with pTomato[10] overnight at 4 °C and washed by centrifugation before being incubated with HEK cells. It turned out that the sonication of particles after centrifugation was inappropriate as DNA is known to be cleaved

[10]pJEFY6-2A-tomato is a plasmid DNA that can be expressed into a red fluorescent protein within the cell.

under such conditions. This also became apparent in a heavily decreased performance of standard lipofectamine gene transfer agent implemented as a control. Under such conditions, the gene transfection efficiency of **MSN-Poly(DAEMA)**$_a$ and **MSN-Poly(DAEMA)**$_b$ accounted for 38 % and 28 % of lipofectamine. A slightly lower transfection efficiency of **MSN-Poly(DAEMA)**$_b$ is most likely a result of lower amounts of polymer chains on MSNs. Further optimisation of the surface chemistry of MSNs and an improved cell transfection protocol could enable the application of **MSN-Gd·L$_i$-Poly(DAEMA)**$_b$ as pH-responsive MRI CAs and gene delivery vectors.

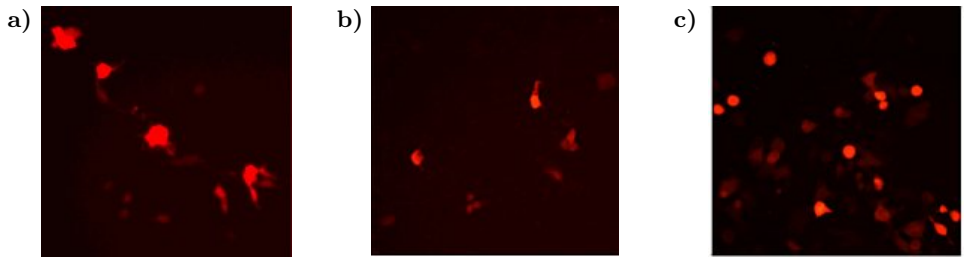


Figure 4.17: Fluorescence images showing expressed pTomato protein with a) **MSN-poly(DAEMA)**$_a$, b) **MSN-poly(DAEMA)**$_b$ and c) lipofectamine as pDNA delivery vectors.

4.3 Conclusion

pH-responsive polymer-coated mesoporous silica nanoparticles were prepared by either "grafting-from" or "grafting-onto" free radical polymerisation in order to probe the pH responsiveness of Gd^{3+} chelates tethered to particles through either water access or local mobility. For the former, Gd^{3+} complexes were incorporated into the mesopores and the contrast was regulated by poly(2-(diethylamino)ethyl methacrylate) brushes localised at the periphery of the mesopores. At low pH, when polymeric chains were swollen, water access was allowed. In a collapsed state, on the other hand, the water influx was blocked and the MRI contrast totally diminished. A reversible

increase in r_1 from 0.3 mM^{-1} s^{-1} to 11.7 mM^{-1} s^{-1} has been observed upon reduction in pH from 7.4 to 4.0 when $q = 1$ Gd^{3+} chelates were incorporated into MSNs and subsequently coated with pH-responsive polymer chains. A slightly lower increase in r_1 from 0.1 mM^{-1} s^{-1} to 4.1 mM^{-1} s^{-1} upon a change in pH from 7.4 to 4.0 was detectable when $q = 0$ were swapped for $q = 1$ Gd^{3+} complexes within the mesopores. The increased water access upon lower pH was also confirmed by ^{17}O NMR since the water exchange rate was two times faster at low than at high pH.

The contributions to stimuli-triggered changes in MRI contrast are not always as well-defined and a combination of different factors may be accountable. For example, to probe MRI contrast regulation by local mobility either octa- or nonadentate Gd^{3+} complexes were tethered to polymers cross-linked on the surface of MSNs. In this case, polymer chains were ionised at high pH resulting in increased mobility and reduced MRI contrast intensity, whereas at low pH, the collapsed chains elongated local rotational correlation times. As a consequence, a pH change from 7.4 to 4.0 resulted in a 40 % increase in r_1 from 4.1 mM^{-1} s^{-1} to 7.1 mM^{-1} s^{-1} and from 2.5 mM^{-1} s^{-1} to 4.3 mM^{-1} s^{-1} in poly(methacrylic acid) coated MSNs loaded with $q = 1$ and $q = 0$ Gd^{3+} CAs, respectively. In addition, poly(methacrylic acid) was also observed to quench the relaxivity of $q = 1$ Gd^{3+} chelates by partially substituting the inner-sphere water molecule at pH values higher than its pKa at pH 5.0, which gives the complex an imperfect octa- and nonadentate character as determined by luminescence measurements.

One can nevertheless be confident that a better environmentally responsive MRI contrast change can be achieved when Gd^{3+} complexes are doped into a confined rigid environment and when $q = 1$ contrast agents are implemented since both provide a higher intrinsic relaxivity in response to a stimuli due to a favourable interplay of physicochemical parameters, such as higher hydration number and local rotational correlation times among others.

Chapter 5

Effect of Internal Mobility on Molecular and Nanoparticulate ^{19}F MRI Contrast Agents

5.1 Introduction

With a chemical shift span of about 400 ppm, negligible background signal and excellent sensitivity second only to ^{1}H nucleus, MRI based on the ^{19}F nucleus has many merits that justify its usage. Although ^{19}F MRI[168] was discovered only four years later than ^{1}H MRI,[3] it is still not in clinical use due to the lack of suitable imaging agents. Multiple ^{19}F NMR signals, local rotational restriction, low signal-to-noise ratio as well as hydro- and lypophobicity proved to be the main reasons why the heavily fluorinated emulsion contrast agents have been unsuccessful on numerous occasions. There are also several differences between fluoroalkyl and alkyl groups that complicate the applications of ^{19}F MRI probes. Beside higher electronegativity (3.98 for fluorine compared to 2.20 for hydrogen), CF_3 groups are much larger than the CH_3 ones (92 Å^3 compared to 54 Å^3), while carbon-fluorine bonds are by 75 kJ/mol more stable than the carbon-hydrogen bonds, thus resulting in strengthened and rigid carbon-carbon bonds. As a consequence, heavily reduced conformational freedom and low polaris-

ability of fluorine atoms, which keep their dense electron cloud close to the nucleus and which result in low van der Waals forces between molecules, are responsible for thermal and chemical stability as well as for self-aggregation and phase separation due to hydrophobicity and lipophobicity among others, thus substantially lowering water solubility of fluorocarbons.[169, 170, 171, 172]

Fluorine MRI probes, which are mostly composed of fluorocarbons, must therefore be incorporated into emulsions, dendrimers,[173] polyamine hydrogels[174] or liposomes.[175] To date, only a few symmetric superfluorinated molecular probes have been reported including water-insoluble perfluoro[15]-crown-5-ether (20 fluorine atoms)[107] and PERFECTA (36 fluorine atoms)[68] as well as a water-soluble fluorinated imaging tracer ^{19}FIT (27 fluorine atoms)[175] and a recently published heavily PEGylated dendrimeric fluorophore (48 symmetric fluorines).[98] As the overall motivation is to prepare dual stimuli-responsive ^{19}F/^{1}H MRI contrast agents, the objective of this chapter is to investigate the water insolubility and rigidity issues of the ^{19}F MRI probes and synthesise a kinetically stable nanoparticulate or molecular imaging agent with high fluorine content, a single ^{19}F NMR signal and short relaxation times. For this purpose, a whole range of different scaffolds was tested ranging from rigid ultrasmall nanoparticles, polymer particles, nanocapsules to molecular quaternary ammonium-based first-generation dendrimers with flourine species incorporated by either chemical conjugation, complexation or encapsulation.

5.2 Results and Discussion

In order to show that fluorine atoms incorporated into a rigid environment do not exhibit any fluorine signals in solution NMR, fluorinated MSNs (**MSN-PFOTS**)[1] were obtained by co-condensation of TEOS with perfluorooctyltriethoxysilane (PFOTS).

[1]Hydrodynamic diameter: 93.2 ± 2.0 nm, PdI = 0.2, ζ-potential: -28.5 ± 1.5 mV. Further experimental details are presented on P. 189, while the additional FTIR and NMR spectra can be found on P. 209.

MSNs fluorinated by PFOTS were stable in ethanol, but not in water. Although containing as much as 18 wt % fluorine according to the fluorine elemental analysis and exhibiting 35.8 % weight loss upon heating to 800 °C (Fig. 5.1 a)), ^{19}F resonances could only be detected by solid-state NMR (Fig. 5.1 b)) since the ^{19}F NMR relaxation times were too short for detection by liquid NMR.

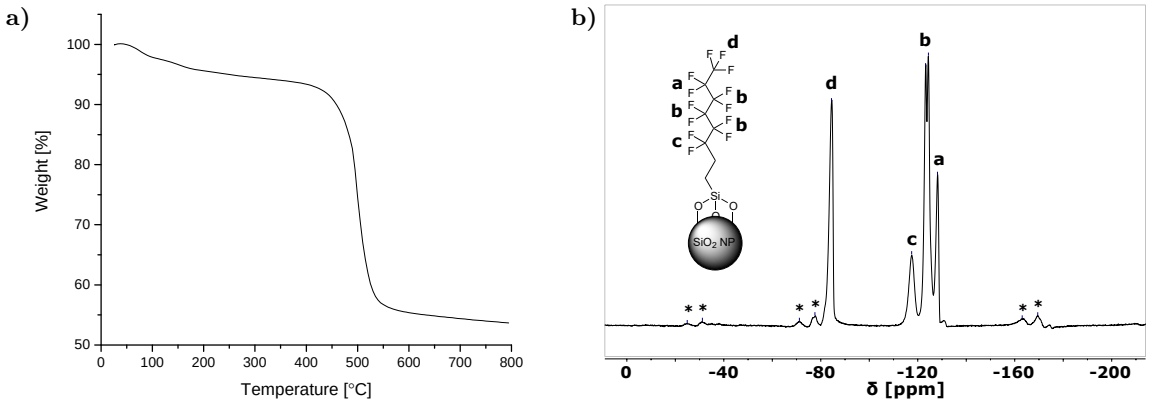


Figure 5.1: a) TGA plot shows percent mass loss versus temperature in **MSN-PFOTS**, wherein 36 % mass loss was observed due to decomposition of fluorocarbons around 480 °C. b) Solid-state ^{19}F NMR spectrum shows the CF_3 group at -85 ppm and a set of CF_2 groups between -115 ppm and -130 ppm. The low-intensity lines in the spectrum are spinning sidebands.

Even when the particle size was reduced to 10 nm[176] and stabilised in water by PEG chains, the ^{19}F NMR signals were detectable only by solid-state ^{19}F NMR and not by solution NMR again indicating the importance of both local and global mobilities of fluorine environment. These water-soluble particles denoted as **uMSN-PEG-PFOTS**[2] (Fig. 5.2 c)) were prepared by co-condensation of tetramethyl orthosilicate with [methoxy(triethylenoxy)$_{6\text{-}9}$ propyl]trimethoxy silane followed by post-grafting with perfluorooctyltriethoxysilane. Due to excellent dispersibility in water provided by the PEG chains, a ζ-potential as low as -36.7 mV and a hydrodynamic diameter of 10.1 $\pm$ 2.6 nm (PdI = 0.2) were obtained.

The close proximity of the silica surface thus restricts the mobility of conjugated

[2]Further experimental details can be found on P. 189.

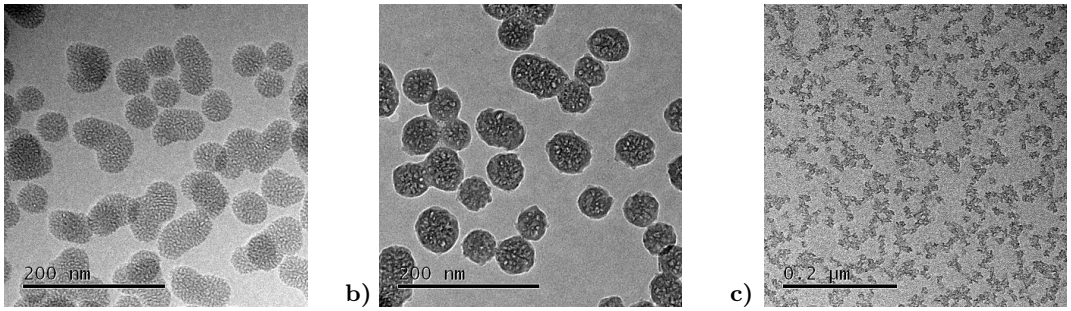


Figure 5.2: TEM images of **MSN-PFOTS** a) before and b) after TGA. TEM image c) shows ultra-small silica nanoparticles labelled with perfluorooctyltriethoxysilane (**uMSN-PEG-PFOTS**). The scale bars on the images all correspond to 200 nm.

fluorinated probes. If one inserts a cleavable linker between silica and fluorine moieties, it would be expected that the ^{19}F NMR signal in solution is recovered upon linker cleavage. For this purpose, 4-(trifluoromethyl)benzoic acid (FBA) was conjugated to the MSNs (**MSN-SS-FBA**) via a redox-active cystamine linker as depicted in Fig. 5.3 and characterised by solid-state NMR as shown in App. B.2 and App. B.3 on P. 210. The **MSN-SS-FBA** particles were obtained by step-wise carbodiimide coupling of cystamine and FBA onto carboxyl-functionalised MSNs.[3] As expected, the rigid environment of the silica surface quenched the ^{19}F NMR signal in solution. Only upon dithiothreitol (DTT) addition, the disulphide bridge was reduced to thiols and the ^{19}F MRI probe was released, resulting in the appearance of a solution ^{19}F NMR signal (Fig. 5.3 b)). ^{19}F T_1 and T_2 relaxation times in water were determined to be 646 $\pm$ 76 ms and 8 $\pm$ 3 ms, respectively, which is significantly lower than the ^{19}F T_1 and T_2 values of FBA dissolved in methanol, which account for 2190 $\pm$ 50 ms and 760 $\pm$ 90 ms, respectively. Note further that the ζ-potential increased from -24.3 mV to -17.8 mV, when DTT was added and FBA released. Despite the release, FBA might still have been either aggregated or trapped within the pores and associated with silica since the released fluorinated probe is insoluble in water, hence the low relaxation times. This might also be related to the fact

[3]Further experimental details can be found on P. 190.

that upon DTT treatment and the appearance of the ^{19}F NMR signal in water, the ^{19}F resonance disappeared with time and never reappeared again regardless of how much DTT was added.

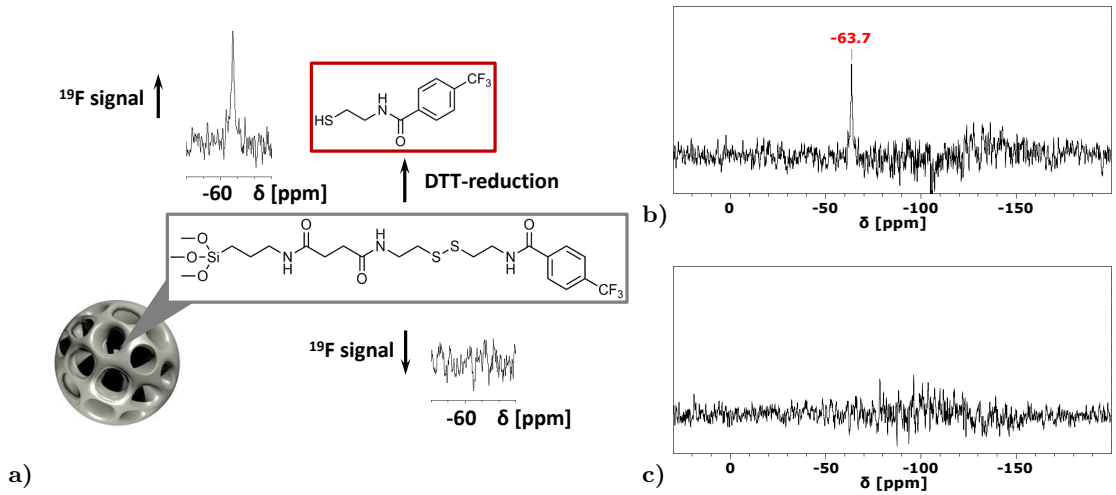


Figure 5.3: a) Schematic representation of redox-active 4-(trifluoromethyl)benzoic acid incorporated into MSNs (**MSN-SS-FBA**) through a cystamine linker. ^{19}F NMR solution spectra c) before and b) after the addition of dithiothreitol show that ^{19}F NMR signal was recovered after the destruction of disulphide bonds linking the ^{19}F NMR probe with the silica surface.

5.2.1 Mobile Fluorine Incorporation into MSNs via Polymers

In attempts to increase the tumbling rate and dynamics of local molecular motions, a polymeric shell was prepared on the mesoporous silica nanoparticles by surface-induced ATRP[4] as described in Ch. 4, since polymers proved to be excellent hosts for ^{19}F MRI reporters.[93] 2-bromoisobutyryl initiator-anchored MSNs were coated with either poly(2-(diethylamino)ethyl methacrylate) (poly(DAEMA)) or poly(2-aminoethyl methacrylate) (poly(AEMA)) (Fig. 5.4) as well as with either poly(trifluoroethyl methacrylate) (as in **MSN-Poly(DAEMA-TFMA)**)[5] or poly(perfluorodecyl acrylate) (as in **MSN-Poly(DAEMA-PFA)**), all of which were

[4]Further experimental details can be found on P. 190.
[5]Hydrodynamic diameter = 382 ± 78 nm, PdI = 0.4, ζ-potential = 32.1 ± 2.8 mV.

relatively stable in water with slight precipitation observable overnight. The polymer coatings were visible in TEM images (Fig. 5.5), while the mesopores beneath the polymers were almost indiscernible compared to unmodified MSNs depicted in Fig. 2.11 on P. 54. Despite the presence of the fluorinated probes being confirmed by FTIR (Fig. 5.4) in the form of the asymmetric and symmetric C-F stretches that give rise to the strong bands found between 1100 cm^{-1} and 1300 cm^{-1}, the ^{19}F resonances in liquid-state NMR were always absent even at low pH and when the initiator sites were increased in order to prevent brushes from collapsing onto the surface. The ^{19}F resonances could also not be observed when either pentafluorophenol (as in **MSN-Poly(DAEMA)-PFP**) or 4-(trifluoromethyl)benzoic acid (as in **MSN-Poly(AEMA)-FBA**)[6] were incorporated at the very end of the polymer chains[7] by either Williamson ether synthesis or carbodiimide coupling, respectively.

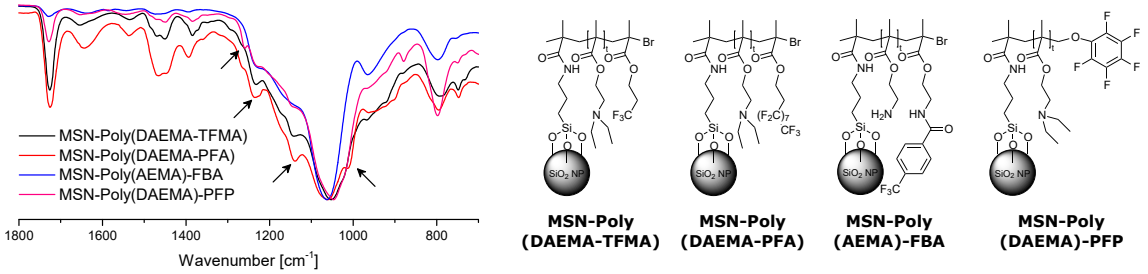


Figure 5.4: FTIR spectra and schematic representation of fluorinated polymer-coated mesoporous silica nanoparticles showed C-F stretching bands at 1010 cm^{-1}, 1140 cm^{-1}, 1170 cm^{-1}, 1230 cm^{-1} and 1260 cm^{-1} as indicated by the arrows.

Since the observation of a solution ^{19}F NMR signal and its shape depend on nuclear magnetic relaxation times and chemical exchanges, it can be assumed that the rate of an exchange process between two different states of fluorine is intermediate or slow on the NMR time scale most likely due to intersegmental and polymer chain interactions with the silica surface. For that reason, only C-F stretching vibrations

[6] Hydrodynamic diameter = 256 ± 43 nm, PdI = 0.3, ζ-potential = 19.7 ± 3.1 mV.

[7] Solid-state NMR spectra can be found in App. B.3 and App. B.4 on P. 210 as well as in App. B.5 and App. B.6 on P. 211.

in the FTIR spectra and ^{19}F resonances in the solid-state NMR can be observed.

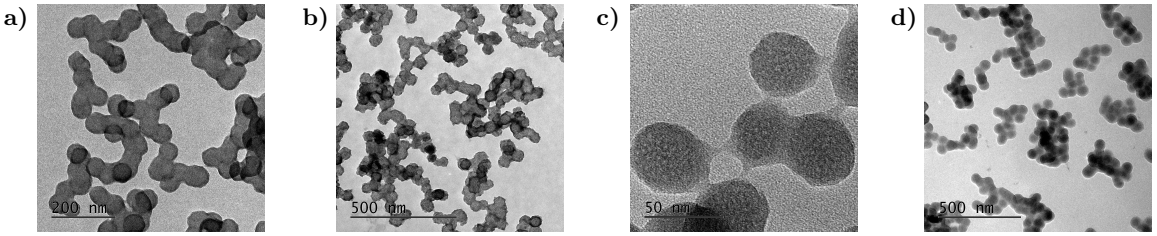


Figure 5.5: TEM images of a) **MSN-Poly(DAEMA-TFMA)**, b) **MSN-Poly(DAEMA-PFA)**, c) **MSN-Poly(AEMA)-FBA** and d) **MSN-Poly(DAEMA)-PFP**. The scale bars correspond to a) 200 nm, b) 500 nm, c) 50 nm and d) 500 nm. The first three images were stained by phosphotungstic acid.

As one may assume that tight polymer chain packing and paramagnetic impurities caused by residual copper from the ATRP polymerisation might result in ^{19}F resonances invisible to the solution-based NMR, MSNs functionalised with fluorinated branched third generation dendrimers based on melamine were prepared. For this purpose, aminated MSNs were alternately reacted step-wise with cyanuric acid and ethylenediamine until the third generation was reached as described in Ref. [177].[8] Next, ethyl 2,2,2-trifluoroacetate was prepared by reaction of trifluoroacetic acid with ethanol under acidic conditions[178] and reacted with melamine-based dendrimer-tethered MSNs to yield trifluoroacetylamide-functionalised water-dispersible **MSN-Dendri-CF$_3$** (Fig. 5.6).[9] The same result was found: a fluorine peak could only be observed in solid-state NMR and not in solution NMR in water, thus ruling out that the signal in the previous example was quenched by paramagnetic impurities, but rather by either tight polymer chain packing or proximity and interaction with the silica surface.

[8] Further experimental details can be found on P. 191.

[9] Hydrodynamic diameter = 216 ± 19 nm, PdI = 0.3, ζ-potential = 21.4 ± 3.2 mV. The TEM image of the particles can be found in App. B.6 on P. 211, while their respective FTIR and solid-state NMR spectra are presented in App. B.7 on P. 211 and in App. B.8 on P. 212.

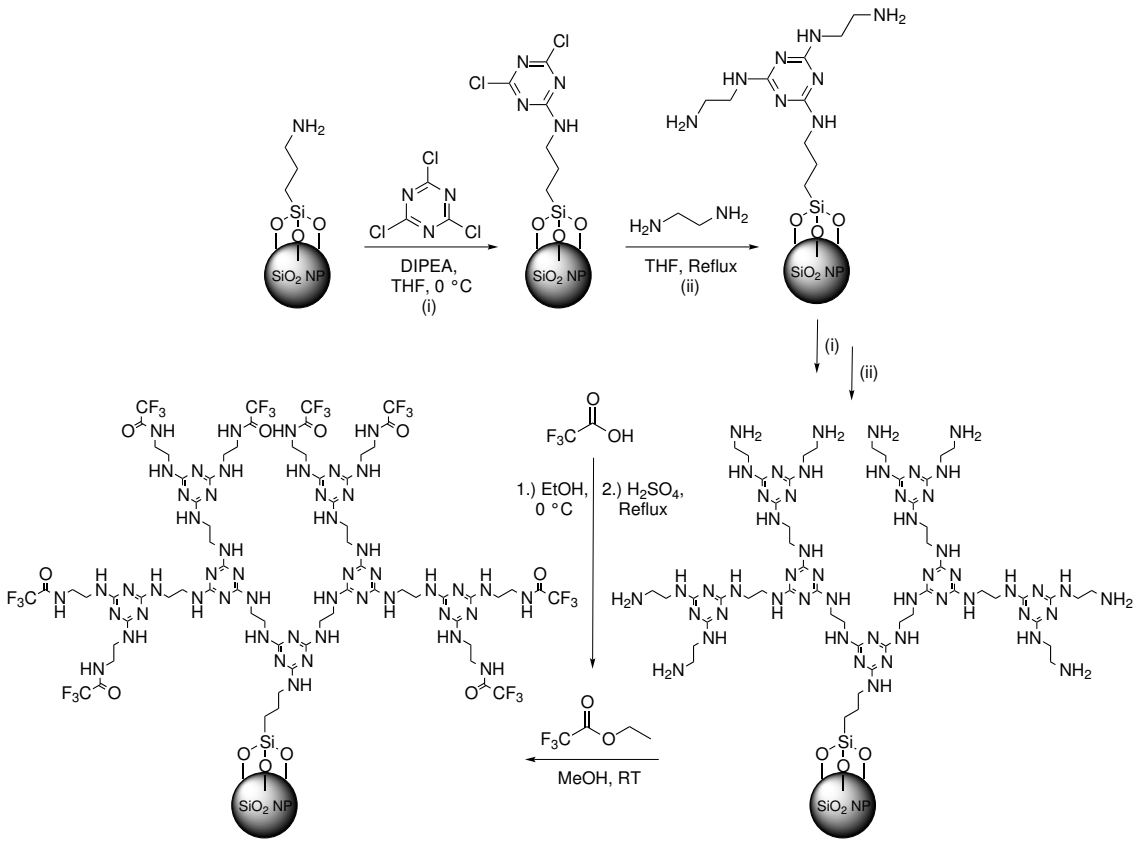


Figure 5.6: Step-wise preparation of melamine-based fluorinated branched dendrimers tethered to the surface of mesoporous silica nanoparticles (**MSN-Dendri-CF$_3$**).

5.2.2 Nanoencapsulated Fluorinated Oil

Since the molecular rotation of polymers on silica nanoparticles is highly restricted due to the reasons explained in the previous section and since the NMR signals from the fluorinated probe are strongly suppressed, it was attempted to encapsulate fluorinated oil droplets within a silica shell. In addition, perfluorocarbon emulsions containing perfluorooctyl bromide[179] or perfluoropolyethers[180] used as ^{19}F MRI imaging agents in (pre-)clinical studies have proven to accumulate excessively in internal organs due to their very lipophilic nature.[181] This could be also prevented by encapsulation.

The first attempt of preparation of oleic acid filled silica nanocapsules with dispersed 3,5-bis(trifluoromethyl)benzoic acid (BFB) and encapsulating

dimethyloctadecyl[3-(trimethoxysilyl)-propyl]ammonium chloride (DTSA), which acted as the quaternary ammonium surfactant and template for the silanisation reaction of tetraethoxysilane (TEOS), yielded silica nanoparticles (**NS-OA-BFB**) measuring around 200 nm in diameter. However, instead of forming capsules, the particles were covered or stabilised with oleic acid containing intercalated BFB (Fig. 5.7).[10] As with 4-(trifluoromethyl)benzoic acid entrapped inside the mesopores of MSNs (*cf.* discussion on P. 114), the ^{19}F T_1 and T_2 relaxation times decreased to 600 ± 10 ms and 4.1 ± 0.2 ms, respectively, while at the concentration of 10 mg/mL, their signal was just high enough to be imaged by MRI (signal-to-noise ratio = 30, linewidth = 170 Hz). As in detail described in Experimental Procedures on P. 164, all ^{19}F MRI images reported in this thesis were acquired using gradient echo multi-slice (GEMS) sequence at 7.0 T with samples dispersed in water and placed in Eppendorf tubes. Hereby, it is important to note that the signal-to-noise ratio (SNR) increases as the square root of the number of scans (nt).

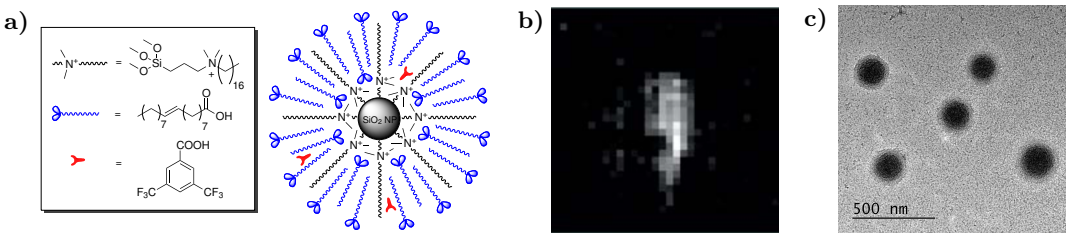


Figure 5.7: a) Schematic representation, b) ^{19}F MRI and c) TEM images of **NS-OA-BFB**. MRI parameters: GEMS, TR = 0.5 s, TE = 0.4 ms, nt = 16, flip = 90°, matrix = 32 x 32, FOV = 50 mm x 50 mm, Thk = 10 mm, concentration = 10 mg/mL.

In order to increase the amount of incorporated fluorine content, encapsulation of a fluorinated oil by silica was subsequently attempted. Silica nanocapsules containing perfluorodecalin (PFD) have been previously reported as oxygen carriers and contrast agents for ultrasound imaging.[182] The procedure implemented tetramethyl

[10] Hydrodynamic diameter: 297.2 ± 5.8 nm, PdI = 0.3, ζ-potential = -25.6 ± 1.4 mV. The FTIR spectrum can be found in App. B.7 on P. 211.

orthosilicate as a template for silanisation, and a surfactant known as pluronic F-68, which contains polypropylene oxide and polyethylene oxide chains that adsorb onto fluorinated droplets and provide stabilisation in water. This approach yielded highly polydisperse and unstable silica nanocapsules despite dialysis. For this reason, DTSA was employed once again as a silanisation template bearing both organosiloxane and quarternary ammonium surfactant groups, while TEOS was used as a silanol coating source (Fig. 5.8).

In the case that not enough TEOS or too much DTSA were implemented in a reaction, unstable nanocapsules were obtained, as depicted in App. B.9 on P. 212 (**NCS-PFD**$_a$ and **NCS-PFD**$_b$). When TEOS was used in 3.2- and 2.1-fold excess compared to DTSA and PFD, respectively, relatively monodispersed and, most importantly, centrifugable PFD-filled silica nanocapsules measuring 130 nm in diameter with approximately 10-14 nm thick silica shells were obtained (**NCS-PFD**$_c$).[11] Unfortunately, the structural properties and cis-trans isomerism of the PFD manifest themselves in multiple ^{19}F NMR resonances (Fig. 5.9), which reduce signal intensity and can induce image artefacts.[183] **NCS-PFD**$_c$ nanocapsules thus exhibited typical multiple ^{19}F NMR resonances with T_1 and T_2 of about 1290 ± 60 ms and 15 ± 2 ms, respectively (T_1/T_2 = 85 and SNR = 400 at 3 mg/mL).

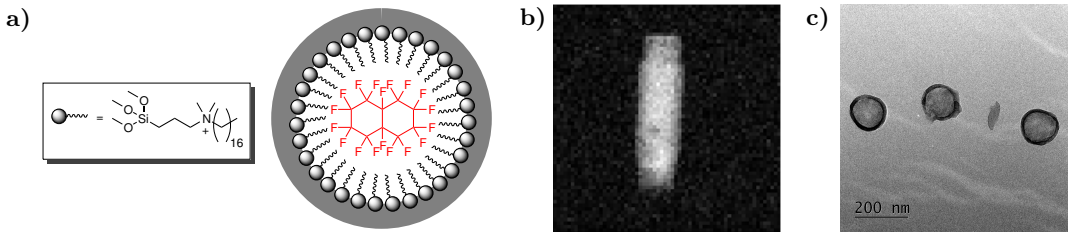


Figure 5.8: a) Schematic representation, b) ^{19}F MRI and c) TEM images of **NCS-PFD**$_c$ with PFD-based liquid core. MRI parameters: GEMS, TR = 0.5 s, TE = 1 ms, nt = 4, flip = 90°, matrix = 64 x 64, FOV = 32 mm x 32 mm, Thk = 10 mm, SNR = 400, concentration = 3 mg/mL.

[11] Further experimental details can be found on P. 192, hydrodynamic diameter = 215.3 ± 2.3 nm, PdI = 0.3, ζ-potential = 28.1 ± 1.6 mV.

Interestingly, almost no fluorine could be detected by solid-state NMR (App. B.10 on P. 213) indicating the importance of the fluid environment for excellent detection by solution NMR. In the future, if available, it would be better to utilise perfluoro[15]-crown-5-ether with only one single ^{19}F resonance, which would further increase the SNR and thus ^{19}F MRI contrast. Beside increasing the ^{19}F NMR signal intensity characteristics and echogenicity for ultra-sound imaging, such silica nanocapsules filled with fluorocarbons would also exhibit excellent oxygen carrying capacity, therefore potentially acting as theranostic contrast agents.

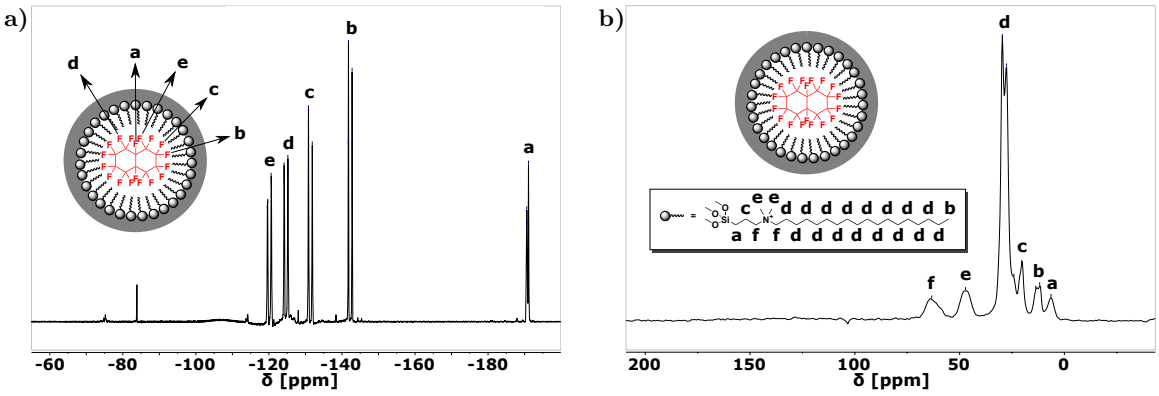


Figure 5.9: a) ^{19}F solution and b) ^{13}C CP/MAS NMR spectra show that the fluorine and carbon moieties of PFD and DTSA are featured within liquid and solid compartments of **NCS-PFD**$_c$ nanocapsules, respectively. The multiple ^{19}F NMR peaks are a result of cis-trans isomerism, wherein tertiary fluorines on the intersection between cyclohexanes can be located either on the opposite (trans-isomer) or the same side (cis-isomer) of each other.

5.2.3 Polyelectrolyte Micelles with Symmetric ^{19}F MRI Probes

Alternatively, it is possible to obtain water-soluble polymer particles with a single ^{19}F resonance through either covalent incorporation of fluorinated methacrylate by co-polymerisation or through complexation of carboxylated ^{19}F MRI probes by ion pairing with tertiary aminated polymer nanoparticles. For this purpose, polymeric nanoparticles (**Poly(DAEMA)**$_a$) were prepared by emulsion polymerisation[184] of 2-(diethylamino)ethyl methacrylate (DAEMA) cross-linked

with ethylene glycol dimethylacrylate (EGDMA).[12] Upon complexation with trifluoroacetic acid (**TFA**) in a MeOH/H_2O mixture and redispersion in H_2O following purification by centrifugation, polymer NPs denoted as **Poly(DAEMA)$_a$-TFA** were obtained.[13] Although **Poly(DAEMA)$_a$-TFA** exhibited a strong ^{19}F NMR signal (linewidth = 4.9 Hz, $T_1/T_2 = 2.6$) with the following relaxation times: $T_1 = 1263 \pm 19$ ms and $T_2 = 481 \pm 47$ ms,[14] the size of such particles increased by almost a factor of four (hydrodynamic diameter = 1625.6 ± 35.6 nm, PdI = 0.5).

Smaller particles (hydrodynamic diameter = 616.4 ± 12.2 nm, PdI = 0.1) were obtained when complexation was performed with a bis-carboxylated ^{19}F MRI reporter 2,2,3,3-tetrafluoro-1,4-butanedicarboxylic acid (**F$_4$Ac**, Fig. 5.10), which was prepared by reacting tetrafluoro butanediol with butyl-2-bromoacetate prior to deprotection of *tert*-butyl groups.[15]

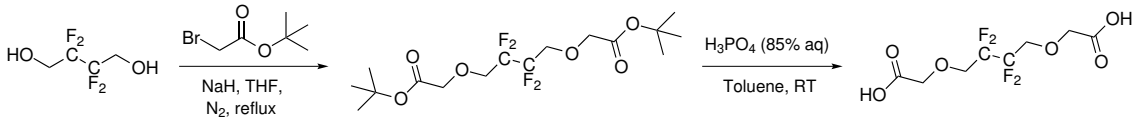


Figure 5.10: Synthesis of bis-carboxylated fluorinated reporter **F$_4$Ac**.

The resulting particles denoted as **Poly(DAEMA)$_a$-F$_4$Ac** (Fig. 5.11) displayed lower ^{19}F NMR relaxation times most likely due to the smaller size of the particles and the higher molecular weight of **F$_4$Ac**. At pH 4.0, the ^{19}F relaxation times of $T_1 = 480 \pm 10$ ms and $T_2 = 10.6 \pm 0.6$ ms were obtained (linewidth = 90 Hz, $T_1/T_2 = 45.3$). Slightly lower relaxation times at higher pH ($T_1 = 430 \pm 10$ ms, $T_2 = 3.7 \pm 0.2$ ms, linewidth = 130 Hz and $T_1/T_2 = 116.2$ at pH 7.4), on the other hand, correlate with collapsed polymer chains because of the deprotonated tertiary amines. This indicates that at a pH range of 4.0-7.4, **F$_4$Ac** is associated with the

[12] Hydrodynamic diameter = 444.0 ± 5.2 nm, PdI = 0.1, $\zeta = 28.2 \pm 0.4$ mV.
[13] Experimental details can be found on P. 193.
[14] The corresponding ^{19}F NMR spectrum can be found in App. B.12 on P. 213.
[15] Experimental details can be found on P. 170 and characterisation data in App. B.11-B.13 on P. 213.

particles through either hydrogen bonding or ion pairing.

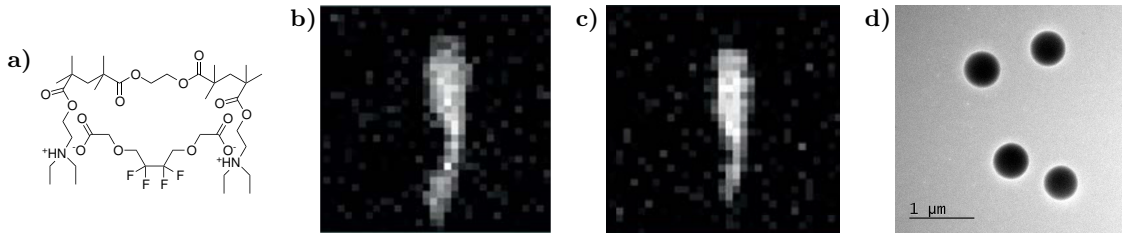


Figure 5.11: a) Schematics illustrating ion pair interactions between polymeric nanoparticles and ^{19}F MRI probe based on bis-carboxylic acid (**Poly(DAEMA)$_a$-F$_4$Ac**). MRI images at b) pH 4.0 (SNR = 50) and c) pH 7.4 (SNR = 50) were taken with the following parameters: GEMS, TR = 0.5 s, TE = 0.7 ms, nt = 16, flip = 90°, matrix = 32 x 32, FOV = 32 mm x 32 mm, Thk = 10 mm, lb = 50, concentration = 20 mg/mL. d) TEM image of **Poly(DAEMA)$_a$-F$_4$Ac** particles.

Since these complexes are driven through non-covalent, particularly electrostatic interactions and might be ion-exchanged *in vivo*, the formation of a silica shell on **Poly(DAEMA)$_a$-TFA** and **Poly(DAEMA)$_a$-F$_4$Ac** was attempted. The surface of **Poly(DAEMA)$_a$** namely consists of basic tertiary amines that are capable of initiating the sol-gel process of tetraethyl orthosilicate. The resulting particles are denoted as **Poly(DAEMA)$_a$-TFA-Si** NPs[16] and **Poly(DAEMA)$_a$-F$_4$Ac-Si** NPs.[17] Instead of a continuous shell, the exterior of such particles consisted in both cases of countless silica nanoparticles, which measured approximately 30 nm in diameter and which were stacked upon one another (Fig. 5.12, App. B.14 on P. 214). This was probably due to an inhomogeneous surface charge distribution and the presence of complexed carboxylated fluorinated reporters. Contrary to expectations, the ^{19}F NMR signals were in both cases heavily reduced as a result of the increased rigidity of the nanoparticulate system. The ^{19}F T_1/T_2 ratio of **Poly(DAEMA)$_a$-TFA-Si**, for example, increased from 2.6 to 666.8 compared to **Poly(DAEMA)$_a$-TFA** due to a severely reduced transverse relaxation time (T_1 = 1267 ± 19 ms, T_2 = 1.9 ± 0.2 ms).

[16]Hydrodynamic diameter = 1037.0 ± 98.0 nm, PdI = 0.5, ζ = 47.2 ± 0.8 mV.
[17]Hydrodynamic diameter = 1116.0 ± 50.2 nm, PdI = 0.4, ζ = 35.6 ± 1.4 mV.

The ^{19}F T_2 value of **Poly(DAEMA)-F$_4$Ac-Si**, on the other hand, remained the same, while T_1 plummeted 1.7-fold to $T_1 = 259.1 \pm 62.9$ ms ($T_2 = 5.6 \pm 1.2$ ms, $T_1/T_2 = 46.3$, linewidth = 193.2 Hz).

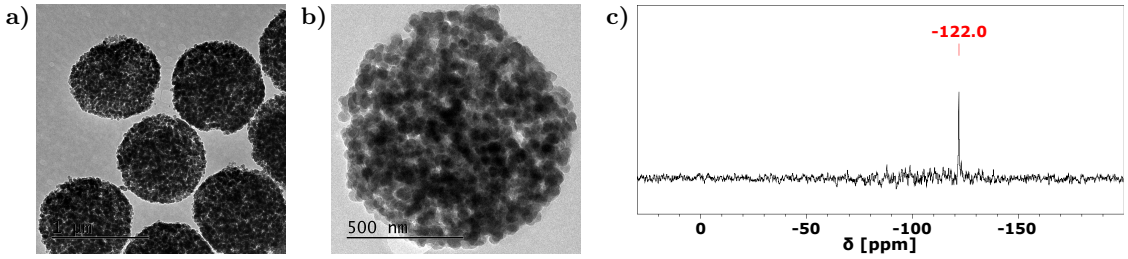


Figure 5.12: a-b) TEM images and c) heavily reduced ^{19}F NMR signal of silica coated polymers (**Poly(DAEMA)$_a$-F$_4$Ac-Si**, dispersed in H_2O, concentration = 20 mg/mL) pre-complexed with **F$_4$Ac**.

Interestingly, when smaller starting polymeric particles (**Poly(DAEMA)$_b$**) were prepared[18] and only a few pre-synthesised silica particles were located on the exterior surface (the resulting composites are denoted as **Poly(DAEMA)$_b$-F$_4$Ac-Si**),[19] the ^{19}F NMR signal was not suppressed ($T_1 = 452 \pm 3$ ms, $T_2 = 9.8 \pm 2.1$ ms, linewidth = 122 Hz, Fig. 5.13). The results are similar to the parent **Poly(DAEMA)$_b$-F$_4$Ac**, while the T_1/T_2 ratio was once again maintained at around 46 indicating that only a complete surface coverage by silica NPs reduces the ^{19}F NMR signal. Such polymer/silica nanocomposites could be useful for incorporation of multiple modalities that require either a more or less rigid scaffold, such as paramagnetic and fluorinated MRI probes for either ^{1}H or ^{19}F MRI, respectively.

In order to compare the relaxation times of non-covalently and covalently associated ^{19}F MRI probes with polymeric nanoparticles, 2,2,3,3-tetrafluoro-1,4-butanedimethacrylate (**F$_4$M$_2$**) bearing four symmetric fluorine atoms was prepared (Fig. 5.14).[20] Initially, preparation of a dimethacrylate composed of 12 symmetric

[18] Hydrodynamic diameter = 361.5 ± 7.4 nm, PdI = 0.1. Experimental details are presented on P. 192.
[19] Hydrodynamic diameter = 503.7 ± 9.4 nm, PdI = 0.1, $\zeta = 20.2 \pm 0.6$ mV.
[20] Further experimental details can be found on P. 172, NMR spectra are presented in Ap. B.15 and Ap. B.16 on P. 215.

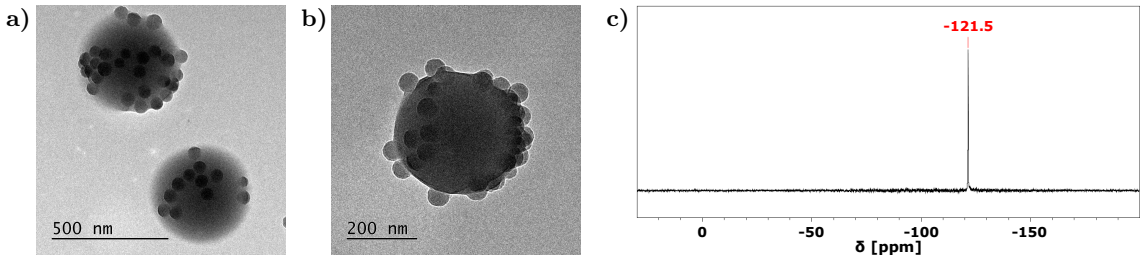


Figure 5.13: a-b) TEM images and c) ^{19}F NMR signal of polymers complexed with $\mathbf{F_4Ac}$ and functionalised with silica particles ($\mathbf{Poly(DAEMA)}_b$-$\mathbf{F_4Ac}$-**Si**, dispersed in H_2O, concentration = 20 mg/mL).

fluorine atoms was attempted ($\mathbf{F_{12}M_2}$) to further boost the ^{19}F NMR signal, however, its synthesis starting from perfluoropinacol, resulted in low yields probably due to inaccessible acidic hydroxyl functionalities placed next to bulky trifluoromethyl groups (App. B.15 on P. 215).

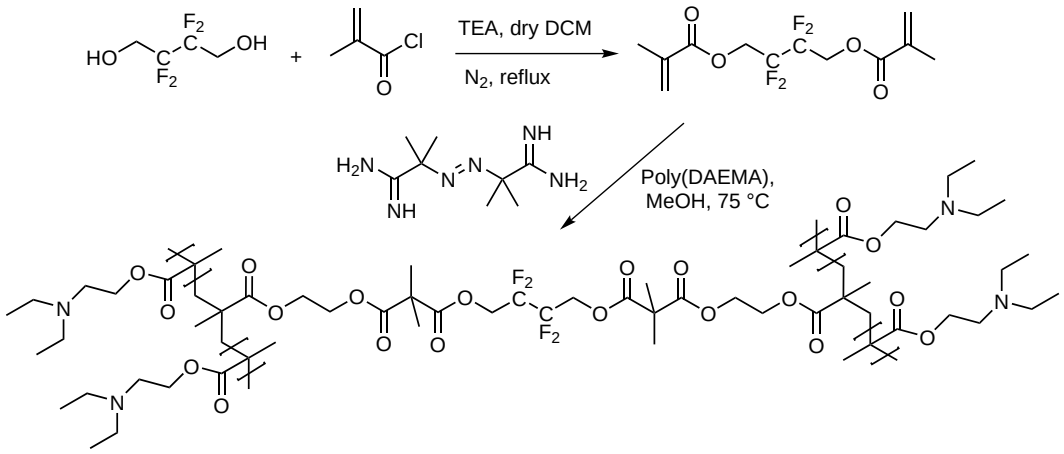


Figure 5.14: Preparation of 2,2,3,3-tetrafluoro-1,4-butanedimethacrylate ($\mathbf{F_4M_2}$) and its incorporation into polymeric nanoparticles **Poly(DAEMA)-**$\mathbf{F_4M_2}$, wherein one of the options of the $\mathbf{F_4M_2}$ co-polymerisation is presented.

In case the polymeric particles were prepared by emulsion polymerisation of poly(2-(diethylamino)ethyl methacrylate) cross-linked with $\mathbf{F_4M_2}$ instead of ethylene glycol dimethylacrylate, large particles (> 2 μm) were obtained without any visible ^{19}F NMR signal. Core $\mathbf{Poly(DAEMA)}_a$ micelles were therefore prepared first and subsequently co-polymerised with $\mathbf{F_4M_2}$ resulting in $\mathbf{Poly(DAEMA)}_a$-$\mathbf{F_4M_2}$

particles.[21] These exhibited a strong ^{19}F NMR signal (T_1 = 293 ± 3 ms, T_2 = 32 ± 5 ms, linewidth = 250 Hz at pH 7.4 and T_1 = 292 ± 2 ms, T_2 = 38 ± 6 ms, linewidth = 270 Hz at pH 4.0). Upon a reduction in pH from 7.4 to 4.0, the ^{19}F T_1/T_2 ratio slightly decreased from 9.2 to 7.7 (Fig. 5.15) as a result of tertiary amine protonation. When smaller **Poly(DAEMA)$_b$-F$_4$M$_2$** particles with a hydrodynamic diameter of 604.3 ± 35.8 nm (PdI = 0.1) were prepared by reacting **F$_4$M$_2$** with **Poly(DAEMA)$_b$** polymeric micelles, which measured about 300 nm in diameter (App. B.18 on P. 216), the ^{19}F T_1/T_2 ratio increased by 20-30 % (T_1 = 280 ± 10 ms, T_2 = 24 ± 2 ms, linewidth = 130 Hz at pH 7.4 and T_1 = 300 ± 10 ms, T_2 = 27 ± 1 ms, linewidth = 90 Hz at pH 4.0). Reduced ^{19}F transverse relaxation times and lower ^{19}F relaxation time responses to pH change in contrast to **Poly(DAEMA)$_a$-F$_4$M$_2$** are a result of reduced local rotational freedom in smaller particles.

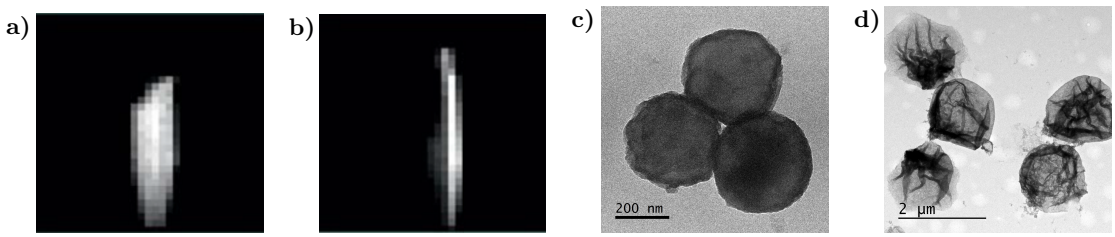


Figure 5.15: ^{19}F MRI images of **Poly(DAEMA)$_a$-F$_4$M$_2$** at a) pH 4.0 (SNR = 490) and b) pH 7.4 (SNR = 440). MRI parameters: GEMS, TR = 0.5 s, TE = 0.7 ms, nt = 16, flip = 90°, matrix = 32 x 32, FOV = 32 mm x 32 mm, Thk = 10 mm, lb = 50, concentration = 20 mg/mL. TEM images show **Poly(DAEMA)$_a$** c) before and d) after **F$_4$M$_2$** incorporation, whereby the resulting particles resemble collapsed microcapsules.

This subsection once again confirms that fluorine nuclei are heavily influenced by local motions. The restriction of their local environment leads to diminishing transverse relaxation times, increased ^{19}F T_1/T_2 ratios and ^{19}F NMR signals disappearing into the baseline. Interestingly, ^{19}F MRI probes incorporated into the polymeric par-

[21] Hydrodynamic diameter = 1160 ± 124 nm, PdI = 0.1, ζ-potential = 45.1 ± 0.4 mV. The FTIR spectrum of the particles can be found in App. B.17 on P. 216.

ticles via electrostatic interactions (**Poly(DAEMA)$_a$-F$_4$Ac**) appeared to be more susceptible to the change in local environment than the covalently bound probes (**Poly(DAEMA)$_a$-F$_4$M$_2$**) since upon pH decrease, the ^{19}F T_1/T_2 ratios decreased by 61 % and 16 % from 116.2 to 45.3 and from 9.2 to 7.7, respectively. Probably, **F$_4$Ac** was incorporated not just onto the surface, but also towards the inner part of the nanoparticles. This is because the particles are formed almost entirely out of diethylaminoethyl groups, while **F$_4$M$_2$** could only react with partially polymerised dimethacrylates (EGDMA). These were more densely populated towards the surface since the particle growth stops with the lack of available monomers during its formation. It can thus be assumed that in a pure polymeric environment, electrostatic interactions influence the appearance of the ^{19}F NMR signal at least as strongly as the covalent interactions.

5.2.4 Quaternary Ammonium Salts as ^{19}F MRI Probes

Since polymeric particles described in the previous section must be highly concentrated in order to get a decent MRI signal, the next goal was to further maximise the fluorine content of the molecular fluorinated probe by employing a quaternary ammonium salt (QAS) as the template for fluorine functionalisation. Perfluoroalkylated quaternary ammonium salt gemini surfactants, for example, have been synthesised in the past as water-soluble catalysts for Mannich reactions.[185]

Novel non-PEGylated fluorinated quaternary ammonium salts containing either 9, 12, 18, 24 or 36 fluorine atoms were prepared and their effects on ^{19}F NMR relaxation times investigated in solution and polyelectrolyte emulsion.[22] In order to prepare a symmetric fluorinated probe, triethanolamine was reacted by Steglich esterification with either 4-(trifluoromethyl)benzoic acid (denoted by *a*) or 3,5-

[22]Further experimental details and NMR data can be found on P. 172-178 and P. 216-222, respectively.

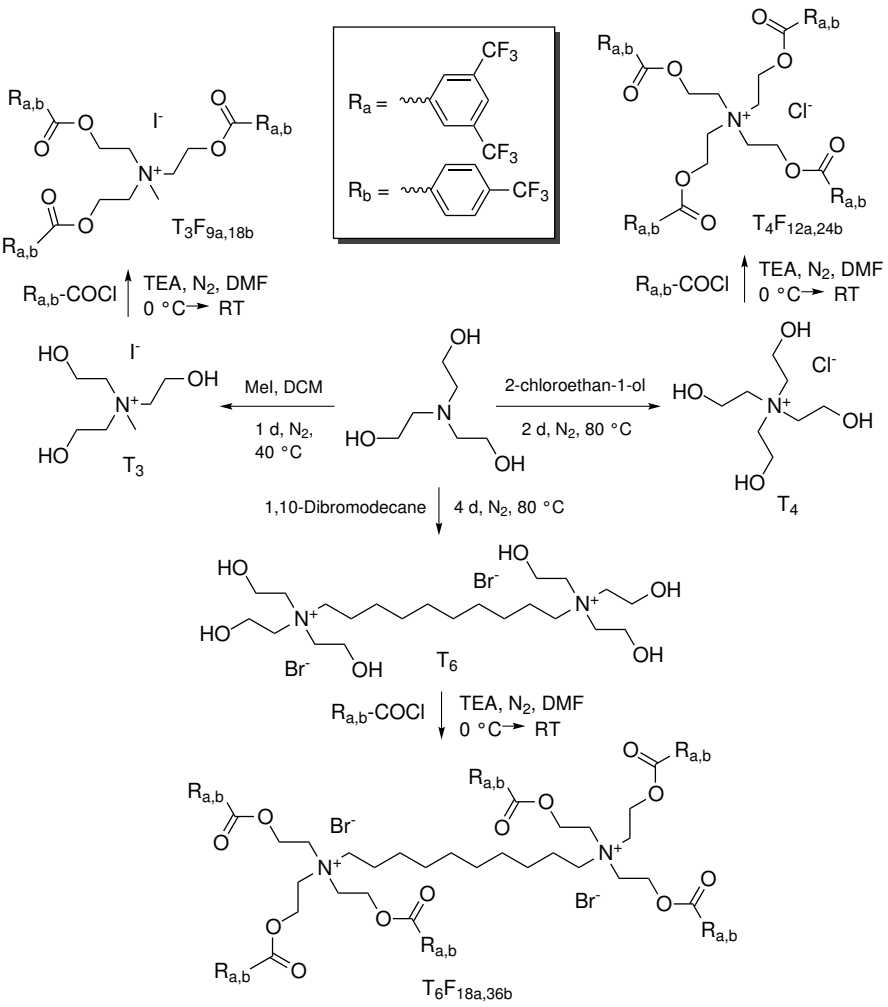


Figure 5.16: Synthetic procedure for preparation of fluorinated QASs.

bis(trifluoromethyl)benzoic acid (denoted by b) to yield $\mathbf{T_0F}_{9a}$ or $\mathbf{T_0F}_{18b}$,[23] respectively, which were both insoluble in H_2O or methanol. Any alkylation of $\mathbf{T_0F}_{18b}$ was impossible and protonation could be achieved only with strong acids. $\mathbf{T_0F}_{9a}$, on the other hand, could be more easily protonated and out of any attempted alkylations (*e.g.* with bromo allyl, bromo ethanol, diiodo propane and diiodo decane at 40-80 °C) only methylation with methyl iodide was successful.

Since the effects of steric crowding and lower hydration as well as the induction effects of mono- and bis(trifluoromethyl)benzoates strongly reduce the basic character

[23]The subscript number in $\mathbf{F}_N$ represents the number of incorporated fluorine atoms.

Table 5.1: Table showing details of ^{19}F NMR relaxation times of fluorinated quaternary ammonium salts in methanol and water at 20 °C at 7.0 T. **-OH$^-$** denotes QASs being passed through Amberlite, while **-PSS** represents QASs after complexation with polystyrene sulphonate.

	T_1 **[ms], MeOH**	T_2 **[ms], MeOH**	T_1 **[ms], H_2O, -OH$^-$**	T_2 **[ms], H_2O, -OH$^-$**	T_1 **[ms], H_2O, -PSS**	T_2 **[ms], H_2O, -PSS**
$\mathbf{T_3F}_{9a}$	1300 ± 30	450 ± 60	1450 ± 20	580 ± 70	2400 ± 400	460 ± 90
$\mathbf{T_3F}_{18b}$	1550 ± 40	620 ± 90	1650 ± 40	720 ± 90	1800 ± 100	430 ± 90
$\mathbf{T_4F}_{12a}$	910 ± 20	290 ± 40	1790 ± 80	400 ± 60	2000 ± 80	420 ± 30
$\mathbf{T_4F}_{24b}$	920 ± 30	300 ± 50	1850 ± 40	410 ± 40	1800 ± 100	410 ± 40
$\mathbf{T_6F}_{18a}$	1100 ± 20	250 ± 40	1200 ± 20	520 ± 40	1900 ± 100	390 ± 90
$\mathbf{T_6F}_{36b}$	1200 ± 100	350 ± 90	1580 ± 70	600 ± 80	1530 ± 60	440 ± 90

of tertiary amine, it was necessary to alkylate the latter with either methyl iodide, chloroethanol or dibromodecane initially yielding either three, four or six fluorination sites, respectively, in a QAS ($\mathbf{T}_i$, i = 3, 4 or 6 as depicted in Fig. 5.16). Due to difficulties with the purification by column chromatography, the ester synthesis of the 4-(trifluoromethyl)benzoyl chloride and 3,5-bis(trifluoromethyl)benzoyl chloride was performed by acylation without DMAP. Hereby, instead of TEA, diethylaminomethylated polystyrene can be used as a base, which can be easily removed by filtration. The resulting QASs are denoted as $\mathbf{T_3F}_{9a}$, $\mathbf{T_4F}_{12a}$ and $\mathbf{T_6F}_{18a}$, when trifluoromethyl benzoate was incorporated. When bis(trifluoromethyl)benzoate was conjugated to QASs, these are denoted as $\mathbf{T_3F}_{18b}$, $\mathbf{T_4F}_{24b}$ and $\mathbf{T_6F}_{36b}$. Since all products were insoluble in water, their ^{19}F NMR T_1 and T_2 values were determined in methanol and found to be around 900-1600 ms and 290-620 ms, respectively (Tab. 5.1). The highest respective ^{19}F T_1/T_2 ratios of 4.4 and 3.4 were observed in $\mathbf{T_6F}_{18a}$ and $\mathbf{T_6F}_{36b}$, while the lowest respective T_1/T_2 ratios of 2.9 and 2.4 were observed in $\mathbf{T_3F}_{9a}$ and $\mathbf{T_3F}_{18b}$. This suggests that both the size of the molecule and the number of benzyl rings contribute to higher T_1/T_2 ratios rather than the number of fluorine groups, especially since $\mathbf{T_6F}_{18a}$ and $\mathbf{T_3F}_{18b}$ have the same number of fluorine atoms. The nature of

counter anions also has a considerable impact on the observed relaxation times. For example, ^{19}F T_1 and T_2 values attained their minimum in middle-sized $\mathbf{T_4F}_{12a}$ and $\mathbf{T_4F}_{24b}$ species, which were both bearing Cl^- as the smallest counter anion.

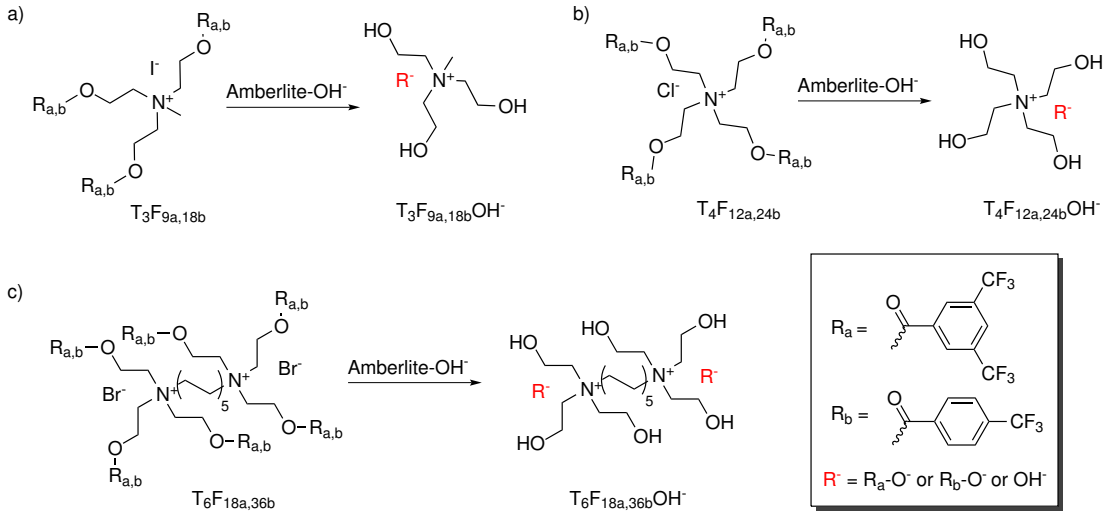


Figure 5.17: Ion-exchange by Amberlite-OH^- caused hydrolysis of fluorinated benzoates. The resulting QASs with benzoates acting as counter anions were thus soluble in water.

When QASs were passed through a NaOH-treated Amberlite column neutralised by excess water, all products became water-soluble. However, as Amberlite is a strongly basic polymeric resin, mass spectrometry of the resulting hydroxyl-exchanged QASs revealed only hydrolysed products with fluorinated benzoates acting as counter anions (Fig. 5.17 as well as App. B.32 and App. B.33 on P. 224), thus explaining the reason behind water solubility. When Amberlite was not treated with NaOH, the extent of ester hydrolysis was the same, except that the resulting QASs with chloride counter anions seemed to be slightly more agglomerated (Fig. 5.18). For example, ^{19}F T_2 values of $\mathbf{T_3F}_{9a}$**-Cl**$^-$ ($T_1 = 1180 \pm 10$ ms, $T_2 = 170 \pm 10$ ms) were quite reduced compared to their hydroxyl-bearing counterparts $\mathbf{T_3F}_{9a}$**-OH**$^-$ ($T_1 = 1450 \pm 20$ ms, $T_2 = 580 \pm 70$ ms).

Instead of exchanging counter anions for small anions, an interesting question arose if the molecular adducts would retain their mobility in case the halide

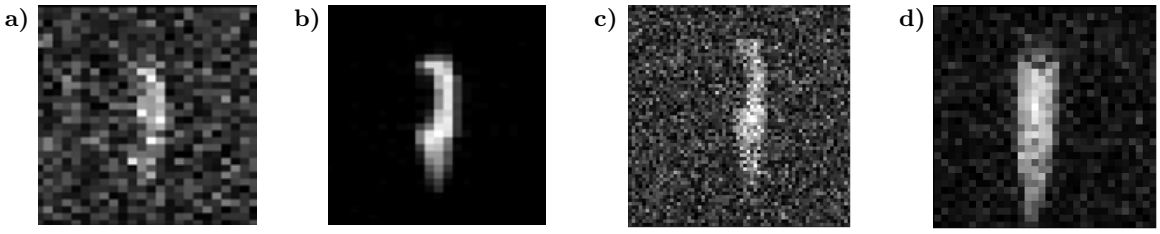


Figure 5.18: ^{19}F MRI images of a) $\mathbf{T_3F_{9a}}$**-Cl**$^-$ (SNR = 20), b) $\mathbf{T_3F_{9a}}$**-OH**$^-$ (SNR = 100), c) $\mathbf{T_3F_{18b}}$**-Cl**$^-$ (SNR = 40) and d) $\mathbf{T_3F_{18b}}$**-OH**$^-$ (SNR = 80) in water after ester hydrolysis when run through an Amberlite column. MRI parameters: GEMS, a-b): TR = 1 s, TE = 6.5 ms, nt = 4, c-d): TR = 1 s, TE = 0.8 ms, nt = 4, flip = 90°; matrix = 32 x 32, FOV = 40 mm x 40 mm, Thk = 10 mm; concentration = a), c): 20 mg/mL and b), d): 30 mg/mL.

counter anions were exchanged for PEGylated polyanions based on methacrylic acid (**Poly(MAA$_{1x}$-PEG$_{3x}$)**, PEG:MAA = 3:1), which would act as solubility enhancers. When **Poly(MAA$_{1x}$-PEG$_{3x}$)-T$_4$F$_{12a}$** (App. B.29 on P. 222) was obtained by anion exchange employing silver(I)-oxide treatment,[186] the polyelectrolyte emulsion became soluble in water. However, the ^{19}F NMR signal was very broad ($T_1 = 858 \pm 24$ ms, $T_2 = 54 \pm 1$ ms, $T_1/T_2 = 15.9$) decreasing with a higher ratio of $\mathbf{T_4F_{12a}}$ ($T_1 = 46 \pm 7$ ms, $T_2 = 8 \pm 2$ ms, $T_1/T_2 = 5.8$), while a higher ratio of PEG chains in the polymeric counter anions also did not decrease the ^{19}F T_1/T_2 ratio.

Alternatively, water-soluble polystyrene sulphonate (**PSS**) was chosen as a polyanion and the ion-exchange was again performed with silver(I)-oxide treatment. The resulting polyelectrolytes were also soluble in water. They exhibited higher zeta-potentials than **PSS** alone, while UV-vis spectra showed a typical decrease in λ_{max} (hypsochromic shift) and absorptivity (hyperchromic effect) in the spectrum of the QASs complexed with acidic **PSS** (App. B.31 on P. 223). This time, excellent ^{19}F NMR signals were obtained in water (App. B.30 on P. 223) with relaxation times similar to those of the parent QASs dissolved in methanol (Tab. 5.1). However, shorter relaxation times were expected due to ion pairing with polymers bearing much higher molecular weight and due to concomitant mobility reduction. Proton NMR spectra (App. B.30) suggest that polystyrene sulphonate might have been involved in

ester hydrolysis since the benzyl resonances exhibit lower intensities, *i.e.* decreased integration numbers, compared to the ethyl groups of QASs.

Besides the hydrophobicity of trifluoromethyl groups, π-π stacking interactions between molecular adducts might be another reason for the poor solubility of the obtained fluorinated QASs as blue light emission upon irradiation with 366 nm UV-light was observed when $\mathbf{T}_4\mathbf{F}_{12a}$ was dissolved in D_2O. Therefore, a possible solution could be to replace the trifluoromethyl benzoyl groups with the trifluoroacetyl ones. Unfortunately, the hydroxyl groups of $\mathbf{T}_3$, $\mathbf{T}_4$ and $\mathbf{T}_6$ QASs could not be directly trifluoroacetylated either by 1-(trifluoroacetyl)imidazole or by trifluoroacetic anhydride (**TFAA**) due to the close proximity of strongly electron-withdrawing quaternary ammonium group. All reactions (App. B.34 on P. 224) resulted in non-, mono- or rarely di-substituted products as revealed by mass spectrometry.

Increasing the distance of fluorination sites proved challenging, and therefore hydroxyl groups were converted into amines first, followed by trifluoroacetylation by **TFAA** (Fig. 5.19).[24] When direct one-pot conversion at high temperatures was attempted overnight, the quaternary amines were converted into tertiary amines in addition to the hydroxyl conversion into primary amines ($\mathbf{T}_0(\mathbf{NH}_2)_4$). These could be easily modified into trifluoroacetamides by **TFAA** in the presence of sodium bicarbonate resulting in water-soluble $\mathbf{T}_0\mathbf{F}_{9c}$ with ^{19}F T_1 and T_2 relaxation times of 1710 $\pm$ 30 ms and 490 $\pm$ 60 ms, respectively. Since trifluoroacetyl amide linkages can be cleaved hydrolytically, trifluoroacetamides were converted into trifluoroethylamines ($\mathbf{T}_0\mathbf{F}_{9cRed}$) to promote stability of the fluorinated probe. The resulting ^{19}F T_1 and T_2 values were elongated and reduced to 2560 $\pm$ 20 ms and 320 $\pm$ 50 ms, respectively, thus increasing the T_1/T_2 ratio from 3.5 to 8.0. Although both compounds contain a bulky electron withdrawing trifluoromethyl group, the internal rotational barrier for amide in $\mathbf{T}_0\mathbf{F}_{9c}$ is higher than the one for secondary amine in $\mathbf{T}_0\mathbf{F}_{9cRed}$,

[24] Further experimental details and NMR spectra can be found on P. 178-180 and P. 225-226, respectively.

resulting in slower internal rotation.

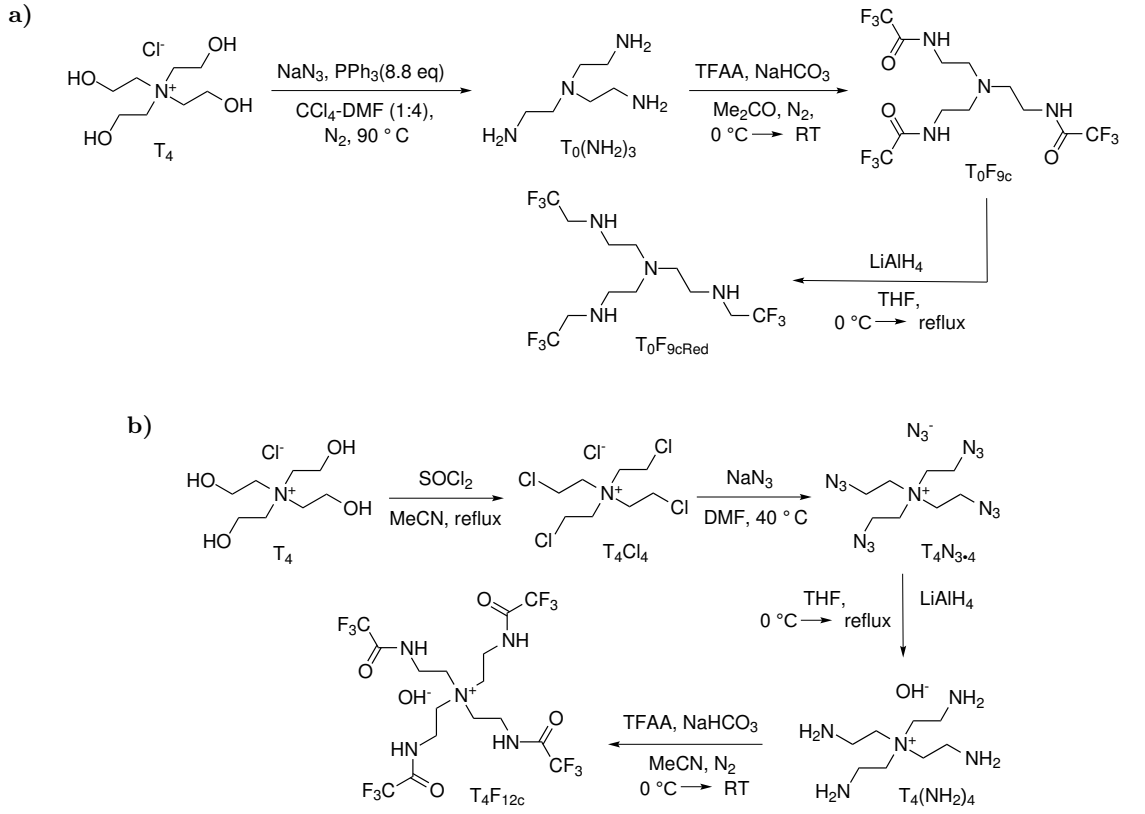


Figure 5.19: Synthetic route of a) $\mathbf{T_0F_{9c}}$ and b) $\mathbf{T_4F_{12c}}$.

If the quarternary structure is to be retained, the amine conversion has to be performed step-wise at lower temperatures. The involved reactions must be conducted extremely carefully as intermediates include a chemical warfare analogue ($\mathbf{T_4Cl_4}$), of which production for future reference is strongly restricted, and $\mathbf{T_4N_{3\text{-}4}}$, which contains more azides than a theoretically stable molecule allows for. Careful reduction of azides yielded amines that could be converted into trifluoroacetyl amides. The resulting water-soluble product bearing 12 fluorine atoms ($\mathbf{T_4F_{12c}}$)[25] exhibited ^{19}F T_1 and T_2 relaxation times of 1840 ± 50 ms and 500 ± 90 ms, respectively, which are similar to the values obtained for $\mathbf{T_0F_{9c}}$. These results once again indicate that

[25]Further experimental details can be found on P. 180.

aliphatic perfluorinated quaternary ammonium systems can indeed be water-soluble and that aryl systems most likely impair water solubility of fluorinated QASs due to π-π-stacking.

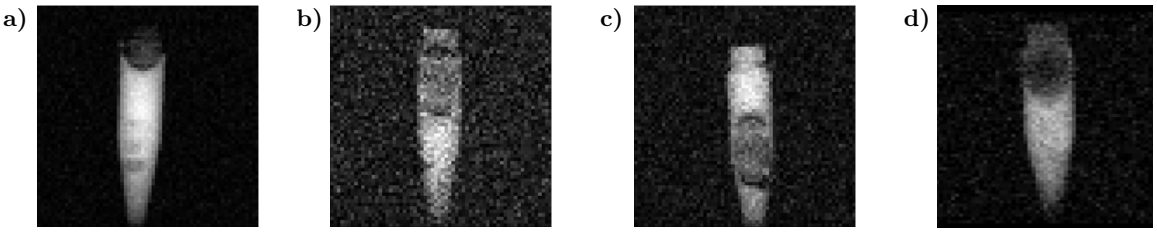


Figure 5.20: ^{19}F MRI images of a) $\mathbf{T_0F_{9c}}$ (SNR = 1200), b) $\mathbf{T_0F_{9cRed}}$ (SNR = 300), c) $\mathbf{T_4F_{12c}}$ (SNR = 520) and d) **PEI-CF$_3$-Cl$^-$** (SNR = 610) in H_2O. MRI parameters: GEMS, a-c): TR = 500 ms, TE = 1 ms, nt = 16, flip = 90°, matrix = 64 x 64, FOV = 32 mm x 32 mm, Thk = 10 mm; d) TR = 200 ms, TE = 1 ms, nt = 4, flip = 90°, matrix = 64 x 64, FOV = 32 mm x 32 mm, Thk = 10 mm; concentration = a): 4 mg/mL, b-c): 2 mg/mL, d): 10 mg/mL.

The simple and inexpensive trifluoroacetyl amidation approach was also implemented in the fluorination of branched polyethyleneimine (PEI, 800 g/mol), which contains several primary amine groups and is also the most popular polymer used to deliver genes into various human cell types. This is because its cationic nature can facilitate entrance into the cells.[187] The reaction of ethyl 2,2,2-trifluoroacetate[26] with PEI yielded a product denoted as **PEI-CF$_3$**, which is unstable in water (T_1 = 2480 ± 80 ms, T_2 = 620 ± 90 ms were obtained in MeOH). The ^{19}F MRI probe solubility in water was improved when the tertiary amines were quaternised by methylation and when iodide and residual trifluoroacetate anions were ion-exchanged with chloride by passing the product through Amberlite.[27] The resulting **PEI-CF$_3$-Cl$^-$** gave also an excellent ^{19}F MRI signal in water (T_1 = 1270 ± 40 ms, T_2 = 320 ± 30 ms) indicating once again the importance of stabilisation of fluorinated QASs by a suitable counter ion.

[26]Measurements in water yielded the following ^{19}F NMR relaxation times: T_1 = 2500 ± 30 ms and T_2 = 460 ± 30 ms. Over time, the compound becomes unstable and precipitates.

[27]Further experimental details and NMR spectra can be found on P. 194 and P. 227, respectively.

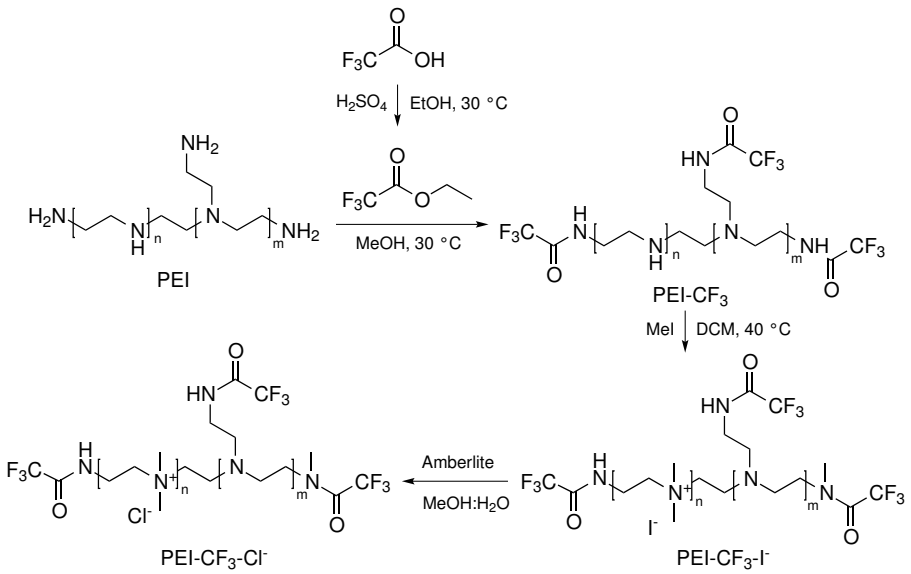


Figure 5.21: The synthetic route of fluorinated and quaternarised **PEI-CF$_3$-Cl$^-$**.

5.3 Conclusion

In summary, fluorine nuclei in constrained environments exhibit faster relaxation times, especially transverse relaxation times and broader signals with poorer signal-to-noise ratios than identical nuclei in less constrained environments. For example, the proximity or interaction of fluorine moieties with a silica surface could only be detected by solid-state NMR regardless of whether the fluorine was incorporated into dendrimers or polymers tethered to silica surface or if it was directly conjugated to ultra-small mesoporous silica nanoparticles measuring 10 nm in diameter. Indeed, the only silica-based species with a detectable ^{19}F NMR signal has been reported when trifluoroacetamide was incorporated into cubic octameric polyhedral oligomeric silsesquioxane (POSS) measuring 1.5 nm in diameter.[109]

Polymers, on the other hand, provide a better scaffold for ^{19}F MRI applications than rigid silica nanoparticles (Fig. 5.22). By incorporating symmetric dimethacrylate and carboxylate ^{19}F MRI reporters into the poly(2-(diethylamino)ethyl methacrylate) particles via electrostatic interactions or covalent bonding, respectively, water-soluble

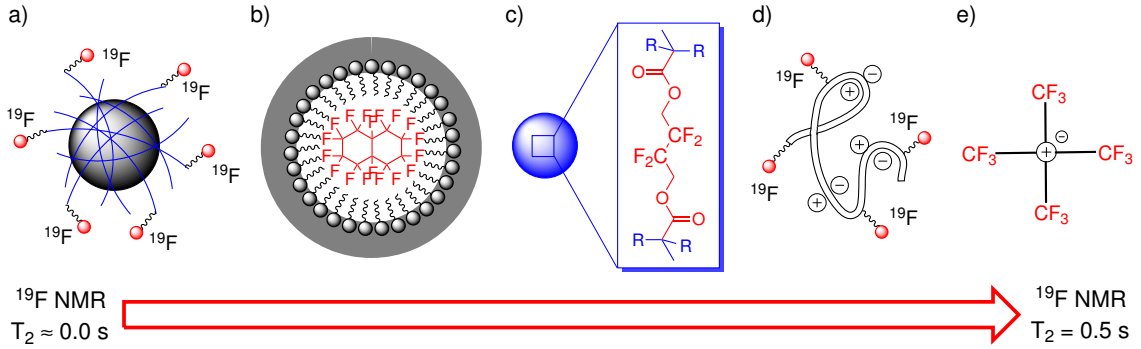


Figure 5.22: Overview of the impact of fluorine environment on ^{19}F NMR signal and relaxation times. No ^{19}F NMR signal is obtained when the global environment is rigid, while excellent ^{19}F MRI contrast can be acquired when the ^{19}F T_1/T_2 ratio is as close to 1 as possible with T_2 being as high as possible.

^{19}F MRI nanoprobes with high signal-to-noise ratios that are able to endow multiple functionalities have been obtained. It has been shown that for polymeric micelles measuring 300-1000 nm in diameter, it is more beneficial for ^{19}F NMR T_1/T_2 ratios if the fluorine moiety is incorporated in the periphery rather than in the core as the latter substantially reduces the local mobility of fluorine species. Therefore, in the polymeric systems, ^{19}F NMR relaxation times can be tuned by size adjustment and fluorine incorporation into a specific location within the micelles.

Besides the ion pairing of ^{19}F MRI probes with polyelectrolytes and PEGylated polyelectroclytes, dendrimer-like quaternary ammonium salts were also investigated. Although a heavily PEGylated water-soluble dendrimeric fluorophore containing 48 symmetric fluorines incorporated into tetrasubstituted benzenes[98] was reported to exhibit a high ^{19}F NMR signal, it can be concluded from this work that aryl systems impair water solubility, which is substantially improved by introduction of aliphatic fluorinated quaternary ammonium systems (Fig. 5.23). Both aryl and alkyl fluorinated quaternary salts were incorporated by anion exchange into polymeric counter anion chains, whereby alkyl-based systems again exhibited improved water solubility and ^{19}F NMR signal. The properties of counter ions are thus at least as important as the optimised design of fluorinated quaternary ammonium salts themselves.

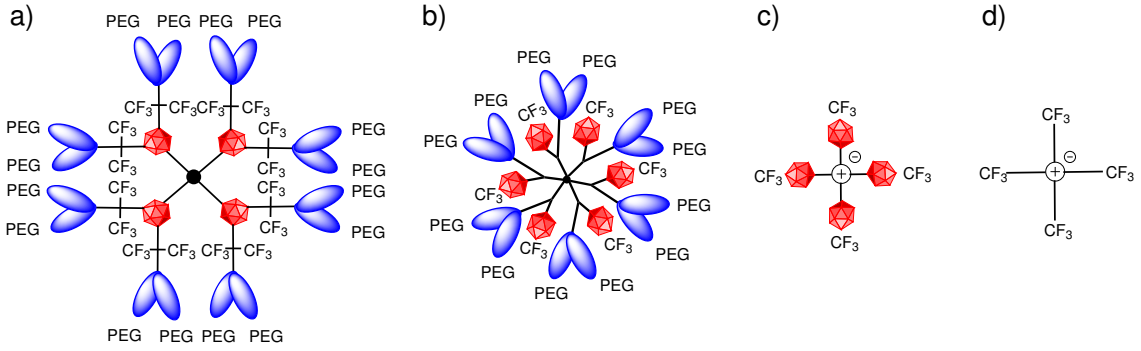


Figure 5.23: Comparison of fluorinated PEGylated dendrimers and quaternary ammonium salts. a) PEGylated fluorinated dendrimers reported by Bo *et al.* [98] and d) fluorinated alkyl QASs deliver excellent ^{19}F NMR signal in water, while b) PEGylated fluorinated dendrimers[28] and c) fluorinated benzyl QASs are either sparingly soluble or insoluble in water, thus resulting in no ^{19}F NMR signal in solution. Red icosahedrons denote benzyl rings, while blue ellipsoids represent PEG chains.

It is nevertheless plausible to conclude that silica-based nanocapsules containing a fluorinated oil present the most promising and least toxic ^{19}F MRI probe. Kikuchi *et al.* [96] implemented a surfactant containing a basic pyridyl catalyst group that could start the sol-gel process of TEOS, while the long alkyl chains interacted with fluorocarbon-phospholipid nanoemulsion, thus inducing formation of nanocapsules.[96] The system discussed in this work, implemented perfluorodecalin as a ^{19}F MRI probe incorporated into silica nanocapsules via dimethyloctadecyl[3-(trimethoxysilyl)-propyl]ammonium chloride, which was used as a surfactant and template for the sol-gel process. These particles exhibited an excellent ^{19}F NMR signal and were centrifugable due to a thicker silica shell. Incorporating a 100 % concentrated fluorinated oil into the nanocapsules might be the only clinically implementable ^{19}F MRI formulation due to the very limited sensitivity of ^{19}F MRI imaging, while the protective silica coating could prove very beneficial for *in vivo* applications as a result of reduced cytotoxicity and unperturbed fluorine mobility.

[28] Unpublished results obtained in collaboration with Prof. Mireille Blanchard-Desce, University of Bordeaux. The organic nanodots exhibited a strong fluorescence signal visible throughout the cytoplasm and even in the nucleoli of the cells. However, despite their excellent photophysical properties in water, the ^{19}F NMR signal could only be detected in organic solvents.

Chapter 6

Dual $^{19}F/^{1}H$ Nanoparticulate MRI Contrast Agents

6.1 Introduction

Because of the omnipresence of the ^{1}H and the complete absence of the ^{19}F NMR signal in the human body, ^{1}H and ^{19}F MRI techniques complement each other in their information content. ^{1}H MRI is advantageous for assembling anatomical, physiological and biochemical information about the human body and is therefore a valuable tool for disease diagnosis. ^{19}F MRI, on the other hand, is a tracer type method and is suited for collecting information about drugs in the body, and thus has the potential to become a valuable tool for image-guided drug therapy as well as for cell tracking.[188] As described in Ch. 1, Aime *et al.* [68] combined both modalities to test their applicability for pH mapping, wherein the sulphonamide arm was responsible for a pH-dependent change in the q value of Gd^{3+} complex, while the ^{19}F MRI probe acted as a reporter since both MRI-active moieties were incorporated into poly-β-cyclodextrin.[68] In one part of this chapter, PEGylated and quaternised pH-responsive polymers will be investigated, which are composed of $q = 1$ Gd^{3+} complexes and of either water-insoluble or water-soluble fluorinated monomers.

Another part of the chapter will, on the other hand, focus on the direct para-

magnetic enhancement of a fluorinated probe by ternary complex formation with a bis-Gd^{3+} chelate in an attempt to improve the ^{19}F MRI sensitivity since the acquisition of sufficient signal intensity in a reasonable time is still the foremost disadvantage of ^{19}F MRI,[89] and since it can be enhanced through the introduction of a proximate paramagnetic centre, such as a lanthanide chelate.[103] A weak ternary complex, for example, was reported to form when two coordinated inner sphere water molecules bound to Gd^{3+}-DO3A were replaced by trifluorolactate leading to a decrease in ^{19}F NMR longitudinal relaxation time to 23 ms at 7.0 T.[108]

Among 1,3-dicarboxylates, isophthalates reversibly ligate to two lanthanides in kinetically stable DO3A binding pockets linked by a 3-functionalised *meta*-xylyl bridge.[189] Davies *et al.* [190] have recently investigated the binding properties of trifluoroethoxy isophthalic acid to binuclear α,α'-bis(Ln^{3+}-DO3A)-5-amino-*m*-xylene ($\mathbf{Ln_2{\cdot}L_3}$), wherein the two inner-sphere solvent molecules are replaced by trifluoroethoxy isophthalate ($\mathbf{F_3IPA}$) as depicted in Fig. 6.1, however, these complexes are not soluble in water.

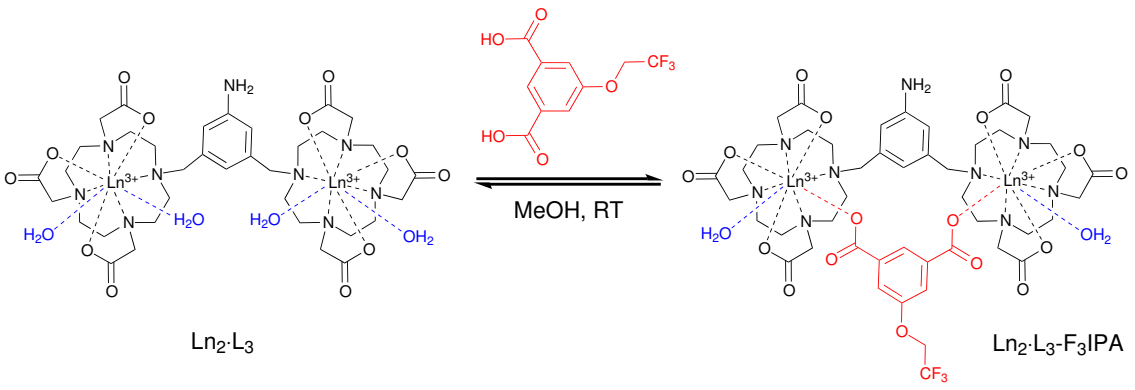


Figure 6.1: Binding of the fluorinated isophthalic acid ($\mathbf{F_3IPA}$) to the binuclear lanthanide chelate ($\mathbf{Ln_2{\cdot}L_3}$).

The largest 60-fold ^{19}F NMR longitudinal relaxation enhancement accompanied by the highest association constant ($7.0\text{-}8.3 \cdot 10^4$ M^{-1}) was achieved in the pH range from 6.0-7.0 in methanol. This is because the binding affinity of dicarboxy-

lates varies considerably with pH due to protonation of the fluorinated ligand at low pH (pKa $\approx$ 3.3). Conformational alternations of binding pockets of lanthanide complexes might also play an important role.[191] In the following sections, such bidentate binding mechanism has been implemented for preparation of a self-assembled water-soluble $^{19}F/^{1}H$ MRI nanoparticulate probe by tethering the binuclear *m*-xylyl bridged DO3A ($\mathbf{Ln_2{\cdot}L_3}$) to silica-based nanoparticles followed by self-assembly with trifluoroethoxy isophthalic acid ($\mathbf{F_3IPA}$).

6.2 Results and Discussion

6.2.1 Paramagnetically Enhanced ^{19}F NMR Relaxation in Water-Soluble Mesoporous Silica Nanoparticles

The main disadvantage of the ternary $\mathbf{Ln_2{\cdot}L_3}$-$\mathbf{F_3IPA}$ complex is its insolubility in water due to the hydrophobic fluorinated ligand, which considerably reduces its applicability *in vivo*. In order to probe the effect of silica surface and mesopore confinement on ^{19}F and ^{1}H NMR relaxation enhancement in water, α,α'-bis(LnDO3A)-5-amino-*m*-xylene ($\mathbf{Ln_2{\cdot}L_3}$) was conjugated to carboxylated silica-based nanoparticles by carbodiimide coupling, which was optimised with the help of solid-state NMR and FTIR by incorporating aniline instead of $\mathbf{Ln_2{\cdot}L_3}$ into carboxylated MSNs.[1] The highest amount of $\mathbf{Ln_2{\cdot}L_3}$ was incorporated into mesoporous silica nanoparticles ($9.9 \cdot 10^3$ μg/g) when these were prepared by an aqueous Stöber technique via 15 μmol % co-condensation of (3-aminopropyl)triethoxysilane as close to the periphery as possible followed by carboxylation with succinic anhydride. Subsequent conjugation of $\mathbf{Ln_2{\cdot}L_3}$ yielded particles denoted as $\mathbf{MSN\text{-}Ln_2{\cdot}L_3}$ with ζ-potential of -23.1 $\pm$ 1.6 mV and hydrodynamic diameter of 138.3 $\pm$ 2.3 nm, PdI = 0.1 (Fig. 6.4).

[1] Further experimental details can be found on P. 195, whereas accompanying NMR and FTIR spectra of the control aniline coupling to the MSNs instead of $\mathbf{Ln_2{\cdot}L_3}$ can be found in App. B.40 and App. B.39 on P. 227.

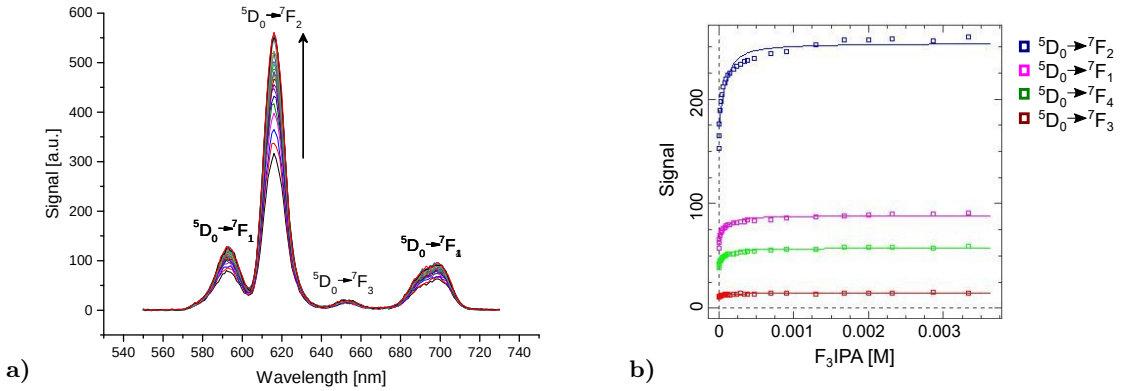


Figure 6.2: Graphs showing a) luminescence spectra and b) corresponding fittings of titration data of **MSN-Eu$_2$·L$_3$** (Eu^{3+} = 0.1 mM) with **F$_3$IPA** in MeOH. The fitted curves correspond to each of the bands with the excitation at 394 nm, wherein the increase in emission intensity correlates to the removal of quenching hydroxyl groups of methanol from the coordination sphere by **F$_3$IPA**.

The binding of **F$_3$IPA** to the europium derivative of **MSN-Eu$_2$·L$_3$** (q = 1.7) was confirmed by luminescence titrations in methanolic solution (Fig. 6.2), wherein the luminescence emission intensity was enhanced as **F$_3$IPA** bonded to Eu^{3+}, thereby replacing the quenching hydroxyl oscillator groups. The titration was performed as long as the plateaux of emission increments of $^5D_0 \rightarrow ^7F_1$, $^5D_0 \rightarrow ^7F_2$, $^5D_0 \rightarrow ^7F_3$ and $^5D_0 \rightarrow ^7F_4$ transition bands were reached. The association constant of $K_a = 2.5 \cdot 10^4$ M^{-1} was derived from the emission intensities by fitting the observed luminescence data with Dynafit using a non-linear least-squares iterative analysis based on the Levenberg-Marquardt algorithm.[191] Although the ligation was almost as strong as the binding of **F$_3$IPA** to molecular **Eu$_2$·L$_3$** ($K_a = 7.8 \cdot 10^4$ M^{-1}), it was not strong enough to withstand any purification procedures, such as dialysis or centrifugation/sonication cycles, which immediately removed the ligated **F$_3$IPA**.

Upon ligation of **F$_3$IPA** to **MSN-Gd$_2$·L$_3$** in methanol, drying and subsequent redispersion in water, the ^{19}F NMR T_1 and T_2 relaxation times were reduced to 81.8 ± 3.5 ms and 2.2 ± 0.7 ms, respectively. This corresponds to a 19-fold ^{19}F longitudinal relaxation rate enhancement compared to **F$_3$IPA** dissolved in MeOH (T_1 = 1552.0 ± 29.9 ms and T_2 = 308.2 ± 33.7 ms) and 14-fold ^{19}F longitudinal re-

laxation rate enhancement in contrast to **F$_3$IPA** stirred with MSNs without the lanthanide complex (T_1 = 1108.0 ± 55.7 ms and T_2 = 17.4 ± 3.7 ms). These particles were used as a lanthanide-free nanoparticle control. The reduced ^{19}F T_2 value in the latter is most likely a result of **F$_3$IPA** being physisorbed onto MSNs. Only slightly decreased T_1 in the control, on the other hand, indicates that the observed decrease in ^{19}F relaxation times in **MSN-Gd$_2$·L$_3$-F$_3$IPA** can be indeed attributed to the binding of **F$_3$IPA** to the lanthanide as also confirmed by luminescence titrations.

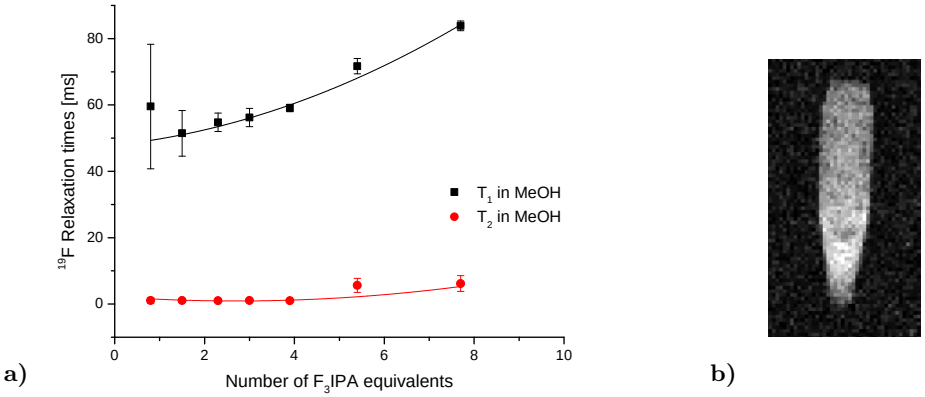


Figure 6.3: a) Graph shows ^{19}F NMR relaxometric titrations of **MSN-Gd$_2$·L$_3$** (65 mg/mL) with trifluoroethoxy isophthalic acid performed in MeOH, whereby the last point of the measurement, which equalled to 32 mM suspension of **F$_3$IPA**, was imaged by b) ^{19}F MRI using a 7.0 T instrument at RT. It is important to note that the image was obtained in 3.5 hours due to a low amount of the fluorinated probe and high ^{19}F NMR T_1/T_2 ratio. MRI parameters: TR = 0.05 s, TE = 0.7 ms, nt = 4096, matrix = 96 x 64, FOV = 48 mm x 32 mm, Thk = 5 mm, SNR = 25.

The binding of **F$_3$IPA** was also investigated by ^{19}F NMR relaxometric titrations of **MSN-Gd$_2$·L$_3$** with **F$_3$IPA** performed in MeOH (Fig. 6.3). Similarly to the luminescence titrations (Fig. 6.2), which suggested that 4 equivalents of **F$_3$IPA** per Eu^{3+} are necessary to saturate the luminescence emission intensity, relaxometric titrations also revealed that the ^{19}F T_1 values increased only marginally from 51.5 ± 6.9 ms to 59.1 ± 1.1 ms when the concentration of **F$_3$IPA** was increased from 1 to 4 equivalents per Gd^{3+}. At 8 equivalents of **F$_3$IPA** (*i.e.* 5 mg of **F$_3$IPA** per 39 mg **MSN-Ln$_2$·L$_3$**), the ^{19}F T_2 value was still quite short at 6.2 ± 1.3 ms, while the ^{19}F longitudinal re-

laxation time was elongated to more than 83.9 ± 1.5 ms, which was far lower than the ^{19}F T_1 value of free **F_3IPA**.

Table 6.1: Table showing ^{19}F relaxation times and ^{1}H relaxivities in H_2O (at pH 6.0-7.0 at 20 °C at 7.0 T), as well as q values of **Eu_2·L_3** and the association constants of **F_3IPA** in MeOH. Error margins represent cumulative errors arising from triplicate repetitions of T_1 and T_2 measurements. ^{19}F relaxation times were obtained by complexation of the following ratios of **F_3IPA**:**Gd_2·L_3**: 1:1, 1.5:1 and 1.5:1, for **Gd_2·L_3**, **NS-MAA-Gd_2·L_3** and **MSN-Gd_2·L_3** samples, respectively. [*a*] Indicates relaxation times of molecular species (**Gd_2·L_3-F_3IPA**) dissolved in methanol.

	^{19}F T_1 [ms], H_2O, pH 6-7	^{19}F T_1 [ms], H_2O, pH 6-7	^{1}H r_1 [mM^{-1} s^{-1}], H_2O, pH 6-7	^{1}H r_2 [mM^{-1} s^{-1}], H_2O, pH 6-7	Gd [μg/g NP]	q value	K_a [M^{-1}] of F_3IPA
Ln_2·L_3-F_3IPA	24.1 ± 1.4[a]	14.3 ± 1.8[a]	/	/	/	1.8	$7.8{\cdot}10^4$
NS-Ln_2·L_3-F_3IPA	47.9 ± 1.9	6.1 ± 0.9	11.3 ± 1.3	138.2 ± 13.4	6614 ± 99	1.7	$4.2{\cdot}10^3$
NS-Poly(MAA)-Ln_2·L_3-F_3IPA	19.9 ± 4.5	5.6 ± 1.7	18.7 ± 5.3	232.3 ± 57.9	7422 ± 201	2.0	$1.2{\cdot}10^3$
MSN-Ln_2·L_3-F_3IPA	81.8 ± 3.5	2.2 ± 0.7	6.5 ± 0.1	76.1 ± 2.3	9960 ± 63	1.7	$2.5{\cdot}10^4$

Most likely, **F_3IPA** binds to the lanthanide through only one of its carboxylate arms, which becomes noticeable when more than two equivalents of **F_3IPA** are present in suspension. Indeed, when a monodentate benzoic acid analogue 3-(2,2,2-trifluoroethoxy)-benzoic acid was incubated with either **Gd_2·L_3** or **MSN-Gd_2·L_3**, the ^{19}F NMR relaxation times were found to be within error margin of their paramagnetically enhanced **F_3IPA** counterparts, *i.e.* T_1 = 25.2 ± 1.8 ms, T_2 = 15.3 ± 2.5 ms and T_1 = 82.3 ± 5.6 ms, T_2 = 4.9 ± 1.7 ms, respectively. The results thus indicate that there is no difference between paramagnetic enhancements when monodentate or bidentate fluorinated benzoic acids are implemented as ^{19}F MRI probes. They also show that bidentate fluorinated benzoic acids can bind to the lanthanide through one of the carboxylate pendants. Since **Ln_2·L_3** and **MSN-Ln_2·L_3** possess q values of around 2, it is only possible that there are at most four **F_3IPA**

species bound per $\mathbf{Ln_2{\cdot}L_3}$. The further four species might be a result of the proximate hydrogen-bonded $\mathbf{F_3IPA}$-solvent network in the paramagnetically enhanced secondary coordination sphere. Alternatively, the exchange rate of the lanthanide-ligated $\mathbf{F_3IPA}$ with the outer-sphere $\mathbf{F_3IPA}$ species might be sufficiently fast so that essentially no elongation of the ^{19}F relaxation times can be observed on the NMR scale upon addition of four equivalents of $\mathbf{F_3IPA}$ per lanthanide. The assumption of all four inner sphere solvent molecules being displaced by $\mathbf{F_3IPA}$ is also supported by the low ^{1}H longitudinal relaxivity, which accounted only for 6.5 ± 0.1 $\mathrm{mM^{-1}\ s^{-1}}$ in $\mathbf{MSN\text{-}Gd_2{\cdot}L_3\text{-}F_3IPA}$ ternary complex. This is very low for a $q = 2$ CA incorporated into the periphery of the mesopores.

6.2.2 Reduced ^{19}F NMR T_1/T_2 Ratios by Dinuclear Lanthanide Complex Conjugation to Polymer-Coated Silica Nanoparticles

In order to decrease the ^{19}F NMR T_1/T_2 ratio by increasing the transverse relaxation times, *m*-xylyl bridged bis-DO3A was incorporated into a slightly more fluidic local environment of poly(methacrylic acid)-coated non-porous silica nanoparticles denoted as $\mathbf{NS\text{-}Poly(MAA)\text{-}Ln_2{\cdot}L_3}$. The polymer coating was prepared by the free radical polymerisation technique described in Ch. 3, followed by $\mathbf{Ln_2{\cdot}L_3}$ incorporation via carbodiimide coupling.[2] Although the association constant of $\mathbf{F_3IPA}$ to $\mathbf{NS\text{-}Poly(MAA)\text{-}Eu_2{\cdot}L_3}$ accounted for only $1.2 \cdot 10^3$ $\mathrm{M^{-1}}$, which is smaller by a factor of two compared to the K_a of $\mathbf{MSN\text{-}Eu_2{\cdot}L_3}$ (Fig. 6.5), ^{19}F T_1 values as low as 19.9 ± 4.5 ms and T_2 values as high as 5.6 ± 1.7 ms were obtained when $\mathbf{F_3IPA}$ was ligated to $\mathbf{NS\text{-}Poly(MAA)\text{-}Gd_2{\cdot}L_3}$ and redispersed in water. Such 80-fold PRE-induced increase in ^{19}F longitudinal relaxation rate in water is within the error margin of the ^{19}F relaxation enhancement of the molecular $\mathbf{Gd_2{\cdot}L_3}$ in MeOH

[2] Further experimental details can be found on P. 194-195, ^{19}F NMR spectrum is presented in App. B.42 on P. 228.

(Tab. 6.1). As a result of longer T_2, the T_1/T_2 ratio and ^{19}F NMR signal linewidth were both reduced by 10-fold and 3-fold to 3.6 and 104 Hz, respectively, compared to **MSN-Gd$_2$·L$_3$-F$_3$IPA** (^{19}F T_1/T_2 = 37, linewidth = 277 Hz).

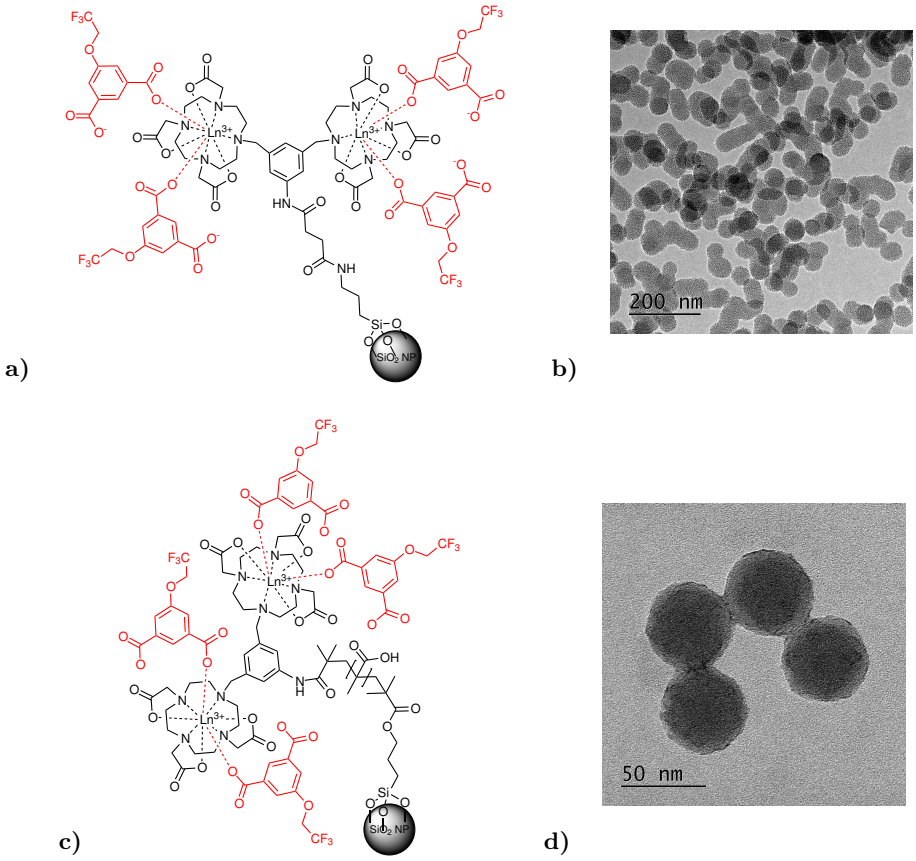


Figure 6.4: Schematic depictions and TEM images of nanoparticle scaffolds illustrate a-b) mesoporous (**MSN-Ln$_2$·L$_3$**) and c-d) polymer coated non-porous (**NS-Poly(MAA)-Ln$_2$·L$_3$**) silica NPs bearing **Ln$_2$·L$_3$**.

In addition to the flexible local environment provided by the polymers, which help to increase the ^{19}F T_2 relaxation time, the reduced ^{19}F T_1 value compared to **MSN-Gd$_2$·L$_3$** might be a result of a more suitable conformation of the biding pocket. This is because the conformational freedom is higher than when the complex is restricted either by the size of the mesopore or by the shorter amide linker to the polymer that limits the rotation about the C-N bond, which bridges the two macrocycles to the aryl ring. In contrast, the propylsuccinamide linker in **MSN-Gd$_2$·L$_3$**

is much longer (Fig. 6.4). Since the size of $\mathbf{Gd_2{\cdot}L_3}$ with ligated $\mathbf{F_3IPA}$ is about 2 nm and the diameter of the pores in this type of MSNs is around 3 nm, it might be possible that the water access to Gd^{3+} is not favourable when the pores are jammed with $\mathbf{Gd_2{\cdot}L_3}$ complexes that possess four coordinated $\mathbf{F_3IPA}$ species. Therefore, the hydrophilic polymer and the absence of pores may induce the boost in ^{1}H r_1 relaxivity to 18.7 $\pm$ 0.1 mM^{-1} s^{-1} in **NS-Poly(MAA)-$\mathbf{Gd_2{\cdot}L_3}$-$\mathbf{F_3IPA}$**, which equals to a 2.9-fold increase in ^{1}H r_1 in comparison to **MSN-$\mathbf{Gd_2{\cdot}L_3}$-$\mathbf{F_3IPA}$** (Tab. 6.1). This might be the reason, why the binding constant of $\mathbf{F_3IPA}$ to **MSN-$\mathbf{Eu_2{\cdot}L_3}$** is 20-times stronger than the K_a of $\mathbf{F_3IPA}$ to **NS-Poly(MAA)-$\mathbf{Eu_2{\cdot}L_3}$**. The assumption that the size restriction of the pores limits the proton relaxivity and increases the binding constant of $\mathbf{F_3IPA}$, was also supported by a 1.7-fold increase in ^{1}H r_1 and 6-fold weaker K_a (App. B.41 on P. 228), when $\mathbf{F_3IPA}$ was ligated to $\mathbf{Ln_2{\cdot}L_3}$, which itself was pre-conjugated to non-porous silica nanoparticles via the same propylsuccinamide linker.

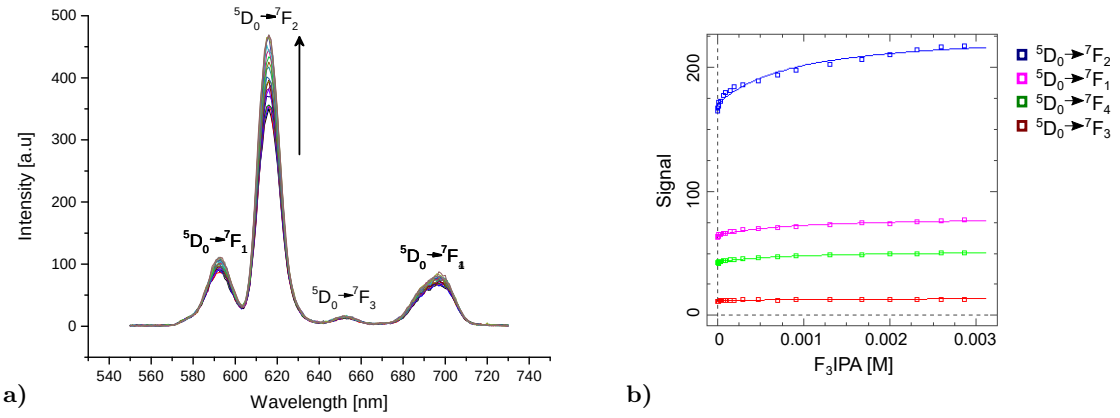


Figure 6.5: Graphs showing a) luminescence spectra and b) fittings of titration data for a $3.3 \cdot 10^{-5}$ mol solution of **NS-Poly(MAA)-$\mathbf{Eu_2{\cdot}L_3}$** with $\mathbf{F_3IPA}$ in MeOH. The fitted curves correspond to each of the bands with the excitation at 394 nm, whereby the increase in emission intensity correlates to the removal of quenching hydroxyl groups of methanol from the coordination sphere by $\mathbf{F_3IPA}$.

To summarise, the confinement of $\mathbf{Ln_2{\cdot}L_3}$ within the mesopores of silica nanopartilces significantly improves the binding association of $\mathbf{F_3IPA}$ with the lanthanide

compared to the 6-times weaker K_a of **F_3IPA** determined for **Ln_2·L_3** conjugated to non-porous silica nanoparticles. The efficient replacement of the inner-coordination sphere solvent molecules by the ^{19}F MRI probe was confirmed by luminescence titrations, which together with ^{19}F NMR relaxometric titrations suggest that all four solvent molecules coordinated to **Ln_2·L_3** are replaced by **F_3IPA** species through only one of their two carboxylate arms, resulting in a reduced proton relaxivity. The most significant issue, however, is the large ^{19}F NMR T_1/T_2 ratio, which broadens the ^{19}F NMR signal and reduces the applicability of such systems to *in vivo* MRI. The incorporation of **F_3IPA** and **Ln_2·L_3** into polymer-coated non-porous silica nanoparticles decreases the ^{19}F NMR T_1/T_2 ratio by a factor of 10 compared to the mesopore-confined system due to a higher local flexibility of the polymer chains. Nevertheless, this still cannot compensate for the low amount of fluorinated probes incorporated into the particles due to the low amount of tethered **Ln_2·L_3** complexes, which are precious and were thus used sparingly.

6.2.3 pH-Responsive PEGylated and non-PEGylated Polymeric Dual ^{19}F/^{1}H MRI Contrast Agents

As the sensitivity of a paramagnetically enhanced ^{19}F MRI probe was not increased enough for the dilute fluorinated species to be detected easily by ^{19}F MRI, ^{19}F/^{1}H NMR signal responses were investigated on polymeric micelles, which were able to incorporate higher amounts of fluorinated species. In addition, these provided a higher signal-to-noise ratio (SNR), water solubility and mobility of the fluorine groups. pH-responsive polymeric nanoparticles denoted as **Poly(TFMA-MAA-PEG)** with a liquid-like fluorophilic core consisting of self-assembled statistical polymers such as methacrylic acid, 2,2,2-trifluoroethyl methacrylate (**TFMA**) and poly(ethylene glycol)$_{4\text{-}5}$ methyl ether methacrylate (Fig. 6.6), were prepared by free radical polymerisation reaction with 2,2′-azobis(2-methylpropionamidine) hydrochlo-

ride.[3] The presence of PEGylated side chains was absolutely necessary for fluorinated polymers to be dissolved in water.

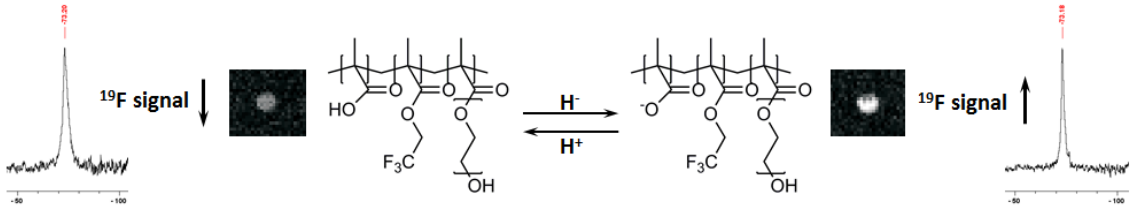


Figure 6.6: At high pH, pH-responsive fluorinated polymeric micelles **Poly(TFMA-MAA-PEG)** exhibit a higher SNR and, consequently, a higher ^{19}F NMR signal due to electrostatic repulsion of charged poly(methacrylic acid) side chains. The SNR and the magnitude of the ^{19}F NMR signal at low pH are reduced since poly(methacrylic acid) is protonated and collapsed. MRI parameters: TR = 0.5 s, TE = 0.7 ms, nt = 32, flip = 90°, matrix = 32 x 32, FOV = 32 mm x 32 mm, Thk = 10 mm, concentration = 10 mg/mL.

The resulting micelles could only be purified by extraction and dialysis due to their small size. They measured 18.5 ± 5.7 nm in diameter (PdI = 0.1, ζ-potential = 9.1 ± 0.9 mV) at pH 4.0, whereas at pH 7.4, their size increased only slightly to 18.9 ± 6.7 nm (PdI = 0.2, ζ-potential = -20.2 ± 1.7 mV). At pH 7.4, the poly(methacrylic acid) chains were negatively charged (^{19}F T_1 = 370 ± 10 ms, T_2 = 1.9 ± 0.2 ms, linewidth = 700 Hz) and exhibited a signal-to-noise ratio that was 40 % higher and a linewidth that was 30 % lower than at pH 4.0, when the poly(methacrylic acid) chains were protonated and collapsed (^{19}F T_1 = 380 ± 10 ms, T_2 = 1.7 ± 0.2 ms, linewidth = 1000 Hz). The difference in MRI contrast as a result of protonation is depicted in Fig. 6.6.

The next step was to incorporate a Gd^{3+} probe in order to explore the effects of proximate Gd^{3+} on the pH responsiveness of fluorine and protic relaxation times. For this purpose, a monoamide q = 1 Gd^{3+}-DOTA methacrylate ($\mathbf{Gd{\cdot}L_4}$)[4] was synthesised by reacting DOTA-tris(tBu)-NHS-ester with 2-aminoethyl methacrylate hy-

[3] The respective experimental procedure and characterisation data can be found on P. 196 and P. 229.

[4] Further experimental details can be found on P. 181, while the NMR spectra are presented in App. B.48 on P. 230.

drochloride, followed by deprotecting the *tert*-butyl groups with TFA and metallating the chelate with $GdCl_3 \cdot 6H_2O$ (Fig. 6.7).

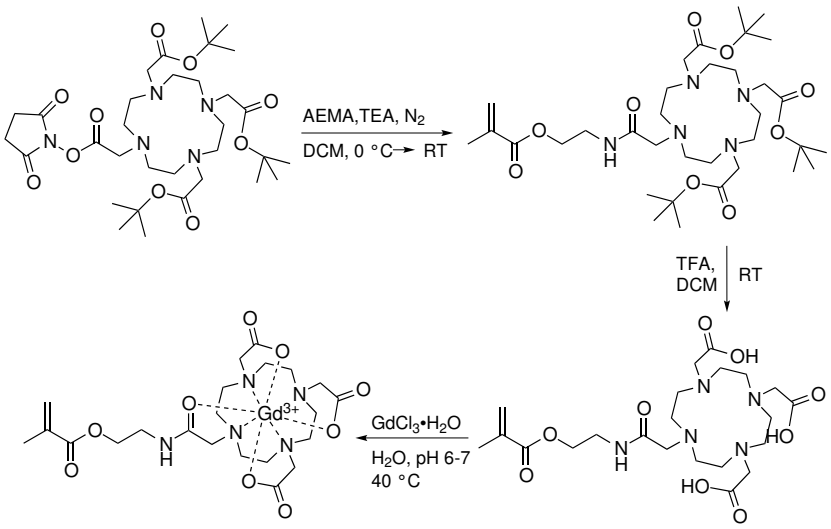


Figure 6.7: Reaction scheme of $\mathbf{Gd{\cdot}L_4}$ preparation.

When $\mathbf{Gd{\cdot}L_4}$ was co-polymerised with methacrylic acid, 2,2,2-trifluoroethyl methacrylate and poly(ethylene glycol)$_{4\text{-}5}$ methyl ether methacrylate, the obtained particles[5] measured 19.1 ± 3.3 nm in hydrodynamic diameter (ζ-potential = -22.7 ± 4.3 mV). The gadolinium content was determined to be around 376 ppm by an NMR procedure based on bulk magnetic susceptibility shifts as described on P. 163. The resulting **Poly(TFMA-MAA-PEG-Gd·L$_4$)** polymers exhibited a strong ^{19}F NMR signal with $T_1 = 410 \pm 10$ ms and $T_2 = 40 \pm 3$ ms in water at pH 7.4, whereas at pH 4.0, the suspension became very viscous due to protonation of methacrylic acid, which together with the increased proximity of $\mathbf{Gd{\cdot}L_4}$ resulted in complete ^{19}F NMR signal disappearance (Tab. 6.2, Fig. 6.8). The Gd^{3+} complex also contributed to a pH-responsive proton longitudinal relaxivity (Fig. 6.12, Tab. 6.3).[6] This increased from 5.6 ± 0.9 mM^{-1} s^{-1} at pH 7.4, when the poly(methacrylic acid) chains were deprotonated and ionised, to 11.4 ± 0.6 mM^{-1} s^{-1} at pH 4.0, when the

[5]The accompanying FTIR spectrum can be found in App. B.54 on P. 233.
[6]The corresponding fitted proton relaxation rates can be found on P. 235.

polymer chains were collapsed as a result of protonation.

The polymers comprised of negatively charged poly(methacrylic acid) chains were thus swollen at basic pH and collapsed at acidic pH. If methacrylic acid was swapped for positively charged 2-(diethylamino)ethyl methacrylate (DMA), such polymers were swollen at acidic pH and collapsed at basic pH. As a result, the ^{19}F relaxation time responses to the pH were expected to be anti-correlated to those observed in **Poly(TFMA-MAA-PEG)**. Indeed, when analogous **Poly(TFMA-DMA-PEG)** were prepared,[7] the ^{19}F relaxation times increased from $T_1 = 400 \pm 50$ ms and $T_2 = 9.5 \pm 0.9$ ms at pH 7.4 to $T_1 = 420 \pm 20$ ms and $T_2 = 16.0 \pm 9.0$ ms at pH 4.0, when the poly(2-(diethylamino)ethyl methacrylate) chains were protonated and swollen. This was confirmed by the respective ζ-potentials and hydrodynamic diameters, which increased from 11.7 ± 0.6 mV and 27.7 ± 3.8 nm (PdI = 0.3) at pH 7.4 to 31.3 ± 1.3 mV and 103.3 ± 27.6 nm (PdI = 0.4) at pH 4.0.

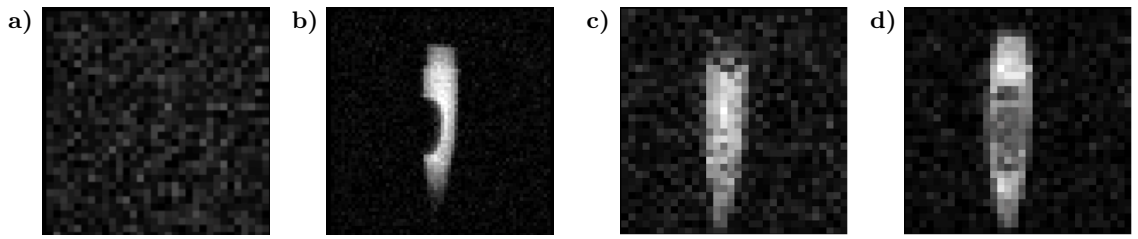


Figure 6.8: ^{19}F MRI images of **Poly(TFMA-MAA-PEG-Gd·L$_4$)** at a) pH 4.0 (SNR = 0) and b) pH 7.4 (SNR = 150) as well as of c) **Poly(TFMA-DMA-PEG)** (SNR = 110) and d) **Poly(TFMA-DMA-PEG-Gd·L$_4$)** (SNR = 130) at pH 4.0. MRI parameters: TR = 500 ms, TE = 1 ms, nt = 16, sw = 100 kHz, matrix = 64 x 64, FOV = 40 mm x 40 mm, concentration = 15 mg/mL.

When **Gd·L$_4$** was co-polymerised with **TFMA**, PEG and 2-(diethylamino)ethyl methacrylate monomers, **Poly(TFMA-DMA-PEG-Gd·L$_4$)** micelles were obtained. A ^{19}F NMR signal could only be detected at low pH, when the following ^{19}F relaxation times could be determined: $T_1 = 373 \pm 7$ ms and $T_2 = 2.6 \pm 0.2$ ms,

[7] The respective experimental procedure and characterisation data can be found on P. 196 and P. 229.

whereas at high pH, the fluorine signal again disappeared as a combined result of a higher viscosity or order parameter and the increased proximity of **Gd·L$_4$**. Simultaneously, protic r_1 values decreased from 10.7 ± 0.1 mM^{-1} s^{-1} at pH 7.4 to 5.8 ± 0.3 mM^{-1} s^{-1} at pH 4.0 as a consequence of lower rotational correlation time and swollen polymeric chains.

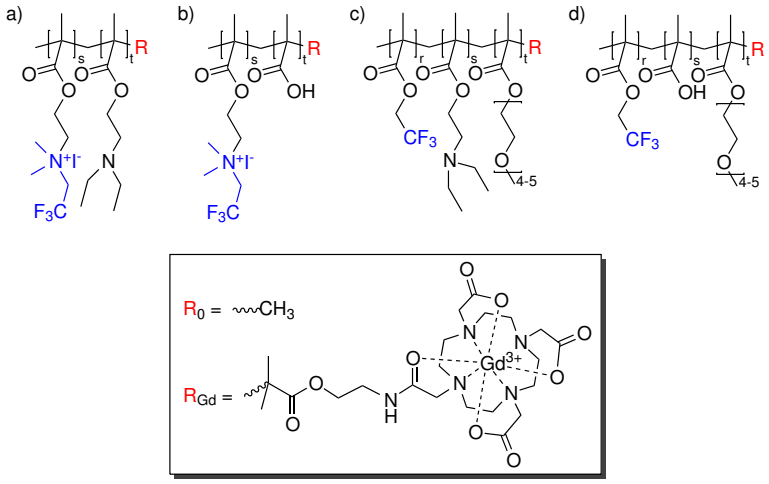


Figure 6.9: Overview of fluorinated polymers containing either water-soluble **FQMA**: a) **Poly(FQMA-DMA)** and b) **Poly(FQMA-MAA)** or water-insoluble **TFMA**: c) **Poly(TFMA-DMA-PEG)** and d) **Poly(TFMA-MAA-PEG)** with or without **Gd·L$_4$**.

Poly(TFMA-MAA-PEG-Gd·L$_4$) and **Poly(TFMA-DMA-PEG-Gd·L$_4$)** therefore both exhibited a ^{19}F NMR signal by an "all-or-nothing" principle at either high or low pH, respectively (Fig. 6.8). Since 2,2,2-trifluoroethyl methacrylate is water-insoluble and requires incorporation of PEGylated methacrylates for its applicability as a water-soluble ^{19}F MRI probe, a new water-soluble quaternary ammonium based fluorinated monomer, which does not require additional solubility enhancing PEG chains when incorporated into polymers, was prepared. The question was, if the ^{19}F NMR signal was observable at both low and high pH and if so, if the relaxation times were still pH-responsive. Initially, an allyl-functionalised triethanol ammonium salt was prepared in order to accommodate three trifluoromethyl

groups (App. B.47 on P. 230), however, it turned out that the allyl group was too close to the strongly electron-withdrawing quaternary ammonium. As a result, its polymerisation failed at various conditions (*i.e.* by ATRP or free radical polymerisation at high temperature with or without an electron-donating monomer or solvent). For this reason, a simple water-soluble 2,2,2-trifluoro-*N*-(2-(methacryloyloxy)ethyl)-*N,N*-dimethylethan-ammonium iodide (**FQMA**, Fig. 6.10) was synthesised by trifluoroacetylating ethanolamine with the latter also acting as an internal base, followed by reduction of trifluoroacetamide, methylation of the resulting secondary amine and final functionalisation with methacrylate.[8]

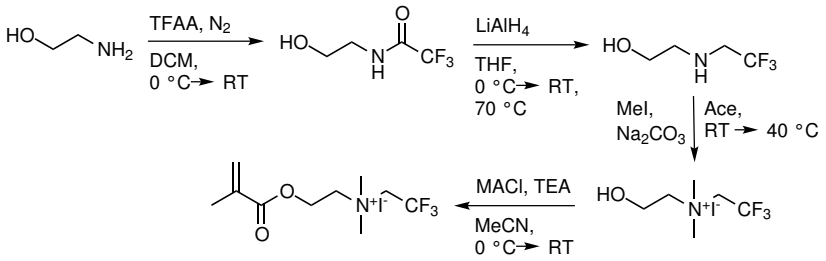


Figure 6.10: Reaction scheme of **FQMA** monomer preparation.

For comparison, **FQMA** was incorporated into either poly(2-(diethylamino)ethyl methacrylate) or poly(methacrylic acid) with or without $\mathbf{Gd{\cdot}L_4}$ by random free radical polymerisation reaction with 2,2′-azobis(2-methylpropionamidine) hydrochloride as an initiator (Fig. 6.9).[9] The ζ-potentials of **Poly(FQMA-DMA)** and **Poly(FQMA-MAA)** decreased by 67 % and 54 %, respectively, with higher pH (Fig. 6.11), similarly to **Poly(TFMA-MAA-PEG)** and **Poly(TFMA-DMA-PEG)**. The highest and lowest ζ-potentials of **Poly(FQMA-DMA)** and **Poly(FQMA-MAA)**, on the other hand, were found to be lower than those of

[8]Further experimental details can be found on P. 182-184, while the accompanying NMR spectra can be found on P. 231-232.

[9]Further experimental details can be found on P. 196. The structures were characterised by NMR, FTIR and MALDI-TOF, which can be found in App. B.53-B.57 on P. 233-234.

their **TFMA**-doped counterparts most likely due to the presence of **FQMA** bearing quaternary ammonium iodide salt and the absence of PEG chains (Fig. 6.11). As with **Poly(TFMA-MAA-PEG)**, the hydrodynamic diameter of **Poly(FQMA-MAA)** increased only from 9.2 ± 0.4 nm to 9.5 ± 1.3 nm upon pH increase from 4.0 to 7.4. The change of the hydrodynamic diameter in **Poly(FQMA-DMA)** (from 16.7 ± 8.1 nm at pH 7.4 to 93.8 ± 18.9 nm at pH 4.0) was also comparable to its **TFMA**-bearing counterpart.

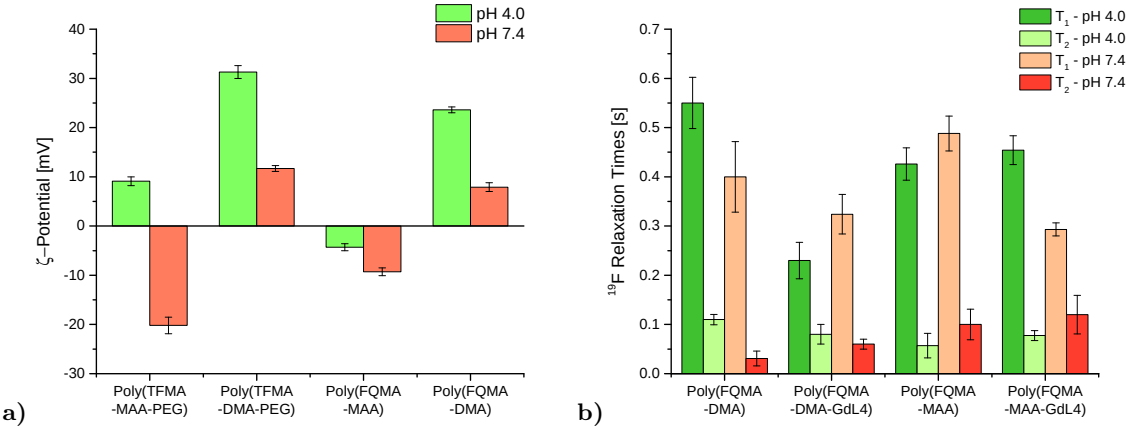


Figure 6.11: a) ζ-potentials of fluorinated polymers based on **TFMA** or **FQMA** monomers and b) ^{19}F relaxation times of **FQMA**-functionalised polymers with and without **Gd·L**$_4$ measured at RT at 9.4 T.

The ^{19}F NMR signals of **Poly(FQMA-DMA)** and **Poly(FQMA-MAA)** were observable at both low and high pH with the ^{19}F T_1/T_2 ratio either decreasing or increasing at low pH by 61 % or 35 %, respectively (Fig. 6.11). In the case of **Poly(FQMA-DMA)**, ^{19}F T_1 and T_2 relaxation times increased from 400 ± 70 ms and 31 ± 13 ms at pH 7.4 to 550 ± 50 ms and 110 ± 11 ms at pH 4.0 due to ionised poly(2-(diethylamino)ethyl methacrylate) chains. The ^{19}F T_1 and T_2 values of **Poly(FQMA-MAA)**, on the other hand, decreased from 488 ± 35 ms and 100 ± 30 ms at pH 7.4 to 426 ± 32 ms and 57 ± 20 ms at pH 4.0 due to protonated and collapsed poly(methacrylic acid) chains. In terms of the change in the ^{19}F T_1/T_2 ratio, the pH response was higher in **Poly(FQMA-DMA)** (61 % change)

than in **Poly(FQMA-MAA)** (34 % change). As a result of improved water solubility and internal mobility, the signal-to-noise ratio of **Poly(FQMA-DMA)** and **Poly(FQMA-MAA)** remained constant throughout the physiologically relevant pH and the ^{19}F T_1/T_2 ratio of quaternary ammonium polymers decreased by a factor of 5-40 when compared with their PEGylated **TFMA**-functionalised counterparts.

Table 6.2: Table showing details of ^{19}F relaxation times in H_2O (at pH 4.0 and 7.4 at 20 °C at 7.0 T). Error margins represent cumulative errors of T_1 and T_2 assessment arising from one sample batch.

	^{19}F T_1 [ms], H_2O, pH 4.0	**^{19}F T_2 [ms], H_2O, pH 4.0**	**^{19}F T_1 [ms], H_2O, pH 7.4**	**^{19}F T_2 [ms], H_2O, pH 7.4**	**^{19}F T_1/T_2 H_2O, pH 4.0**	**^{19}F T_1/T_2 H_2O, pH 7.4**
Poly(TFMA-MAA-PEG-Gd·L$_4$)	/	/	410 ± 50	40 ± 10	/	10.3
Poly(TFMA-DMA-PEG-Gd·L$_4$)	373 ± 10	2.6 ± 0.2	/	/	143.5	/
Poly(FQMA-MAA-Gd·L$_4$)	560 ± 30	60 ± 10	470 ± 30	130 ± 9	9.3	3.6
Poly(FQMA-DMA-Gd·L$_4$)	250 ± 30	80 ± 9	440 ± 60	60 ± 10	3.1	7.3

Interestingly, the ^{19}F T_1/T_2 ratio was further reduced, when **Gd·L$_4$** was incorporated into polymers to yield **Poly(FQMA-DMA-Gd·L$_4$)** and **Poly(FQMA-MAA-Gd·L$_4$)** (Fig. 6.12 and Tab. 6.2). While the ^{19}F T_2 values increased with the ionisation of either poly(2-(diethylamino)ethyl methacrylate) or poly(methacrylic acid) chains similarly to their diamagnetic counterparts, the ^{19}F T_1 values decreased with ionisation and were even lower than when the polymers were collapsed and unionised. For instance, when the pH was decreased from 7.4 to 4.0, the ^{19}F T_2 values of **Poly(FQMA-DMA-Gd·L$_4$)** increased from 60 ± 10 ms to 80 ± 9 ms, whereas the ^{19}F T_1 values decreased from 440 ± 60 ms to 250 ± 30 ms. Despite the decrease of the latter, the ^{19}F T_1/T_2 ratio in both cases still followed the same trend as their diamagnetic counterparts. The paramagnetic analogues thus also decreased

with ionised polymer chains by 40-60 %. In addition, the signal-to-noise ratios were similar at both low and high pH. Although the paramagnetic effect in this case is negligible due to a distance between the lanthanide and fluoride larger than 8 Å, its presence certainly has a greater effect on ^{19}F T_1 than on ^{19}F T_2 values, which are more strongly affected by the rotational correlation time.

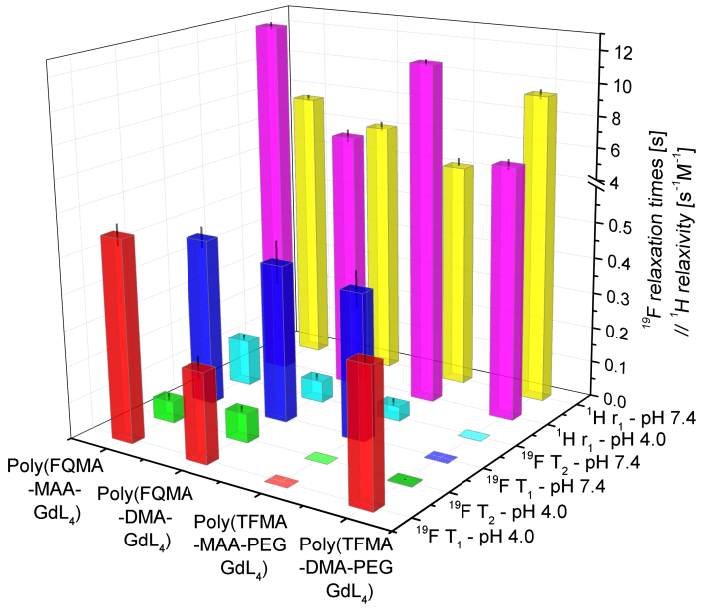


Figure 6.12: ^{19}F relaxation times and ^{19}H relaxivities of fluorinated polymers with and without **Gd·L$_4$** measured at 20 °C at 7.0 T.

The proton longitudinal relaxivity in **Poly(FQMA-MAA-Gd·L$_4$)**, on the other hand, increased with lower pH from 7.3 ± 0.2 mM^{-1} s^{-1} at pH 7.4 to 12.7 ± 0.3 mM^{-1} s^{-1} at pH 4.0 (Fig. 6.12, Tab. 6.3).[10] This 43 % change is only slightly lower than the 63 % difference observed in **Poly(TFMA-MAA-PEG-Gd·L$_4$)**. It corresponds to a reverse response of the ^{19}F T_1 and T_2 changes as the collapsed polymers reduce the ^{19}F relaxation times and simultaneously increase the ^{1}H relaxivity due to elongated rotational correlation time of the polymeric complex. The ^{1}H longitudinal relaxivity of **Poly(FQMA-DMA-Gd·L$_4$)**, on the other hand,

[10] Fitted proton relaxation rates can be found on P. 235.

does not change with pH and remains constant at 6.2 ± 0.4 mM^{-1} s^{-1}, although the ^{1}H r_2 values do change from 11.3 ± 1.2 mM^{-1} s^{-1} to 17.1 ± 1.9 mM^{-1} s^{-1} upon pH change from 4.0 to 7.4. The polymers also exhibit a higher pH response in ^{19}F relaxation times, hydrodynamic diameters and ζ-potentials in comparison to **Poly(FQMA-MAA-Gd·L$_4$)**. This might be a result of **Gd·L$_4$** being located towards the periphery of the micelles or next to the already charged **FQMA** as the proton longitudinal relaxivity of the analogous polymers with doped **TFMA** and PEG chains decreased by 38 % at low pH due to the swelling of poly(2-(diethylamino)ethyl methacrylate).

Table 6.3: Table showing details of ^{1}H relaxivities in H_2O (at pH 4.0 and 7.4 at 7.0 T). Error margins represent cumulative errors of T_1 and T_2 assessment arising from one sample batch.

	^{1}H r_1 [mM^{-1} s^{-1}], H_2O, pH 4.0	^{1}H r_2 [mM^{-1} s^{-1}], H_2O, pH 4.0	^{1}H r_1 [mM^{-1} s^{-1}], H_2O, pH 7.4	^{1}H r_2 [mM^{-1} s^{-1}], H_2O, pH 7.4	^{1}H r_2/r_1 H_2O, pH 4.0	^{1}H r_2/r_1 H_2O, pH 7.4	Gd [μg/g]
Poly(TFMA-MAA-PEG-Gd·L$_4$)	11.4 ± 0.2	50.2 ± 10.1	4.2 ± 0.5	17.4 ± 3.7	4.4	4.1	376
Poly(TFMA-DMA-PEG-Gd·L$_4$)	5.8 ± 0.3	10.9 ± 2.5	9.4 ± 0.3	33.9 ± 0.9	1.9	3.6	1971
Poly(FQMA-MAA-Gd·L$_4$)	12.7 ± 0.2	30.5 ± 2.8	7.3 ± 0.2	12.6 ± 2.9	2.4	1.7	3342
Poly(FQMA-DMA-Gd·L$_4$)	6.2 ± 0.4	11.3 ± 0.4	6.1 ± 0.3	1.7 ± 1.2	1.8	2.8	2805

The **Poly(FQMA-MAA-Gd·L$_4$)** polymeric micelles were easily soluble in water. From pH 7.4 to 4.0, they exhibited a notable 43 % and 61 % increase in proton relaxivity and ^{19}F T_1/T_2 ratio, respectively. Since the linewidth and signal-to-noise ratio of the ^{19}F NMR signal are retained, they could act as double ^{19}F/^{1}H pH-responsive probes with the ^{19}F MRI probe also acting as a tracker and concentration reporter when defining a calibration curve for the concentration as the signal is not broadened and the change in ^{19}F relaxation times is moderate. **Poly(TFMA-MAA-PEG-Gd·L$_4$)** and **Poly(TFMA-DMA-PEG-Gd·L$_4$)**, on the other hand, both exhibit a

^{19}F NMR signal by "all-or-nothing" principle at either high or low pH, respectively, due to lower solubility and substantially reduced internal freedom when the polymers are in a collapsed state. By incorporating ^{19}F MRI reporters and Gd^{3+} probes into pH-responsive poly(2-(diethylamino)ethyl methacrylate) or poly(methacrylic acid) scaffold, it is thus possible to prepare probes that have either a better ^{19}F NMR signal or increased ^{1}H relaxivity at either acidic or basic pH. The ^{19}F MRI contrast agent could thus be primarily used for tracking and concentration reporting purposes and secondarily as a supplemental pH-responsive probe.

6.3 Conclusion

To conclude, paramagnetic ^{19}F and ^{1}H NMR enhancements were achieved when α,α'-bis-(Ln^{3+}-DO3A)-5-amino-*m*-xylene was conjugated to mesoporous or polymer-coated non-porous silica nanoparticles and ligated to trifluoroethoxy isophthalic acid. Especially in polymer-coated silica nanoparticles, an 80-fold paramagnetically triggered increase of ^{19}F longitudinal relaxation rate was achieved in water (from 0.6 s^{-1} to 50.3 s^{-1}) compared to trifluoroethoxy isophthalic acid dispersed in a $MeOH/H_2O$ mixture. Although all four solvent molecules in the inner-coordination sphere could be replaced by four trifluoroethoxy isophthalic acid molecules through only one of their two carboxylate arms, the paramagnetic enhancement failed to increase the sensitivity of ^{19}F MRI sufficiently, especially in nanoparticulate systems, where ^{19}F NMR transverse relaxation times are further reduced due to the rigid surface.

Pure polymers, on the other hand, provide a better, less constrained scaffold for ^{19}F MRI imaging than inflexible polymer-coated nanoparticles. Besides offering lower ^{19}F NMR T_1/T_2 ratios, they provide numerous ways of tuning ^{19}F relaxation times and ^{1}H relaxivities through a change in conformation from an extended flexible to rigid globular form. For example, when water-insoluble fluorinated monomers and $q = 1$

Gd^{3+}-DOTA methacrylates ($\mathbf{Gd{\cdot}L_4}$) were incorporated into polymers, of which solubility was increased by the presence of PEGylated side chains, such polymers exhibited an "all-or-nothing" ^{19}F MRI response to a change in pH depending on whether their pH-responsive entity was based on either poly(2-(diethylamino)ethyl methacrylate) or poly(methacrylic acid). This further triggered a pH response in ^{1}H relaxivity that was less pronounced and behaved oppositely to its ^{19}F NMR counterpart. In other words, while ^{1}H relaxivity increased due to collapsed polymers and higher rotational correlation time, the ^{19}F NMR signal was absent.

In order to maintain a ^{19}F NMR signal throughout the physiologically relevant pH range, a new and simple water-soluble fluorinated monomer 2,2,2-trifluoro-*N*-(2-(methacryloyloxy)ethyl)-*N,N*-dimethylethan-ammonium iodide was synthesised and together with $\mathbf{Gd{\cdot}L_4}$ incorporated into the pH-responsive polymers. The resulting micelles exhibited high water solubility and maintained similar linewidth and signal-to-noise ratio of the ^{19}F NMR signal at both low and high pH. While the largest pH response in ^{19}F relaxation times was achieved in poly(2-(diethylamino)ethyl methacrylate)-functionalised polymers, the strongest pH-triggered response in ^{1}H relaxivities was observed in poly(methacrylic acid)-based polymers. These could thus be implemented as a dual $^{19}F/^{1}H$ MRI probe since they exhibit a 43 % and 61 % increase in ^{1}H r_1 and ^{19}F T_1/T_2 ratio, respectively, upon pH change from 7.4 to 4.0. When the pH-responsive component is exchanged by a suitable environmentally responsive moiety, such dual $^{19}F/^{1}H$ MRI probes can be easily applicable to a plethora of physiological responses.

Chapter 7

Experimental Procedures

7.1 Materials and Methods

Reaction Conditions. All solvents used were laboratory grade and all reagents were implemented as supplied by commercial sources (mostly from Sigma-Aldrich, Alfa Aesar and VWR International) unless otherwise stated, while deionised water (18 MΩ·cm) from a Millipore Milli-Q water purification system was used in the preparation of all aqueous solutions. Reactions requiring anhydrous conditions under an atmosphere of dry nitrogen were carried out using an mBraun Labstar glove box and a Schlenk line connected to an Edwards vacuum pump.

Purification Procedures. A Buchi rotary evaporator equipped with an anti-splash adapter was used to remove solvents from samples. Thin layer chromatography was carried out with silica gel or neutral aluminium oxide plates (Merck TLC plates), which are fluorescent under UV irradiation at 254 nm. Column chromatography was performed using silica gel (Merck Silica Gel 60, 230-400 mesh) or neutral aluminium oxide (Merck Aluminium Oxide 90, activity II-III, 70-230 mesh), while anion exchange chromatography was executed with Amberlite IRA-400 exchange resin in the chloride form (Sigma-Aldrich). Beckman Coulter Allegra 6 centrifuge and Pierce

SnakeSkin dialysis tubing with a molecular weight cut-off point of 3 kDa and 10 kDa in combination with a Soxhlet extractor were implemented in the purification of the nanoparticulate samples.

Mass Spectrometry. Electrospray mass spectra were obtained on Agilent 6120 and Waters LCT Premier instruments operating in positive or negative ion mode with methanol or dichloromethane as the carrier solvent.

FTIR. FTIR spectra were recoded on Bruker Tensor 27 and Bio-Rad FTS-6000 infrared spectrophotometers in the 600-4000 cm^{-1} range.

pH Measurements. All pH measurements were performed using a Jenway 3320 pH meter attached to a Sigma-Aldrich micro pH combination electrode, calibrated using pH 4.00 ± 0.02, 7.00 ± 0.02 and 10.00 ± 0.02 buffer solutions provided by Sigma-Aldrich. Diluted aqueous solutions of either NaOH and HCl or, where required, NaOD and DCl in D_2O were used for pH adjustments. For measurements in D_2O, the pD was calculated from the following relation: $pD = pH_{reading} + 0.41$, where $pH_{reading}$ is the pH measured with a glass electrode.[162]

UV-Spectroscopy. UV-Vis absorption spectra were recorded on a UV PC-2401 Shimadzu instrument in quartz cuvettes (1 mL, 10 mm). UV-vis data are referenced against a blank spectrum of ultrapure water prior to each set of measurements and were obtained in an absorbance mode (200-800 nm).

Dynamic Light Scattering. Dynamic light scattering and ζ-potential assessments of nanoparticles or polymers with a concentration of 0.5 mg/mL were performed on a Zetasizer Nano Malvern instrument at 20 °C. Prior to measurements, the samples were dried and redispersed either in ultrapure H_2O or in various buffer solutions (*i.e.* ethanolamine (pH 10.0), phosphate (pH 6.5, 6.8, 7.4 and 8.0),

HEPES (pH 6.8 and 7.4), MES (pH 6.0), acetate (pH 5.0) and formate (pH 4.0)). The hydrodynamic diameter and polydispersity index (PdI) were determined after three repetitions were obtained with a 532 nm laser. The scattered light was detected at an angle of 173°. The measured autocorrelation functions were implemented to obtain a second-order cumulant fit of the diffusion coefficient, which was then inserted into the Stokes-Einstein equation to calculate the hydrodynamic diameter.[192]

TEM Imaging. TEM images were taken at a voltage of 200 kV at the Research Complex at Harwell with a JEOL JEM-2100 microscope. Samples were prepared on a formvar/carbon-coated 300-mesh copper grid by leaving a droplet of the nanoparticle suspension to dry for a few hours. The image analysis was carried out using the ImageJ software tool.

Thermogravimetric Analysis. Thermogravimetric analyses of dried nanoparticle samples (ca. 30 mg) placed in a ceramic specimen holder were performed either on a Netzsch STA 409 PC/PG or on a Mettler Toledo TGA/DSC 1 System. The temperature was increased at a rate of 5 °C/min from RT to 800 °C under an inert N_2 atmosphere.

BET Measurements. Nitrogen sorption isotherms were measured at 77 K with a Micromeritics TriStar II instrument. Before measurements, dry samples (ca. 30-60 mg) were vacuum degassed overnight at 150 °C on a Flow Prep instrument. MicroActive for TriStar II Plus software was used to carry out the calculations of pore size distributions determined by the Barrett, Joyner and Halenda (BJH) approach,[193] as well as surface areas (S_{BET}) calculated with a multipoint BET method.[194]

NMR. ^{1}H, ^{13}C and ^{19}F NMR spectra were recorded in commercially available deuterated solvents from Sigma-Aldrich on Bruker-400 (^{1}H at 399.96 MHz,

^{13}C at 100.57 MHz, ^{19}F at 376.34 MHz) and Bruker-500 (^{1}H at 499.77 MHz, ^{13}C at 125.67 MHz, ^{19}F at 470.25 MHz) spectrometers.

Phantom Preparation, ^{1}H NMR Relaxation Time Measurements and Relaxivity Determination. The preliminary measurements of T_1 and T_2 relaxation times of ^{1}H nucleus in ultrapure water containing Gd^{3+}-DOTA doped nanoparticles, which are not reported in this work, were performed in capillaries in order to reduce the ^{1}H NMR signal overflow at 298 K at 300 MHz on Varian as well as at 400 MHz and 500 MHz on Bruker Avance NMR spectrometers. Shimming was performed prior to each experiment in order to minimise the B_0 field inhomogeneity. After the 90° pulse calibration, T_1 was obtained by using the inversion recovery NMR pulse sequence, which inverts the equilibrium magnetisation by a 180° pulse along the z-axis and then measures the exponential recovery of the magnetisation component M_z during variable delays τ. The observable magnetisation is created by the final 90° pulse, which turns M_z into the xy-plane, followed by the acquisition time. The most well fitted plot of $M_z(\tau)$ obtained by repeated experiments with variable τ allows the calculation of T_1 by implementing Eq. (1.10) reported on P. 10. While Varian automatically represents the fitted results, Bruker's TopSpin software obtains a 1D spectrum for each τ value stored in a 2D data set, which can be further baseline corrected and later integrated and fitted either within TopSpin or with Bruker's Dynamics Centre software. T_2, on the other hand, was obtained by the Carr-Purcell-Meiboom-Gill (CPMG) sequence, which changes the equilibrium magnetisation by a 90° pulse along the x-axis into the xy-plane. A sequence of 180° pulses along the y-axis refocuses the signal by spin echoes. The exponential decay of the echo amplitude $M_{xy}(\tau)$ is a result of the effective T_2, which can be calculated by Eq. (1.5) on P. 4 after an exponential decay fit is found by choosing a suitable variable delay time τ.

The reported measurements of T_1 and T_2 relaxation times of the ^{1}H nucleus were performed in blue tag sealed 0.2 mL syringes in either ultrapure water or buffer

solutions (as outlined in the Dynamic Light Scattering Section on P. 160) placed in a 3D-printed holder. The amount of Gd (usually around 0.002-0.1 mM) incorporated into the nanoparticles was determined by either ICP-MS or BMS methods as described in the next section. Either two or three different batches of the same sample were prepared and evaluated. For each batch, three relaxation time points at different Gd concentrations were recorded. The measurements and MRI image acquisitions were performed by Dr. Alexandr A. Khrapitchev at 293 K using a horizontal bore Varian at 4.7 T and 7.0 T as well as an Agilent Technologies MR spectrometer at 9.4 T using a spin echo multi slice (SEMS) diffusion sequence with a slice thickness of 2 mm, a matrix size of 64 x 64 and a field of view of 32 mm x 32 mm.

Proton longitudinal and transverse relaxivity values were calculated from the slope of a linear regression of R_i ($\frac{1}{T_i}, i = 1, 2$) versus Gd concentration with an intercept of the diamagnetic contribution $\frac{1}{T_{i,dia}}$ being fitted to the data as given by Eq. (1.6) on P. 6.

Procedure for Gadolinium Concentration Measurement. The Gd concentration was determined either by Viridian Partnership with inductively coupled plasma mass spectrometry (ICP-MS) or with bulk magnetic susceptibility (BMS) shift measurements. For the latter, 1 % TMS in $CDCl_3$ was placed into a capillary, which was sealed and placed into an NMR tube containing either only diamagnetic 1 % *tert*-butyl alcohol dissolved in D_2O or a paramagnetic Gd^{3+} sample of interest dissolved in a 1 % *tert*-butyl alcohol and D_2O mixture. The ^1H NMR chemical shift of the *tert*-butyl alcohol signal in the presence of a paramagnetic metal corresponds to the bulk magnetic susceptibility shift Δ_X. The procedure has been reported in detail in Ref. [195], and the concentration could be determined via the following equation:

$$\Delta_X = \frac{4\pi[Gd]s}{T}\left(\frac{\mu_{eff}}{2.84}\right)^2 \cdot 10^3, \tag{7.1}$$

where μ_{eff} is the effective magnetic moment, which in this case equals 7.94 for Gd^{3+}, s refers to the shape and location of the sample in the magnetic field, $[Gd]$ denotes the concentration of Gd^{3+} in the sample and T is the absolute temperature.

^{19}F NMR Relaxation Analysis. ^{19}F NMR longitudinal and transverse relaxation times were measured at a temperature of 298 K using the inversion recovery and CPMG techniques, respectively, without proton decoupling, on Varian-300, Bruker-400 and Bruker-500 spectrometers operating at respective fluorine frequencies of 282 MHz, 376 MHz and 470 MHz. The relaxation times measured by ^{19}F NMR are detailed in Fig. 6.3 and Fig. 6.11 on P. 142 and P. 153, respectively, as well as in Tab. 6.1 on P. 143 and in App. B.43 on P. 228. The unreported preliminary results were also measured by ^{19}F NMR. Although these samples were prepared multiple times for characterisation purposes, all ^{19}F NMR measurements were performed only once. With the exception of these samples, all other reported ^{19}F T_1 and T_2 measurements were performed by Dr. Alexandr A. Khrapitchev using a horizontal bore Varian MR scanner at 7.0 T. For the acquisition of MRI images, a gradient echo multi slice (GEMS) sequence mostly with a slice thickness (Thk) of 5 or 10 mm and a flip angle of 90° were implemented. Samples with concentrations ranging from 2-30 mg/mL were dispersed in ultrapure water or buffer solutions and pipetted into Eppendorf tubes, which was the reason why air bubbles always remained visible. Spectral width (sw) and line broadening factor (lb) are mostly set to 100 kHz and 100, respectively, unless otherwise stated. The matrix size, the repetition time (TR), the echo time (TE), the field of view (FOV) and the number of scans (nt) usually vary from sample to sample, which is always noted in the description of an MRI image.

Variable-Temperature ^{17}O NMR. ^{17}O NMR measurements were performed using a Bruker-500 spectrometer. A Bruker VT-1000 temperature control unit was used to stabilise the temperature, which was precalibrated with ethylene glycol and

methanol for application at high and low temperatures (with 300 K being the breaking point), respectively. The temperature was measured by a substitution technique. Aqueous solutions of the nanoparticles with incorporated paramagnetic complexes contained 2.8 % of the ^{17}O isotope (CortecNet, France). The ^{17}O NMR signal was locked on D_2O sealed in a glass capillary fitted into a 10 mm NMR tube. The BMS corrections were implemented to the reported chemical shifts. Longitudinal and transverse relaxation rates were obtained by the inversion recovery and Carr-Purcell-Meiboom-Gill spin echo techniques, respectively.

^{1}H-^{1}H DQ MAS. The back-to-back (BABA) sequence[196] was selected for excitation and reconversion of DQ coherences under 40 kHz MAS. BABA pulse lengths were set to either 2.3 μs, 2.5 μs or 5000 μs, the recycle delay accounted for 5 s. 32 single experiments with steps of 70 ms and a phase increment of the excitation pulses of 45° were conducted to detect the double-quantum spectrum.

Solid-State NMR Measurements. Solid-state NMR analyses of ^{13}C and ^{29}Si nuclei were both referenced to tetramethylsilane, while ^{19}F NMR spectra were externally referenced to Teflon, whereby the Teflon resonance was taken to be at -123.2 ppm, on a scale where $\delta_{CFCl_3} = 0$ ppm. Solid state ^{29}Si, ^{13}C and ^{19}F NMR spectra were recorded at 79.5 MHz, 100.6 MHz and 376.2 MHz, respectively, on a Bruker Avance 3HD spectrometer operating at a proton frequency of 400.1 MHz and using either the cross-polarisation pulse sequence (CP/MAS, 10k number of scans, a contact time of 3-10 ms, a recycle delay of 10 s) or the direct-polarisation technique (DP/MAS, 6k number of scans, a recycle delay of 10 s) under magic-angle spinning and proton dipolar decoupling. The experiments were conducted at the MAS speed of 5 kHz and at a sweep width of 1000 kHz. Samples do not need any special treatment, apart from quick drying, before being packed into a 4 mm zirconia rotor and sealed for the solid-state NMR analysis.

Luminescence Measurements. Emission spectra were obtained on a Cary Eclipse spectrometer (phosphorescence mode, $\lambda_{ex} = 394$ nm, a decay time of 0.02 ms, a delay time of 0.1 ms, a gate time of 5 ms, a slit size of 10 nm). Suspensions with Eu^{3+}-DOTA complexes incorporated into nanoparticles were prepared in H_2O and pipetted into a quartz cuvette with a path length of 1 cm. A 10 mM phosphate solution was then titrated into the Eu^{3+}-containing solution, while recording the response by phosphorescence spectra. The area under each Eu^{3+} transition peak was used to determine the binding association constant using the Dynafit software.

To determine the hydration numbers, lifetime measurements in H_2O or D_2O were carried out using a Horiba Fluorolog 3 spectrometer with $\lambda_{ex} = 394$ nm, a slit size of 14 nm and a delay time of 0.05 ms, whereby the sample was excited by a short pulse of light, followed by monitoring the intensity of light I emitted during the set delay yielding a decay curve that was fitted to the following function:

$$I = A_0 + A_1 e^{-kt}, \tag{7.2}$$

where A_0 is the intensity after completion of the decay, A_1 is the pre-exponential factor and k is the decay rate constant for the excited state, which can be translated by inversion into the luminescence lifetime τ.[79]

Procedure for Cleaving Grafted Polymer Brushes from Particles for MALDI-TOF Measurements. In this work, tetrabutylammonium bromide instead of the usually implemented trioctylmethylammonium chloride[197] was used as a phase-transfer agent to transport HF from the aqueous to the organic phase. Firstly, the particles were dissolved in H_2O (1.61 mL) and toluene (2.00 mL). After the addition of tetrabutylammonium bromide (0.05 mmol), HF (48 % aq, 0.39 mL) was added and the mixture was stirred for 2 hours at RT. After neutralisation with Na_2CO_3 (aq), the polymers dispersed in the organic phase were subjected to

MALDI-TOF measurments.

MALDI-TOF Measurements. Samples were analysed with a Waters MALDI Micro MX mass spectrometer operated in the reflectron mode. 2,5-dihydroxy benzoic acid matrix was used for MALDI-TOF analysis of polymers/oligomers, while trans-2-[3-(4-*t*-butylphenyl)-2-methyl-2-propenylidene]malononitrile (DCTB) was used for Gd^{3+}-doped polymers/oligomers.

Transmetallation Study with $MgCl_2$. The transmetallation study was adapted from a procedure described by Ref. [120] using zinc as the competing ionic species. Gd^{3+}-DOTA-functionalised MSNs (**MSN-Gd·L**$_1$ and **MSN-Gd·L**$_2$) were stirred with or without zinc chloride (1 equiv to the Gd amount determined by ICP-MS) in phosphate buffer (pH 7.4) at 37 °C for 48 hours. The proton relaxation times were then measured at 7.0 T on a Varian Mercury 300 MHz NMR spectrometer.

Free Gd^{3+} Detection with Arsenazo(III). Procedures for the determination of free Gd^{3+} ions can be performed by UV-vis spectroscopic determination of Gd^{3+} complexed with either xylenol orange or arsenazo(III) (2,7-bis(arsonophenylazo)-1,8-dihydroxy-naphthalene-3,6-disulphonic acid).[198] In this report, colorimetric studies were performed with arsenazo(III) in water in 1:1 ratio to gadolinium as determined by ICP-MS. The absorbance spectrum of nanoparticles was taken as a baseline before arsenazo(III) (10^{-6} M) was added.

Cell Culture and Confocal Imaging.[165] Human cervical carcinoma HeLa cells grown in 2 mL Dulbecco's Modified Eagle Medium (DMEM), which was supplemented with 10 % fetal bovine serum and 1 % penicillin-streptomycin, were plated onto polycarbonate glass-bottom petri dishes (FluoroDish) for 24 h at 37 °C in a humidified incubator in an atmosphere of 5 % CO_2 and 95 % room air. Next, the culture medium was disposed and the cells were washed lightly twice with Dulbeco's

phosphate-buffered saline (PBS). The particles suspended in 1:10 PBS:DMEM mixture were then pre-warmed to 37 °C, added to the cell dishes and incubated for 24 h. The cells were then fixed with 4 % paraformaldehyde and labelled stepwise with fluorescent dyes (LysoTracker Red and Hoechst 33342) before being imaged with a Nikon Eclipse Ti-E inverted microscope equipped with an A1 confocal laser system, Plan Apo oil immersion 100x objective and Melles Griot diode pumped solid state lasers (DPSS) at 404 nm, 488 nm, 561 nm and 637 nm.

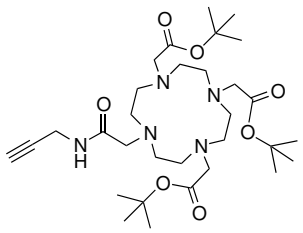
Cytotoxicity. *In vitro* cytotoxicity was performed using Alamar Blue assay following the manufacturer protocol, while the fluorescence was monitored using an excitation wavelength of 540 nm and an emission wavelength of 590 nm. This assay indirectly measures the total number of viable cells by implementing a fluorometric growth indicator reazurin that changes colour and fluoresces upon chemical reduction, and is thus able to quantitatively measure the proportion of damaged or non-viable cells to the healthy ones.[199]

7.2 Syntheses

All commercial reagents were used as received unless otherwise noted. The NMR chemical shifts of multiplets are stated in the range of their occurrence. All chemical shifts are given in ppm. Values of the coupling constant J are given in Hz; the following abbreviations are used for the description of NMR spectra: singlet (s), broad singlet (bs), doublet (d), triplet (t), quartet (q), doublet of doublets (dd), doublet of triplets (dt) and multiplet (m).

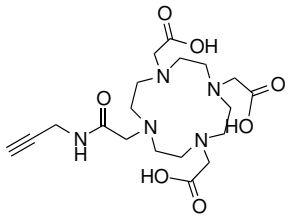
Ln·$\mathbf{L_2}$. Propargyl monoamide Ln^{3+}-DOTA derivative was prepared after a modified procedure described by Mindt *et al.* [125] Briefly, *t*Bu-protected DOTA-NHS (0.05 mmol) was dissolved in dry DCM (1.5 mL). *N,N*-diisopropylethylamine (0.15

mmol) and propargyl amine (0.1 mmol) pre-dissolved in dry DCM were subsequently added to the reaction mixture. The mixture was stirred at RT for 4 h and washed with citric acid solution and water. After drying over $MgSO_4$, the product was purified by neutral alumina chromatography with a DCM/MeOH mixture. Yield: 20 %, ^{1}H NMR (400 MHz, Chloroform-*d*): δ_H 5.66 (s, 1H), 3.92 (dd, J = 5.8 Hz, 2.5 Hz, 2H), 3.23 (s, 1H), 3.19 (s, 3H), 3.06 (s, 2H), 2.82 (s, 1H), 2.64 (s, 14H), 2.10 (s, 3H), 1.47 (s, 9H), 1.46 (s, 18H); ESI/MS$^+$ m/z 609.4 [M], 610.5 [M+H]$^+$, 632.4 [M+Na]$^+$.



Tri-*tert*-butyl 2,2',2"-(10-(2-oxo-2-(prop-2-yn-1-ylamino)ethyl)-1,4,7,10-tetraazacyclododecane-1,4,7-triyl)triacetate

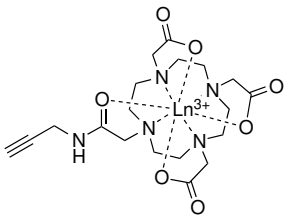
DOTA(tBu)$_3$-propargyl amide was then dissolved in a DCM/TFA (4:1) mixture and stirred at RT for 18 h. Removal of the volatile components was proceeded by drying with rotavap and redispersing the product with solvents that form aezotropes with trifluoroacetic acid, such as acetone, toluene and water. Further extraction with DCM/H_2O yielded an orange oil (yield: 80 %). ESI/MS$^+$ m/z 464.2 [M+Na]$^+$.



2,2',2"-(10-(2-oxo-2-(prop-2-yn-1-ylamino)ethyl)-1,4,7,10-tetraazacyclododecane-1,4,7-triyl)triacetic acid

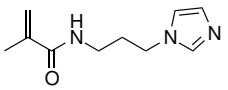
The deprotected DOTA-propargyl amide product was dissolved in water before $LnCl_3{\cdot}6H_2O$ (0.8 equiv) was added, the pH was adjusted to 6.5 with NaOH and the reaction mixture was stirred at 50 °C overnight. Ln^{3+}-DOTA propargyl monoamide derivative (**Ln**·$\mathbf{L}_2$) was purified several times by precipitation of free Ln^{3+} at high

pH. The presence of free Ln^{3+} was followed by mass spectrometry. ESI/MS$^+$ m/z 619.1 [M(Gd^{3+})+Na]$^+$ or 614.1 [M(Eu^{3+})+Na]$^+$.



Ln·L$_2$

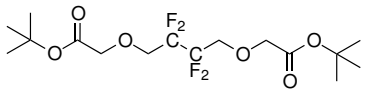
HIMA. *N*-(3-(imidazol-1-yl)propyl)methacrylamide was prepared after a modified method reported in Ref. [200]. 1-(3-Aminopropyl)imidazole (40 mmol) was dissolved in 10 mL dry DMF and placed on ice. Next, methacryoyl chloride (40 mmol) was added dropwise. When the addition was completed, the mixture was left stirring overnight at RT. The product was then precipitated into EtOAc, and after rotavap evaporation dissolved in aqueous sodium bicarbonate solution and extracted into DCM. After drying, the product was further purified by neutral alumina gel column chromatography and eluted with a gradient starting from 100 % DCM to 10 % MeOH in DCM to yield a pale yellow oil (30 %). ^{1}H NMR (400 MHz, Chloroform-*d*): δ_H 7.46 (s, 1H), 7.02 (s, 1H), 6.90 (s, 1H), 6.73 (bs, 1H), 5.66 (s, 2H), 5.26 (s, 2H), 3.90 (dt, J = 17.4 Hz, 7.0 Hz, 2H), 3.15 (q, J = 6.5 Hz, 1H), 1.96 (m, 2H), 1.65 (s, 3H); ^{13}C NMR (400 MHz, Chloroform-*d*): δ_C 169.02, 139.83, 136.97, 129.19, 119.52, 118.91, 44.62, 36.70, 25.12, 18.17. ESI/MS$^+$ m/z 194.2 [M+H]$^+$.



***N*-(3-(1H-imidazol-1-yl)propyl)methacrylamide**

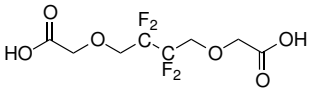
F$_4$Ac. To obtain **2,2'-((2,2,3,3-tetrafluorobutane-1,4-diyl)bis(oxy))diacetic acid**, 2,2,3,3-tetrafluoro-1,4-butanediol (2 mmol) was first dissolved in 5 mL dry THF under N_2 atmosphere. After the flask was placed on ice, sodium hydride (3 equiv) was slowly added, the temperature was increased to RT and the mixture was

stirred for 1 h prior to dropwise addition of *tert*-butyl bromoacetate (2.2 equiv) on ice. The reaction was followed by TLC. As soon as it was complete, it was quenched with water. The product was extracted with brine and washed with water before being purified on a silica column with a 9:1 hexane/ethyl acetate mixture (+1 % TEA) to yield a colourless oil (70 %). ^{1}H NMR (300 MHz, Chloroform-d): δ_H 4.07-3.84 (m, 8H), 1.37 (q, J = 1.8 Hz, 18H); ^{19}F NMR (283 MHz, Chloroform-d): δ_F -122.43 (t, J = 14.3 Hz). ESI/MS$^+$ m/z 413.2 $[M+Na]^+$.



Di-*tert*-butyl 2,2'-((2,2,3,3-tetrafluorobutane-1,4-diyl)bis(oxy))diacetate

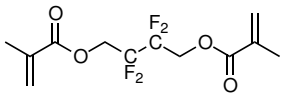
For *tert*-butyl ester deprotection, the product was dissolved in toluene prior to dropwise addition of aqueous phosphoric acid (85 wt %, 30 mmol). After stirring at RT for 6 hours, the mixture was dissolved in water and extracted with ethyl acetate in order to yield 2,2'-((2,2,3,3-tetrafluorobutane-1,4-diyl)bis(oxy))diacetic acid (**F_4Ac**, pink solid, 90 %). ^{1}H NMR (300 MHz, Methanol-d_4): δ_H 4.25-4.20 (m, 4H), 4.16-4.01 (m, 4H); ^{19}F NMR (283 MHz, Methanol-d_4): δ_F -122.43 (t, J = 14.3 Hz). ESI/MS$^-$ m/z 279.1 $[M]^-$.



2,2'-((2,2,3,3-tetrafluorobutane-1,4-diyl)bis(oxy))diacetic acid

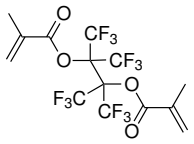
F_4M_2. For the synthesis of **2,2,3,3-tetrafluorobutane-1,4-diyl bis(2-methylacrylate)**, 2,2,3,3-tetrafluoro-1,4-butanediol (2.2 mmol) was dissolved in 10 mL dry DCM under N_2 atmosphere. After the addition of TEA (3.2 equiv) and methacryloyl chloride (3.0 equiv), the mixture was refluxed at 65 °C for 6 hours. The product was extracted in DCM with 5 % citric acid aqueous solution (3x), 5 % sodium bicarbonate solution (3x) and H_2O (3x). The organic layer was then dried over $MgSO_4$. The extracted product was purified by a silica column with a hex-

ane/ethyl acetate (8:1) mixture to yield an orange oil (60 %). ^{1}H NMR (300 MHz, Chloroform-*d*): δ_H 6.14 (s, 2H), 5.61 (d, J = 2.6 Hz, 2H), 4.55 (tt, J = 11.7 Hz, 2.8 Hz, 4H), 1.90 (m, 6H); ^{19}F NMR (283 MHz, Chloroform-*d*): δ_F -121.05 (dd, J = 25.4 Hz, 3.9 Hz, 4F). ESI/MS$^+$ m/z 299.1 [M+H]$^+$.



2,2,3,3-tetrafluorobutane-1,4-diyl bis(2-methylacrylate)

$\mathbf{F_{12}M_2}$. In order to synthesise **1,1,1,4,4,4-hexafluoro-2,3-bis(trifluoromethyl)butane-2,3-diyl bis(2-methylacrylate)**, 2,2,3,3-tetrafluoro-1,4-butanediol (2.2 mmol) was dissolved in 10 mL dry acetonitrile under N_2 atmosphere in a flask placed on ice. After dropwise addition of TEA (3.2 equiv) and methacryloyl chloride (3.0 equiv), the mixture was stirred at 0 °C for 1 hour and at reflux for 6 hours. The product was extracted in DCM with 5 % citric acid aqueous solution (3x), 5 % sodium bicarbonate solution (3x) and H_2O (3x). The organic layer was then dried over $MgSO_4$ and the product was purified by a silica column with a heptane/cyclohexane (8:1) mixture to yield a colourless oil (8 %). ^{1}H NMR (300 MHz, Chloroform-*d*): δ_H 6.15 (p, J = 1.0 Hz, 2H), 5.75 (dt, J = 2.6 Hz, 1.0 Hz, 2H), 1.89 (m, 6H); ^{19}F NMR (283 MHz, Chloroform-*d*): δ_F -64.28. ESI/MS$^+$ m/z 471.2 [M+H]$^+$, 493.2 [M+Na]$^+$.

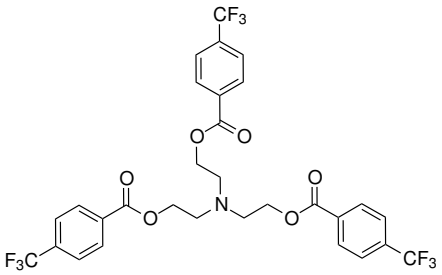


1,1,1,4,4,4-hexafluoro-2,3-bis(trifluoromethyl)butane-2,3-diyl bis(2-methylacrylate)

$\mathbf{T_0F_{9a}}$, $\mathbf{T_0F_{18b}}$. A 50 mL round bottom flask was charged with triethanolamine, *N'*-dicyclohexyl carbodiimide (3.3 equiv), 4-dimethylaminopyridine (0.03 equiv) and dry MeCN (20 mL). For $\mathbf{T_0F_{9a}}$ and $\mathbf{T_0F_{18b}}$, 4-(trifluoromethyl)benzoic

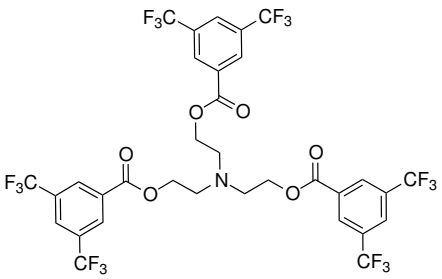
acid (3.2 equiv) and 3,5-bis(trifluoromethyl)benzoic acid (3.2 equiv), respectively, were reacted with the reaction mixture overnight at RT. Both products were purified by filtration, extraction (with 4 % HCl, 5 % $NaHCO_3$ and H_2O) and purification through a silica column with a hexane/ethyl acetate mixture (8:1 and 10:1 for $\mathbf{T_0F}_{9a}$ and $\mathbf{T_0F}_{18b}$, respectively). Yield: 50-60 %.

$\mathbf{T_0F}_{9a}$: ^{1}H NMR (400 MHz, Chloroform-d): δ_H 7.93 (d, J = 8.2 Hz, 6H), 7.49 (d, J = 8.2 Hz, 1H), 4.38 (t, J = 5.7 Hz, 6H), 3.00 (t, J = 5.7 Hz, 6H). ^{19}F NMR (376 MHz, Chloroform-d): δ_F -63.27; ^{13}C NMR (101 MHz, Chloroform-d): δ_C 165.19, 134.44 (q, J = 32.7 Hz), 133.05, 129.82, 127.66-118.87 (q, 273.4 Hz), 125.32 (q, J = 3.8 Hz), 63.31, 53.35. ESI/MS$^+$ m/z 666.2 $[M+H]^+$.



Nitrilotris(ethane-2,1-diyl) tris(4-(trifluoromethyl)benzoate)

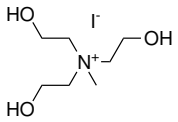
$\mathbf{T_0F}_{18b}$: ^{19}F NMR (376 MHz, Chloroform-d): δ_F -64.49. ^{1}H NMR (400 MHz, Chloroform-d) δ_H 8.27 (s, 6H), 7.88 (s, 3H), 4.42 (t, J = 5.8 Hz, 6H), 3.04 (t, J = 5.9 Hz, 6H); ^{13}C NMR (101 MHz, Chloroform-d): δ_C 163.60, 132.10 (q, J = 34.1 Hz), 132.00, 129.48, 126.36 (m), 122.71 (q, J = 272.7 Hz), 63.80, 53.45. ESI/MS$^+$ m/z 870.1 $[M+H]^+$.



Nitrilotris(ethane-2,1-diyl) tris(3,5-bis(trifluoromethyl)benzoate)

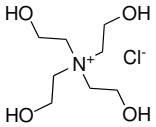
T_3, T_4, T_6. Synthesis of quaternary ammonium salts was performed by loading triethanolamine into a Schlenk tube with a Young valve (the same products obtained by different synthetic procedures were reported in Ref. [201] and [202]). After the addition of either methyl iodide, chloroethanol or 1,10-dibromodecane, the reaction was carried out at either 40 °C, 70 °C or 80 °C, respectively, under N_2. Dry DCM was used for the synthesis of $\mathbf{T}_3$, while no solvents were used for the preparation of $\mathbf{T}_4$ and $\mathbf{T}_6$. The products were washed with acetone and recrystalised several times. Yield: 60-80 %.

$\mathbf{T}_3$: ^{1}H NMR (400 MHz, Deuterium Oxide): δ_H 4.14-3.94 (m, 6H), 3.69-3.48 (m, 6H), 3.21 (s, 3H); ^{13}C NMR (101 MHz, Deuterium Oxide): δ_C 73.45-58.58 (m), 55.30, 51.88-48.75 (m). ESI/MS$^-$ m/z 417.9 $[M+2I]^-$, ESI/MS$^+$ m/z 164.2 $[M]^+$.



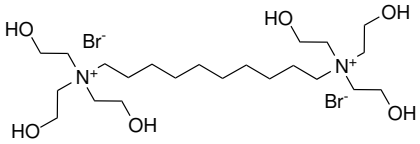
2-hydroxy-*N*,*N*-bis(2-hydroxyethyl)-*N*-methylethan-1-aminium iodide

$\mathbf{T}_4$: ^{1}H NMR (400 MHz, Deuterium Oxide): δ_H 3.99 (s, 8H), 3.66 (s, 8H). ^{13}C NMR (101 MHz, Deuterium Oxide): δ_C 66.75-58.98 (t, 2.5 Hz), 55.00. ESI/MS$^-$ m/z 264.0 $[M+2Cl]^-$, ESI/MS$^+$ m/z 194.2 $[M]^+$.



Tetrakis(2-hydroxyethyl)ammonium chloride

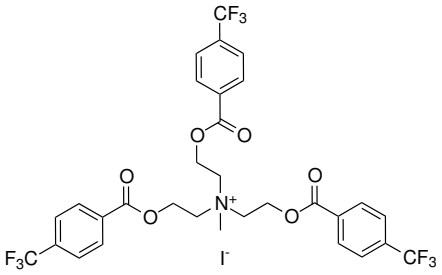
$\mathbf{T}_6$: ^{1}H NMR (400 MHz, Deuterium Oxide): δ_H 3.96 (t, J = 4.9 Hz, 12H), 3.72-3.49 (m, 12H), 3.47-3.35 (m, 4H), 1.69 (s, 4H), 1.26 (d, J = 15.0 Hz, 12H); ^{13}C NMR (101 MHz, Deuterium Oxide): δ_C 61.02, 60.89, 54.96, 28.22, 28.02, 25.35, 21.35. ESI/MS$^-$ m/z 677.1 $[M+3Br]^-$, ESI/MS$^+$ m/z 219.2 $[M/2]^+$, 519.3 $[M+Br]^+$.



N^1,N^1,N^1,N^{10},N^{10},N^{10}-hexakis(2-hydroxyethyl)decane-1,10-diaminium bromide

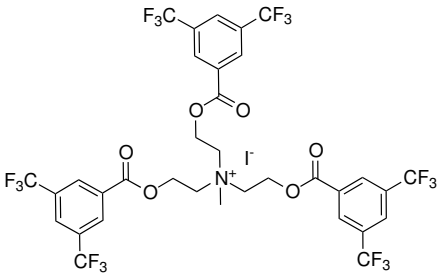
T_3F_{9a}, T_3F_{18b}, T_4F_{12a}, T_4F_{24b}, T_6F_{18a}, T_6F_{36b}. For the synthesis of fluorinated quaternary ammonium salts, $\mathbf{T}_3$ was dissolved in dry MeCN, while $\mathbf{T}_4$ and $\mathbf{T}_6$ were dissolved in dry DMF. To reaction mixtures containing either $\mathbf{T}_3$, $\mathbf{T}_4$ or $\mathbf{T}_6$, either 3.6, 4.3 or 8.5 equivalents of triethylamine (or diethylaminomethyl-polystyrene), respectively, were added under N_2 atmosphere, sonicated and placed on ice. After everything was dissolved, either 3.5, 4.2 or 8.2 equivalents of either 4-(trifluoromethyl)benzoyl chloride or 3,5-bis(trifluoromethyl)benzoyl chloride were added dropwise and the reaction proceeded overnight at RT. When 4-(trifluoromethyl)benzoyl chloride was implemented, either $\mathbf{T}_3\mathbf{F}_{9a}$, $\mathbf{T}_4\mathbf{F}_{12a}$ or $\mathbf{T}_6\mathbf{F}_{18a}$ were formed, while addition of 3,5-bis(trifluoromethyl)benzoyl chloride yielded either $\mathbf{T}_3\mathbf{F}_{18b}$, $\mathbf{T}_4\mathbf{F}_{24b}$ or $\mathbf{T}_6\mathbf{F}_{36b}$. Multiple recrystallisations from various solvent mixtures (*e.g.* DCM/hexane and ether/ethyl acetate among others) afforded pure products. Yield: 30-50 %.

$\mathbf{T}_3\mathbf{F}_{9a}$: ^{1}H NMR (400 MHz, Methanol-d4): δ_H 8.19 (s, 1H), 7.72 (s, 6H), 5.01 (s, 2H), 4.32 (s, 1H), 3.61 (s, 3H); ^{19}F NMR (376 MHz, Methanol-d4): δ_F -64.71. ESI/MS$^-$ m/z 934.0 $[M+2I]^-$, ESI/MS$^+$ m/z 680.2 $[M]^+$.



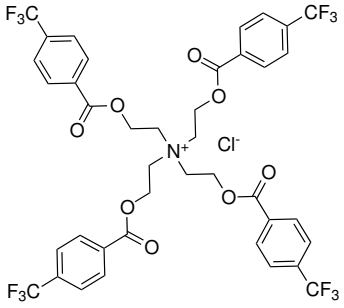
***N*-methyl-2-((4-(trifluoromethyl)benzoyl)oxy)-*N*,*N*-bis(2-((4-(trifluoromethyl)benzoyl)oxy)ethyl)ethan-1-aminium iodide**

$\mathbf{T_3F_{18b}}$: ^{1}H NMR (400 MHz, Methanol-d4): δ_H 8.28 (d, J = 1.6 Hz, 3H), 8.10 (s, 6H), 4.11-3.81 (m, 6H), 3.78-3.53 (m, 6H), 3.17 (s, 3H); ^{19}F NMR (376 MHz, Methanol-d4): δ_F -62.76. ESI/MS$^-$ m/z 1138.2 $[M+2I]^-$, ESI/MS$^+$ m/z 884.0 $[M]^+$.



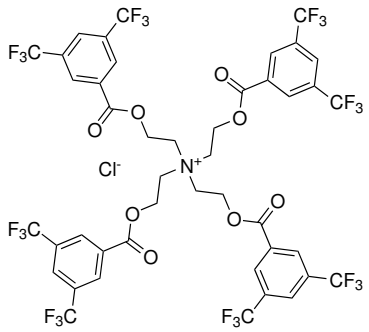
2-((3,5-bis(trifluoromethyl)benzoyl)oxy)-*N*,*N*-bis(2-((3,5-bis(trifluoromethyl)benzoyl)oxy)ethyl)-*N*-methylethan-1-aminium iodide

$\mathbf{T_4F_{12a}}$ ^{1}H NMR (400 MHz, Methanol-d4): δ_H 8.08 (s, 4H), 7.64 (s, 4H), 4.91 (bs, 8H), 4.47-4.07 (bs, 8H); ^{19}F NMR (376 MHz, Methanol-d4): δ_F -64.81; ^{13}C NMR (101 MHz, Methanol-d4): δ_C 163.02, 131.50, 129.45, 126.71, 125.66-117.71 (m), 58.70 (d, J = 41.5 Hz), 7.82. ESI/MS$^-$ m/z 954.0 $[M+2Cl]^-$, ESI/MS$^+$ m/z 882.2 $[M]^+$.



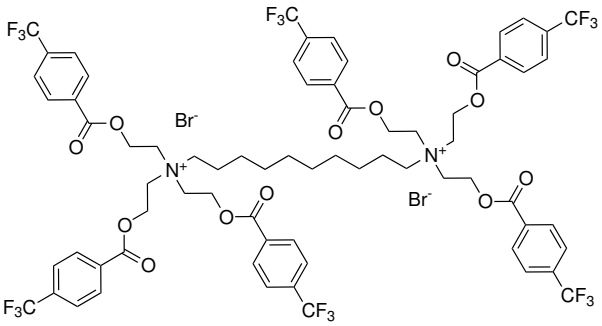
Tetrakis(2-((4-(trifluoromethyl)benzoyl)oxy)ethyl)ammonium chloride

$\mathbf{T_4F_{24b}}$: ^{1}H NMR (400 MHz, Methanol-d4): δ_H 8.38 (s, 8H), 8.15 (s, 4H), 4.96 (bs, 8H), 4.30 (t, J = 4.7 Hz, 8H); ^{19}F NMR (376 MHz, Methanol-d4): δ_F -64.54. ESI/MS$^-$ m/z 1224.0 $[M+2Cl]^-$, ESI/MS$^+$ m/z 1154.0 $[M]^+$.



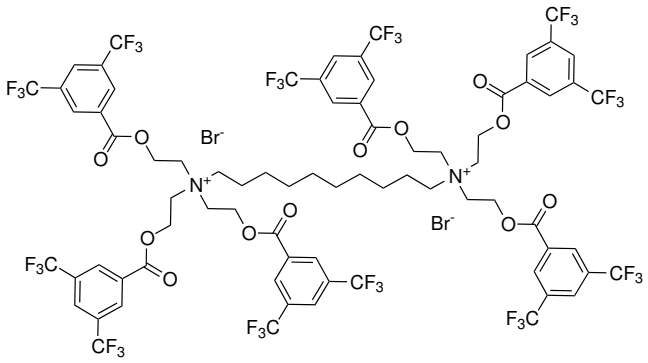
Tetrakis(2-((3,5-bis(trifluoromethyl)benzoyl)oxy)ethyl)ammonium chloride

$\mathbf{T}_6\mathbf{F}_{18a}$: ^{1}H NMR (400 MHz, Methanol-d4): δ_H 8.20 (s, 12H), 7.73 (s, 12H), 5.01 (s, 12H), 4.30 (s, 12H), 3.82 (s, 4H), 1.94 (s, 4H), 1.20 (d, J = 69.4 Hz, 12H). ^{19}F NMR (376 MHz, Methanol-d4): δ_F -64.64; ^{13}C NMR (101 MHz, Methanol-d4): δ_C 164.46, 134.27, 132.67-131.59 (m), 132.54, 129.98, 128.23-119.06 (m), 61.15, 58.17, 28.95 (d, J = 17.2 Hz), 25.99, 22.06. ESI/MS$^+$ m/z 735.2 $[M/2]^+$, 1549.4 $[M+Br]^+$.



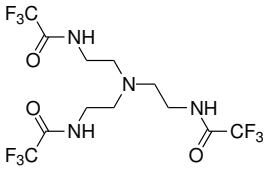
***N*^{1},*N*^{1},*N*^{1},*N*^{10},*N*^{10},*N*^{10}-hexakis(2-((4-(trifluoromethyl)benzoyl)oxy)ethyl)decane-1,10-diaminium bromide**

$\mathbf{T}_6\mathbf{F}_{36b}$: ^{1}H NMR (400 MHz, Methanol-d4): δ_H 9.26-8.17 (m, 12H), 8.15 (s, 6H), 3.88 (d, J = 4.9 Hz, 12H), 3.55 (dd, J = 6.1 Hz, 3.9 Hz, 12H), 3.50-3.33 (m, 4H), 1.71 (s, 4H), 1.22 (t, J = 7.3 Hz, 12H). ^{19}F NMR (376 MHz, Methanol-d4): δ_F -64.54. ESI/MS$^+$ m/z 939.0 $[M/2]^+$, 1959.1 $[M+Br]^+$.



***N*^{1},*N*^{1},*N*^{1},*N*^{10},*N*^{10},*N*^{10}-hexakis(2-((3,5-bis(trifluoromethyl)benzoyl)oxy)ethyl)decane-1,10-diaminium bromide**

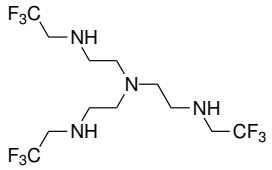
$\mathbf{T_0F_{9c}}$. Tris(2-aminoethyl)amine (ESI/MS$^+$ m/z 147.2 $[M+H]^+$) was dissolved in dry THF (15 mL) and mixed with $NaHCO_3$ (3.6 equiv). Trifluoroacetic anhydride (3.5 equiv) was then added dropwise and the mixture was stirred overnight at RT. The yield of *N,N',N"*-(nitrilotris(ethane-2,1-diyl))tris(2,2,2-trifluoroacetamide), which was purified by filtration, extraction with H_2O/DCM and recrystallisation, was about 70 %. ^{1}H NMR (400 MHz, Methanol-d4): δ_H 3.37 (d, J = 4.9 Hz, 6H), 2.74 (d, J = 6.6 Hz, 6H); ^{19}F NMR (376 MHz, Methanol-d4): δ_F -77.33. ^{13}C NMR (101 MHz, Methanol-d4): δ_C 157.87 (q, J = 37.0 Hz), 116.06 (q, J = 286.5 Hz), 52.29, 37.46. ESI/MS$^+$ m/z 435.1 $[M+H]^+$.



***N,N',N"*-(nitrilotris(ethane-2,1-diyl))tris(2,2,2-trifluoroacetamide)**

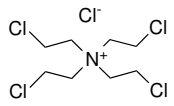
$\mathbf{T_0F_{9cRed}}$. **$\mathbf{T_0F_{9c}}$** was dissolved in dry THF and added dropwise to THF suspension containing lithium aluminium hydride. The temperature was raised from 0 °C to 70 °C, the reaction mixture was stirred for 2 hours and quenched with water and NaOH (aq). After filtration, 90 % of *N*^{1}-(2,2,2-trifluoroethyl)-*N*^{2},*N*^{2}-bis(2-((2,2,2-trifluoroethyl)amino)ethyl)ethane-1,2-diamine was obtained. ^{1}H NMR (400 MHz,

Methanol-d4): δ_H 3.22 (qd, J = 9.8 Hz, 3.6 Hz, 6H), 2.77 (t, J = 5.9 Hz, 6H), 2.59 (t, J = 6.0 Hz, 6H); ^{19}F NMR (376 MHz, Methanol-d4): δ_F -72.88; ^{13}C NMR (101 MHz, Methanol-d4): δ_C 125.81 (q, J = 278.1 Hz), 53.45, 49.87 (q, J = 31.2 Hz), 46.97. ESI/MS$^+$ m/z 393.2 $[M+H]^+$.



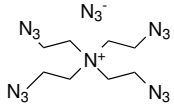
***N*^{1}-(2,2,2-trifluoroethyl)-*N*^{2},*N*^{2}-bis(2-((2,2,2-trifluoroethyl)amino)ethyl)ethane-1,2-diamine**

$\mathbf{T_4Cl_4}$. 8 equiv of thionyl chloride pre-dissolved in dry MeCN were added to $\mathbf{T}_4$ at 40 °C. The mixture was stirred for 3 hours before being washed by acetone and MeCN followed by recrystallisation. The resulting tetrakis(2-chloroethyl)ammonium chloride was obtained in 10 % yield. ^{1}H NMR (400 MHz, Deuterium Oxide): δ_H 5.11-4.57 (m, 8H), 4.24-3.72 (m, 8H). ESI/MS$^+$ m/z 268.0 $[M]^+$; ESI/MS$^-$ m/z 301.9 [M+Cl], 338.0 $[M+2Cl]^-$.



Tetrakis(2-chloroethyl)ammonium chloride

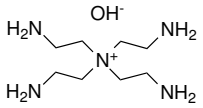
$\mathbf{T_4N_{3\text{-}4}}$. Tetrakis(2-chloroethyl)ammonium chloride was dissolved in dry DMF and stirred at 40 °C for 24 h upon addition of NaN_3. DMF was then removed under vacuum, the product was washed with diethyl ether and recrystallised yielding pure tetrakis(2-azidoethyl)ammonium chloride (yield: 80 %). ESI/MS$^+$ m/z 294.2 $[M]^+$.



Tetrakis(2-azidoethyl)ammonium azide

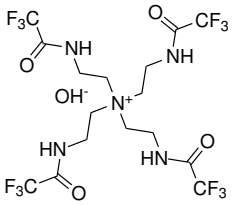
$\mathbf{T_4(NH_2)_4}$. Tetrakis(2-azidoethyl)ammonium chloride was dissolved in dry THF

and added dropwise to a THF suspension containing lithium aluminium hydride under N_2 flow. After 2 h of stirring at 70 °C, the reaction mixture was cooled on ice and quenched with H_2O and NaOH (aq). After filtration and extraction, tetrakis(2-aminoethyl)ammonium hydroxide was obtained in 70 % yield: ^{1}H NMR (400 MHz, Deuterium Oxide): δ_H 3.72-3.62 (m, 8H), 1.83-1.77 (m, 8H). ESI/MS$^-$ m/z 207.1 [M+OH$^-$], 224.2 [M+2OH$^-$]$^-$.



Tetrakis(2-aminoethyl)ammonium hydroxide

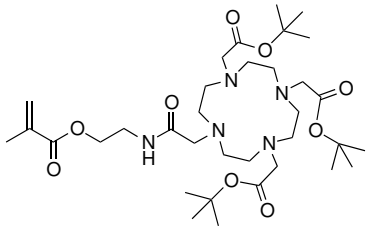
T_4F_{12c}. Tetrakis(2-aminoethyl)ammonium hydroxide was dissolved in dry MeCN and mixed with $NaHCO_3$ on ice before dropwise addition of trifluoroacetic anhydride. Tetrakis(2-(2,2,2-trifluoroacetamido)ethyl)ammonium hydroxide was obtained by filtration and recrystallisation in 60 % yield: ^{1}H NMR (400 MHz, Deuterium Oxide): δ_H 4.00 (dq, J = 5.1 Hz, 2.4 Hz, 8H), 3.68 (t, J = 5.1 Hz, 8H); ^{19}F NMR (376 MHz, Deuterium Oxide): δ_F -77.54; ^{13}C NMR (101 MHz, Deuterium Oxide): δ_C 162.89 (q, J = 35.4 Hz), 116.40 (q, J = 291.8 Hz), 63.75-59.35 (m), 32.72. ESI/MS$^+$ m/z 575.3 [M]$^+$.



Tetrakis(2-(2,2,2-trifluoroacetamido)ethyl)ammonium hydroxide

TFAEt. Ethyl 2,2,2-trifluoroacetate was prepared after a modified procedure reported in Ref. [178]. Trifluoroacetic acid was mixed with EtOH on ice. Next, H_2SO_4 was added dropwise and the reaction mixture was refluxed at 70 °C for 2 hours. The resulting product (yield: 60 %) was purified by phase separation and distillation. ^{1}H NMR (400 MHz, Deuterium Oxide): δ_H 1.86 (s, 1H), -1.15 (s, 1H).

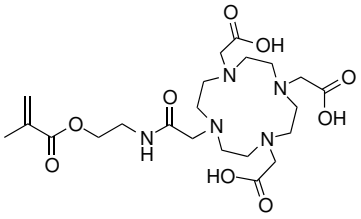
Gd·L$_4$. *t*Bu-protected DOTA-NHS was dissolved in dry DCM and placed on ice before a solution of aminoehtyl methacrylate hydrochloride (1.1 equiv) and TEA (2.2 equiv) in DCM were added. The solution was stirred at RT for 6 hours and washed with citric acid and water. The extracted DCM phase was dried and further purified by neutral alumina chromatography, which was eluted gradually with a MeOH/DCM mixture. *t*Bu-protected methacryloyloxy-DOTA (tri-tert-butyl 2,2',2"-(10-(2-((2-(methacryloyloxy)ethyl)amino)-2-oxoethyl)-1,4,7,10-tetraazacyclododecane-1,4,7-triyl)triacetate) was obtained in 40 % yield: ^{1}H NMR (400 MHz, Chloroform-*d*): δ_H 6.06 (t, J = 1.4 Hz, 1H), 5.49 (t, J = 1.6 Hz, 1H), 5.24 (s, 1H), 4.16 (t, J = 5.9 Hz, 2H), 3.51 (q, J = 6.0 Hz, 2H), 3.27 (d, J = 7.0 Hz, 4H), 2.98 (s, 6H), 2.87 (q, J = 8.6 Hz, 7.0 Hz, 7H), 1.86 (t, J = 1.3 Hz, 3H), 1.39 (s, 34H); ^{13}C NMR (400 MHz, Chloroform-*d*): δ_C 174.23, 170.21, 167.25, 136.03, 125.91, 81.45, 67.95, 63.00, 56.40, 52.46, 38.26, 28.16, 18.31. ESI/MS$^+$ m/z 684.4 [M+H]$^+$, 706.4 [M+Na]$^+$.



Tri-*tert*-butyl 2,2',2"-(10-(2-((2-(methacryloyloxy)ethyl)amino)-2-oxoethyl)-1,4,7,10-tetraazacyclododecane-1,4,7-triyl)triacetate

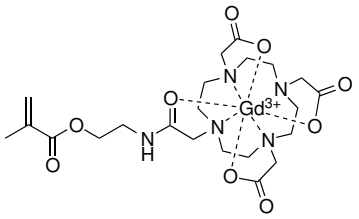
*t*Bu-protected methacryloyloxy-DOTA was then dissolved in a DCM/TFA mixture and stirred at RT for 24 hours. The resulting product was dried several times under vacuum after being dispersed in solvents that form aezotropes with excess TFA such as acetone, toluene and water among others. After DCM/H_2O extraction, *t*Bu-deprotected methacryloyloxy-DOTA (2,2',2"-(10-(2-((2-(methacryloyloxy)ethyl)amino)-2-oxoethyl)-1,4,7,10-tetraazacyclododecane-1,4,7-triyl)triacetic acid) was obtained in 80 % yield. ^{1}H NMR (400 MHz, Methanol-d_4):

δ_H 6.15 (s, 1H), 5.70 (s, 1H), 4.26 (q, J = 6.7 Hz, 2H), 3.31 (s, 14H), 1.96 (s, 3H), 1.56-1.44 (m, 12H). ESI/MS+ m/z 516.2 $[M+H]^+$.



2,2',2"-(10-(2-((2-(methacryloyloxy)ethyl)amino)-2-oxoethyl)-1,4,7,10-tetraazacyclododecane-1,4,7-triyl)triacetic acid

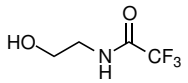
Gd^{3+} metallation of deprotected methacryloyloxy-DOTA was performed in water at pH 6.0-7.0 at 40 °C for 48 h with $GdCl_3{\cdot}6H_2O$. (2-(4,7-bis(carboxymethyl)-10-(2-((2-(methacryloyloxy)ethyl)amino)-2-oxoethyl)-1,4,7,10-tetraazacyclododecan-1-yl)acetoxy) gadolinium (yield: 40 %) was obtained with several redispersion/precipitation cycles triggered by a change in pH since free Gd^{3+} precipitated around pH 8.0. The presence of free Gd^{3+} was followed by mass spectrometry. ESI/MS+ m/z 693.1 $[M+Na]^+$.



Gd·L$_4$

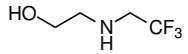
FQMA. Ethanolamine was dissolved in dry DCM (10 mL) and upon dropwise addition of trifluroacetic anhydride (0.5 equiv) on ice, the mixture was stirred overnight at RT. The product was filtered and dried yielding pure 2,2,2-trifluoro-*N*-(2-hydroxyethyl)acetamide (yield: 50 %): ^{1}H NMR (400 MHz, Methanol-d4): δ_H 3.67 (t, J = 5.8 Hz, 2H), 3.42 (t, J = 5.8 Hz, 2H); ^{19}F NMR (376 MHz, Methanol-d4): δ_F -77.39; ^{13}C NMR (101 MHz, Methanol-d4): δ_C 157.89 (q, J = 36.6 Hz), 116.13 (q, J = 286.5 Hz), 59.32, 41.85. ESI/MS$^-$ m/z 156.0 $[M-H]^-$, ESI/MS$^+$ m/z

158.0 $[M+H]^+$.



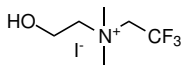
2,2,2-trifluoro-*N*-(2-hydroxyethyl)acetamide

The following procedure is a slightly modified one first reported in Ref. [203]. 2,2,2-trifluoro-*N*-(2-hydroxyethyl)acetamide was dissolved in dry THF and dropwise added to lithium aluminium hydride also pre-dissolved in THF and placed on ice. After the addition was complete, the temperature was raised to 70 °C and stirred for two hours before being quenched with dropwise addition of water and NaOH while stirring the reaction mixture at 0 °C. The product was filtered to obtain 2-((2,2,2-trifluoroethyl)amino)ethan-1-ol (yield: 80 %). ^{1}H NMR (400 MHz, Methanol-d4): δ_H 3.65 (t, J = 5.5 Hz, 2H), 3.27 (q, J = 9.8 Hz, 2H), 2.82 (t, J = 5.5 Hz, 2H); ^{13}C NMR (101 MHz, Methanol-d4): δ_C 125.80 (q, J = 278.1 Hz), 60.42, 50.89, 49.58 (q, J = 31.3 Hz); ^{19}F NMR (376 MHz, Methanol-d4): δ_F -73.18. ESI/MS$^+$ m/z 144.0 $[M+H]^+$.



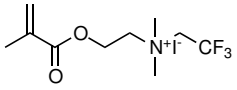
2-((2,2,2-trifluoroethyl)amino)ethan-1-ol

To prepare a water-soluble quaternary ammonium salt, 2-((2,2,2-trifluoroethyl)amino)ethanol was dissolved in anhydrous acetone. After the addition of anhydrous Na_2CO_3 and methyl iodide, the reaction mixture was stirred overnight at 40 °C. The product was filtered, extracted into water by washing with ethyl acetate and purified by recrystallisation. 2,2,2-trifluoro-*N*-(2-hydroxyethyl)-*N,N*-dimethyl-ethyl-1-ammonium iodide was obtained in 70 % yield. ^{1}H NMR (400 MHz, Deuterium Oxide): δ_H 4.46 (q, J = 8.5 Hz, 2H), 4.10 (q, J = 5.1 Hz, 4.6 Hz, 2H), 3.75 (q, J = 5.1 Hz, 4.2 Hz, 2H), 3.40 (d, J = 5.8 Hz, 6H); ^{19}F NMR (376 MHz, Deuterium Oxide): δ_F -62.15. ESI/MS$^+$ m/z 173.2 $[M+H]^+$; ESI/MS$^-$ m/z 425.9 $[M+2I]^-$.



2,2,2-trifluoro-*N*-(2-hydroxyethyl)-*N*,*N*-dimethylethan-1-aminium iodide

Trifluoro-(2-hydroxyethyl)-dimethylethan-ammonium iodide was then dissolved in dry acetonitrile, placed on ice, and stirred overnight at RT upon addition of triethylamine and methacryloyl chloride. The resulting product was purified by filtration, extraction and recrystalisation to yield 60 % of 2,2,2-trifluoro-*N*-(2-(methacryloyloxy)ethyl)-*N*,*N*-dimethyl-ethyl-1-ammonium iodide: ^{1}H NMR (400 MHz, Acetone-d6): δ_H 6.24-6.18 (m, 1H), 5.72 (q, J = 1.6 Hz, 1H), 5.30 (q, J = 8.9 Hz, 2H), 4.89-4.81 (m, 2H), 4.59-4.51 (m, 2H), 3.85 (s, 6H), 1.97 (t, J = 1.2 Hz, 3H); ^{19}F NMR (376 MHz, Acetone-d6): δ_F -62.22 (t, J = 8.9 Hz). ESI/MS$^+$ m/z 240.2 $[M]^+$; ESI/MS$^-$ m/z 493.9 $[M+2I]^-$.



2,2,2-trifluoro-*N*-(2-(methacryloyloxy)ethyl)-*N*,*N*-dimethylethan-1-aminium iodide

7.3 Nanoparticle and Polymer Sample Preparation Methods

MSNs Loaded by Ln·L$_1$ (MSN-Ln·L$_1$). Mesoporous silica nanoparticles (**MSN**) were prepared by a hydrolysis and condensation reaction.[122] Briefly, cetyltrimethylammonium bromide (1.77 mmol) was dissolved by stirring into a mixture of H_2O (16.02 mL, 0.89 mol), EtOH (1.84 mL, 0.04 mol) and triethanolamine (1.03 g, 6.9 mmol) at 80 °C. Next, tetraethylorthosilicate (TEOS, 6.47 mmol) was added, and the solution was stirred at 80 °C for 1 h, at what time a mixture of (3-aminopropyl)triethoxysilane (APTES, 0.01 mmol) and TEOS (0.01 mmol) was added. After an additional hour of stirring, the nanoparticles were centrifuged

and redispersed into an EtOH solution acidified with HCl three times, before being washed three times with EtOH. In order to obtain **MSN-Ln·L$_1$**, **MSNs** were thoroughly dried and dispersed into anhydrous DMF (6 mL), purged with N_2, carboxylated by succinic anhydride (9.99 μmol) overnight at RT, washed by centrifuge four times in EtOH, redispersed in 6 mL DMF, purged with N_2 and activated with 1-hydroxybenzotriazole hydrate (HOBt, 5 μmol) and 1-ethyl-3-(3-dimethylaminopropyl)carbodiimide (EDC, 5 μmol) at RT for 20 minutes. Next, **Ln·L$_1$** (2.5 μmol) was added and the mixture was stirred for further 18 hours. The obtained particles were washed three times in EtOH, three times with an aqueous solution of EDTA trisodium salt (3.8 μmol) and three times with water before being placed into a SnakeSkin dialysis tubing and Soxhlet extracted in MeOH for 24 h, wherein the solvent was replaced three times. The same procedure was used for the preparation of **MSN-Ln·L$_0$** except that **Ln·L$_0$** and only centrifugation/redispersion cycles were used for Gd^{3+} loading and purification, respectively.

MSNs Loaded by Ln·L$_2$ (MSN-Ln·L$_2$). Mesoporous silica nanoparticles were prepared by the same procedure as for **MSN-Ln·L$_1$** except that (3-bromopropyl)-trimethoxysilane (0.01 mmol) was implemented to functionalise the MSNs instead of APTES. Such particles were dispersed in DMF (4 mL) and bromide was substituted by azide by stirring the suspension with sodium azide (0.03 mmol) at 80 °C for 18 hours. The particles were washed three times with H_2O and three times with THF, alternately, before being dispersed in a mixture of H_2O and THF (1:1, 6 mL in total). **Ln·L$_2$** (2.5 μmol), $CuSO_4{\cdot}5H_2O$ (2.5 μmol) and sodium ascorbate (0.01 mmol) were added before the reaction mixture was stirred at RT for 2 days in the dark. The resulting particles were washed three times in an ethanolic solution of sodium diethyldithiocarbamate trihydrate (2.5 μmol) and three times with acetone, alternately, in order to remove copper. After a centrifugation cycle in water, the same EDTA and Soxhlet washing procedures were repeated as explained in the preparation

of the **MSN-Ln·L$_1$** particles.

Non-porous Silica NPs Loaded by Ln·L$_i$ (NS-Ln·L$_i$, $i = 1, 2$). The preparation of non-porous silica nanoparticles was similar to a previously reported method, which can be found in Ref. [127]. TEOS (480 μL) was stirred in a quarternary w/o microemulsion system consisting of cyclohexane (45 mL), 1-hexanol (10.8 mL), H_2O (2.4 mL) and Triton X-100 (10.6 mL) in the presence of NH_4OH (360 μL) that acted as the catalyst. The reaction was allowed to stir at RT for 24 h, followed by nine washing cycles by centrifugation in an acetic acid/methanol mixture (0.8 % v/v) as well as in ethanol in order to break the microemulsion and recover the particles. Further preparation of **NS-Ln·L$_2$** was the same as for **MSN-Ln·L$_2$**, while for the preparation of **NS-Ln·L$_1$**, the non-porous particles were post-grafted with APTES (0.01 mmol) first before applying the procedure described for **MSN-Ln·L$_1$**.

MSN-Gd·L$_1$-Est. 25 mg of **MSN-Gd·L$_1$** were dissolved in 5 mL MeOH containing a drop of H_2SO_4. The mixture was stirred overnight at 60 °C. If too much of H_2SO_4 was implemented, the linkage of **Gd·L$_1$** to the particles was cleaved resulting in extremely reduced protic relaxivities. After four centrifugation/redispersion cycles in EtOH, the particles were dissolved in dry DCM under N_2 and incubated on ice. Upon addition of TEA (45 μmol) and acetic anhydride (30 μmol), the mixture was brought to RT and stirred overnight. Further four centrifugation/redispersion cycles in EtOH followed.

MSN-Gd·L$_2$-Est. 25 mg of **MSN-Gd·L$_2$** were dissolved in 5 mL dry THF. After the addition of triphenylphosphine (30 μmol), the mixture was stirred overnight at RT. After four centrifugation/redispersion cycles in EtOH, the particles were dissolved in dry DCM under N_2 and incubated on ice. Upon addition of TEA (45 μmol) and acetic anhydride (30 μmol), the mixture was brought to RT and stirred overnight.

MSN-Ln·L_1-SO_3^- and MSN-Ln·L_2-SO_3^-. 25 mg of lanthanide-doped mesoporous silica nanoparticles were dried and dissolved in 6 mL dry toluene under N_2. (3-mercaptopropyl)trimethoxysilane (0.1 mmol) was added and the mixture was stirred at 60 °C for 20 h. The resulting particles (**MSN-Ln·L_i-SH**) were centrifuged four times before being redispersed in H_2O_2 (containing 0.1 % H_2SO_4), stirred at RT for 24 h and washed by four centrifugation/redispersion cycles in H_2O.

MSN-Ln·L_1-Poly(DAEMA)$_a$ and MSN-Ln·L_2-Poly(DAEMA)$_a$. MSNs loaded with Ln^{3+}-DOTA (**MSN-Ln·L_1** or **MSN-Ln·L_2**, 50 mg) were functionalised with an amine group by post-grafting with APTES (22 mmol) in dry toluene at 60 °C for 20 mins. The particles were washed four times with EtOH using centrifugation. Next, ATRP initiator-anchored silica nanoparticles were prepared by acylation of amine groups with 2-bromoisobutyryl bromide (143 μmol) and triethylamine (143 μmol). Each of the components was degassed and filled with N_2 before being dissolved in dry THF (6 mL). The reaction proceeded in a N_2 atmosphere on ice for 2 hours before being warmed to RT and stirred for further 18 hours. The ATRP initiator-anchored NPs were purified by three centrifugation/redispersion cycles in EtOH, transferred into a round bottom flask that was also charged with 2-(diethylamino)ethyl methacrylate (DAEMA, 0.86 mmol) and degassed by nitrogen bubbling for 30 mins. The ATRP polymerisation was performed in anisole (7 mL), employing CuBr (10.5 μmol) and *N,N,N',N",N'*-pentamethyldiethylenetriamine (20.9 μmol) to initiate polymerisation, which proceeded at 70 °C overnight in the presence of deactivating $CuBr_2$. The resulting polymer coated NPs were washed three times in an ethanolic solution of sodium diethyldithiocarbamate trihydrate (2.5 μmol) and three times with acetone, alternately, as well as three times by EtOH followed by Soxhlet extraction dialysis in MeOH.

MSN-Ln·L_1-Poly(DAEMA)$_b$ and MSN-Ln·L_2-Poly(DAEMA)$_b$. DAEMA (1.35 mmol) and (3-mercaptopropyl)trimethoxysilane (0.27 mmol) were purged with nitrogen for 30 minutes and dissolved in dry MeCN (10 mL). The polymerisation was triggered by ammonium persulphate (11.8 μmol, pre-dissolved in dry DMSO). After 4 hours of stirring at 70 °C, either **MSN-Ln·L_1** or **MSN-Ln·L_2** (ca. 50 mg) dispersed in EtOH and H_2O were added, and the mixture was left stirring overnight at 70 °C before being centrifuged three times in EtOH and two times in H_2O.

MSN-Poly(MAA). **MSN** particles (50 mg) were functionalised with a methacrylic group by post-grafting with 3-(trimethoxysilyl)propyl methacrylate (12.6 μmol) in a 2:1 ethanol/water mixture with NH_4OH (12.6 μmol) as a base catalyst at RT for 24 h and washed four times with EtOH using centrifugation. Next, methacrylic acid (2.1 mmol), ethylene glycol dimethacrylate (6.9 μmol) and 2,2-azobis(2-methylpropionitrile) (21.9 μmol) were added to the particles dispersed in MeOH (6 mL) in order to initiate the radical polymerisation step at 60 °C. After 3 h of stirring under nitrogen atmosphere, the resulting polymer coated NPs were purified by centrifugation/redispersion cycles in EtOH.

MSN-Poly(MAA)-Ln·L_1. **MSN-Poly(MAA)** particles were dissolved in DMF (4 mL), purged with nitrogen and activated with a mixture of HOBt (5 μmol) and EDC (5 μmol) for 20 minutes before **Ln·L_1** was added and reacted overnight at RT. The particles were purified by the same centrifugation/Soxhlet dialysis approach as described in the procedure for **MSNs-Ln·L_1** on P. 184.

MSN-Poly(MAA)-Ln·L_2. In order to load **MSN-Poly(MAA)** with **Ln·L_2**, the particles were dissolved in DCM (6 mL) and placed in an ice bath (0 °C) under nitrogen atmosphere. Bromoethanol (0.18 mmol), *N,N'*-dicyclohexylcarbodiimide and 4-dimethylaminopyridine were then added and stirred overnight at RT. After

three centrifugation/redispersion cycles in DCM, the particles were dissolved in H_2O (6 mL). NaN_3 (0.20 mmol) was added at 0 °C, and the mixture was left stirring overnight, which was followed by another three centrifugation/redispersion cycles in H_2O. For loading of **MSN-Poly(MAA)-Ln·L$_2$**, 2.5 μmol of the lanthanide complex were added to the particles dissolved in a THF/H_2O mixture (6 mL). $CuSO_4 \cdot 5H_2O$ (2.5 μmol) and sodium ascorbate (0.01 mmol) were next added and the reaction was stirred at RT for 2 days in the dark. The particles were purified by the same centrifugation/Soxhlet dialysis approach as described in the procedure for **MSN-Ln·L$_2$** on P. 185.

MSN-FITC, MSN-FITC-Poly(DAEMA)$_a$ and MSN-FITC-Poly(DAEMA)$_b$. Aminated MSNs were prepared by post-grafting APTES (65.6 μmol for 10 mol % of amination) onto unmodified MSNs (40 mg) in dry DMF under N_2 at RT for 24 h followed by purification with several centrifugation/redispersion cycles in EtOH. The procedures for subsequent polymerisation can be found on P. 187.

MSN-PFOTS. Cetyltrimethylammonium bromide (CTAB, 1.77 mmol) was dissolved by stirring into a mixture of H_2O (16.02 mL, 0.89 mol), EtOH (1.84 mL, 0.04 mol) and triethanolamine (1.69 mmol) at 80 °C. Next, a mixture of TEOS (6.5 mmol) and 1H,1H,2H,2H-perfluorooctyl-triethoxysilane (10 mol %) was added, and stirred at 80 °C for 2 h before being centrifuged three times in EtOH.

uMSN-PEG-PFOTS. Ultra-small mesoporous silica nanoparticles were prepared after a modified procedure reported in Ref. [176]. CTAB (0.2 mmol) and NH_4OH (0.04 mmol) were fully dissolved in 10 mL H_2O at 30 °C before tetramethyl orthosilicate (0.4 mmol) was added into the solution, which was stirred at 30 °C for 24 hours. Next, methoxy(triethylenoxy)propyltrimethoxysilane (0.2 mmol) was added

and the suspension was stirred at 30 °C for 24 h and further at 80 °C for 24 h. The particles were dialysed against acid solution, which was exchanged three times over 24 h and further 24 h against ultrapure water. The solvent was then evaporated on a rotavap, the particles were dissolved in a 2:1 EtOH/H_2O mixture (6 mL, 0.6 μL 30 % NH_4OH) and 1H,1H,2H,2H-perfluorooctyl-triethoxysilane (60 μmol) was post-grafted onto ultra-small MSNs. After 24 h of stirring, the resulting particles were again dialysed against ultrapure water and filtered through a 200 nm syringe filter.

MSN-SS-FBA. Amine functionalised mesoporous silica nanoparticles were first prepared by a Stöber hydrolysis/condensation method followed by post-grafting with (3-aminopropyl)triethoxysilane (0.3 mmol) in dry toluene at 60 °C. After washings by centrifugation in EtOH, the particles were dried, dispersed in dry DMF under N_2 and reacted with succinc anhydride (0.5 mmol) overnight at RT. Following further purification cycles by centrifugation in EtOH, the particles were dried again, dispersed in dry DMF, activated by HOBt (0.6 mmol) and EDC (0.6 mmol) and reacted overnight in the presence of cystamine dihydrochloride (0.3 mmol). The same procedure was repeated again with 4-(trifluoromethyl)benzoic acid (0.3 mmol) instead of cystamine dihydrochloride before the particles were washed for the last time by four centrifugation/redispersion cycles in EtOH.

MSN-Poly(DAEMA-TFMA), MSN-Poly(DAEMA-PFA) and MSN-Poly(DAEMA)-PFP. Initial poly(DAEMA)-coated MSNs were prepared as described in the procedure for obtaining **MSN-Ln·L_1-Poly(DAEMA)$_a$** with the difference in the amounts of 2-bromoisobutyryl bromide initiator and 2-(dimethylamino)ethyl methacrylate, which were increased to 1.7 mmol and 25.6 mmol (per 50 mg MSNs), respectively. For **MSN-Poly(DAEMA-PFA)**, 1H,1H,2H,2H-perfluorodecyl acrylate (1.7 mmol) was reacted under N_2 onto poly(DAEMA)-coated MSNs in dry DMF in the presence of CuBr (5 mol %) and 2,2'-bipyridine (10 mol %).

After two hours stirring at 60 °C, poly(ethylene glycol) methyl ether methacrylate (1.7 mmol) was added and the mixture was stirred overnight. For **MSN-Poly(DAEMA-TFMA)**, 2,2,2-trifluoroethyl methacrylate (1.7 mmol) was reacted onto poly(DAEMA)-coated MSNs instead of 1H,1H,2H,2H-perfluorodecyl acrylate. The reaction was performed overnight without the addition of PEG methacrylate. **MSN-Poly(DAEMA-TFMA)** and **MSN-Poly(DAEMA-PFA)** were both washed three times with an ethanolic solution of sodium diethyldithiocarbamate trihydrate and three times with acetone, alternately, as well as three times with EtOH followed by Soxhlet extraction dialysis in MeOH. For **MSN-Poly(DAEMA)-PFP**, poly(DAEMA)-coated MSNs were dissolved in dry THF containing K_2CO_3 (4 mmol) and purged with N_2 before pentafluorophenol (1.7 mmol) was added. The mixture was refluxed for 24 h and centrifuged several times in EtOH.

MSN-Poly(AEMA)-FBA. 2-aminoethyl methacrylate hydrochloride (12.8 mmol) and 3-(trimethoxysilyl)propyl methacrylate (1.3 mmol) were dissolved in dry MeCN under N_2 at 70 °C. Upon addition of ammonium persulphate pre-dissolved in dry DMSO, the reaction mixture was stirred for 4 hours, before MSNs (50 mg) dispersed in EtOH and H_2O were added and stirred overnight at 70 °C. After purification by several centrifugation/redispersion cycles in EtOH, the particles were dried overnight and dispersed in dry DMF. Next, 4-(trifluoromethyl)benzoic acid was dissolved in dry DMF, activated with HOBt/EDC and added to the nanoparticle suspension. The suspension was stirred overnight at RT and the resulting particles were again purified by centrifugation/redispersion cycles in EtOH.

MSN-dendrimers-CF_3. The dendrimer-functionalised particles were prepared after a modified procedure reported in Ref. [177]. Mesoporous silica nanoparticles (50 mg) were post-grafted with (3-aminopropyl)triethoxysilane (0.2 mmol) before being dispersed in dry THF (8 mL), exposed to cyanuric chloride (0.2 mmol) in the pres-

ence of *N,N*-diisopropylethylamine (0.4 mmol) and stirred at 0 °C for 24 h. Next, after several centrifugations, the particles were again dispersed in dry THF and refluxed for 24 h in the presence of diethylamine (0.4 mmol). After another set of centrifugations, the last two steps were repeated two more times. Dendrimer-functionalised MSNs were then reacted with ethyl 2,2,2-trifluoroacetate[1] (2 mmol) at RT in MeOH. The resulting particles were purified several times by centrifugation.

NS-OA-PFB. Oleic acid was dissolved in EtOH (50 equiv) and mixed by sonication with 3,5-bis(trifluoromethyl)benzoic acid (0.2 equiv). The mixture was heated, while stirring, to 80 °C. Next, dimethyloctadecyl[3-(trimethoxysilyl)propyl] ammonium chloride (DTSA, 0.6 equiv) was added, followed by dropwise addition of tetraethoxysilane (TEOS, 6.7 equiv) and water (1600 equiv). The reaction proceeded overnight. The particles were washed by centrifugation/redispersion cycles in water.

NCS-PFD$_c$. Perfluorodecalin (PFD) nanoemulsions were prepared by dissolving PFD (0.8 mmol) in the presence of DTSA (0.5 mmol) in water (0.6 mol) containing catalytic amounts of NH_4OH. TEOS (1.7 mmol) was then introduced gradually and the mixture was stirred at 30 °C for 24 h. The resulting nanocapsules were carefully centrifuged four times at 10k rpm for 10 mins in water.

Poly(DAEMA)$_a$, Poly(DAEMA)$_b$. Polymer NPs were prepared by a surfactant-free emulsion polymerisation in water adapted from Ref. [184]. For **Poly(DAEMA)$_a$**, 2-(diethylamino)ethyl methacrylate (24.85 mmol) was polymerised at 70 °C for 3 h with ethylene glycol dimethacrylate (0.15 mmol) in H_2O (45 mL). The reaction was initiated by ammonium persulphate (0.22 mmol). Smaller **Poly(DAEMA)$_b$** were obtained when the amount of monomers and the volume of reaction mixture were reduced by 5- and 2-fold, respectively. The particles were

[1]The synthetic procedure can be found on P. 180.

dialysed in H_2O for 3 days (cut-off 10 kDa) and further purified by several centrifugation/redispersion cycles in H_2O.

Poly(DAEMA)$_a$-TFA, **Poly(DAEMA)$_a$-F$_4$Ac**, **Poly(DAEMA)$_a$-TFA-Si**, **Poly(DAEMA)$_a$-F$_4$Ac-Si.** 45 mg of **Poly(DAEMA)$_a$** were dissolved in water and 0.26 mmol of either trifluoroacetic acid (TFA) or 2,2'-((2,2,3,3-tetrafluorobutane-1,4-diyl)bis(oxy))diacetic acid (**F$_4$Ac**) were predisolved in MeOH and added to the reaction mixture, which was stirred overnight at 55 °C. After three centrifugation/redispersion cycles, the resulting particles (either **Poly(DAEMA)$_a$-TFA** or **Poly(DAEMA)-F$_4$Ac**) were redispersed in a H_2O/EtOH (5:1) mixture, and upon addition of tetraethyl orthosilicate (2.6 mmol), again stirred overnight at 55 °C prior to purification by centrifugation in H_2O.

Poly-(DAEMA)$_a$-F$_4$M$_2$, Poly-(DAEMA)$_b$-F$_4$M$_2$. 20 mg of freshly prepared **Poly(DAEMA)$_a$** or **Poly(DAEMA)$_b$** were dissolved in a H_2O/MeOH mixture prior to addition of **F$_4$M$_2$** (0.3 mmol) and ammonium persulphate (100 wt %) pre-dissolved in MeOH and H_2O, respectively. The polymerisation occurred overnight at 60 °C. Residual initiators and fluorinated dimethacrylates were removed by dialysis and centrifugation in H_2O.

Poly(MAA-PEG)-T$_x$F$_y$. Methacrylic acid (1 equiv) and poly(ethylene glycol) methyl ether methacrylate (3 equiv) were dissolved in dry THF and stirred at 60 °C under N_2. Upon addition of 2,2-azobis(2-methylpropionitrile) (0.02 equiv), the reaction mixture was stirred for further 24 hours. The polymers were purified by washings and precipitiation in diethyl ether. The resulting product (1.16 mmol) was dissolved in water, to which silver(I)-oxide (0.58 mmol) was added followed by addition of quaternary ammonium salts (**T$_x$F$_y$**) pre-dissolved in MeOH. The suspension was stirred overnight at RT. After precipitation of AgCl into the H_2O/MeOH (1:1) mixture,

residual non-complexed $\mathbf{T}_x\mathbf{F}_y$ was removed by precipitation in ultrapure water.

PEI-CF_3-Cl^-. In order to synthesise **PEI-CF_3-Cl^-**, branched polyethylenimine (M_W ~800) was dissolved into methanol followed by the addition of freshly prepared ethyl 2,2,2-trifluoroacetate[2] (16 equiv). The mixture was stirred overnight at 30 °C and the organic phase was concentrated to remove MeOH. The product was dissolved in DCM and washed with $NaHCO_3$ (aq) and water before being recrystallised from a minimum amount of DCM and hexane. The product was then dissolved in DCM and stirred at 40 °C with MeI (6 equiv) overnight, purified by washings with DCM, dried, redissolved in a H_2O/MeOH mixture and passed through an Amberlite column in order to exchange the iodide and residual trifluoroacetate counter anions for the chloride ones.

NS-COOH. The non-porous silica particles[3] were further functionalised with a tri-phasic reverse emulsion approach,[204] which produces controlled, thin and ordered layers of particle surface functional groups. Briefly, 50 mg of non-porous silica nanoparticles were dissolved in dry toluene (10 mL) and Triton X-100 (1 mL). After APTES (6.20 μmol) addition, the mixture was stirred for 5 hours at 50 °C before being centrifugated twice in an acetic acid/methanol mixture (0.8 % v/v), which helps to remove Triton X-100 physisorbed onto the silica surface, and four times in ethanol. The particles (50 mg) were then dispersed into dry DMF (3 mL) and stirred overnight at RT with succinic anhydride (9.99 μmol) before being centrifuged and redispersed four times in EtOH.

NS-MAA. Non-porous silica particles were functionalised with a polymerisation initiator by post-grafting 3-(trimethoxysilyl)propyl methacrylate (12.6 μmol) in a 2:1 ethanol/water mixture with NH_4OH (12.6 μmol) as a base catalyst at RT for

[2]The synthetic procedure can be found on P. 180.
[3]The particle preparation procedure is described on P. 186.

24 h and washed four times with EtOH using centrifugation. Next, methacrylic acid (2.1 mmol), ethylene glycol dimethacrylate (6.9 μmol) and ammonium persulphate (21.9 μmol) were added in order to initiate the radical polymerisation step at 70 °C. After 3 h of stirring, the resulting polymer-coated NPs were purified by centrifugation/redispersion cycles in EtOH.

MSN-COOH. Mesoporous silica nanoparticles were prepared by a modified method of hydrolysis and condensation reaction.[122] Briefly, CTAB (1.77 mmol) was dissolved by stirring into a mixture of H_2O (0.89 mol), EtOH (0.04 mol) and triethanolamine (6.9 mmol) at 80 °C. Next, TEOS (6.48 mmol) was added, and the solution was stirred at 80 °C for 1 h, at what time a mixture of APTES (15 μmol) and TEOS (15 μmol) was added. After an additional hour of stirring, the nanoparticles were centrifuged and redispersed into an EtOH solution acidified with HCl before being washed three times in EtOH. The particles (50 mg) were then dispersed into anhydrous DMF (3 mL) and stirred overnight at RT with succinic anhydride (9.99 μmol) before being centrifuged and redispersed four times in EtOH.

MSN-$\mathbf{Ln_2{\cdot}L_3}$, NS-$\mathbf{Ln_2{\cdot}L_3}$ and NS-MAA-$\mathbf{Ln_2{\cdot}L_3}$. For α,α'-bis(LnDO3A)-5-amino-*m*-xylene ($\mathbf{Ln_2{\cdot}L_3}$) coupling, the carboxylated particles (either **NS-COOH**, **NS-MAA** or **MSN-COOH**) were dispersed in 3 mL MES buffer (10 mM, pH 5.6), activated with *N*-hydroxysuccinimide (6 μmol) and 1-ethyl-3-(3-dimethylaminopropyl)-carbodiimide (15 μmol) at RT for 20 min before $\mathbf{Ln_2{\cdot}L_3}$ (2.6 μmol) was added in a bicarbonate buffer (10 mM, pH 8.2). The pH was adjusted for further 10 min to pH 7.4. The reaction mixture was left stirring overnight before being washed by a day long dialysis against 1.5 equivalents of EDTA in water followed by a two day long dialysis in ultrapure water, which was exchanged four times. Lastly, the particles were further purified by six centrifugation/redispersion cycles in EtOH.

Poly(TFMA-DMA-PEG), **Poly(TFMA-MAA-PEG)**, **Poly(TFMA-DMA-PEG-Gd·L_4)**, **Poly(TFMA-MAA-PEG-Gd·L_4).** 2,2,2-Trifluoroethyl methacrylate (10 equiv), poly(ethylene glycol) methyl ether methacrylate (5 equiv) and either 2-(diethylamino)ethyl methacrylate (DMA, 2 equiv) or methacrylic acid (MAA, 2 equiv) were dissolved in dry THF and purged with N_2. **Gd·L_4** (0.001 equiv in dry DMF) was also added in order to obtain **Poly(TFMA-DMA-PEG-Gd·L_4)** and **Poly(TFMA-MAA-PEG-Gd·L_4)**. The reaction mixture was maintained at 75 °C with stirring for 15 min to attain temperature equilibrium before 2,2′-azobis(2-methylpropionamidine) hydrochloride (0.01 equiv) was added and the solution was stirred at 75 °C for 24 hours. The product was purified by dialysis (3 kDa cut-off).

Poly(FQMA-DMA), Poly(FQMA-MAA), Poly(FQMA-DMA-Gd·L_4), Poly(FQMA-MAA-Gd·L_4). FQMA (10 equiv) and either 2-(diethylamino)ethyl methacrylate (DMA, 2 equiv) or methacrylic acid (MAA, 2 equiv) were dissolved in MeOH and purged with N_2. **Gd·L_4** (0.001 equiv in dry DMF) was also added in order to obtain **Poly(FQMA-DMA-Gd·L_4)** and **Poly(FQMA-MAA-Gd·L_4)**. Upon addition of 2,2′-azobis(2-methylpropionamidine) hydrochloride (0.01 equiv), the solution was stirred at 75 °C for 24 hours. The product was purified by dialysis (3 kDa cut-off).

Appendix A

Appendix to Chapters II, III and IV

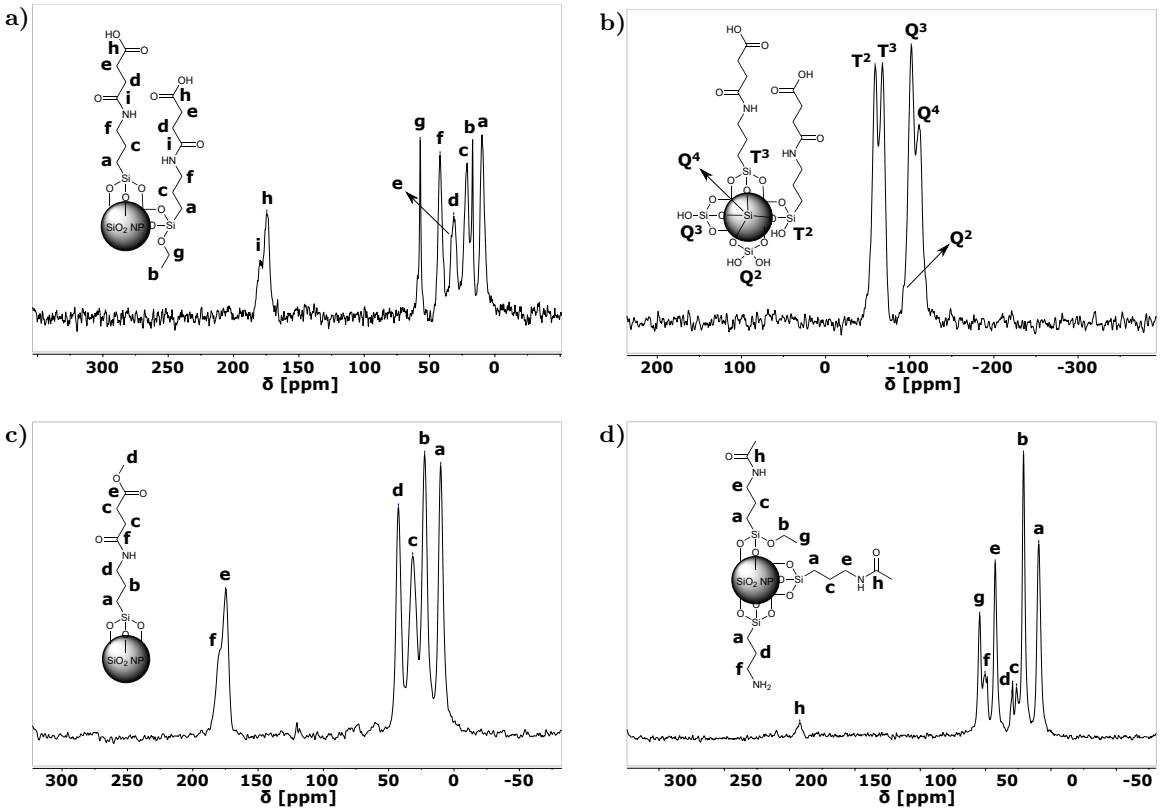


Figure A.1: a) ^{13}C CP/MAS and b) ^{29}Si DP/MAS NMR spectra showing carboxylated MSNs referenced on P. 45 as well as ^{13}C CP/MAS NMR spectra showing c) carboxyl- and d) amine-functionalised MSNs after acetylation as referenced on P. 54.

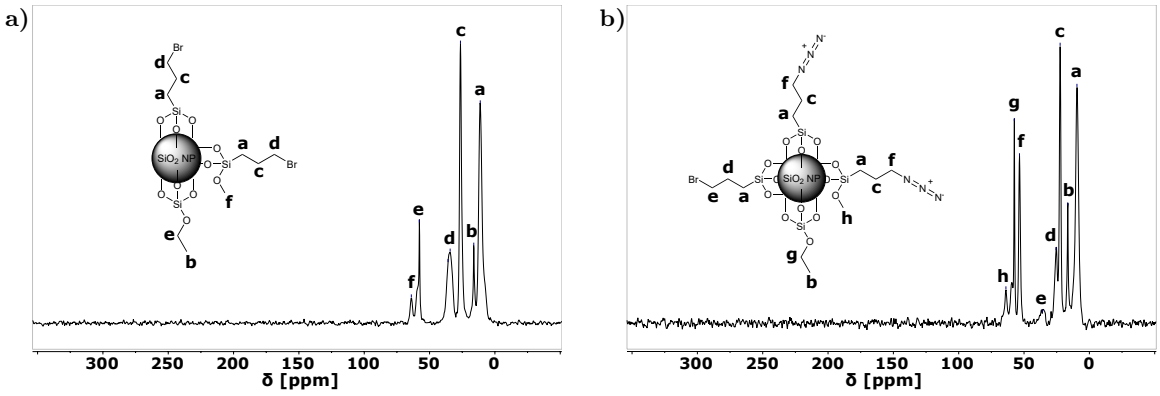


Figure A.2: ^{13}C CP/MAS NMR spectra of a) bromide- and b) azide-functionalised MSNs referenced on P. 48.

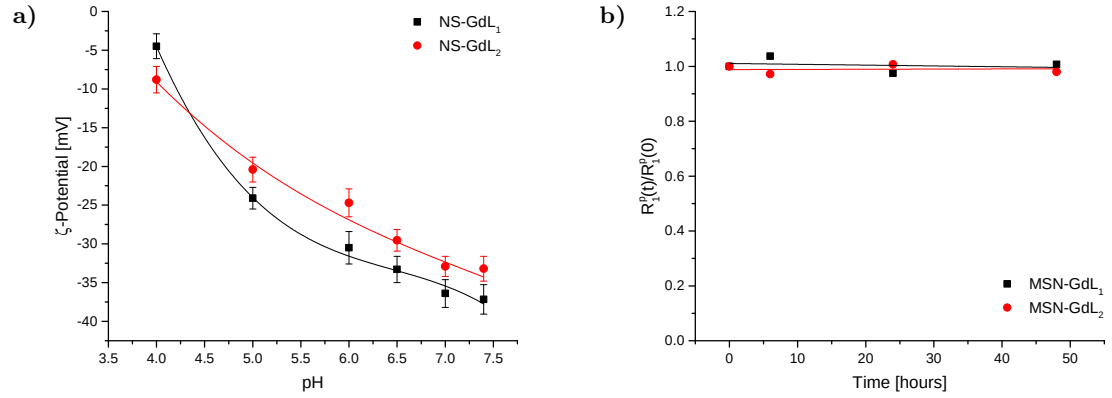


Figure A.3: a) pH-dependence of ζ-potentials of ■ **NS-Gd·L$_1$** and ● **NS-Gd·L$_2$** referenced on P. 53. b) Transmetallation test of ■ **MSN-Gd·L$_1$** and ● **MSN-Gd·L$_2$** particles referenced on P. 50. The graph shows that, over 48 h, **MSN-Gd·L$_1$** and **MSN-Gd·L$_2$** did not undergo transmetallation with zinc ions in phosphate buffer (10 mM, pH 7.4) as this would have resulted in a drastic decrease in ^{1}H NMR relaxation rate ratio $R_1^p(t)/R_1^p(0)$ (measured at 7.0 T, RT) if $GdPO_4$ would have formed and precipitated from released Gd^{3+}.

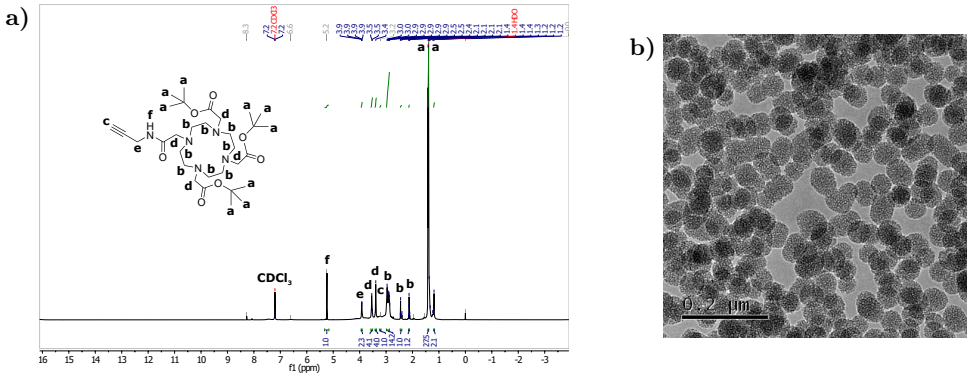


Figure A.4: a) ^{1}H NMR spectrum of *t*Bu-protected precursor of **Ln·L$_2$** in $CDCl_3$ referenced on P. 47. b) TEM image of **MSN-Gd·L$_1$-SO$_3^-$** particles referenced on P. 47.

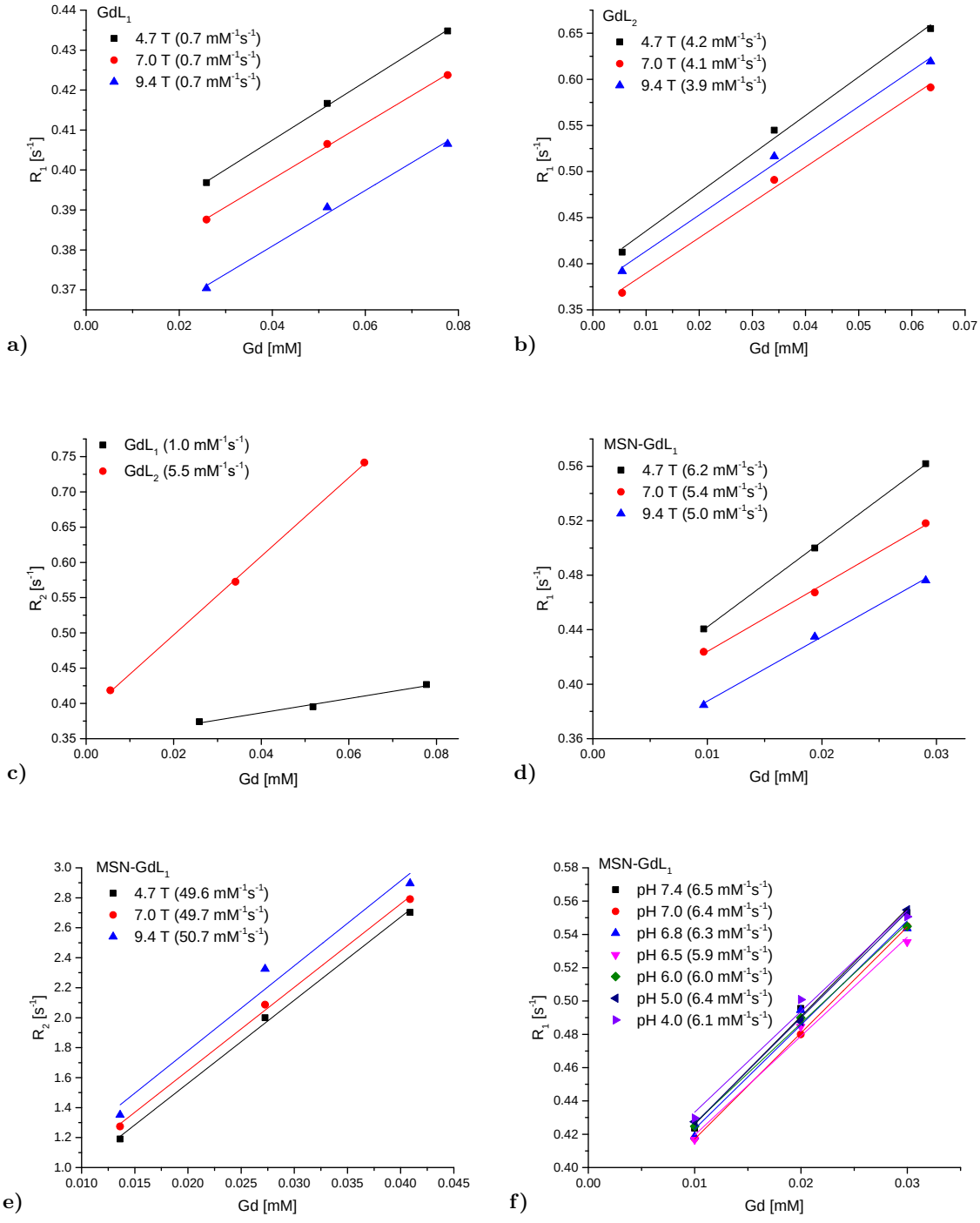


Figure A.5: Linear fits of ^{1}H longitudinal R_1 and transverse R_2 relaxation rates of **Gd·L$_1$**, **Gd·L$_2$** and **MSN-Gd·L$_1$** versus Gd concentration. The rates were measured either at 4.7 T (a-c), f)) or at 4.7 T, 7.0 T and 9.4 T (d), e)). The graphs were fitted to Eq. (1.6) on P. 6. The linear fits of the data points yielded relaxivities that were combined with duplicates and averaged to the values shown in brackets. Referenced on P. 49.

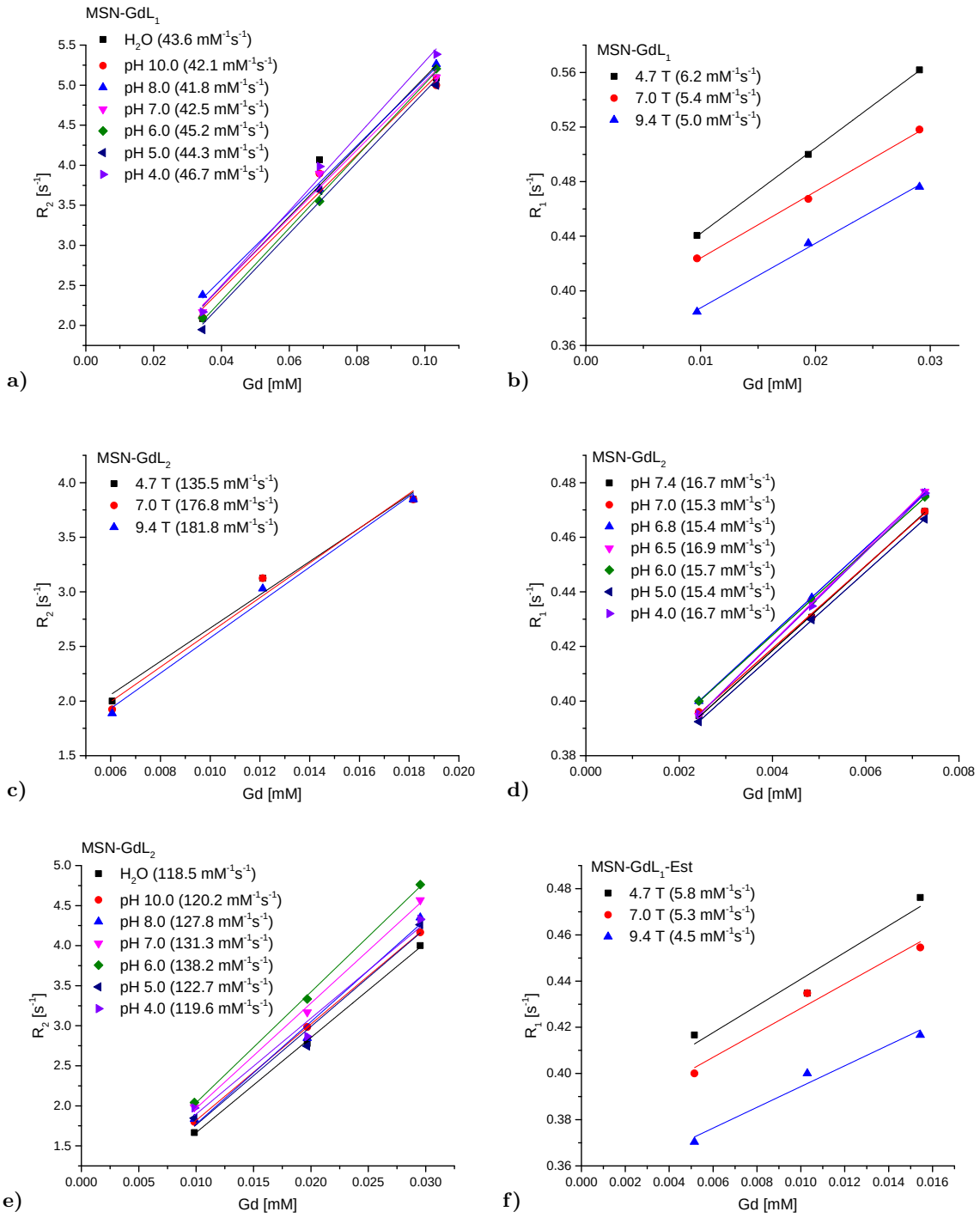


Figure A.6: Linear fits of ^{1}H longitudinal R_1 and transverse R_2 relaxation rates of **MSN-Gd·L$_1$**, **MSN-Gd·L$_2$** and **MSN-Gd·L$_1$-Est** versus Gd concentration as referenced on P. 49 and P. 52. The rates were measured either at 4.7 T (a), d), e)) or at 4.7 T, 7.0 T and 9.4 T (b), c), f)). The graphs were fitted to Eq. (1.6) on P. 6. The linear fits of the data points yielded relaxivities that were combined with duplicates and averaged to the values shown in brackets.

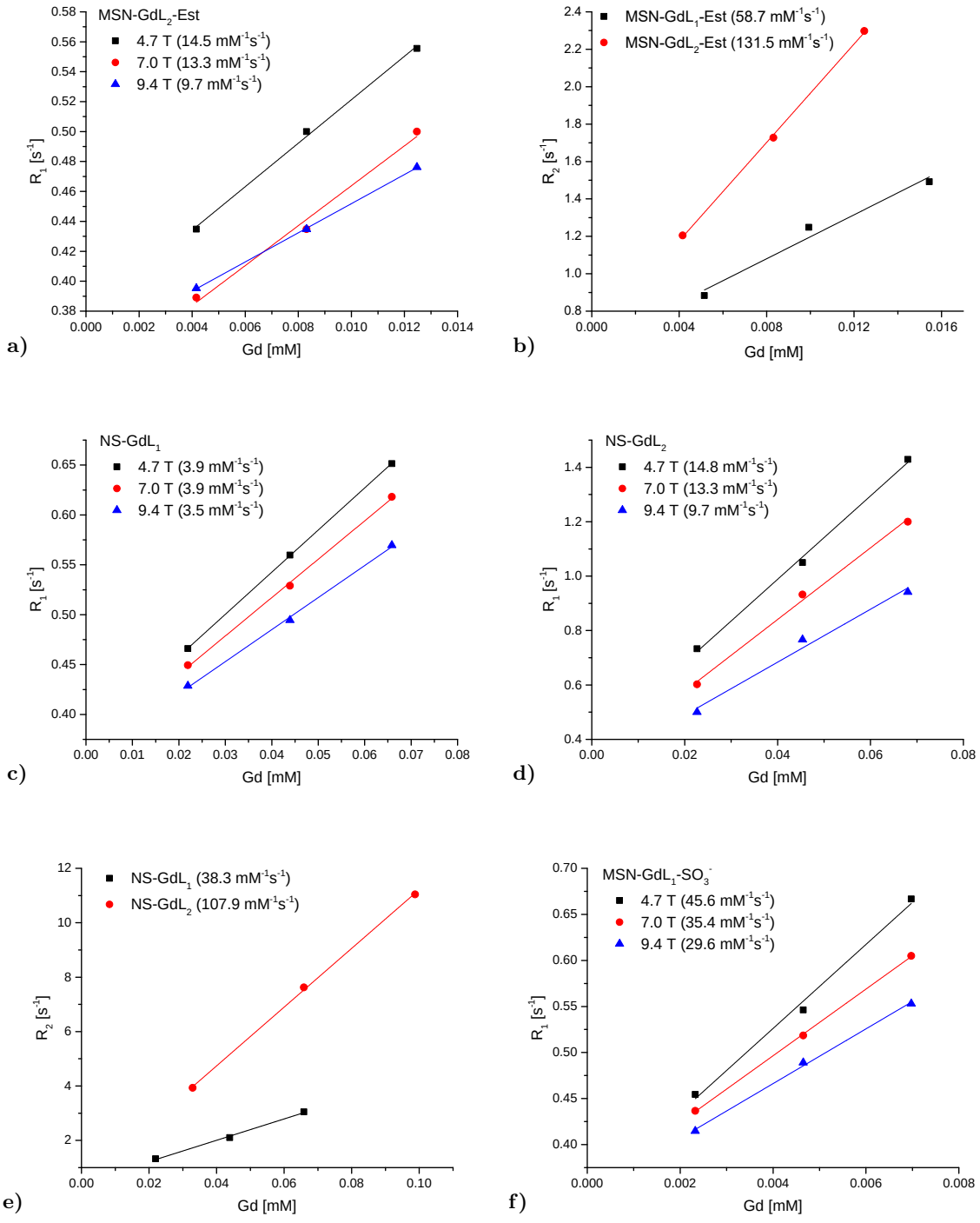


Figure A.7: Linear fits of ^{1}H longitudinal R_1 and transverse R_2 relaxation rates of **MSN-Gd·L$_1$-Est**, **MSN-Gd·L$_2$-Est**, **NS-Gd·L$_1$**, **NS-Gd·L$_2$** and **MSN-Gd·L$_1$-SO$_3^-$** versus Gd concentration as referenced on P. 73. The rates were measured either at 4.7 T (b, e)) or at 4.7 T, 7.0 T and 9.4 T (a), c-d), f)). The graphs were fitted to Eq. (1.6) on P. 6. The linear fits of the data points yielded relaxivities that were combined with duplicates and averaged to the values shown in brackets.

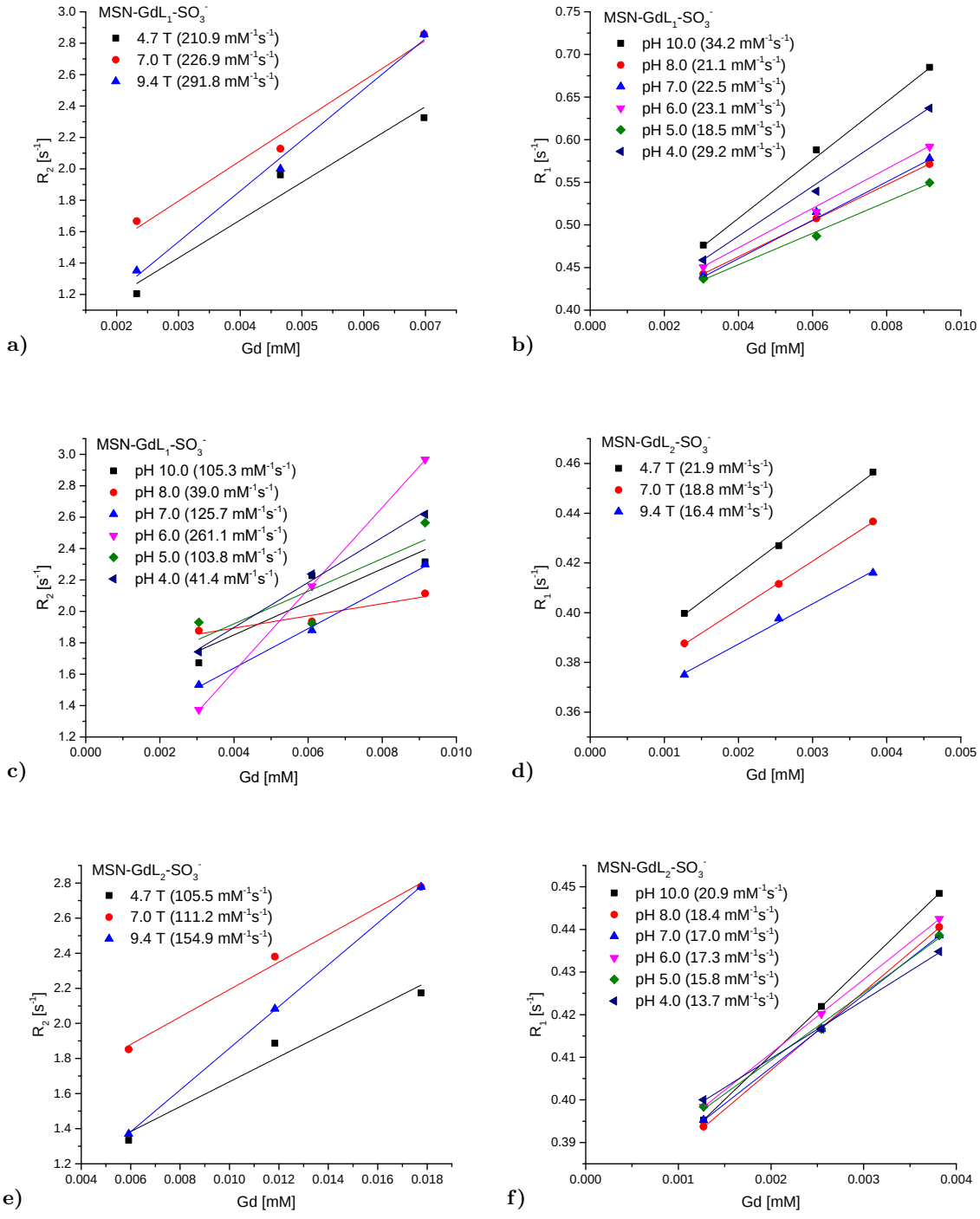


Figure A.8: Linear fits of ^{1}H longitudinal R_1 and transverse R_2 relaxation rates of **MSN-Gd·L$_1$-SO$_3^-$** and **MSN-Gd·L$_2$-SO$_3^-$** versus Gd concentration as referenced on P. 73. The rates were measured either at 4.7 T (b), c), f)) or at 4.7 T, 7.0 T and 9.4 T (a), d), e)). The graphs were fitted to Eq. (1.6) on P. 6. The linear fits of the data points yielded relaxivities that were combined with duplicates and averaged to the values shown in brackets.

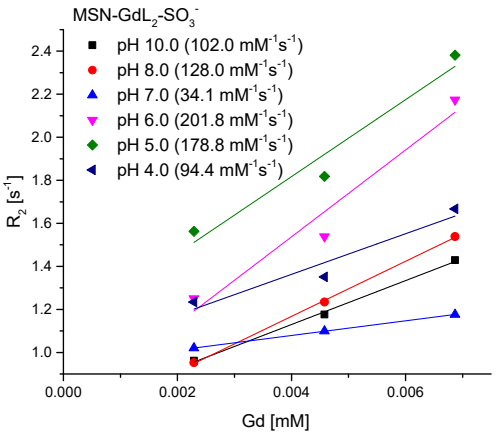


Figure A.9: Linear fits of ^{1}H transverse relaxation rates R_2 of **MSN-Gd·L$_2$-SO$_3^-$** versus Gd concentration. The rates were measured at 4.7 T as referenced on P. 73. The graphs were fitted to Eq. (1.6) on P. 6. The linear fits of the data points yielded relaxivities that were combined with duplicates and averaged to the values shown in brackets.

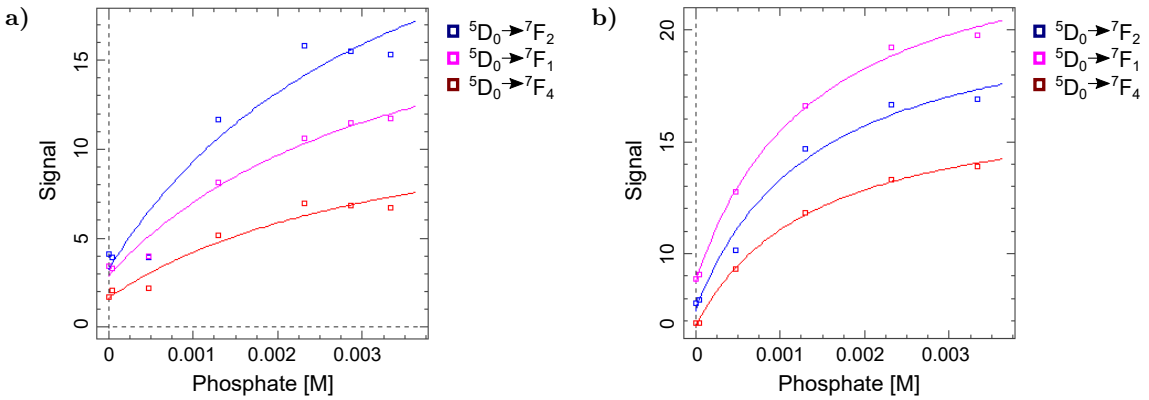


Figure A.10: Dynafit fitting output of the normalised intensities of europium emission bands of a) **MSN-Eu·L$_1$-SO$_3^-$** and b) **MSN-Eu·L$_2$-SO$_3^-$** particles as a function of added molar phosphate concentration as referenced on P. 79. Weak phosphate binding constants of 280 ± 150 M^{-1} and 720 ± 110 M^{-1} could be roughly estimated by least squares iterative analysis using Dynafit for **MSN-Eu·L$_1$-SO$_3^-$** and **MSN-Eu·L$_2$-SO$_3^-$**, respectively.

Table A.1: pH/pD dependency of the rate of depopulation of excited states of Eu^{3+} nanoparticulate counterparts in H_2O and D_2O, respectively, as referenced on P. 78. Luminescence lifetimes were measured at 293 K, λ_{ex} = 394 nm and λ_{em} = 615 nm. The amide NH oscillator has been assumed to contribute 0.075 ms^{-1} to the quenching of the **Eu·L**$_2$ $^5D_0$ excited state. τ_{D_2O} values were determined in D_2O at pD = pH + 0.41.

	MSN-Eu·L$_1$			**MSN-Eu·L$_2$**			**MSN-Eu·L$_1$-SO$_3^-$**			**MSN-Eu·L$_2$-SO$_3^-$**		
pH	τ_{H_2O} $[ms]$	τ_{D_2O} $[ms]$	q	τ_{H_2O} $[ms]$	τ_{D_2O} $[ms]$	q	τ_{H_2O} $[ms]$	τ_{D_2O} $[ms]$	q	τ_{H_2O} $[ms]$	τ_{D_2O} $[ms]$	q
4.0	1.082	1.550	0.035	0.569	1.968	1.109	0.622	0.869	0.249	0.465	0.959	0.939
5.0	1.069	1.617	0.081	0.557	1.881	1.128	0.524	0.768	0.396	0.441	1.423	1.378
6.0	0.958	1.360	0.065	0.588	1.875	0.934	0.717	1.629	0.637	0.429	1.473	1.591
7.0	1.074	1.587	0.061	0.576	2.057	1.110	0.932	1.756	0.304	0.512	1.508	1.158
8.0	1.147	1.657	0.023	0.569	1.697	1.100	0.972	1.690	0.225	0.502	1.538	1.221
10.0	1.108	1.638	0.050	0.565	1.902	1.194	0.933	1.693	0.278	0.517	1.756	1.248

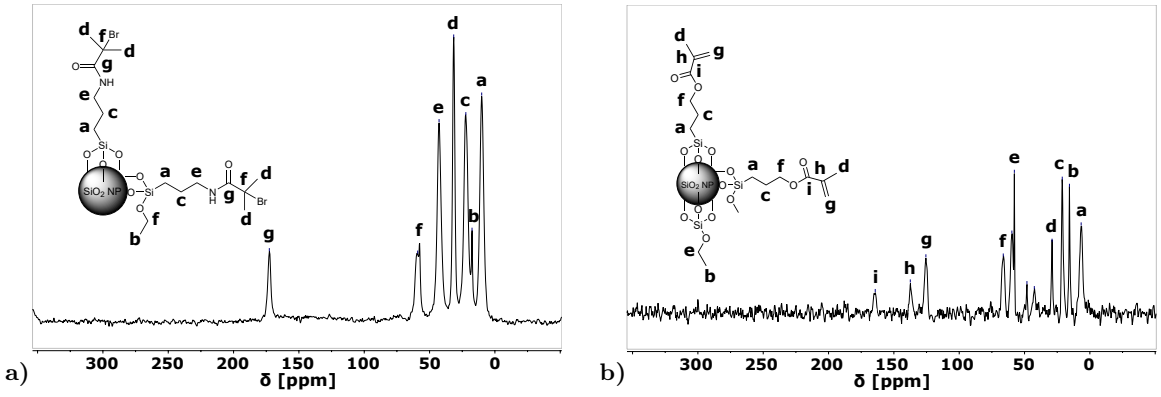


Figure A.11: ^{13}C CP/MAS NMR spectra showing initiator-functionalised MSNs for a) ATRP and b) free radical polymerisation referenced on P. 89.

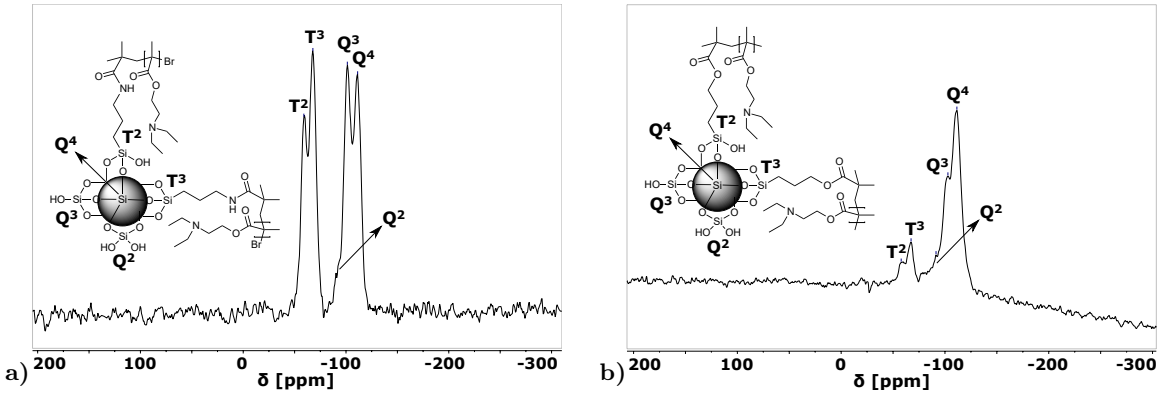


Figure A.12: ^{29}Si DP/MAS NMR spectra of a) **MSN-Poly(DAEMA)**$_a$ and b) **MSN-Poly(DAEMA)**$_b$ referenced on P. 90.

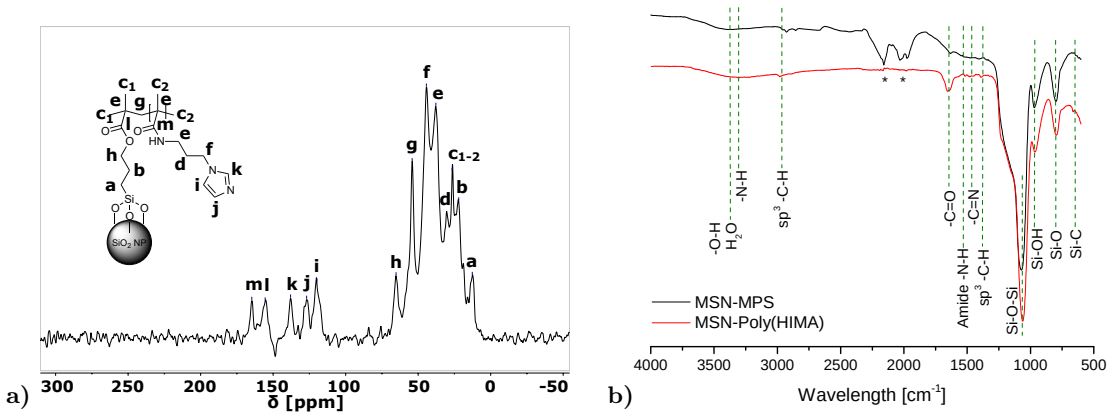


Figure A.13: a) ^{13}C CP/MAS NMR and FTIR spectra of **MSN-Poly(HIMA)** bearing a polymer composed of *N*-(3-imidazol-yl)propyl-methacrylamide referenced on P. 95.

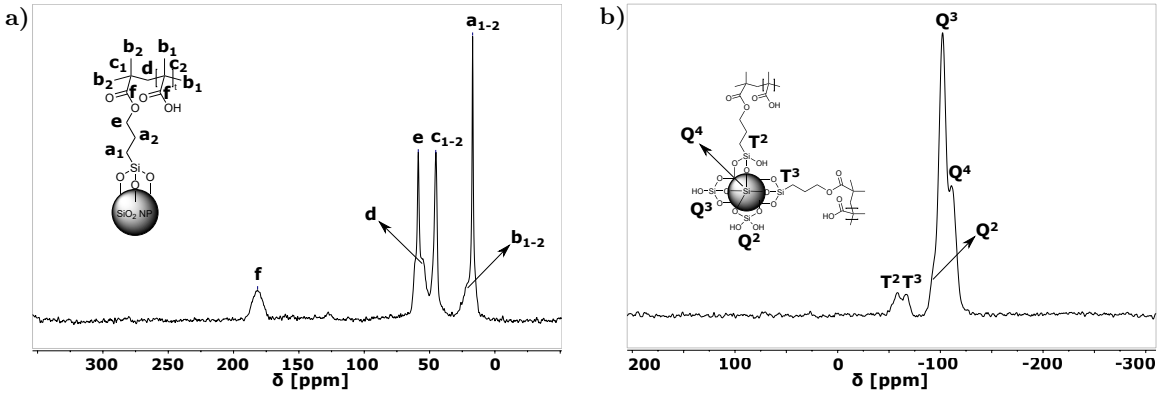


Figure A.14: a) ^{13}C CP/MAS and b) ^{29}Si DP/MAS NMR spectra of **NS-Poly(MAA)** referenced on P. 100.

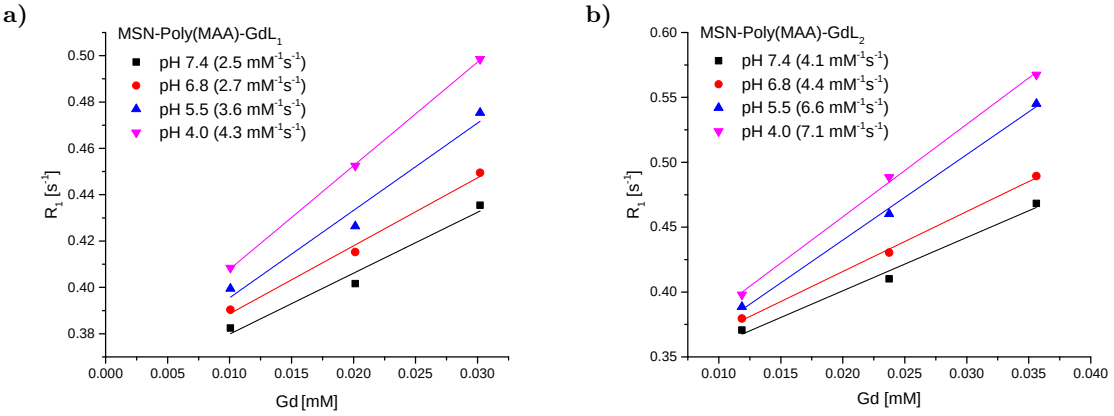


Figure A.15: Linear fits of ^{1}H longitudinal R_1 relaxation rates of a) **MSN-Poly(MAA)-Gd·L$_1$** and b) **MSN-Poly(MAA)-Gd·L$_2$** versus Gd concentration at 4.7 T referenced on P. 101. The graphs were fitted to Eq. (1.6) on P. 6. The linear fits of the data points yielded relaxivities as shown in brackets.

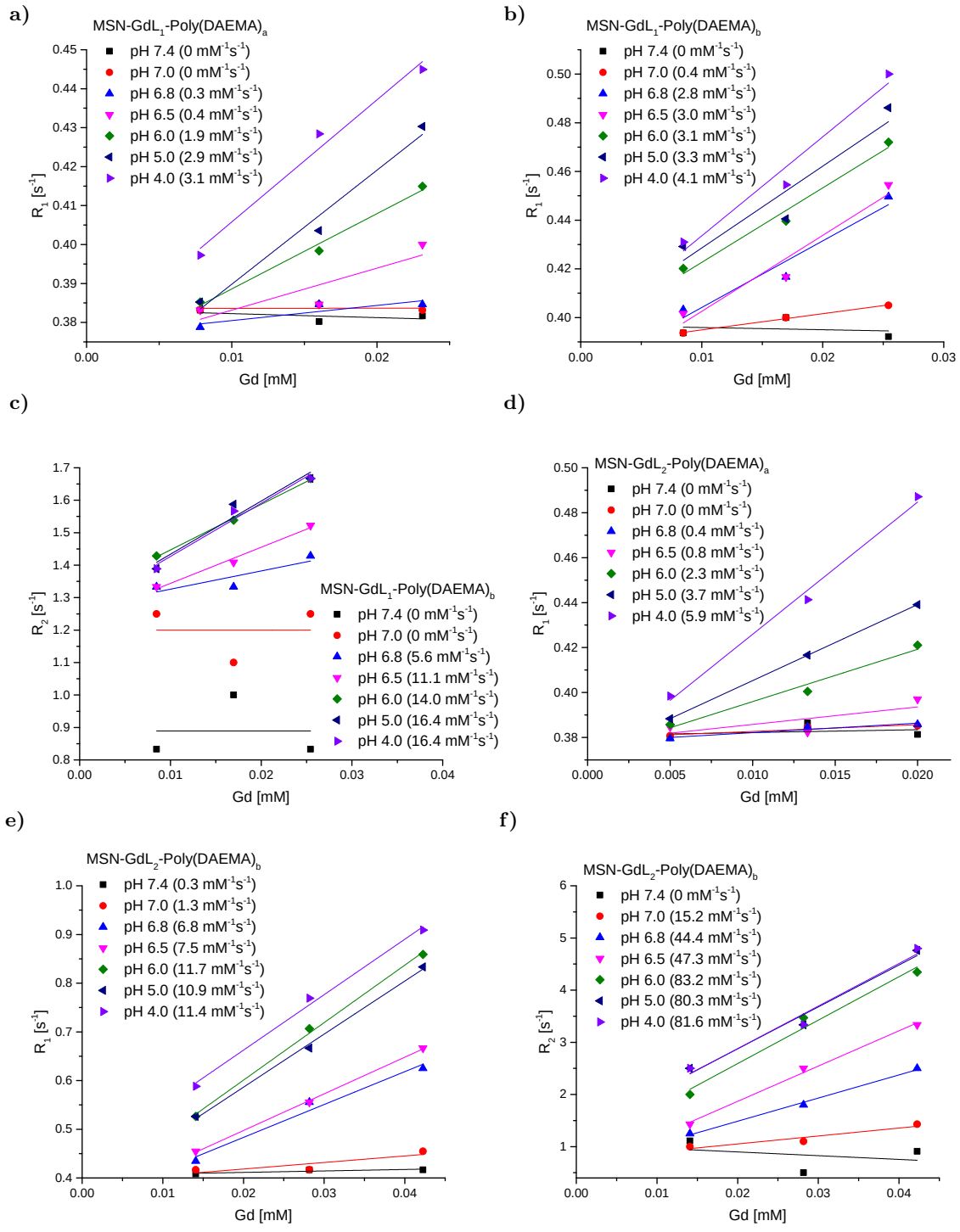


Figure A.16: Linear fits of ^{1}H longitudinal R_1 or transverse R_2 relaxation rates of a) **MSN-Gd·L$_1$-Poly(DAEMA)**$_a$, b-c) **MSN-Gd·L$_1$-Poly(DAEMA)**$_b$, d) **MSN-Gd·L$_2$-Poly(DAEMA)**$_a$ and e-f) **MSN-Gd·L$_2$-Poly(DAEMA)**$_b$ versus Gd concentration as referenced on P. 98. The rates were measured at 4.7 T. The graphs were fitted to Eq. (1.6) on P. 6. The linear fits of the data points yielded relaxivities that were combined with duplicates and averaged to the values shown in brackets.

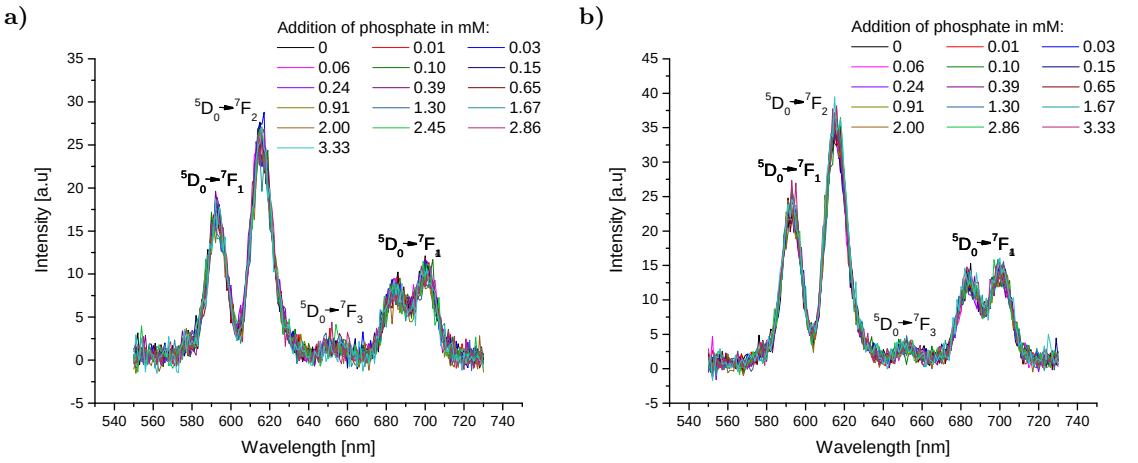


Figure A.17: Comparison of normalised emission spectra of a) **MSN-Eu·L$_1$-Poly(DAEMA)$_b$** and b) **MSN-Poly(MAA)-Eu·L$_1$** referenced on P. 104 as a function of added phosphate (pH 7.4). Conditions: λ_{ex} = 393 nm, 293 K.

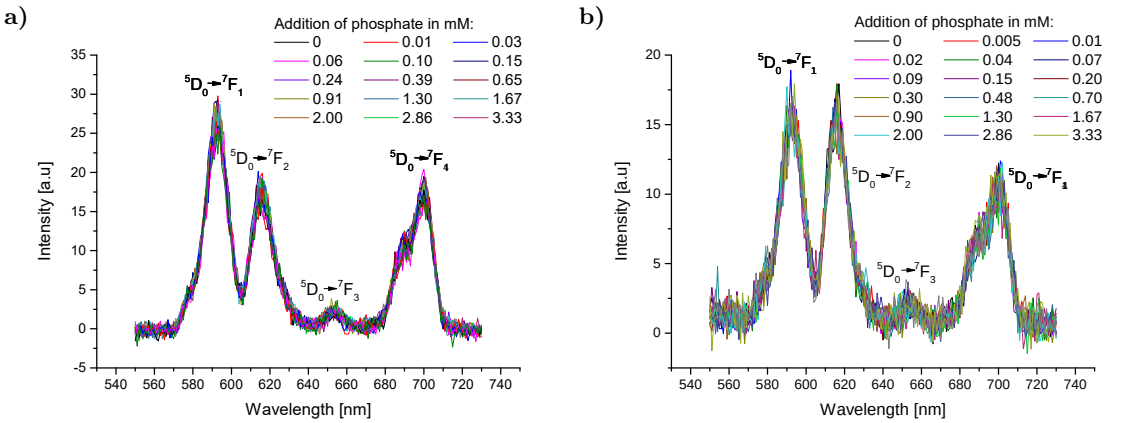


Figure A.18: Comparison of normalised emission spectra of a) **MSN-Eu·L$_2$-Poly(DAEMA)$_b$** and b) **MSN-Poly(MAA)-Eu·L$_2$** referenced on P. 104 as a function of added phosphate (pH 7.4). Conditions: λ_{ex} = 393 nm, 293 K.

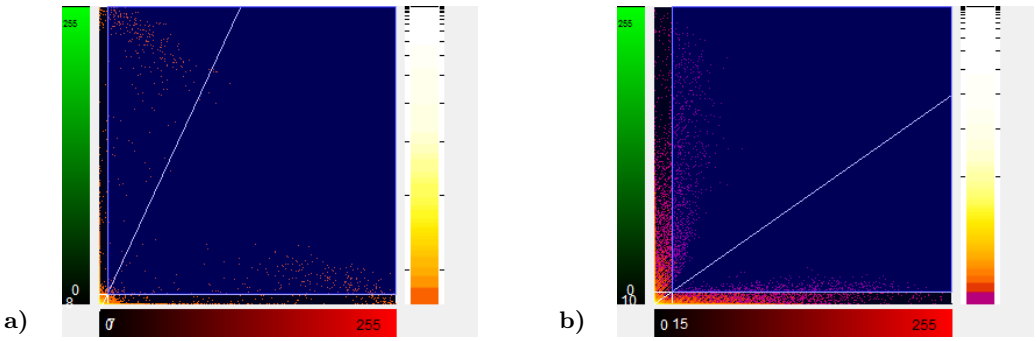


Figure A.19: Scatterplots of co-localisation of red and green channels in a) **MSN-FITC** and b) **MSN-FITC-Poly(DAEMA)$_b$** referenced on P. 108.

Table A.2: pH/pD dependency of the rate of depopulation of excited states of Eu^{3+} nanoparticulate counterparts in H_2O and D_2O, respectively, as referenced on P. 104. Luminescence lifetimes were measured at 293 K, $\lambda_{ex} = 394$ nm and $\lambda_{em} = 615$ nm. The amide NH oscillator has been assumed to contribute 0.075 ms^{-1} to the quenching of the **Eu·L**$_2$ $^5D_0$ excited state. τ_{D_2O} values were determined in D_2O at pD = pH + 0.41.

	MSN-Eu·L$_1$			**MSN-Poly(MAA)**			**MSN-Eu·L$_2$**			**MSN-Poly(MAA)**		
	Poly(DAEMA)$_b$			**-Eu·L$_1$**			**Poly(DAEMA)$_b$**			**-Eu·L$_2$**		
pH	τ_{H_2O} $[ms]$	τ_{D_2O} $[ms]$	q	τ_{H_2O} $[ms]$	τ_{D_2O} $[ms]$	q	τ_{H_2O} $[ms]$	τ_{D_2O} $[ms]$	q	τ_{H_2O} $[ms]$	τ_{D_2O} $[ms]$	q
4.0	1.032	1.422	0.018	1.080	1.072	0.105	0.583	1.891	1.030	0.591	1.568	0.875
5.0	1.034	1.487	0.055	1.073	1.615	0.075	0.593	1.967	1.023	0.636	1.592	0.743
6.0	0.927	1.311	0.079	1.091	1.634	0.066	0.574	1.806	0.960	0.661	1.583	0.667
6.5	0.962	1.448	0.119	1.087	1.652	0.077	0.569	1.715	1.021	0.645	1.576	0.709
6.8	0.964	1.452	0.118	1.088	1.707	0.100	0.560	1.754	1.068	0.668	1.586	0.649
7.0	0.960	1.599	0.199	1.094	1.678	0.075	0.573	1.805	1.038	0.675	1.595	0.646
7.4	0.935	1.406	0.119	1.084	1.630	0.070	0.623	1.697	0.951	0.682	1.580	0.609

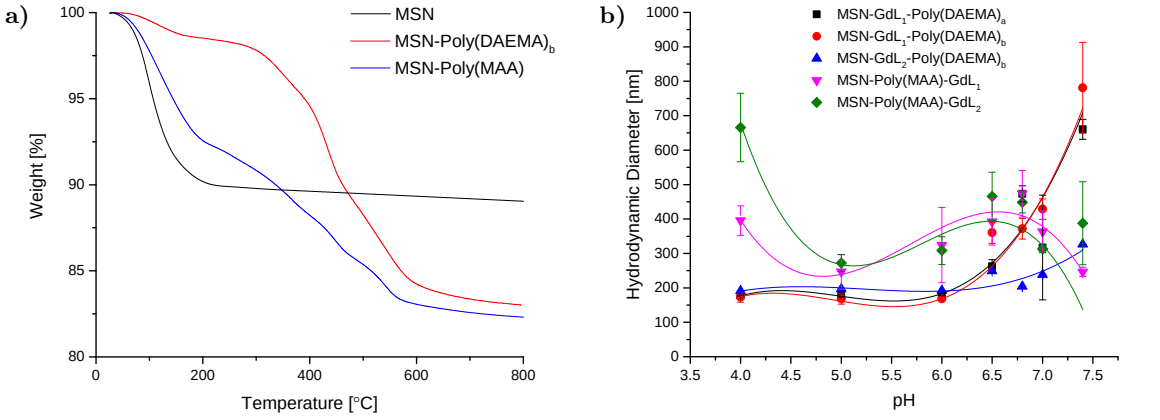


Figure A.20: a) Thermogravimetric analysis of **- MSN**, **- MSN-Poly(DAEMA)$_b$** and **- MSN-Poly(MAA)** showing 0 %, 13 % and 9 % of loss because of the presence of a polymer around 410-440 °C. The weight loss in all three samples around 100 °C corresponds to the evaporation of residual water. b) pH dependency of hydrodynamic diameters of $q = 0$ and $q = 1$ contrast agents loaded poly(DAEMA)-functionalised MSNs (■ **MSN-Gd·L$_1$-Poly(DAEMA)$_a$**, ● **MSN-Gd·L$_1$-Poly(DAEMA)$_b$** and ▲ **MSN-Gd·L$_2$-Poly(DAEMA)$_b$**) as well as poly(MAA)-functionalised MSNs (▼ **MSN-Poly(MAA)-Gd·L$_1$** and ♦ **MSN-Poly(MAA)-Gd·L$_2$**) referenced on P. 91.

Appendix B

Appendix to Chapters V and VI

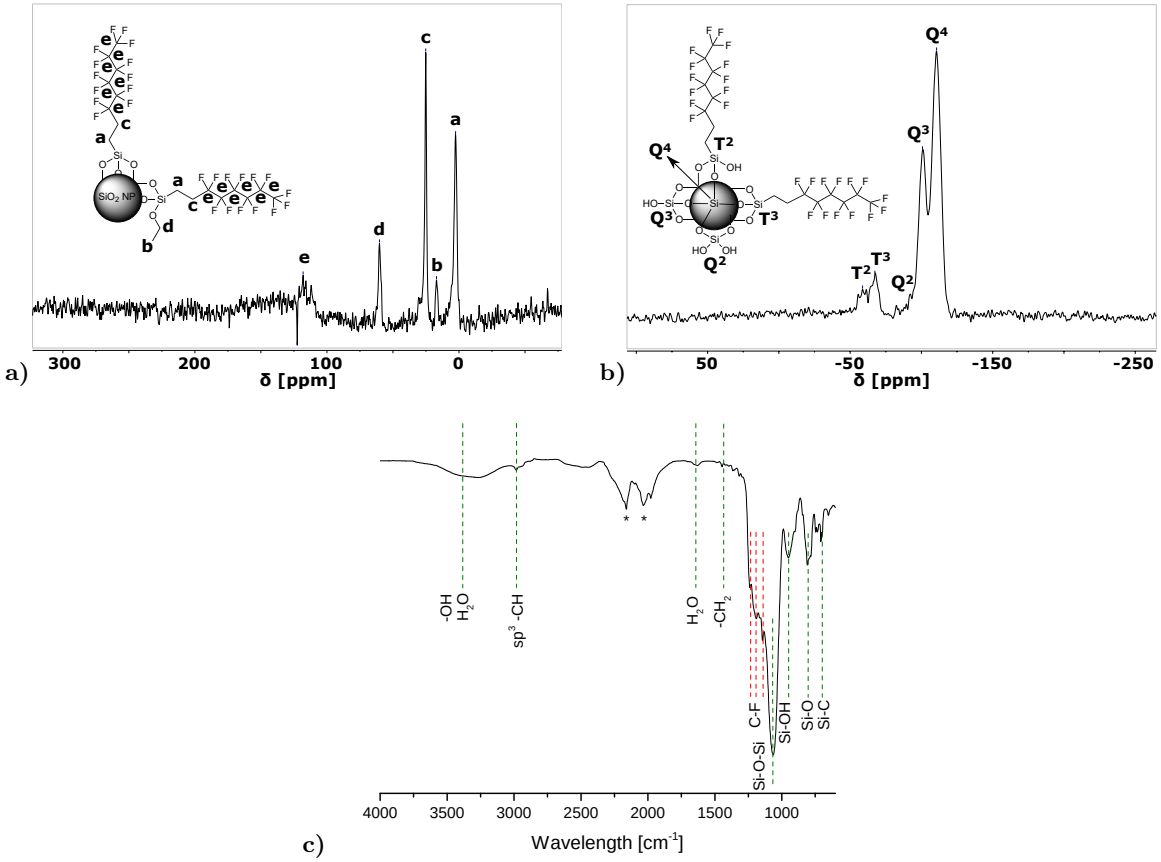


Figure B.1: a) ^{13}C CP/MAS NMR spectrum of **MSN-PFOTS** referenced on P. 112. Fluorine is not decoupled and, as a result, the fluorinated carbons will account for the broadened signals in the range around 120 ppm. b) ^{29}Si DP/MAS NMR spectrum of **MSN-PFOTS** demonstrates a successful PFOTS functionalisation onto the silica surface. c) FTIR shows fluorocarbon stretching bands ($\star$ denote intrinsic diamond absorption).

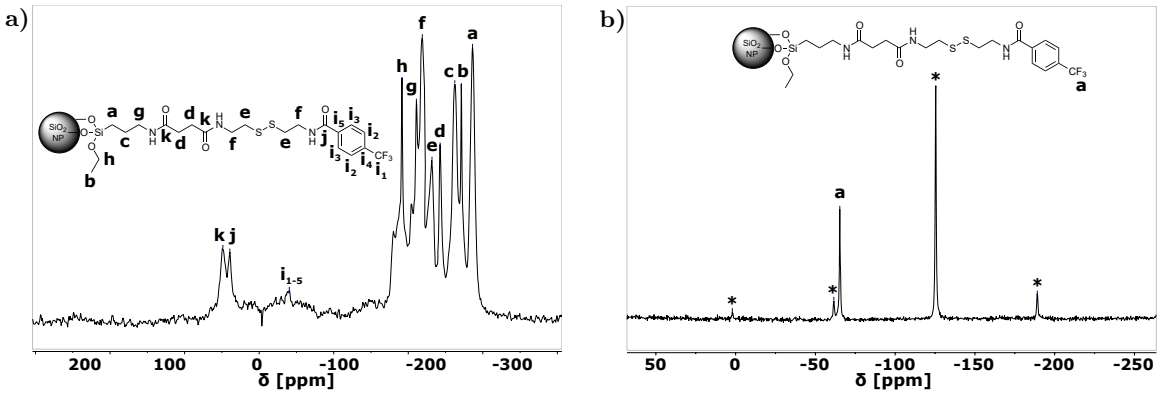


Figure B.2: a) ^{13}C CP/MAS and b) ^{19}F DP/MAS solid-state NMR spectra of **MSN-SS-FBA** referenced on P. 114. Other peaks and sidebands ($\star$) in the fluorine spectrum result from the polytetrafluoroethylene contamination from the sample holder.

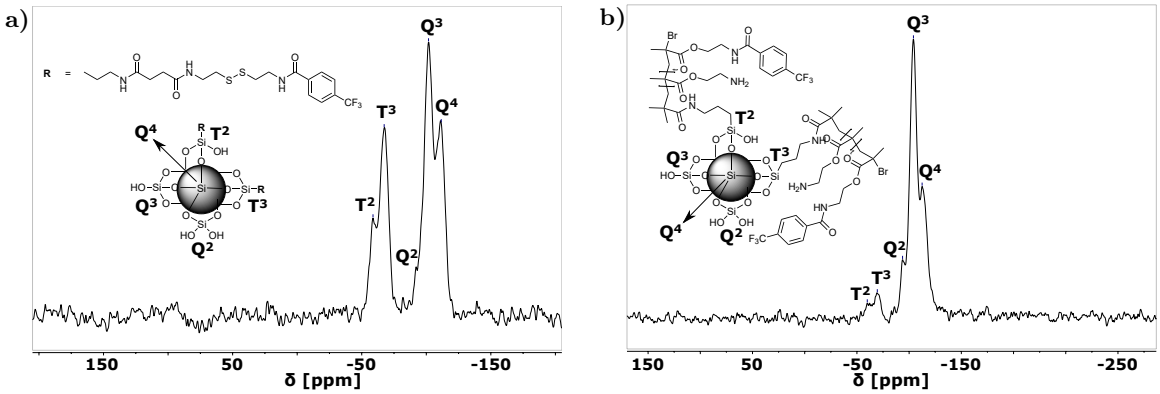


Figure B.3: ^{29}Si DP/MAS solid-state NMR spectra of a) **MSN-SS-FBA** referenced on P. 114 and b) **MSN-Poly(AEMA)-FBA** referenced on P. 116.

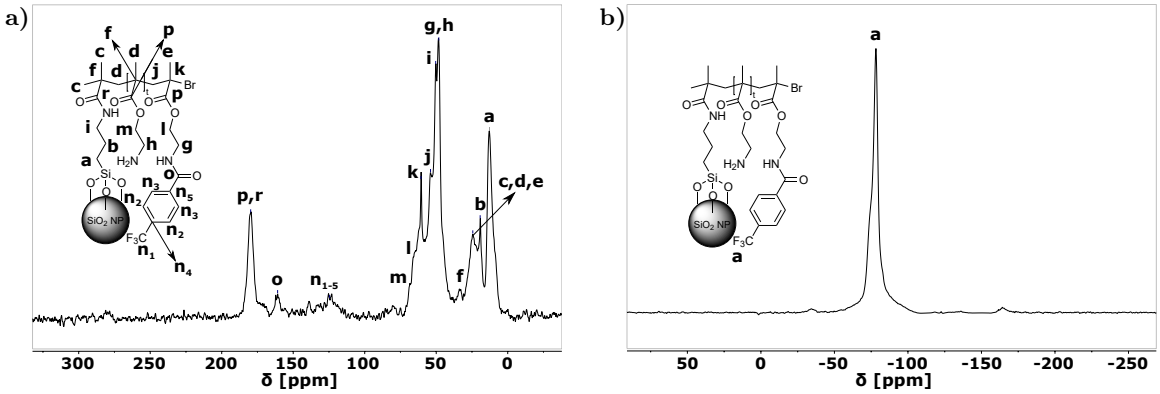


Figure B.4: a) ^{13}C CP/MAS and b) ^{19}F DP/MAS solid-state NMR spectra of **MSN-Poly(AEMA)-FBA** referenced on P. 116.

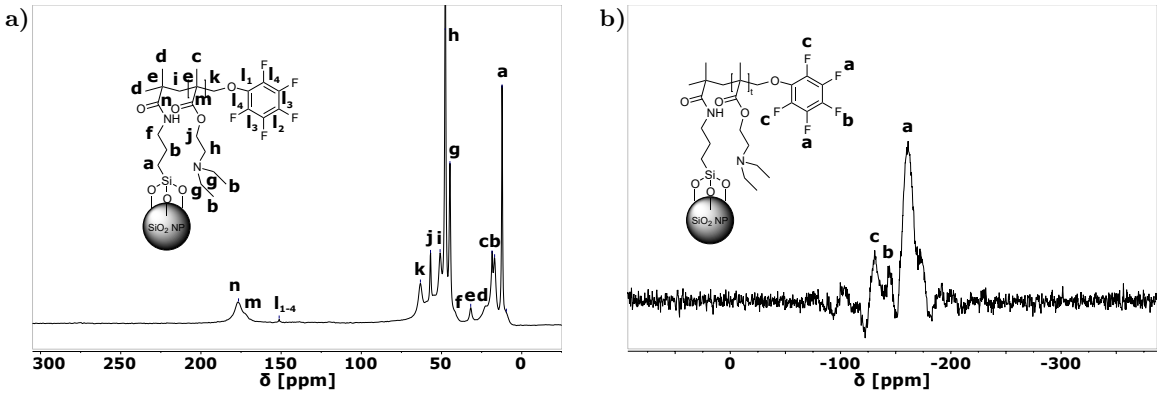


Figure B.5: a) ^{13}C CP/MAS and b) ^{19}F DP/MAS solid-state NMR spectra of **MSN-Poly(DAEMA)-PFP** referenced on P. 116.

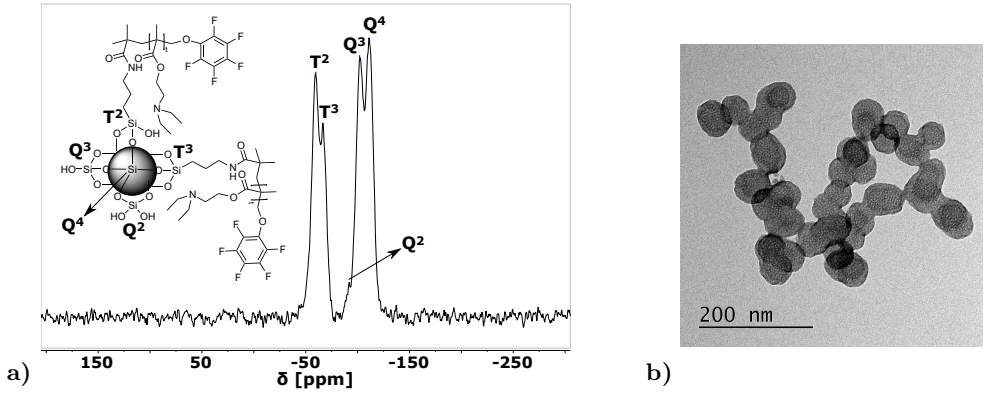


Figure B.6: a) ^{29}Si DP/MAS solid-state NMR spectrum of **MSN-Poly(DAEMA)-PFP** referenced on P. 116. b) TEM image of **MSN-Dendri-CF$_3$** referenced on P. 117.

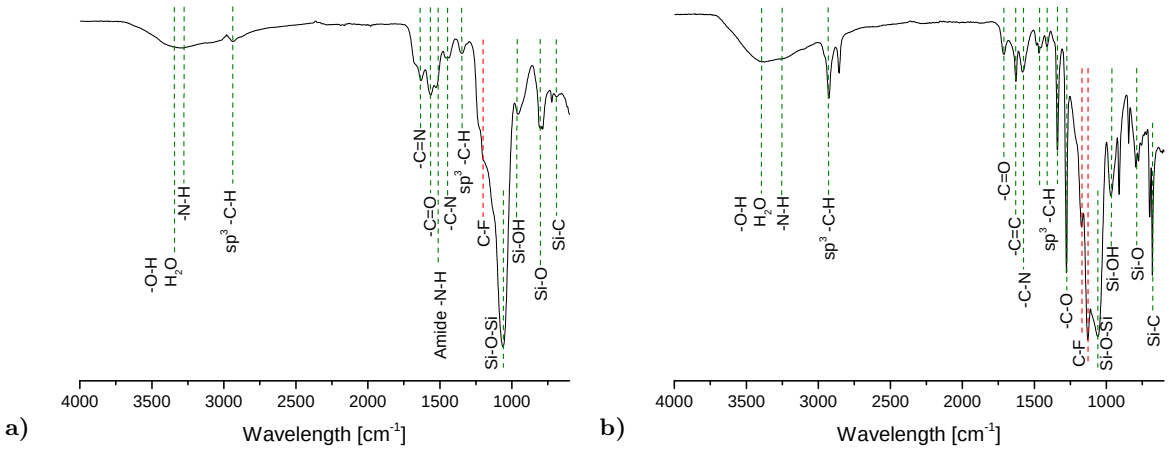


Figure B.7: FTIR spectra of a) **MSN-Dendri-CF$_3$** referenced on P. 117 and b) **NS-OA-BFB** particles referenced on P. 119.

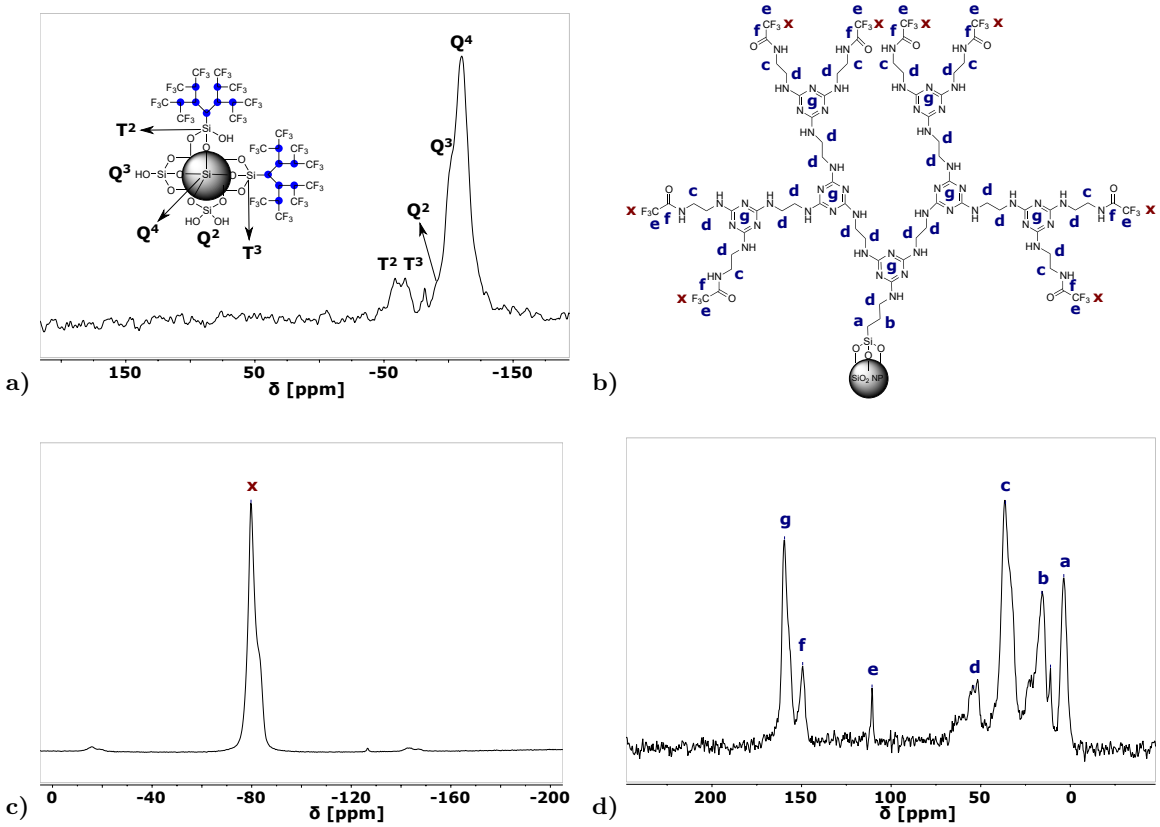


Figure B.8: a) ^{29}Si DP/MAS, c) ^{19}F DP/MAS and d) ^{13}C CP/MAS solid-state NMR spectra of **MSN-Dendri-CF$_3$** referenced on P. 117.

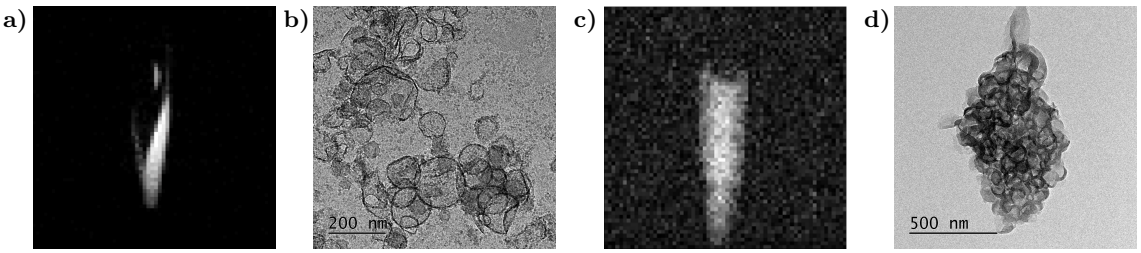


Figure B.9: ^{19}F MRI and TEM images of silica nanocapsules filled with perfluorodecalin referenced on P. 120. a-b) **NCS-PFD$_a$**: SNR = 280, $T_1 = 1430 \pm 10$ ms, $T_2 = 49 \pm 6$ ms, concentration = 2 mg/mL and c-d) **NCS-PFD$_b$**: SNR = 150, $T_1 = 1150 \pm 20$ ms, $T_2 = 18 \pm 4$ ms, concentration = 12 mg/mL. Unstable **NCS-PFD$_a$** or **NCS-PFD$_b$** were obtained when too little tetraethyl orthosilicate or too much dimethyloctadecyl[3-(trimethoxysilyl)propyl]ammonium chloride were implemented. MRI parameters: GEMS, a): TR = 0.5 s, TE = 0.8 ms, nt = 4, flip = 90°, matrix = 64 x 64, FOV = 40 mm x 40 mm, Thk = 5 mm, sw = 10 kHz; c): TR = 0.5 s, TE = 1 ms, nt = 4, flip = 90°, matrix = 64 x 64, FOV = 32 mm x 32 mm, Thk = 5 mm, sw = 100 kHz.

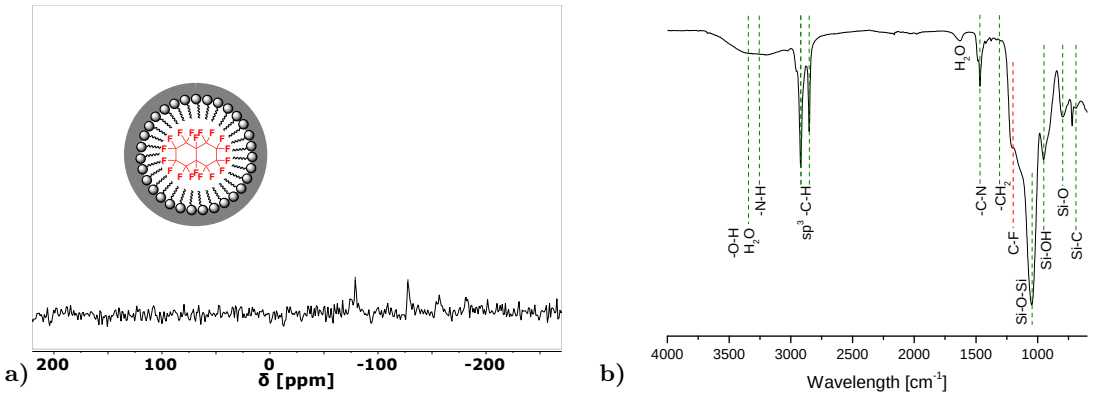


Figure B.10: a) ^{19}F DP/MAS solid-state NMR and b) FTIR spectra of **NCS-PFD**$_c$ show that fluorine is not present in the solid phase, but rather in the liquid phase as confirmed by the solution ^{19}F NMR in Figure 5.9 on P. 121.

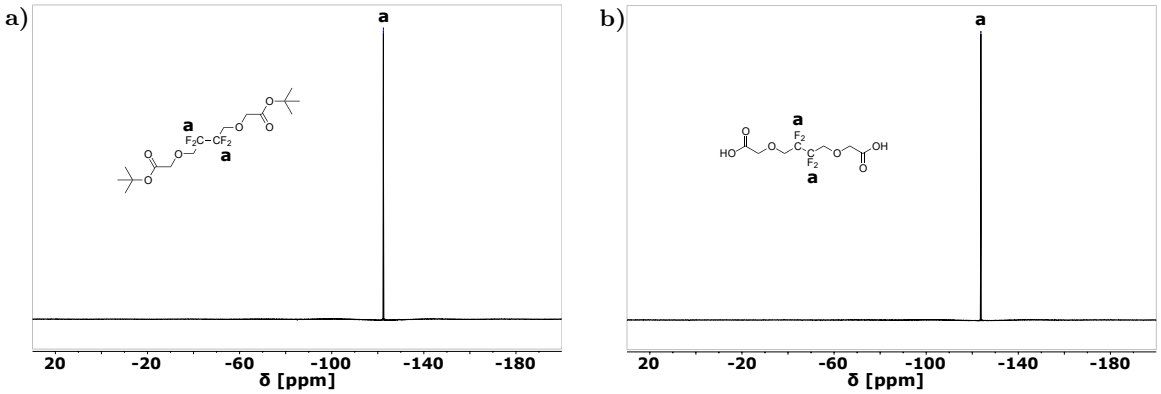


Figure B.11: Solution ^{19}F NMR spectra of a) *t*Bu-protected **F$_4$Ac** and b) *t*Bu-deprotected **F$_4$Ac** referenced on P. 122.

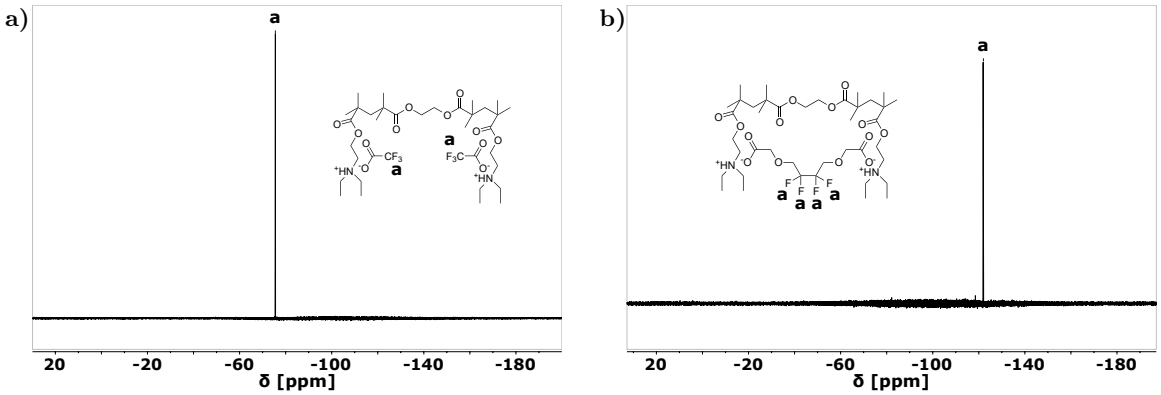


Figure B.12: ^{19}F NMR spectra of polymeric nanoparticles complexed with ^{19}F MRI reporters. a) **Poly(DAEMA)$_a$-TFA** and b) **Poly(DAEMA)$_a$-TFAc** dispersed in H_2O and referenced on P. 122.

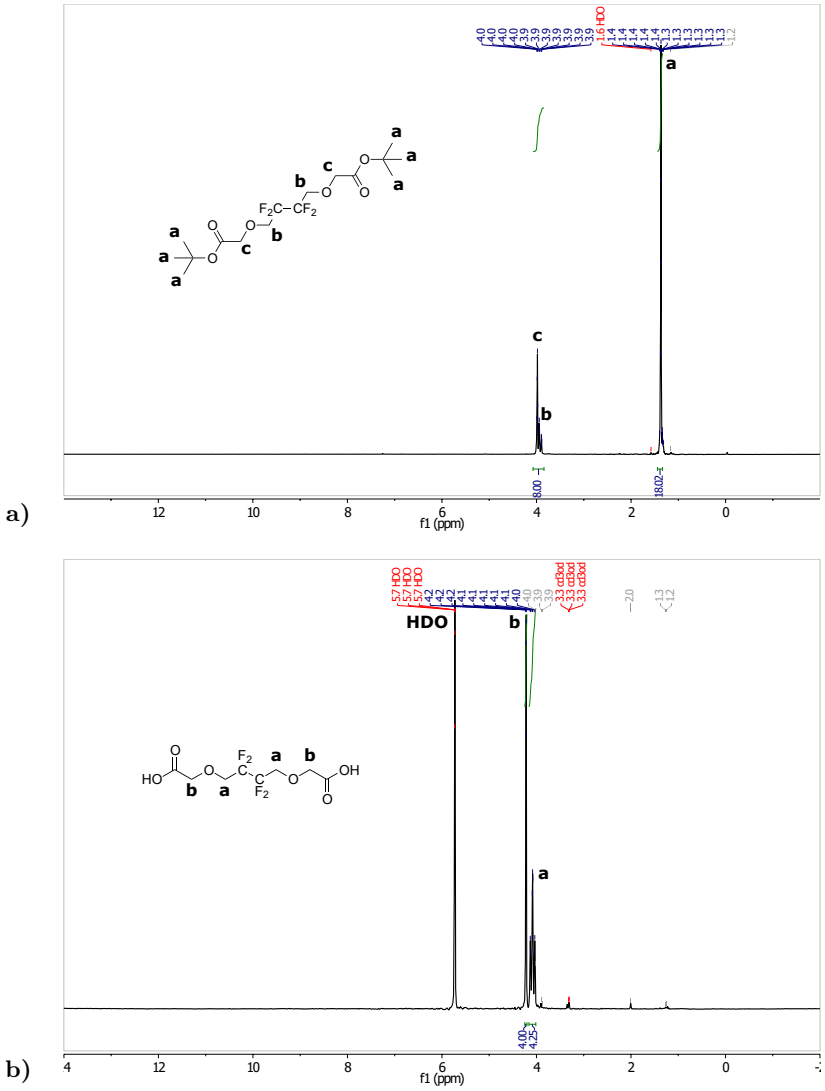


Figure B.13: ^{1}H NMR spectra of a) *t*Bu-protected $\mathbf{F_4Ac}$ and b) *t*Bu-deprotected $\mathbf{F_4Ac}$ as referenced on P. 122.

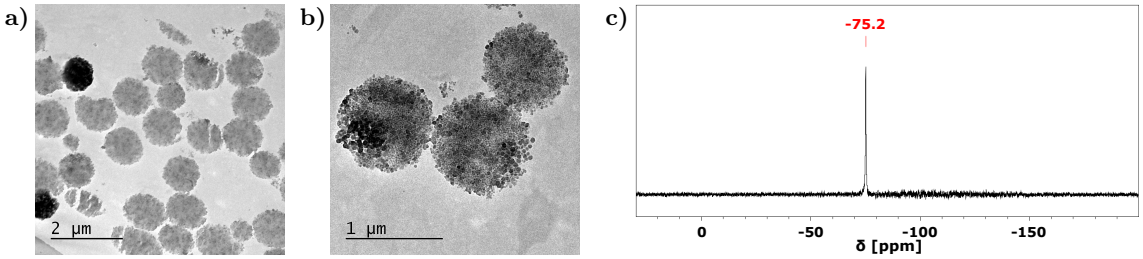


Figure B.14: a-b) TEM images and c) ^{19}F NMR signal of silica coated polymers pre-complexed with trifluoroacetic acid (**Poly(DAEMA)$_a$-TFA-Si**), dispersed in H_2O and referenced on P. 123.

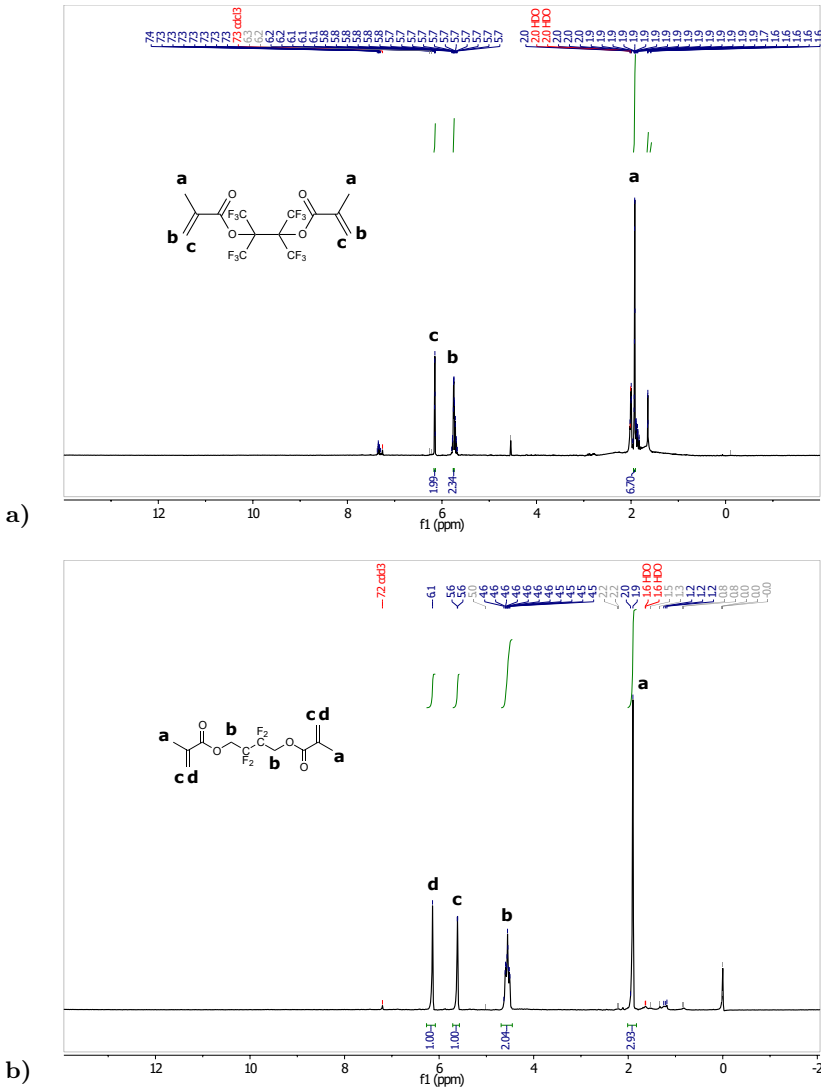


Figure B.15: ^{1}H NMR spectra of symmetric fluorinated ^{19}F MRI reporters a) $\mathbf{F}_{12}\mathbf{M}_2$ and b) $\mathbf{F}_4\mathbf{M}_2$ in MeOD referenced on P. 125.

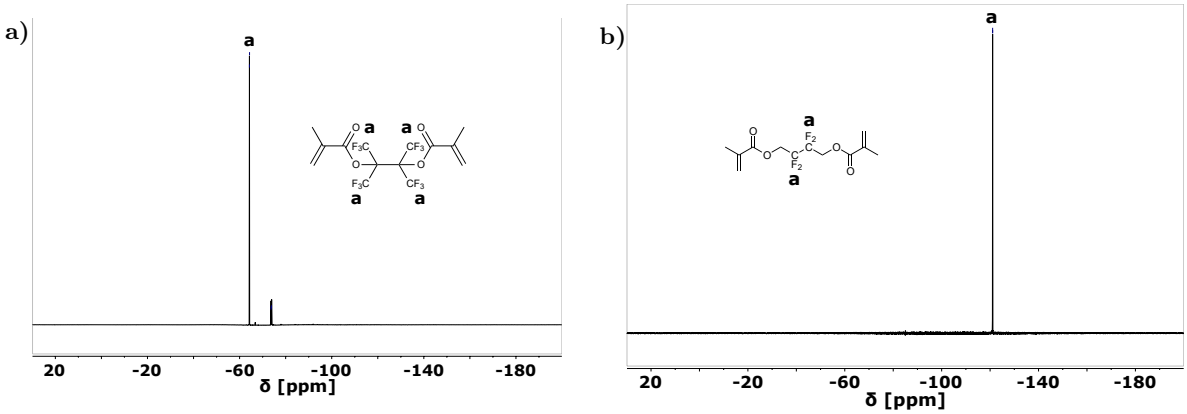


Figure B.16: ^{19}F NMR spectra of a) $\mathbf{F}_{12}\mathbf{M}_2$ and b) $\mathbf{F}_4\mathbf{M}_2$ in MeOD referenced on P. 126.

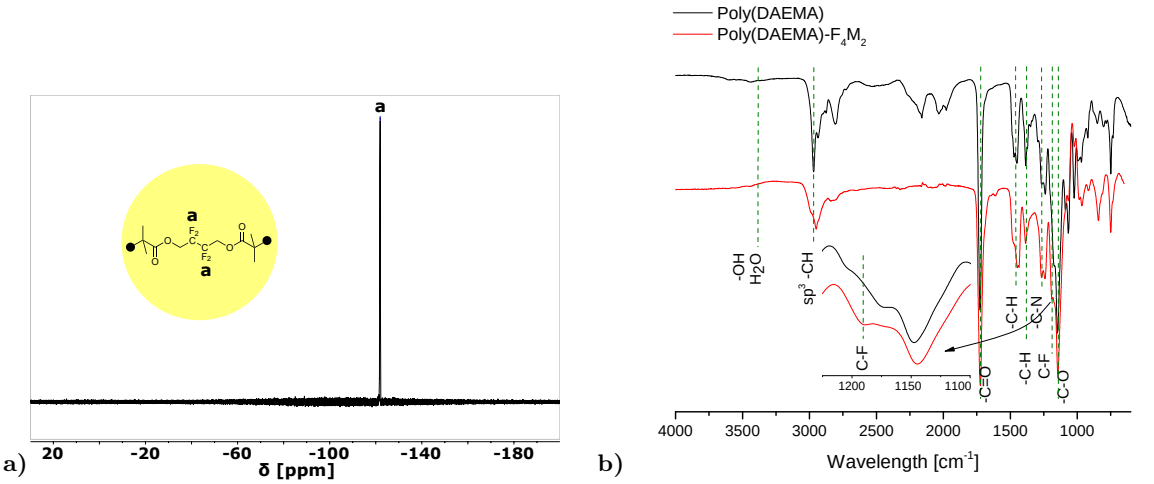


Figure B.17: a) ^{19}F NMR and b) FTIR spectra of poly(DAEMA) cross-linked with $\mathbf{F_4M_2}$ reporter (**Poly(DAEMA)**$_a$**-F**$_4$**M**$_2$) referenced on P. 126. For the NMR measurements, the polymers were dispersed in H_2O.

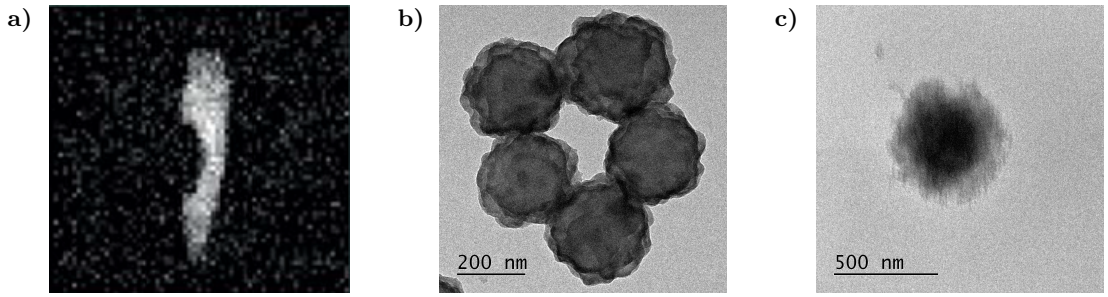


Figure B.18: a) ^{19}F MRI image of **Poly(DAEMA)**$_a$**-F**$_4$**M**$_2$ referenced on P. 126 and obtained with the following MRI parameters: GEMS, TR = 0.5 s, TE = 0.8 ms, nt = 16, flip = 90°, matrix = 64 x 64, FOV = 40 mm x 40 mm, Thk = 5 mm, concentration = 20 mg/mL. TEM images show **Poly(DAEMA)**$_b$ b) before and c) after $\mathbf{F_4M_2}$ incorporation.

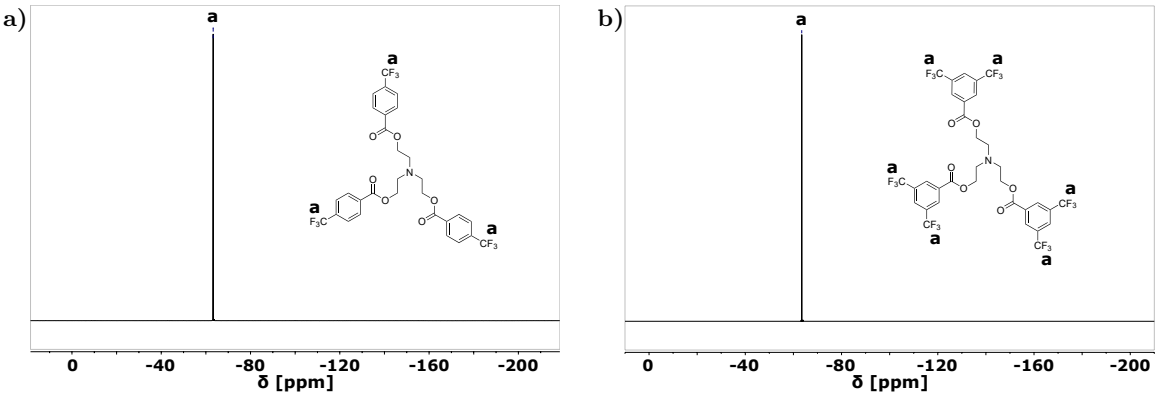


Figure B.19: ^{19}F NMR spectra of a) $\mathbf{T_0F}_{9a}$ and b) $\mathbf{T_0F}_{18b}$ in $CDCl_3$ referenced on P. 127.

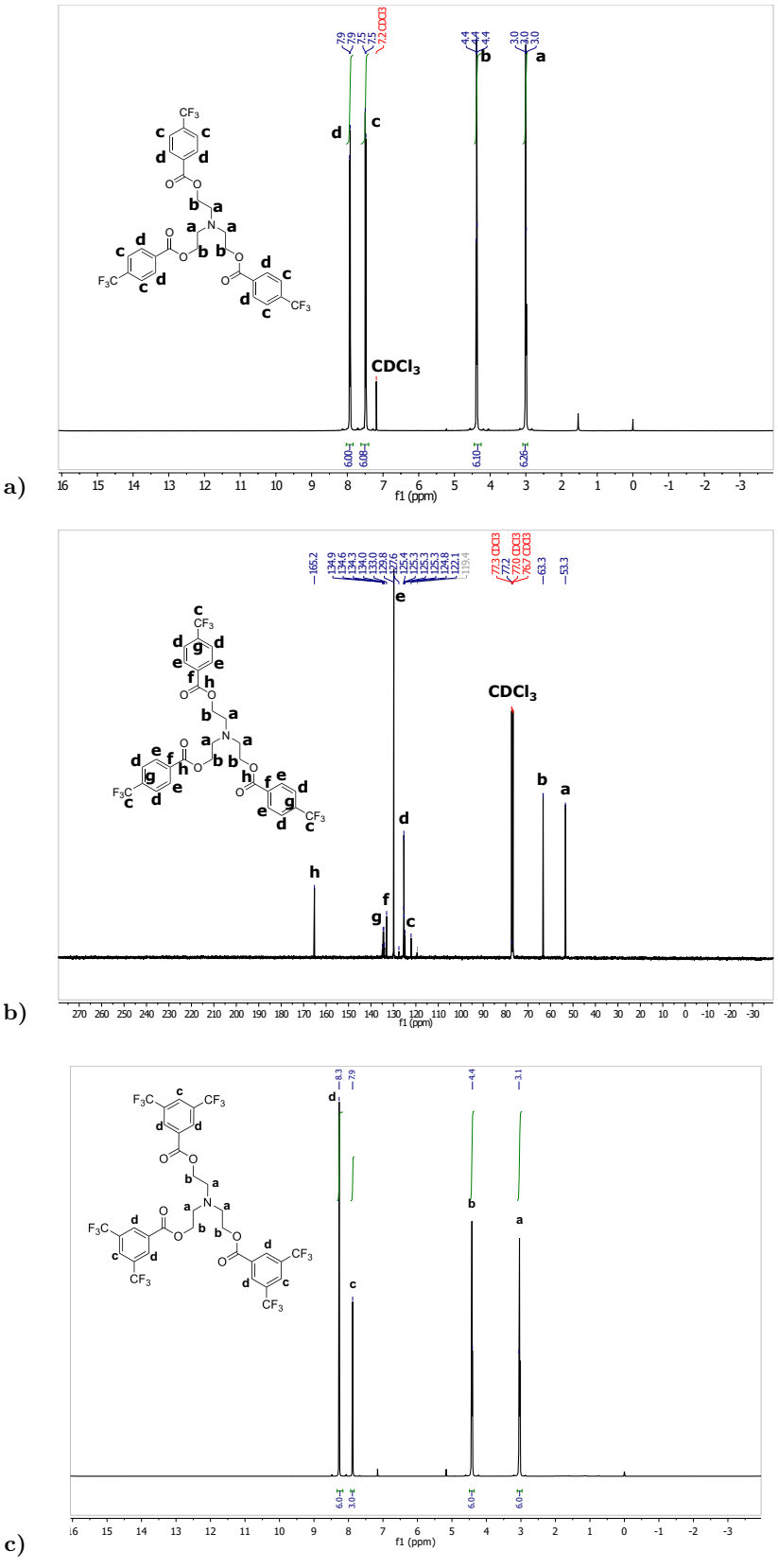


Figure B.20: a) ^{1}H and b) ^{13}C NMR spectra of $\mathbf{T_0F}_{9a}$ as well as c) ^{1}H NMR spectrum of $\mathbf{T_0F}_{18b}$ in $CDCl_3$ referenced on P. 127.

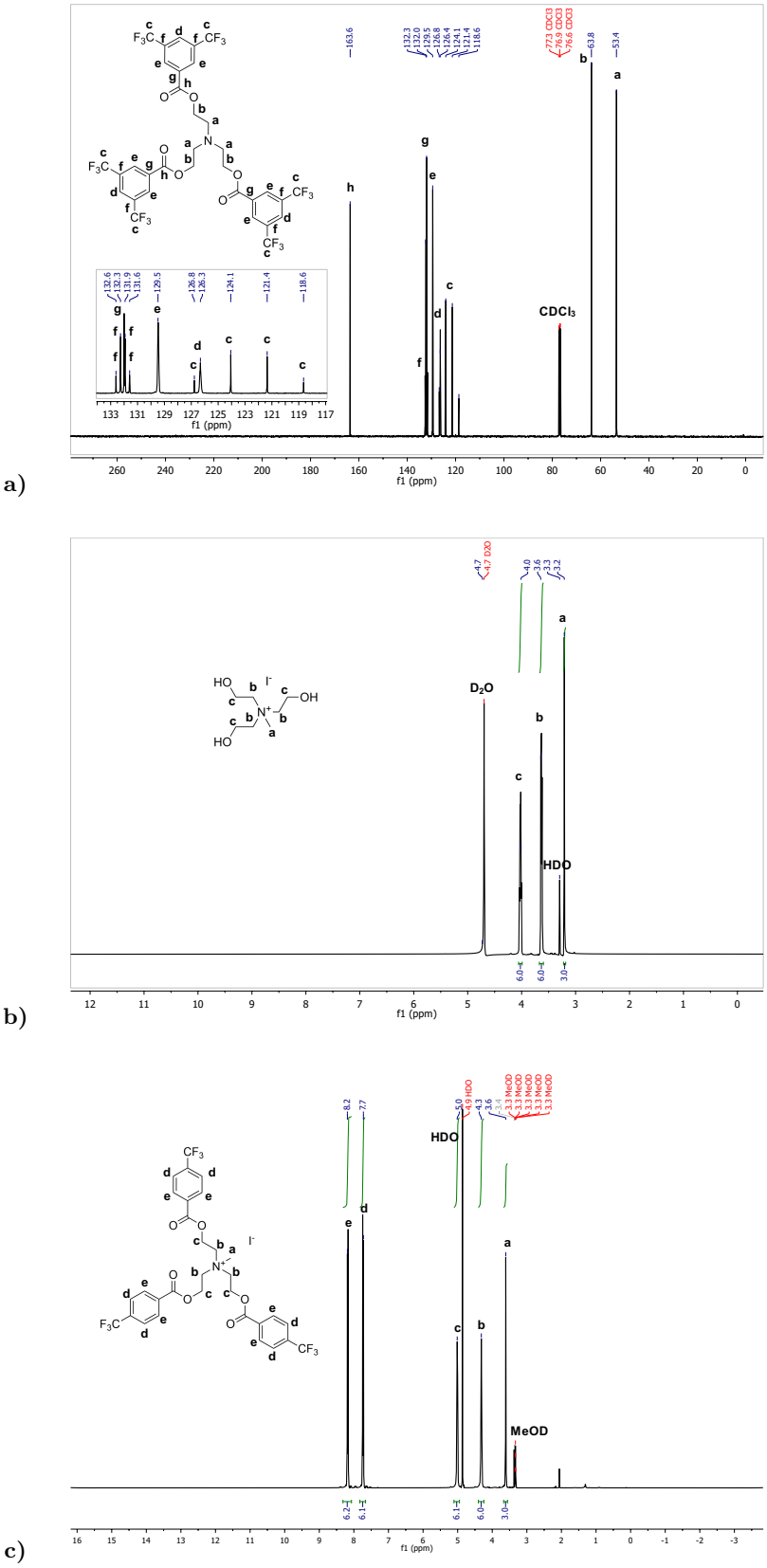


Figure B.21: a) ^{13}C NMR spectrum of $\mathbf{T_0F}_{18b}$ and ^{1}H NMR spectra of b) $\mathbf{T}_3$ in D_2O and c) $\mathbf{T_3F}_{9a}$ in MeOD referenced on P. 127.

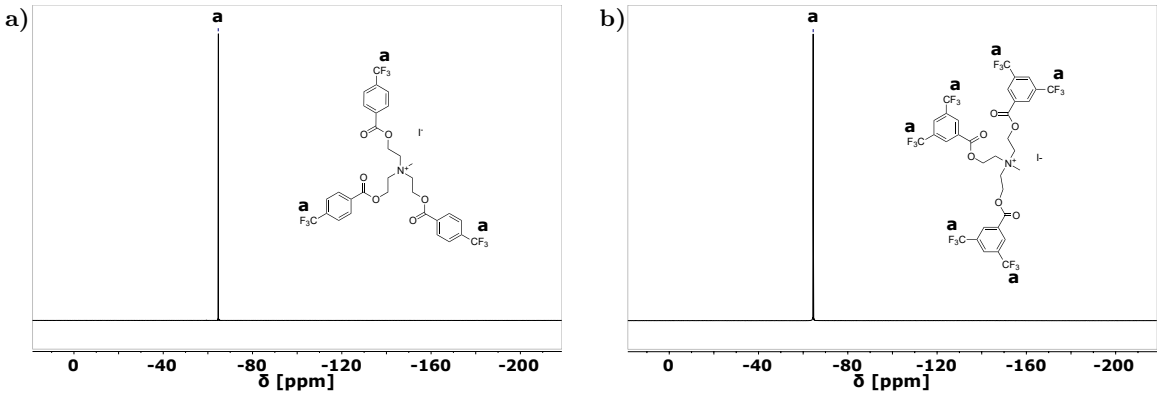


Figure B.22: ^{19}F NMR spectra of a) $\mathbf{T_3F}_{9a}$ and b) $\mathbf{T_3F}_{18b}$ in MeOD referenced on P. 127.

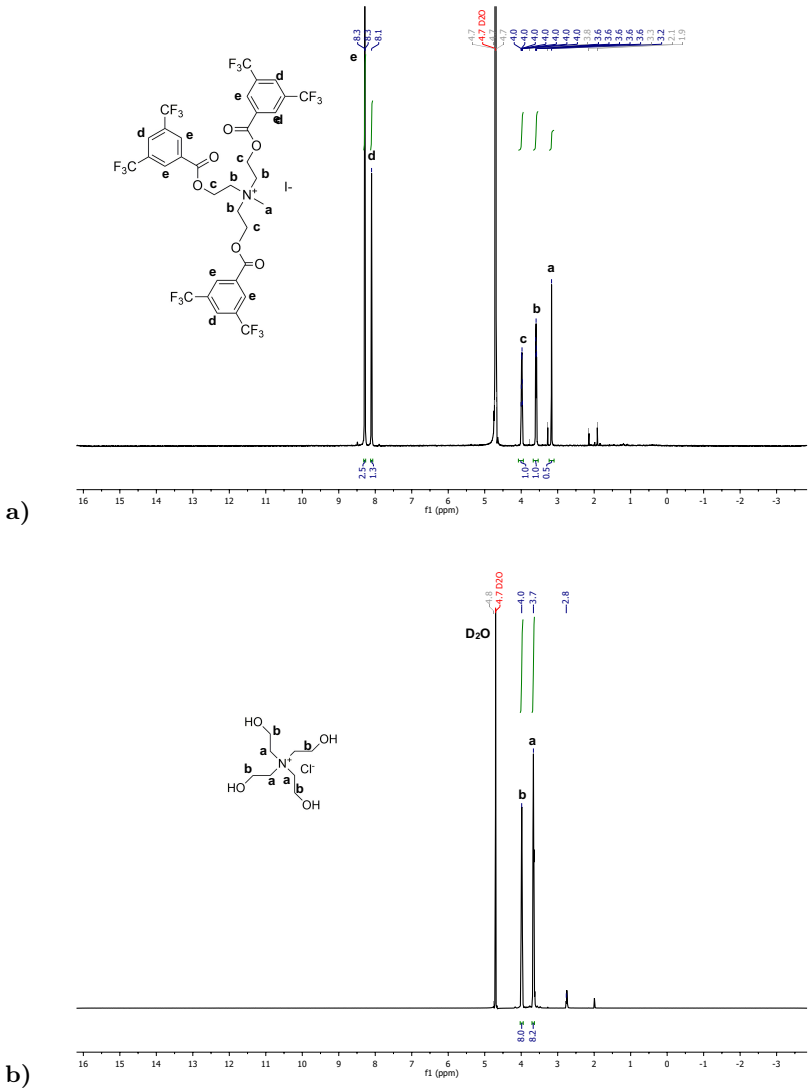


Figure B.23: ^{1}H NMR spectra of a) $\mathbf{T_3F}_{18b}$ and b) $\mathbf{T}_4$ in D_2O referenced on P. 127.

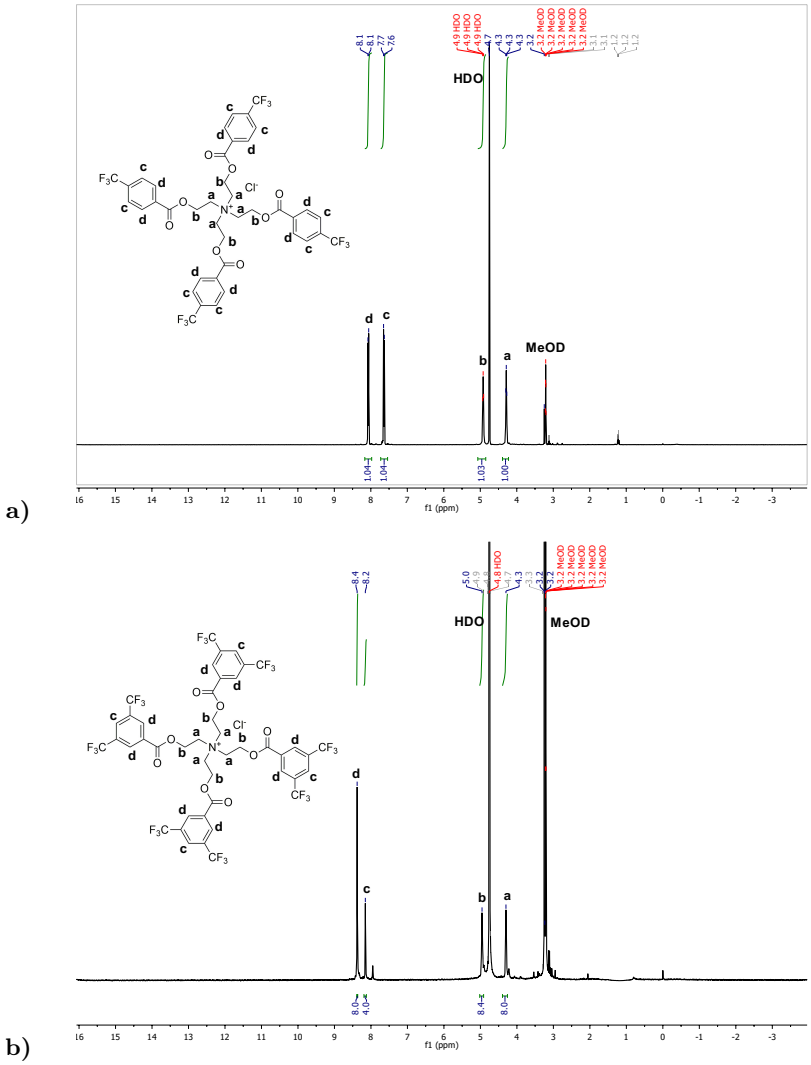


Figure B.24: ^{1}H NMR spectra of a) $\mathbf{T_4F_{12}}_a$ and b) $\mathbf{T_4F_{24}}_b$ in MeOD referenced on P. 127.

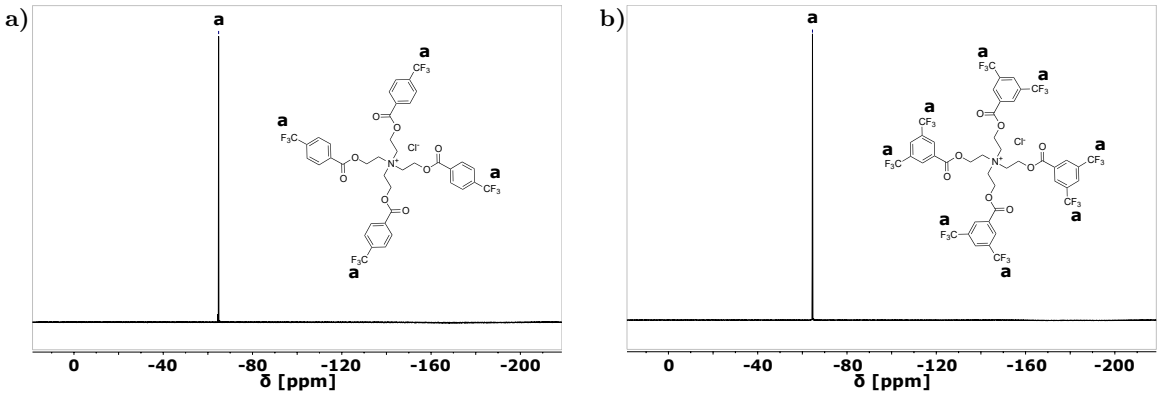


Figure B.25: ^{19}F NMR spectra of a) $\mathbf{T_4F_{12}}_a$ and b) $\mathbf{T_4F_{24}}_b$ in MeOD referenced on P. 127.

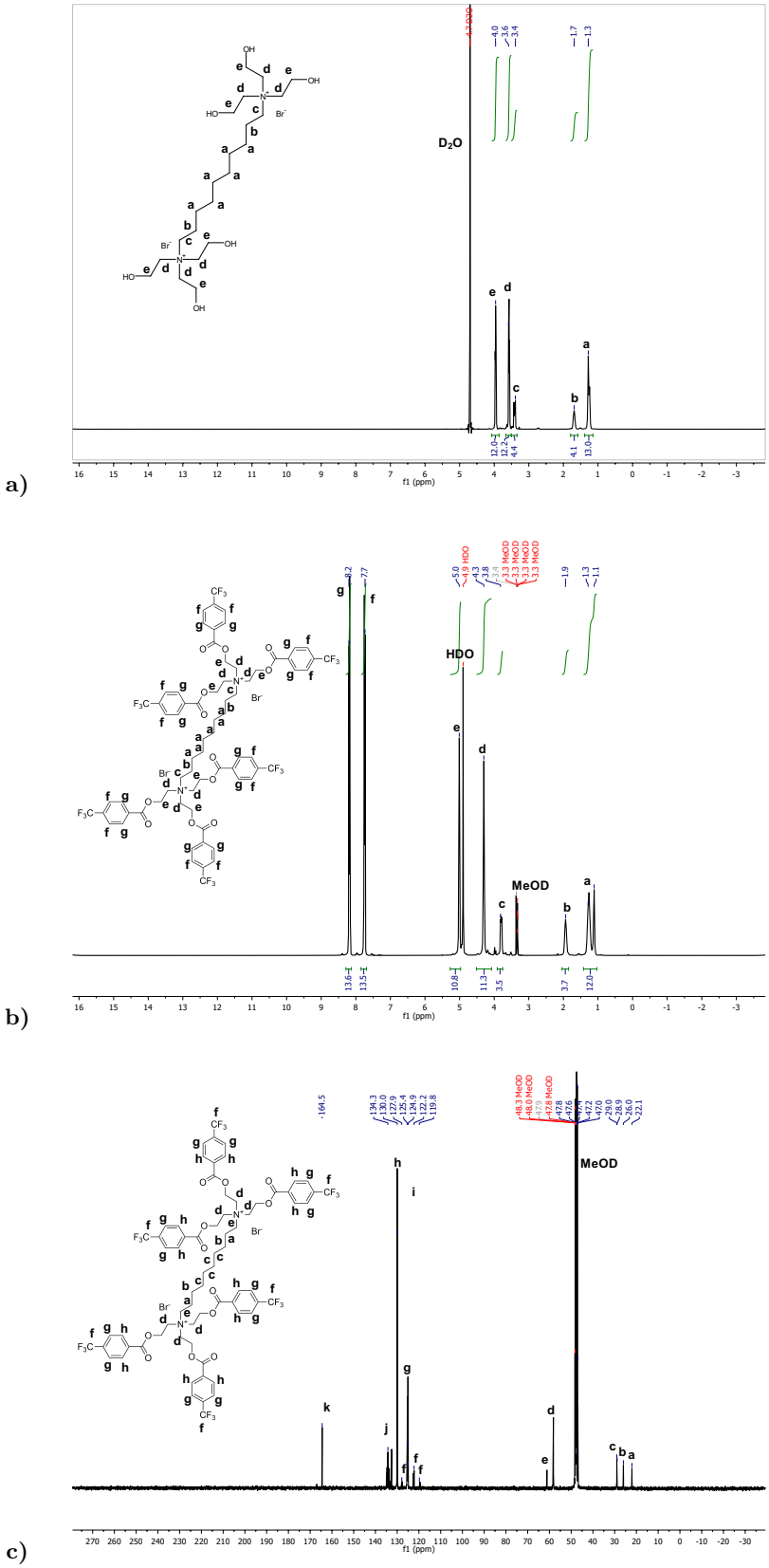


Figure B.26: ^{1}H NMR spectra of a) $\mathbf{T}_6$ in D_2O and b) $\mathbf{T_6F}_{18a}$ in MeOD. c) ^{13}C NMR spectrum of the latter referenced on P. 127.

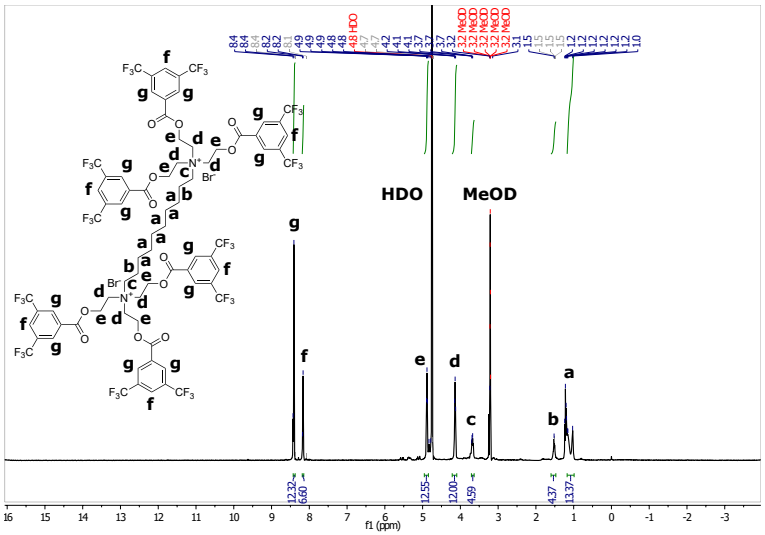


Figure B.27: ^{1}H NMR spectrum of $\mathbf{T_6F_{36b}}$ in MeOD referenced on P. 127.

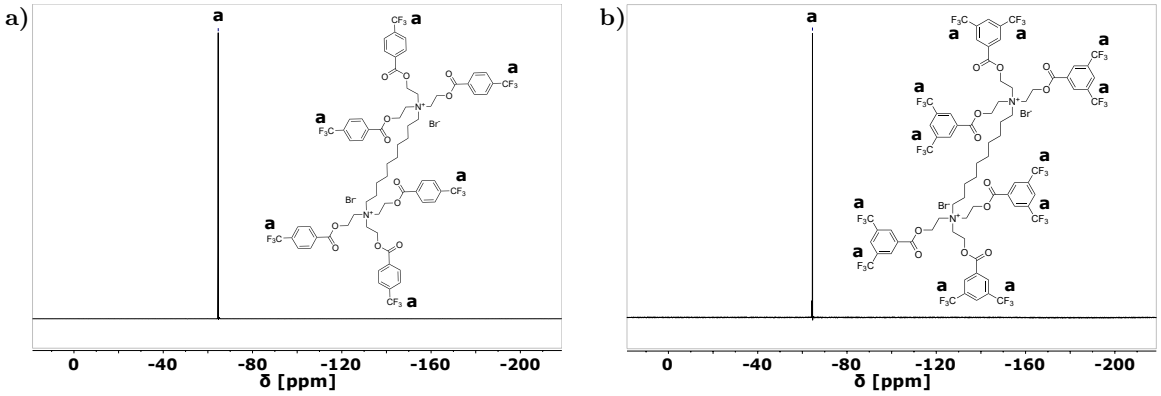


Figure B.28: ^{19}F NMR spectra of a) $\mathbf{T_6F_{18a}}$ and b) $\mathbf{T_6F_{36b}}$ in MeOD referenced on P. 127.

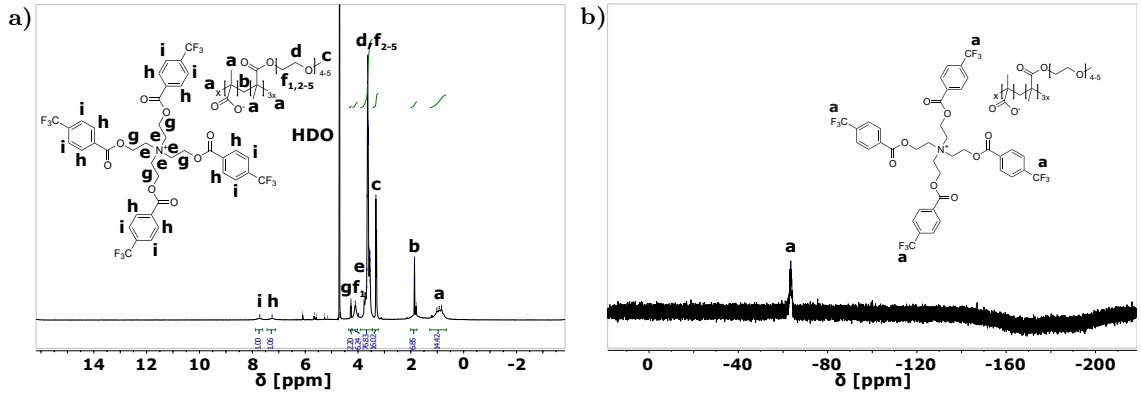


Figure B.29: a) ^{1}H and b) ^{19}F NMR spectra of **Poly(MAA$_1$-PEG$_3$)-T$_4$F$_{12a}$** in D_2O referenced on P. 131.

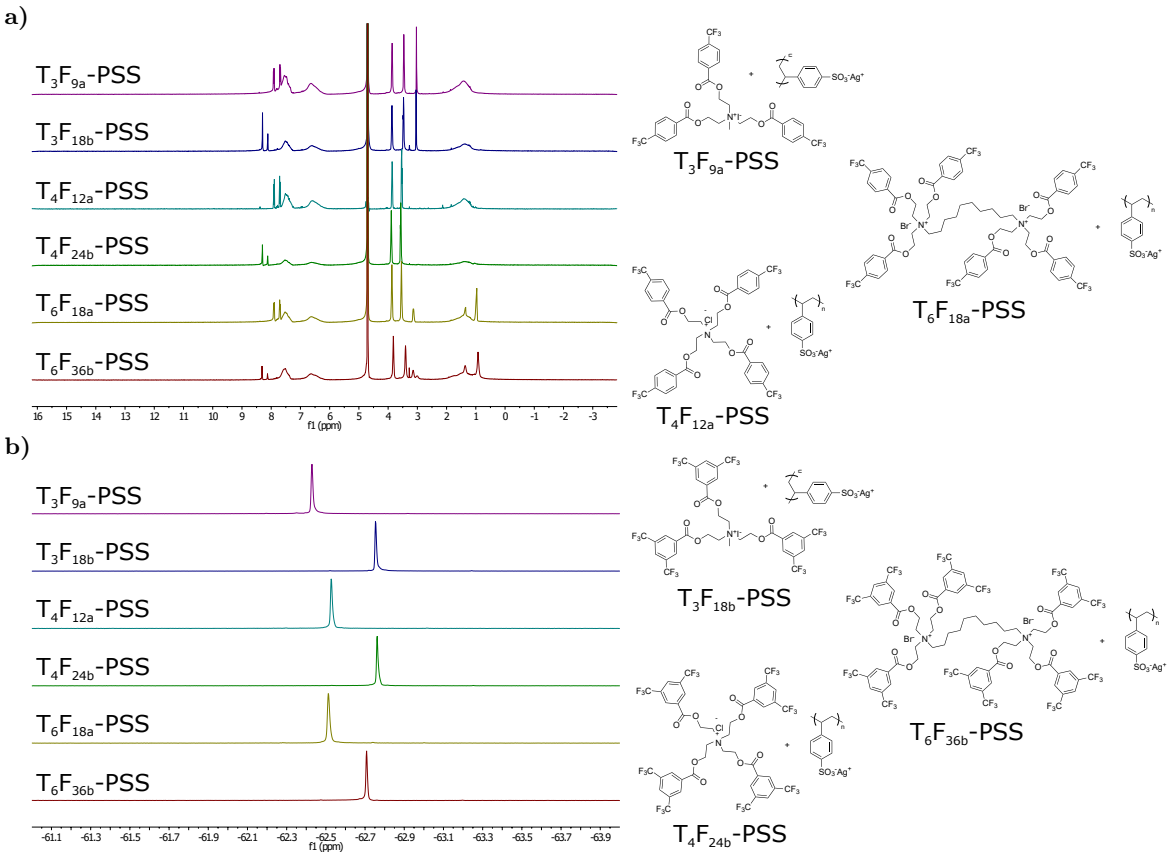


Figure B.30: a) ^{1}H and b) ^{19}F NMR spectra of fluorinated quaternary ammonium salts (in D_2O) reacted with polystyrene sulphonate in the presence of silver(I)-oxide as referenced on P. 131. The chemical shifts show that beside complexation, a hydrolysis of either trifluoromethyl or bis(trifluoromethyl) benzoates occurred.

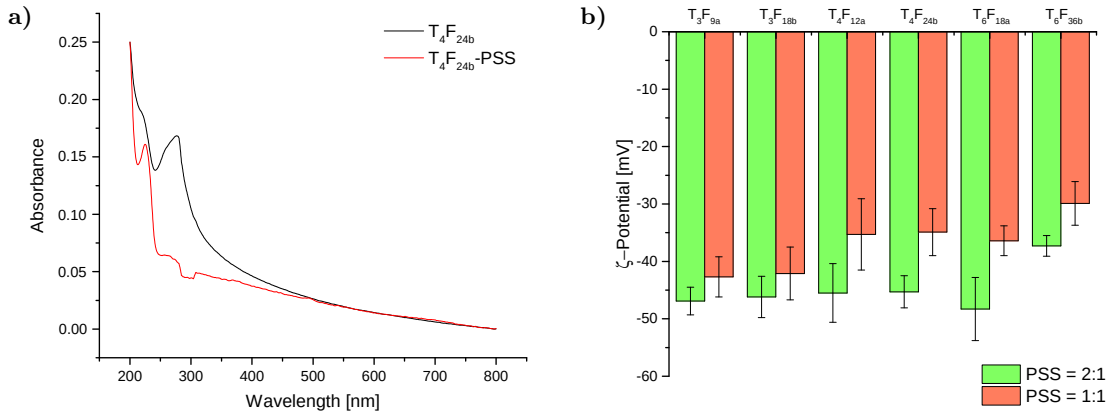


Figure B.31: a) UV-vis spectrum showing the decrease in hypsochromic shift and hyperchromic effect upon $\mathbf{T_4F_{24b}}$ complexation with polystyrene sulphonate resulting in $\mathbf{T_4F_{24b}}$-**PSS** as referenced on P. 131. b) After complexation, all zeta-potentials were higher than the one of pure polystyrene sulphonate, which has a zeta-potential of -53.3 ± 2.4 mV.

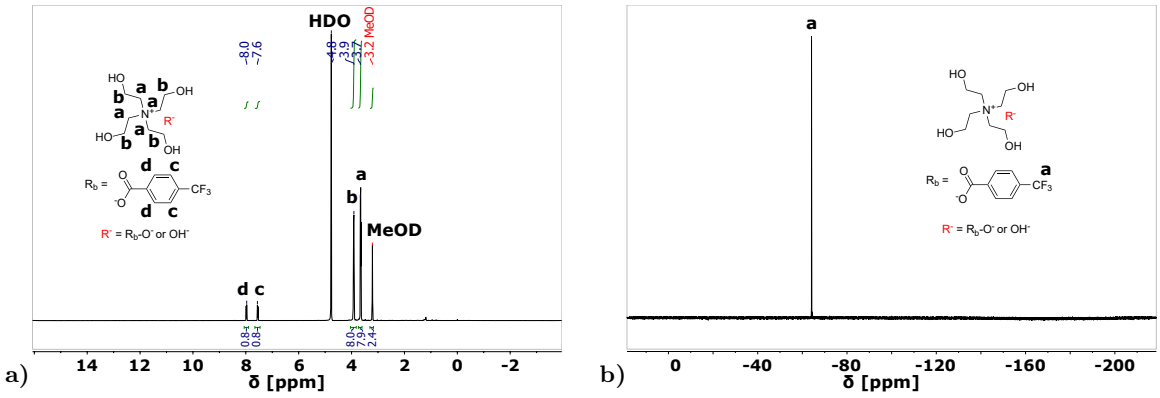


Figure B.32: a) ^{1}H and b) ^{19}F NMR spectra of $\mathbf{T_4F_{12a}}$ in MeOD after the compound was run through an Amberlite column as referenced on P. 130.

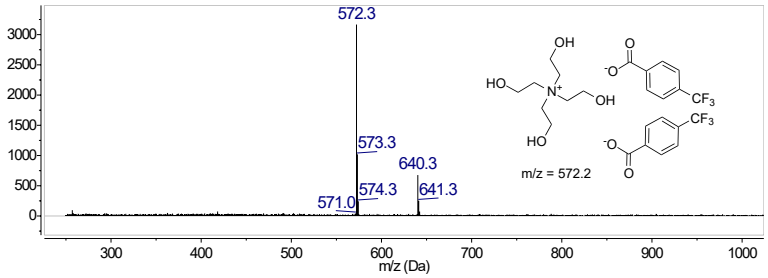


Figure B.33: ESI-TOF mass spectrum of $\mathbf{T_4F_{12a}}$ in MeOD after the compound was run through an Amberlite column as referenced on P. 130.

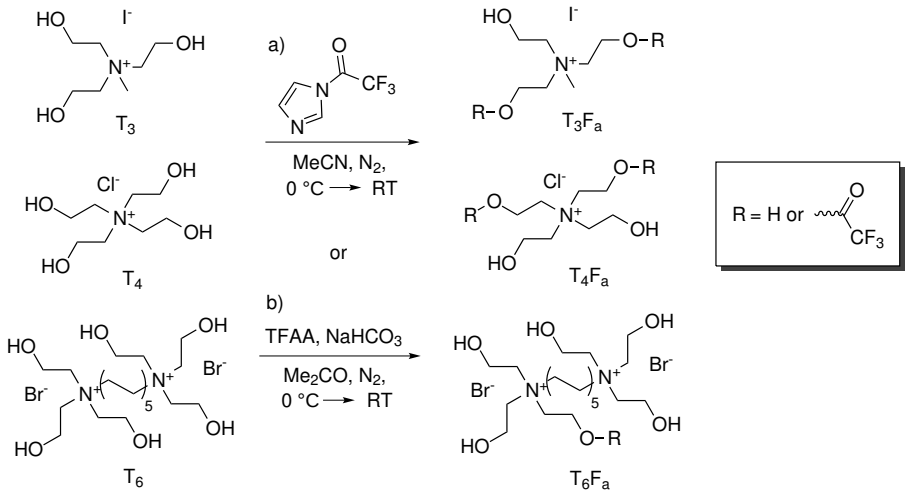
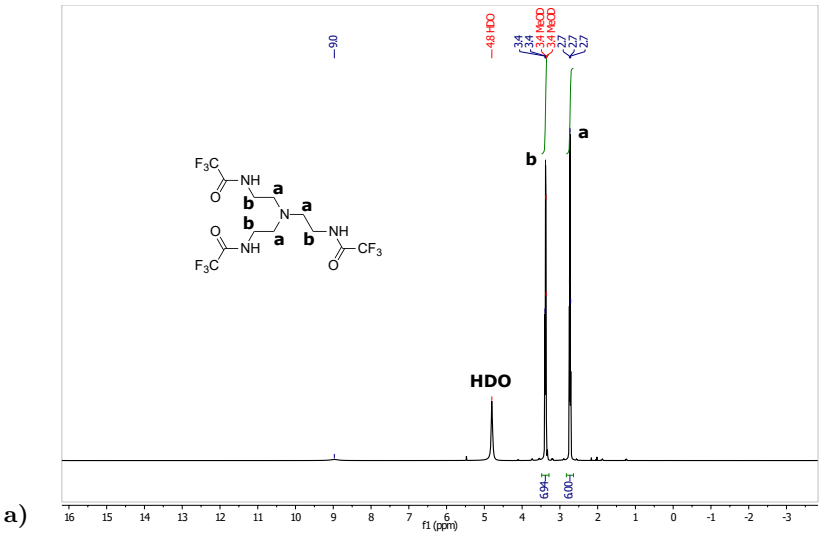
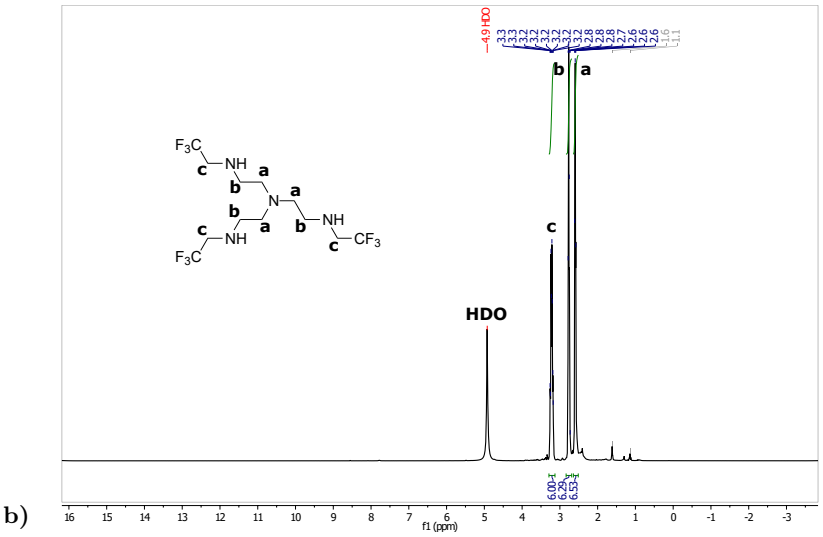


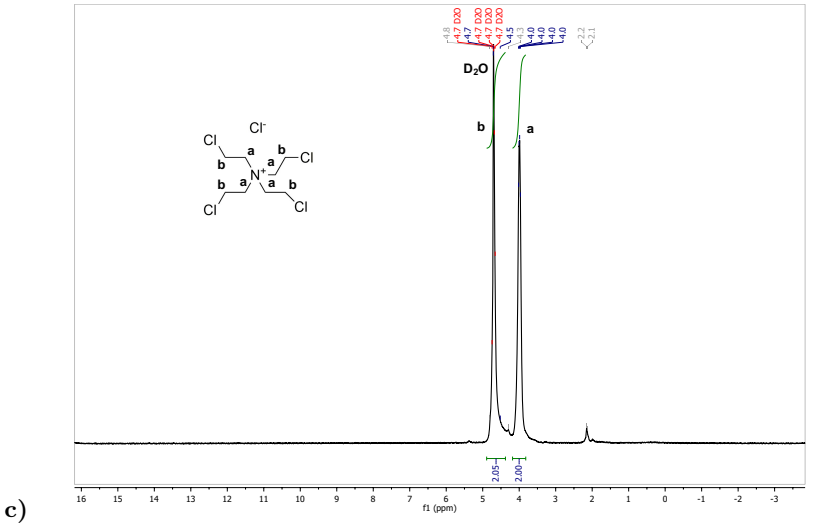
Figure B.34: Attempts of trifluoroacetylation of QASs yielded non-, mono- or disubstituted fluorine-functionalised QASs as referenced on P. 132.



a)



b)



c)

Figure B.35: ^{1}H NMR spectra of a) $\mathbf{T_0F_{9c}}$, b) $\mathbf{T_0F_{9cRed}}$ and c) $\mathbf{T_4Cl_4}$ in D_2O referenced on P. 132.

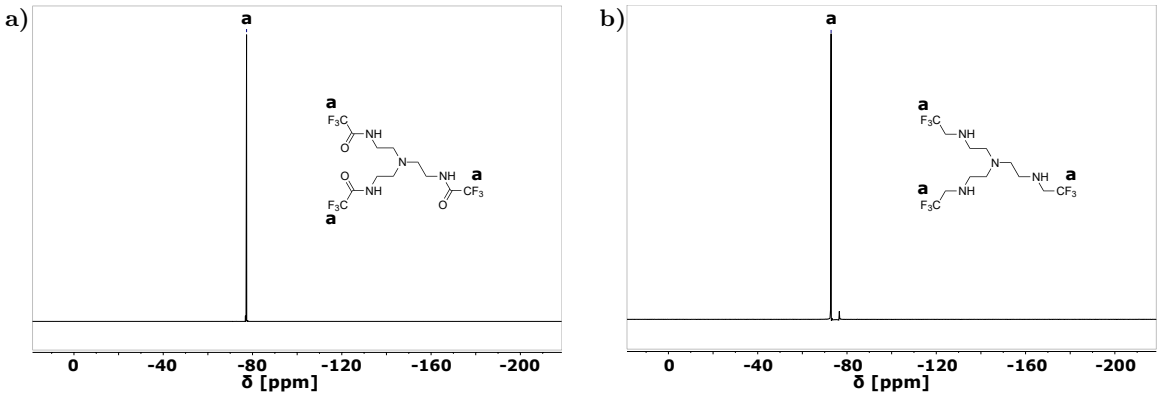


Figure B.36: ^{19}F NMR spectra of a) $\mathbf{T_0F}_{9c}$ and b) $\mathbf{T_0F}_{9cRed}$ in D_2O referenced on P. 132.

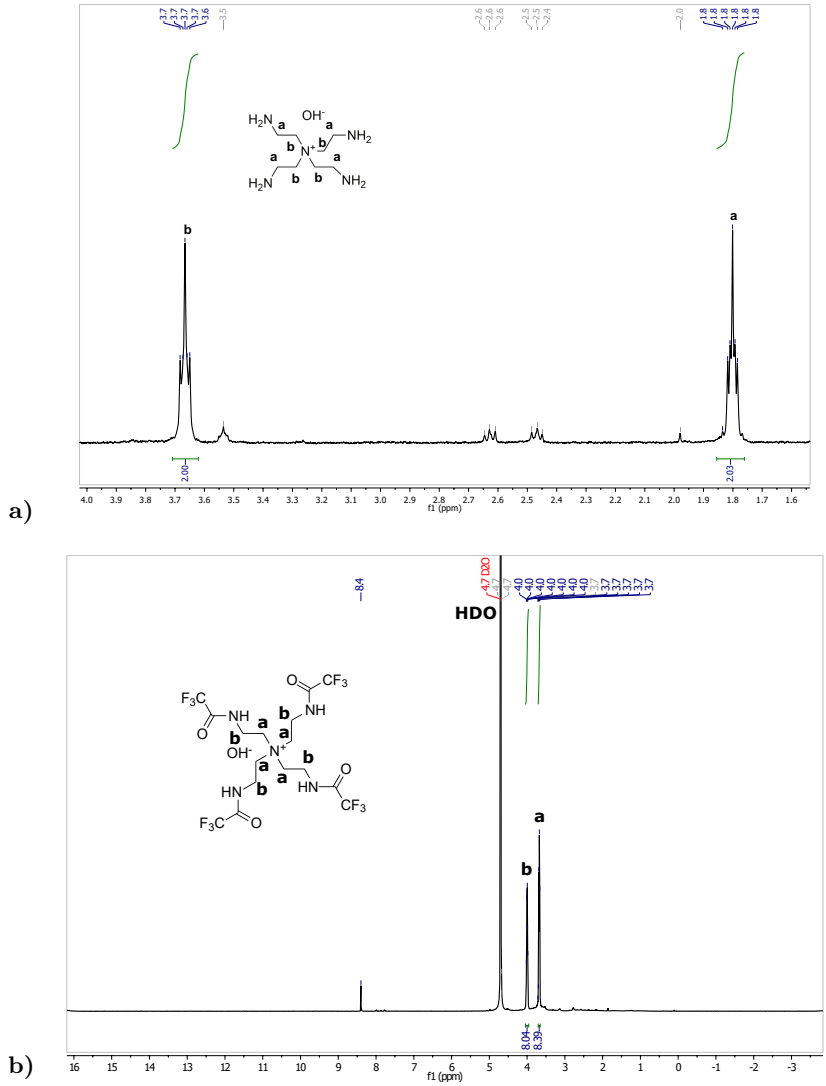


Figure B.37: ^{1}H NMR spectra of a) $\mathbf{T_4(NH_2)_4}$ and b) $\mathbf{T_4F}_{12c}$ in D_2O referenced on P. 132.

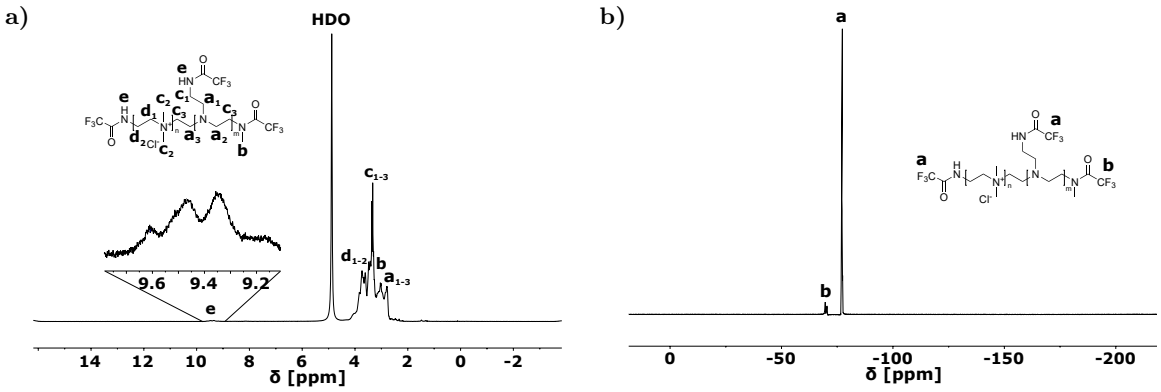


Figure B.38: a) ^{1}H and b) ^{19}F NMR spectra of **PEI-CF$_3$-Cl$^-$** in D_2O referenced on P. 134.

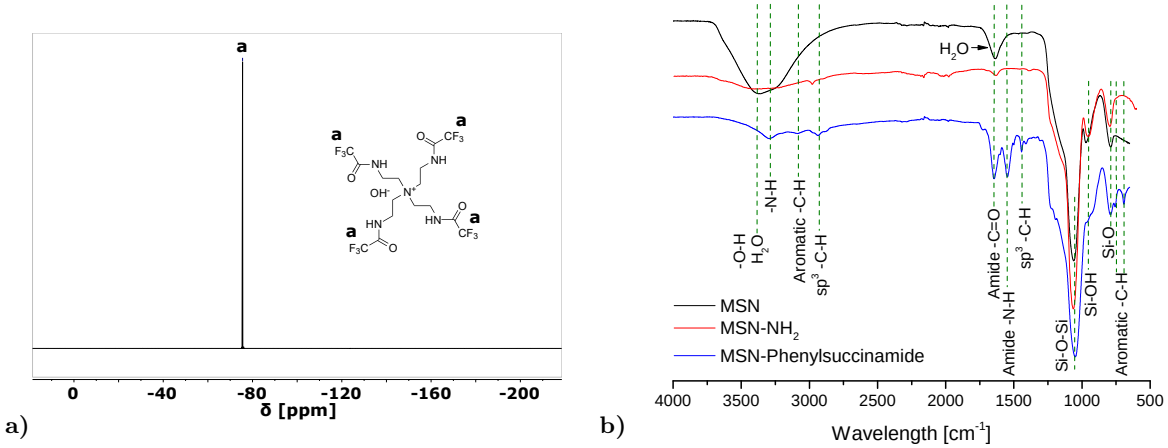


Figure B.39: a) ^{19}F NMR spectrum of $\mathbf{T_4F_{12c}}$ in D_2O referenced on P. 132. b) FTIR spectrum of phenylsuccinamide-functionalised MSNs referenced on P. 140.

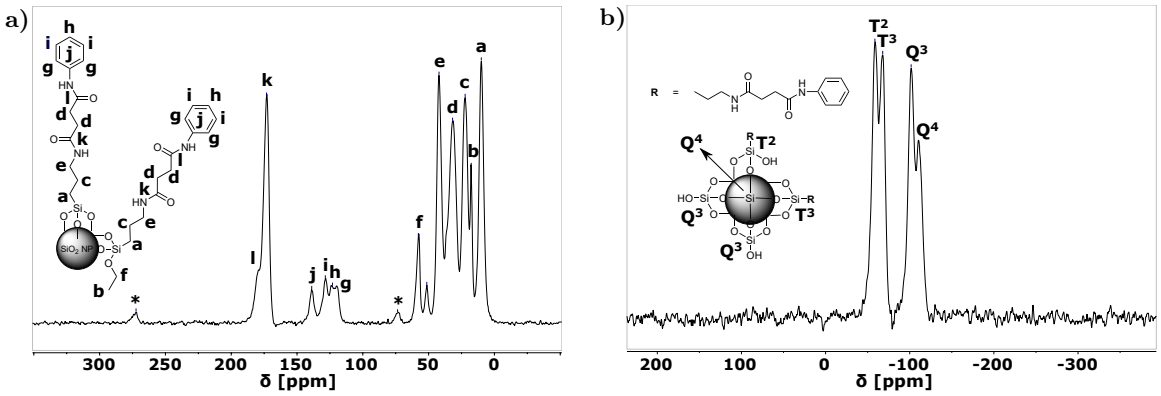


Figure B.40: a) ^{13}C CP/MAS and b) ^{29}Si DP/MAS solid-state NMR spectra showing phenylsuccinamide-functionalised MSNs referenced on P. 140.

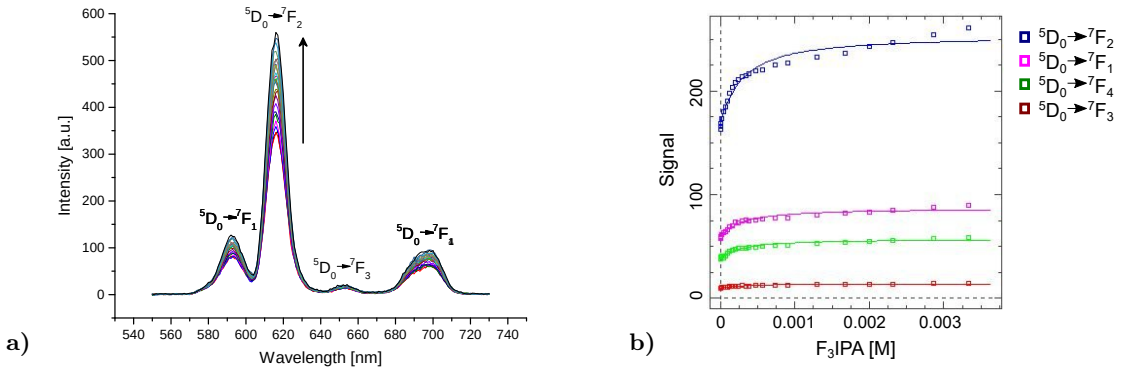


Figure B.41: Graphs showing a) luminescence spectra and b) fittings of titration data for a $7 \cdot 10^{-5}$ M solution of **NS-Eu$_2$·L$_3$** with **F$_3$IPA** in MeOH as referenced on P. 146. The fitted curves correspond to each of the emission bands with the excitation at 394 nm, wherein the increase in emission intensity correlates to the removal of quenching hydroxyl groups of methanol from the coordination sphere by **F$_3$IPA**.

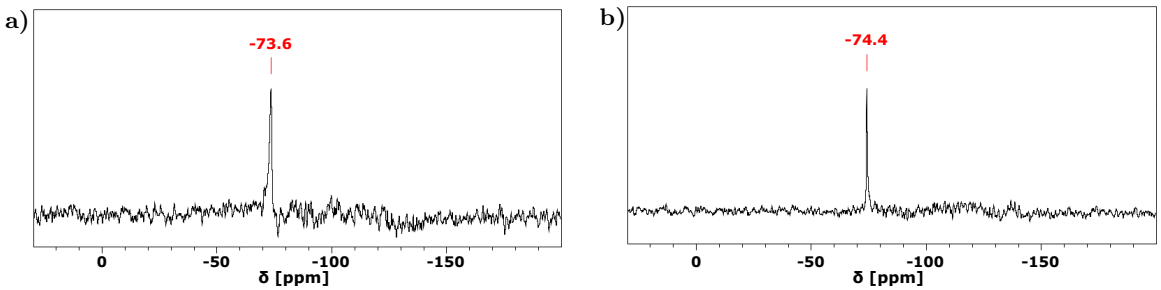


Figure B.42: ^{19}F NMR spectra showing a) **MSN-Gd$_2$·L$_3$-F$_3$IPA** and b) **NS-Poly(MAA)-Gd$_2$·L$_3$-F$_3$IPA** in H_2O, wherein **Gd$_2$·L$_3$** and **F$_3$IPA** were used in 1:1 ratio (**F$_3$IPA** = 1 mg) as referenced on P. 144.

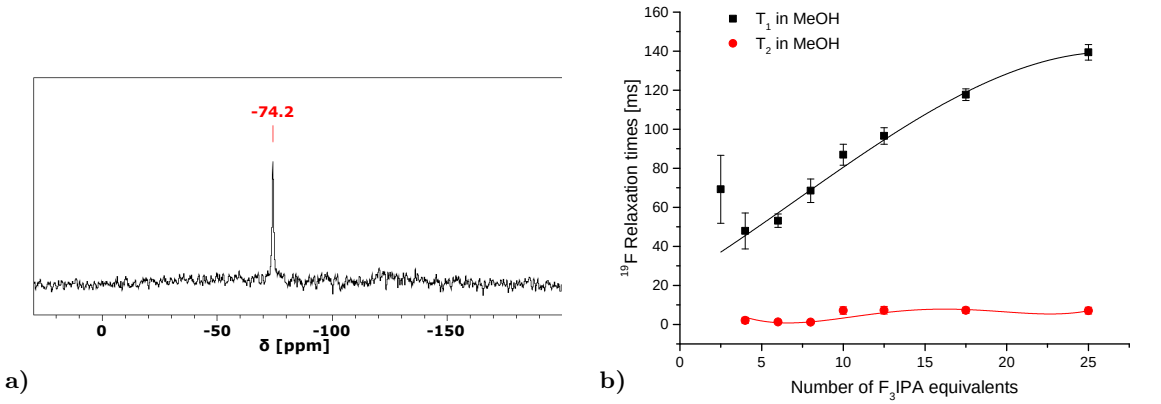


Figure B.43: ^{19}F NMR spectrum showing **NS-Poly(MAA)-Gd$_2$·L$_3$-F$_3$IPA** in H_2O, wherein a) **Gd$_2$·L$_3$** and **F$_3$IPA** were used in 1:1 ratio (**F$_3$IPA** = 1 mg), followed by b) relaxometric NMR titration of up to 25 equivalents **F$_3$IPA** as referenced on P. 146.

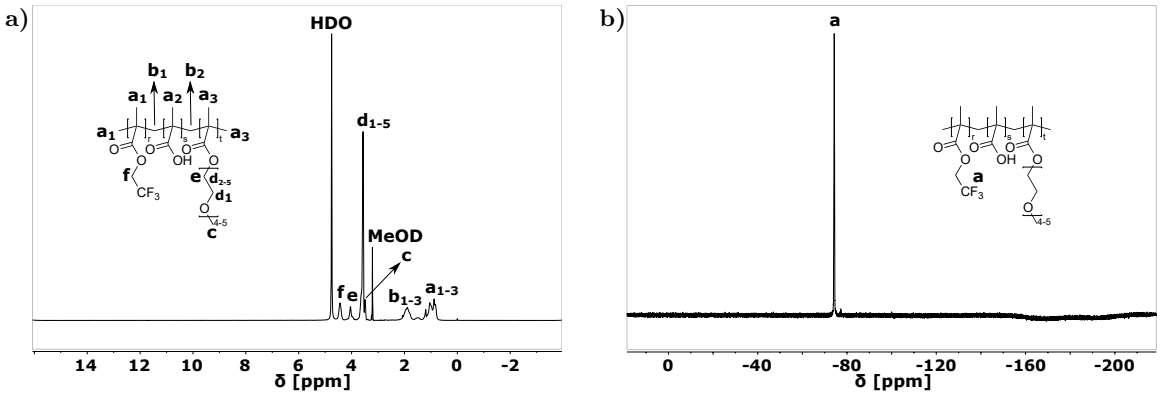


Figure B.44: a) ^{1}H and b) ^{19}F NMR spectra of **Poly(TFMA-MAA-PEG)** in MeOD referenced on P. 147.

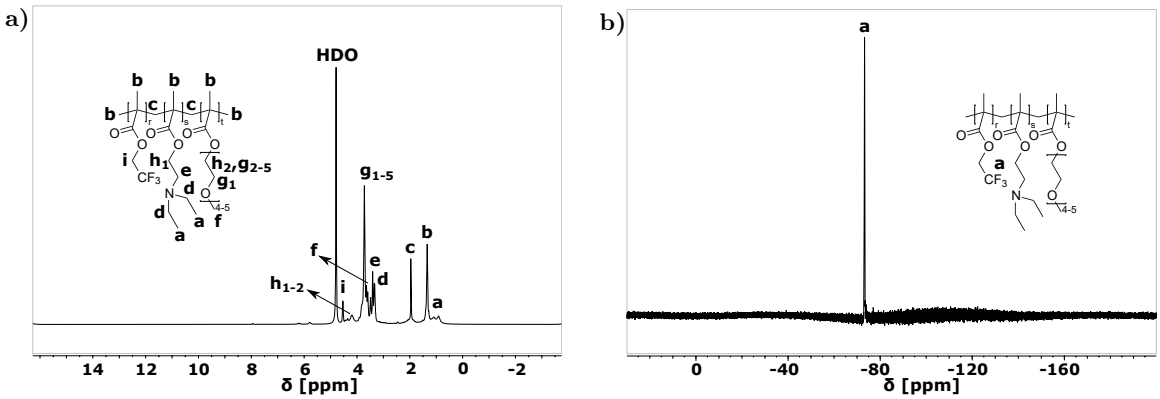


Figure B.45: a) ^{1}H and b) ^{19}F NMR spectra of **Poly(TFMA-DMA-PEG)** in D_2O referenced on P. 150.

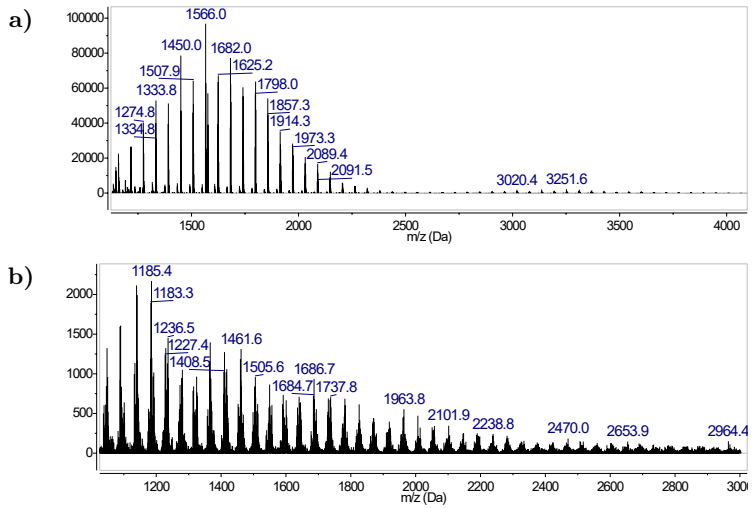


Figure B.46: MALDI-TOF spectra of a) **Poly(TFMA-MAA-PEG)** and b) **Poly(TFMA-DMA-PEG)** referenced on P. 147.

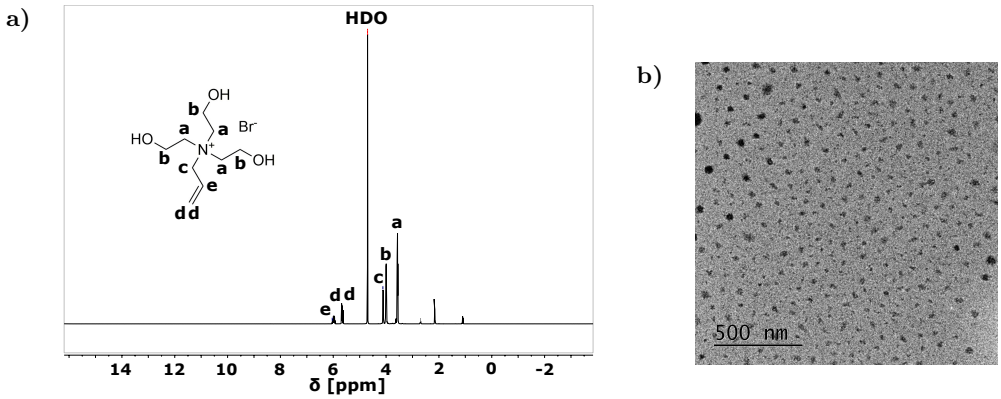


Figure B.47: a) ^{1}H NMR spectrum of allyl-functionalised QAS and b) TEM image of phosphotungstic acid-stained **Poly(FQMA-DMA-Gd·L$_4$)** referenced on P. 152.

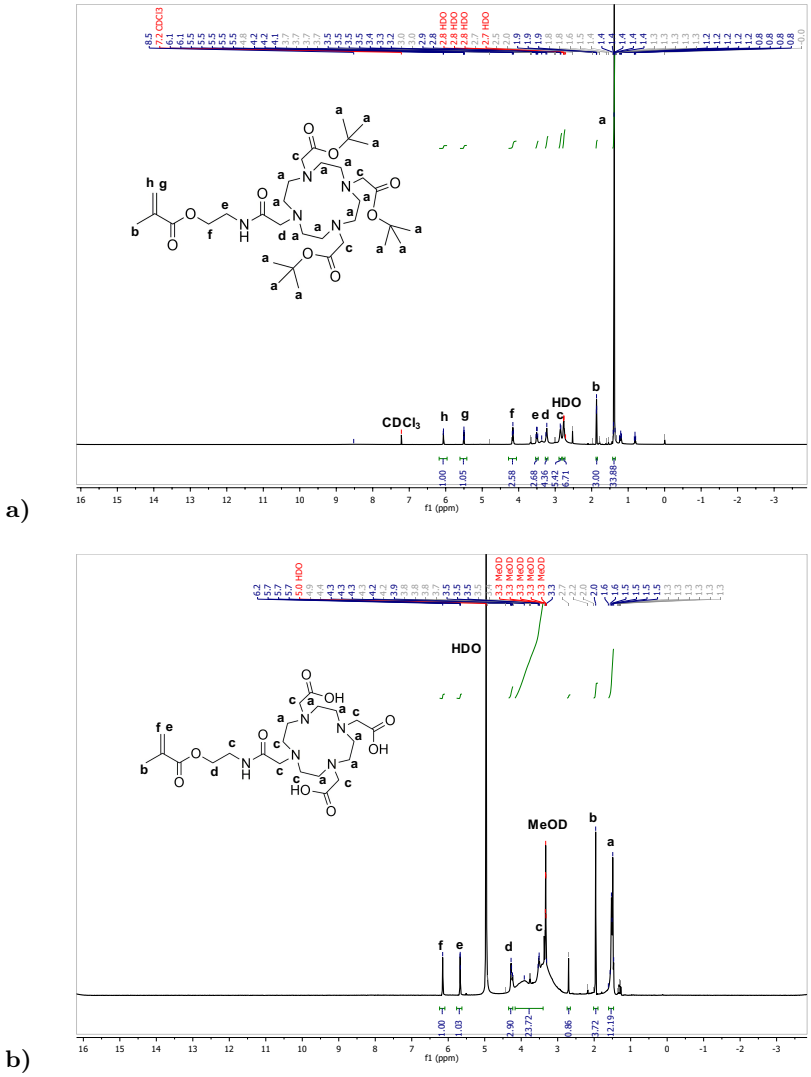


Figure B.48: ^{1}H NMR spectra of a) *t*Bu-protected and b) TFA-deprotected **Gd·L$_4$** precursors referenced on P. 149.

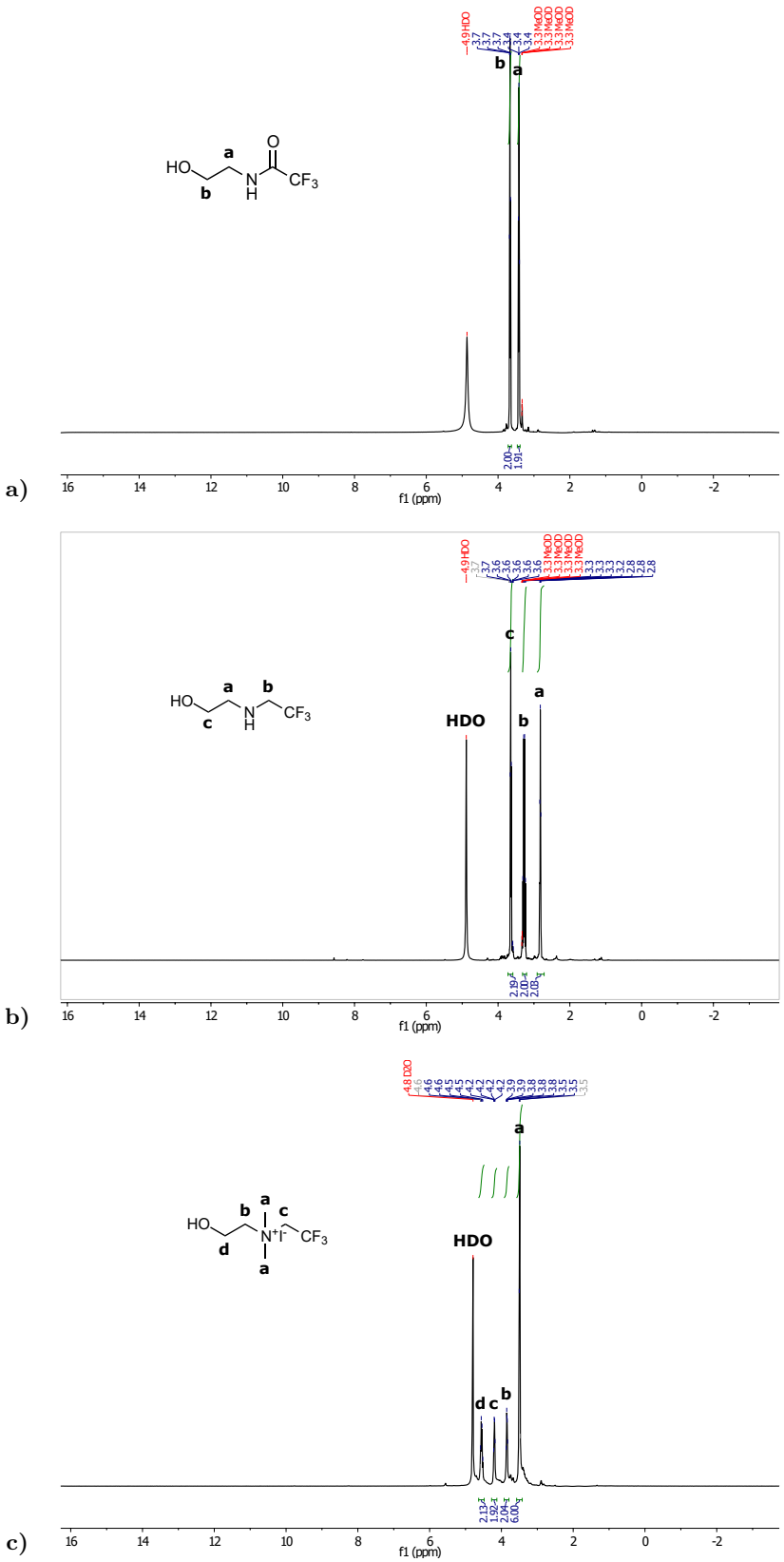


Figure B.49: ^{1}H NMR spectra of a) 2,2,2-trifluoro-*N*-(2-hydroxyethyl)acetamide, b) 2-((2,2,2-trifluoroethyl)amino)ethanol and c) quaternary ammonium iodide derivative of the latter in either MeOD or D_2O as referenced on P. 152.

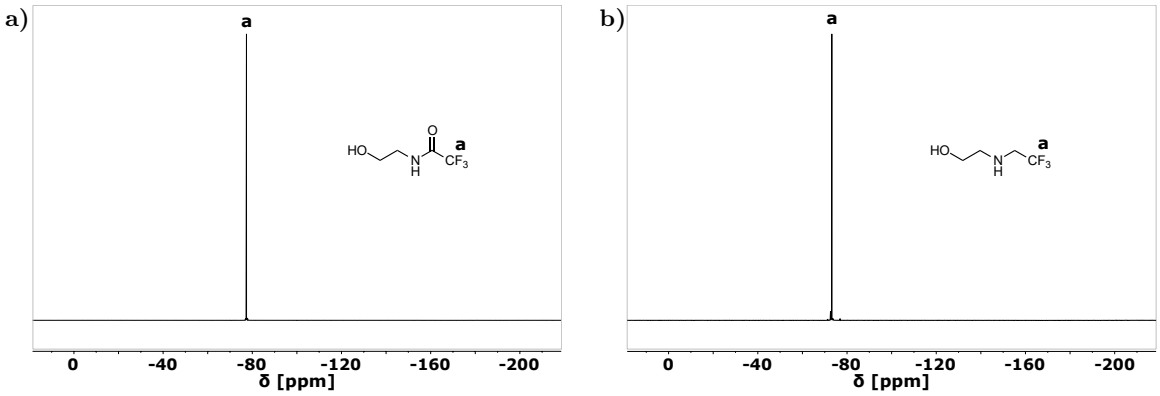


Figure B.50: ^{19}F NMR spectra of a) 2,2,2-trifluoro-*N*-(2-hydroxyethyl)acetamide and b) 2-((2,2,2-trifluoroethyl)amino)ethanol in MeOD as referenced on P. 152.

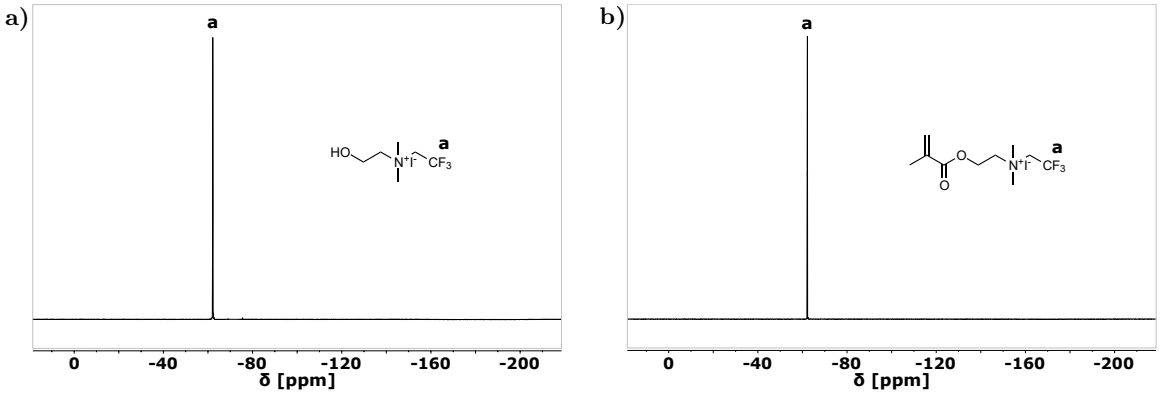


Figure B.51: ^{19}F NMR spectra of a) trifluoro-(2-hydroxyethyl)-dimethylethan-ammonium iodide and b) **FQMA** in D_2O referenced on P. 152.

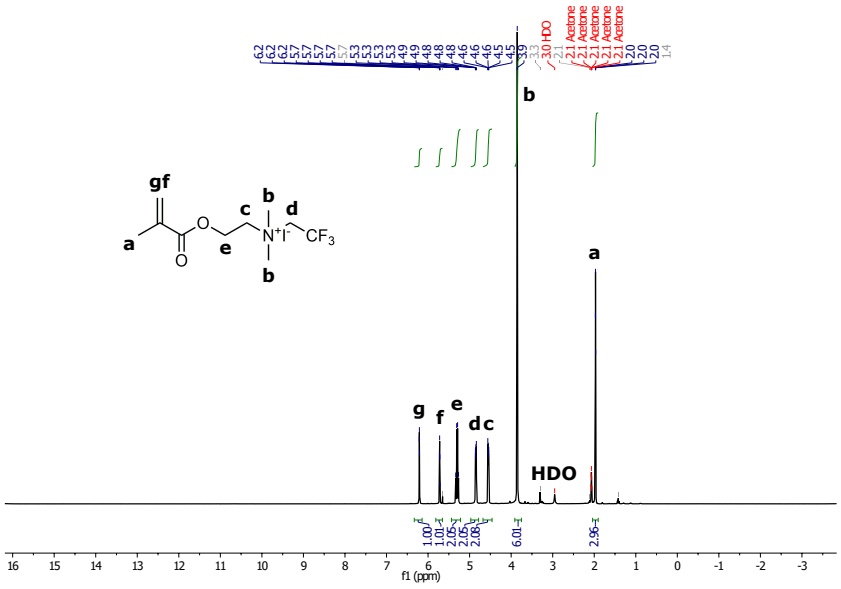


Figure B.52: ^{1}H NMR spectrum of **FQMA** in D_2O referenced on P. 152.

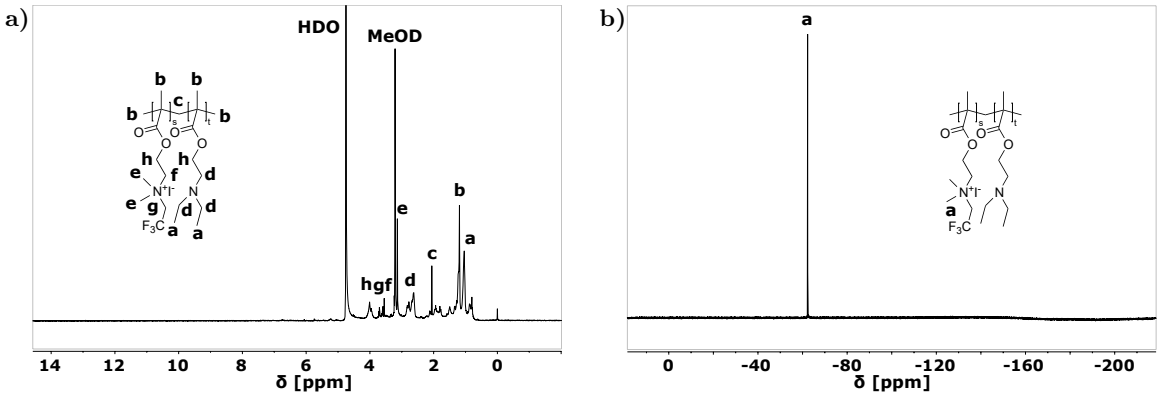


Figure B.53: a) ^{1}H and b) ^{19}F NMR spectra of **Poly(FQMA-DMA)** referenced on P. 152.

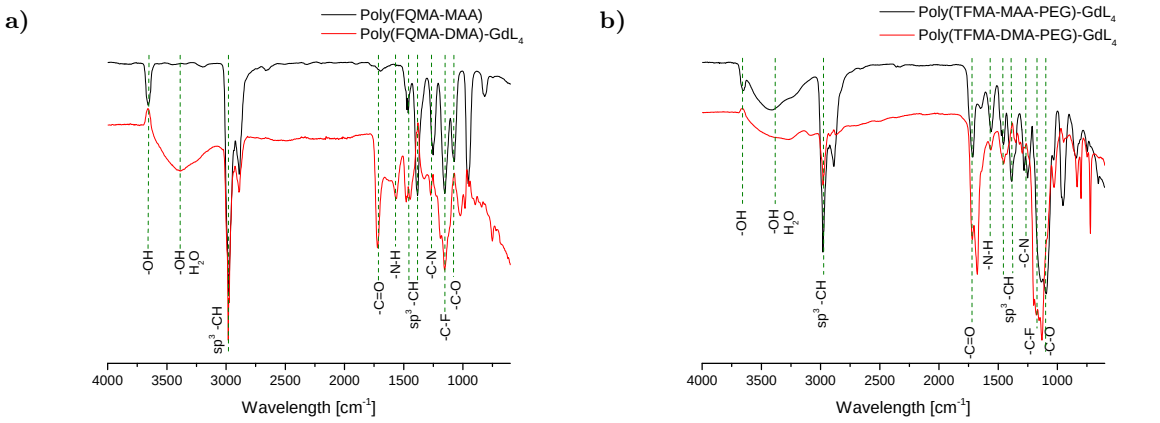


Figure B.54: FTIR spectra of a) **Poly(FQMA-MAA)** and **Poly(FQMA-DMA-Gd·L$_4$)** as well as b) **Poly(TFMA-MAA-PEG-Gd·L$_4$)** and **Poly(TFMA-DMA-PEG-Gd·L$_4$)** as referenced on P. 147-152.

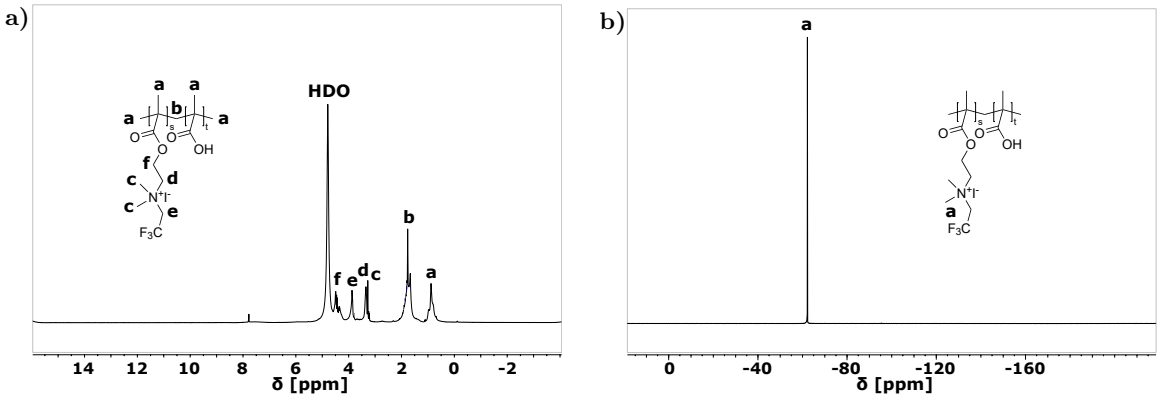


Figure B.55: a) ^{1}H and b) ^{19}F NMR spectra **Poly(FQMA-MAA)** referenced on P. 152.

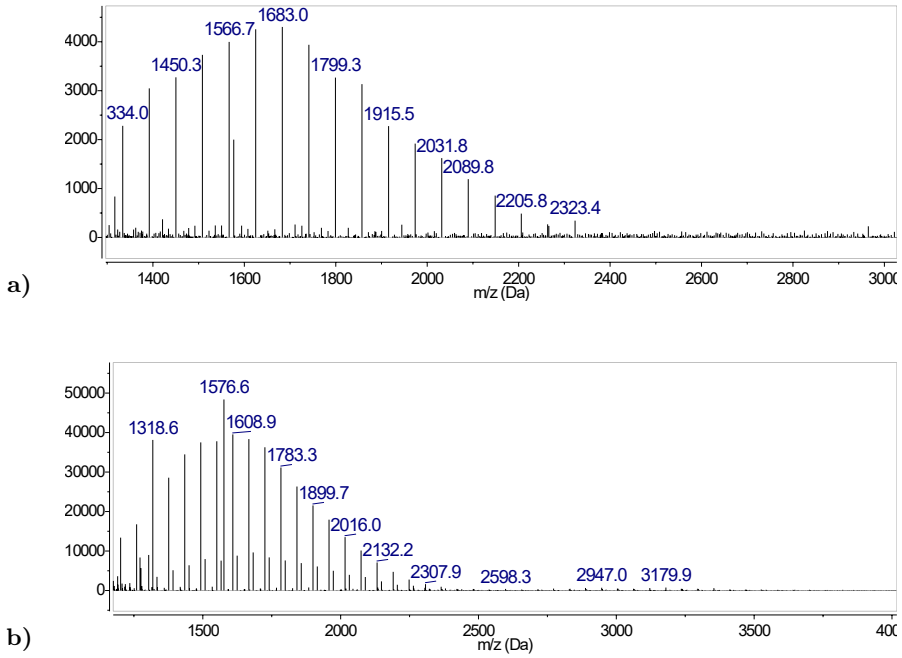


Figure B.56: MALDI-TOF spectra of a) **Poly(FQMA-MAA)** and b) **Poly(FQMA-DMA)** referenced on P. 152.

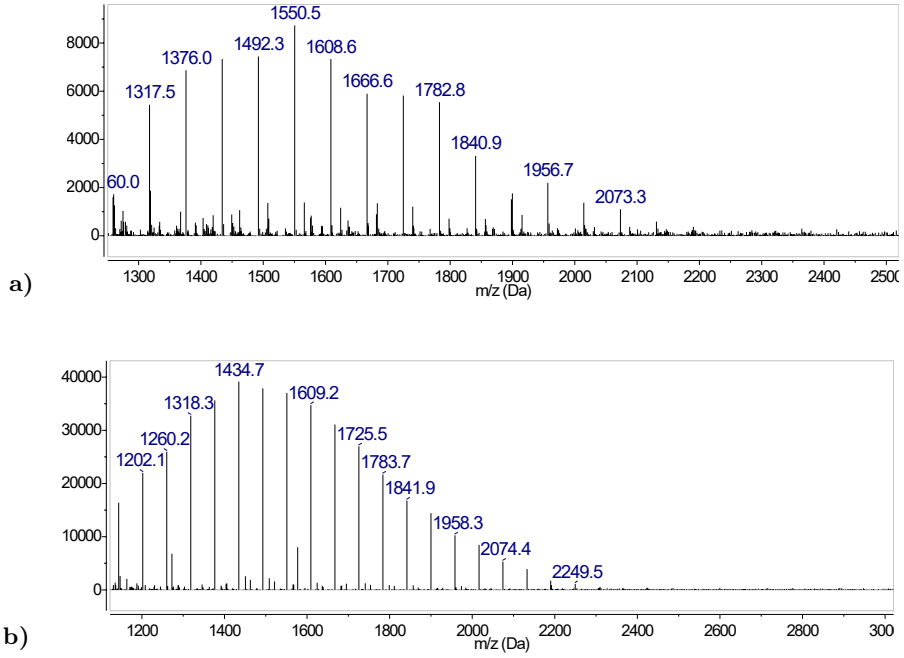


Figure B.57: MALDI-TOF spectra of a) **Poly(FQMA-MAA-Gd·L$_4$)** and b) **Poly(FQMA-DMA-Gd·L$_4$)** referenced on P. 152.

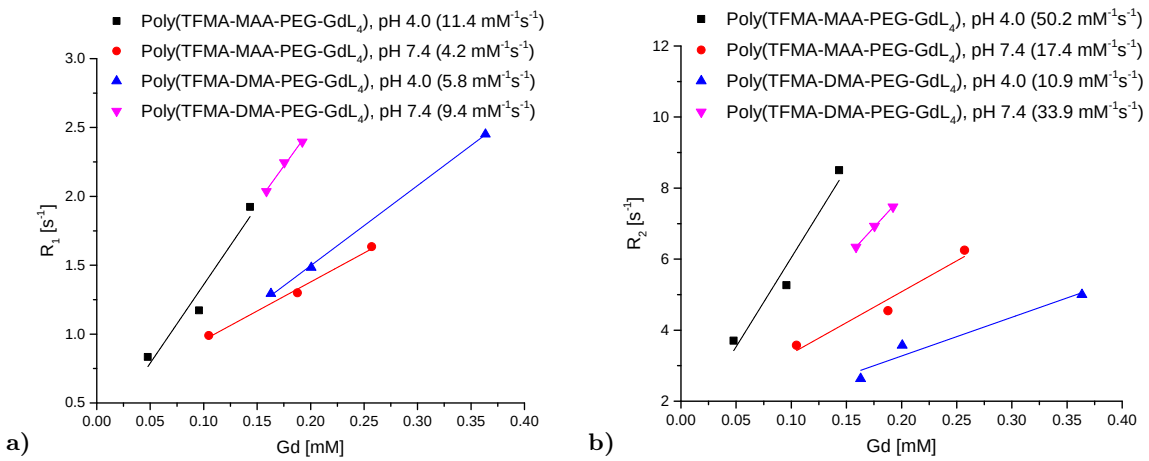


Figure B.58: Linear fits of ^{1}H a) longitudinal R_1 and b) transverse R_2 relaxation rates of **Poly(TFMA-MAA-PEG-Gd·L$_4$)** and **Poly(TFMA-DMA-PEG-Gd·L$_4$)** versus Gd concentration at 7.0 T and 293 K. The graphs are referenced on P. 149 and fitted to Eq. (1.6), which can be found on P. 6. The linear fits of the data points yielded relaxivities as shown in brackets.

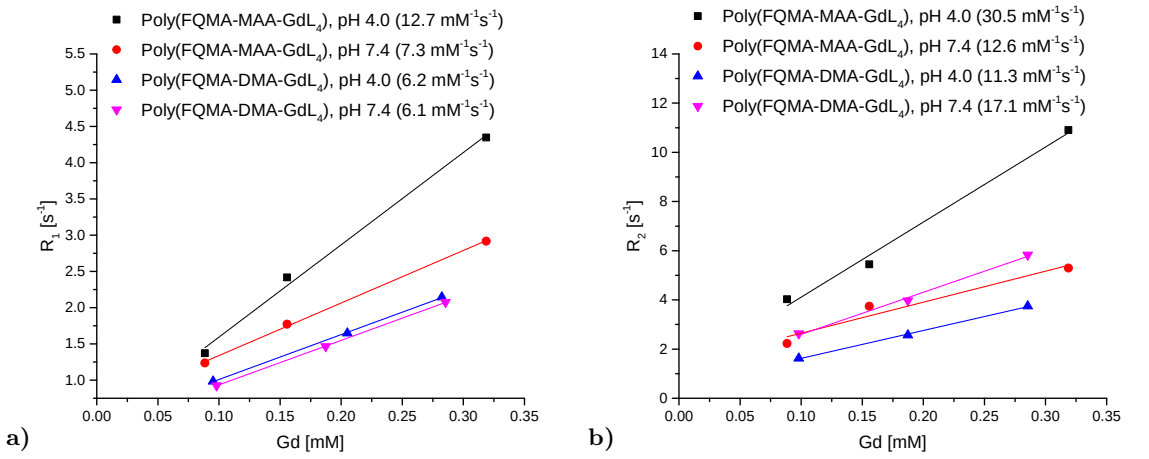


Figure B.59: Linear fits of ^{1}H a) longitudinal R_1 and b) transverse R_2 relaxation rates of **Poly(FQMA-MAA-Gd·L$_4$)** and **Poly(FQMA-DMA-Gd·L$_4$)** versus Gd concentration at 7.0 T and 293 K. The graphs are referenced on P. 155 and fitted to Eq. (1.6), which can be found on P. 6. The linear fits of the data points yielded relaxivities as shown in brackets.

Bibliography

[1] Davies, G.-L.; Kramberger, I.; Davis, J. J. *Chemical Communications* **2013**, *49*, 9704–9721.

[2] Ekanger, L. A.; Allen, M. J. *Metallomics* **2015**, *7*, 405–421.

[3] Lauterbur, P. C. *Nature* **1973**, *242*, 190–191.

[4] Caravan, P. *Chemical Society Reviews* **2006**, *35*, 512–523.

[5] Major, J. L.; Meade, T. J. *Accounts of Chemical Research* **2009**, *42*, 893–903.

[6] Stark, D. D., Bradley, W. G., Bradley, W. G., Eds. *Magnetic Resonance Imaging*, 3rd ed.; C.V. Mosby, 1999; p 2064.

[7] Pankhurst, Q. A.; Connolly, J.; Jones, S. K.; Dobson, J. *Journal of Physics D: Applied Physics* **2003**, R167–R181.

[8] Allison, W. *Fundamental Physics for Probing and Imaging*; Oxford University Press, 2006; p 348.

[9] Bakhmutov, V. I. *NMR Spectroscopy in Liquids and Solids*, 1st ed.; CRC Press, 2015; p 344.

[10] Merbach, A., Helm, L., Tóth, E., Eds. *The Chemistry of Contrast Agents in Medical Magnetic Resonance Imaging*, 2nd ed.; John Wiley & Sons, Ltd, 2013.

[11] van Eldik, R., Hubbard, C., Eds. *Advances in Inorganic Chemistry*, 1st ed.; Elsevier Science Publishing Co Inc, 2003; Vol. 54; p 490.

[12] Bloembergen, N.; Purcell, E.; Pound, R. *Physical Review* **1948**, *73*, 679–712.

[13] Slichter, C. P. *Principles of Magnetic Resonance*, 3rd ed.; Springer-Verlag Berlin Heidelberg, 1990; p 658.

[14] Hashemi, R. H.; Bradley, W. G.; Lisanti, C. J. *MRI: the Basics*, 3rd ed.; Lippincott Williams & Wilkins, 2010; p 400.

[15] Hifumi, H.; Yamaoka, S.; Tanimoto, A.; Citterio, D.; Suzuki, K. *Journal of the American Chemical Society* **2006**, *128*, 15090–15091.

[16] Bottrill, M.; Kwok, L.; Long, N. J. *Chemical Society Reviews* **2006**, *35*, 557–571.

[17] Atlas, S. *Magnetic Resonance Imaging of the Brain and Spine, Volume 1*; Lippincott Williams & Wilkins, 2009; p 1890.

[18] Caravan, P.; Ellison, J. J.; McMurry, T. J.; Lauffer, R. B. *Chemical Reviews* **1999**, *99*, 2293–2352.

[19] Elster, A. D.; Sobol, W. T.; Hinson, W. H. *Radiology* **1990**, *174*, 379–381.

[20] Viswanathan, S.; Kovacs, Z.; Green, K. N.; Ratnakar, S. J.; Sherry, A. D. *Chemical Reviews* **2010**, *110*, 2960–3018.

[21] Aime, S.; Botta, M.; Fasano, M.; Terreno, E. *Chemical Society Reviews* **1998**, *27*, 19–29.

[22] Jalandhara, N.; Arora, R.; Batuman, V. *Clinical Pharmacology and Therapeutics* **2011**, *89*, 920–923.

[23] Kim, W. D.; Kiefer, G. E.; Huskens, J.; Sherry, A. D. *Inorganic Chemistry* **1997**, *36*, 4128–4134.

[24] Botta, M.; Tei, L. *European Journal of Inorganic Chemistry* **2012**, *2012*, 1945–1960.

[25] Yazyev, O. V.; Helm, L. *European Journal of Inorganic Chemistry* **2008**, *2008*, 201–211.

[26] Gonzalez, G.; Powell, D. H.; Tissieres, V.; Merbach, A. E. *Journal of Physical Chemistry* **1994**, *98*, 53–59.

[27] Caravan, P.; Farrar, C. T.; Frullano, L.; Uppal, R. *Contrast Media & Molecular Imaging* **2009**, *4*, 89–100.

[28] Caravan, P.; Greenfield, M. T.; Bulte, J. W. M. *Magnetic Resonance in Medicine* **2001**, *46*, 917–922.

[29] Bloembergen, N.; Morgan, L. O. *The Journal of Chemical Physics* **1961**, *34*, 842–850.

[30] Solomon, I.; Bloembergen, N. *The Journal of Chemical Physics* **1956**, *25*, 261–266.

[31] Villaraza, A. J. L.; Bumb, A.; Brechbiel, M. W. *Chemical Reviews* **2010**, *110*, 2921–2959.

[32] Borel, A.; Helm, L.; Merbach, A. E.; Atsarkin, V. A.; Demidov, V. V.; Odintsov, B. M.; Belford, R. L.; Clarkson, R. B. *Journal of Physical Chemistry A* **2002**, *106*, 6229–6231.

[33] Boros, E.; Gale, E. M.; Caravan, P. *Dalton Transactions* **2015**, *44*, 4804–4818.

[34] Caravan, P. *Chemical Society Reviews* **2006**, *35*, 512–523.

[35] Dumas, S.; Jacques, V.; Sun, W.; Troughton, J.; Welch, J.; Chasse, J.; Schmitt-Willich, H.; Caravan, P. *Investigative Radiology* **2011**, *45*, 600–612.

[36] Aime, S.; Crich, S. G.; Botta, M.; Giovenzana, G.; Palmisano, G.; Sisti, M. *Chemical Communications* **1999**, 1577–1578.

[37] Powell, D. H.; Dhubhghaill, O. M. N.; Pubanz, D.; Helm, L.; Lebedev, Y. S.; Schlaepfer, W.; Merbach, A. E. *Journal of American Chemical Society* **1996**, *118*, 9333–9346.

[38] Swift, T. J.; Connick, R. E.; Poulson, R. E. *The Journal of Chemical Physics* **1959**, *37*, 307–320.

[39] Elhabiri, M.; Abada, S.; Sy, M.; Nonat, A.; Choquet, P.; Esteban-Gómez, D.; Assino, C.; Platas-Iglesias, C.; Botta, M.; Charbonnière, L. J. *Chemistry–A European Journal* **2015**, *21*, 6535–6546.

[40] Dunand, F. A.; Tóth, E.; Hollister, R.; Merbach, A. E. *Journal of Biological Inorganic Chemistry* **2001**, *6*, 247–255.

[41] Jacquesa, V.; Dumas, S.; Sun, W.-C.; Troughton, J. S.; Greenfield, M. T.; Caravan, P. *Investigative Radiology* **2011**, *45*, 613–624.

[42] Lauffer, R. E. *Chemical Reviews* **1987**, *87*, 901–927.

[43] Freed, J. H. *The Journal of Chemical Physics* **1978**, *68*, 4034–4037.

[44] Botta, M. *European Journal of Inorganic Chemistry* **2000**, *2000*, 399–407.

[45] Aime, S.; Batsanov, A. S.; Both, M.; Howard, J. A. K.; Parker, D.; Senanayake, K.; Williams, G. *Inorganic Chemistry* **1994**, *33*, 4696–4706.

[46] Nicolle, G. M.; Toth, E.; Eisenwiener, K. P.; Macke, H. R.; Merbach, A. E. *Journal of Biological Inorganic Chemistry* **2002**, *7*, 757–769.

[47] Peters, J. A.; Djanashvili, K. *European Journal of Inorganic Chemistry* **2012**, 1961–1974.

[48] Tóth, É.; Bolskar, R. D.; Borel, A.; Gonzalez, G.; Helm, L.; Merbach, A. E.; Sitharaman, B.; Wilson, L. J. *Journal of American Chemical Society* **2005**, *127*, 799–805.

[49] Lipari, G.; Szabo, A. *Journal of the American Chemical Society* **1982**, *104*, 4546–4559.

[50] de Smet, M.; Langereis, S.; van den Bosch, S.; Grüll, H. *Journal of Controlled Release* **2010**, *143*, 120–127.

[51] Okada, S.; Mizukami, S.; Kikuchi, K. *Bioorganic & Medicinal Chemistry* **2012**, *20*, 769–774.

[52] Ananta, J. S.; Godin, B.; Sethi, R.; Moriggi, L.; Liu, X.; Serda, R. E.; Krishnamurthy, R.; Muthupillai, R.; Bolskar, R. D.; Helm, L.; Ferrari, M.; Wilson, L. J.; Decuzzi, P. *Nature Nanotechnology* **2010**, *5*, 815–821.

[53] Bruehwiler, D. *Nanoscale* **2010**, *2*, 887–892.

[54] Sur, S.; Heinsbergen, J.; Bryant, R. *Journal of Magnetic Resonance A* **1993**, *103*, 27–33.

[55] Platas-Iglesias, C.; Vander Elst, L.; Zhou, W.; Muller, R. N.; Geraldes, C. F. G. C.; Maschmeyer, T.; Peters, J. A. *Chemistry–A European Journal* **2002**, *8*, 5121–5131.

[56] Carniato, F.; Tei, L.; Dastru, W.; Marchese, L.; Botta, M. *Chemical Communications* **2009**, *15*, 1246–1248.

[57] Grünberg, B.; Emmler, T.; Gedat, E.; Shenderovich, I.; Findenegg, G. H.; Limbach, H.-H.; Buntkowsky, G. *Chemistry–A European Journal* **2004**, *10*, 5689–5696.

[58] Laprise-Pelletier, M.; Meryem Bouchoucha, A.; Jean Lagueux, A.; Chevallier, P.; Roger Lecomte, A.; Gossuin, Y.; Kleitz, F.; Fortin, M.-A. *Journal of Materials Chemistry B* **2015**, *3*, 709–928.

[59] Skår, H.; Liang, Y.; Erichsen, E. S.; Anwander, R.; Seland, J. G. *Microporous and Mesoporous Materials* **2013**, *175*, 125–133.

[60] Aime, S.; Barge, A.; Botta, M.; Parker, D.; De Sousa, A. S. *Journal of the American Chemical Society* **1997**, *119*, 4767–4768.

[61] Nivorozhkin, A. L.; Kolodziej, A. F.; Caravan, P.; Greenfield, M. T.; Lauffer, R. B.; McMurry, T. J. *Angewandte Chemie* **2001**, *40*, 2903–2906.

[62] Que, E. L.; Gianolio, E.; Baker, S. L.; Wong, A. P.; Aime, S.; Chang, C. J. *Journal of the American Chemical Society* **2009**, *131*, 8527–8536.

[63] Martinelli, J.; Fekete, M.; Tei, L.; Botta, M. *Chemical Communications* **2011**, *47*, 3144–3146.

[64] Huang, C.-H.; Nwe, K.; Zaki, A. A.; Brechbiel, M.; Tsourkas, A. *ACS Nano* **2012**, *6*, 9416–9424.

[65] Lin, C.-W.; Tseng, S.-J. J.; Kempson, I. M.; Yang, S.-C.; Hong, T.-M.; Yang, P.-C. *Biomaterials* **2013**, *34*, 4387–4393.

[66] Tannock, I. F.; Rotin, D. *Cancer Research* **1989**, *49*, 4373–4384.

[67] Okada, S.; Mizukami, S.; Kikuchi, K. *ChemBioChem* **2010**, *11*, 785–787.

[68] Gianolio, E.; Napolitano, R.; Fedeli, F.; Arena, F.; Aime, S. *Chemical Communications* **2009**, 6044–6046.

[69] Laus, S.; Sour, A.; Ruloff, R.; Tóth, É.; Merbach, A. E. *Chemistry–A European Journal* **2005**, *11*, 3064–3076.

[70] Aime, S.; Fedeli, F.; Sanino, A.; Terreno, E. *Journal of the American Chemical Society* **2006**, *128*, 11326–11327.

[71] Lowe, M. P.; Parker, D.; Reany, O.; Aime, S.; Botta, M.; Castellano, G.; Gianolio, E.; Pagliarin, R. *Journal of the American Chemical Society* **2001**, *123*, 7601–7609.

[72] Woods, M.; Kiefer, G. E.; Bott, S.; Castillo-Muzquiz, A.; Eshelbrenner, C.; Michaudet, L.; McMillan, K.; Mudigunda, S. D. K.; Ogrin, D.; Tircsó, G.; Zhang, S.; Zhao, P.; Sherry, A. D. *Journal of the American Chemical Society* **2004**, *126*, 9248–9256.

[73] Schopf, E.; Sankaranarayanan, J.; Chan, M.; Mattrey, R.; Almutairi, A. *Molecular Pharmaceutics* **2012**, *9*, 1911–1918.

[74] Vibhute, S. M.; Engelmann, J.; Verbic, T.; Maier, M. E.; Logothetis, N. K.; Angelovski, G. *Organic & Biomolecular Chemistry* **2013**, *11*, 1294–1305.

[75] Gianolio, E.; Porto, S.; Napolitano, R.; Baroni, S.; Giovenzana, G. B.; Aime, S. *Inorganic Chemistry* **2012**, *51*, 7210–7217.

[76] Tang, J.; Sheng, Y.; Hu, H.; Shen, Y. *Progress in Polymer Science* **2013**, *38*, 462–502.

[77] He, C.; Wu, X.; Kong, J.; Liu, T.; Zhang, X.; Duan, C. *Chemical Communications* **2012**, *48*, 9290–9292.

[78] Chang, C. A.; Brittain, H. G.; Telser, J.; Tweedle, M. F. *Inorganic Chemistry* **1990**, *29*, 4468–4473.

[79] Horrocks, W. D.; Sudnick, D. R. *Journal of the American Chemical Society* **1979**, *101*, 334–340.

[80] Beeby, A.; Clarkson, I. M.; Dickins, R. S.; Faulkner, S.; Parker, D.; Royle, L.; de Sousa, A. S.; Williams, J. a. G.; Woods, M. *Journal of the Chemical Society, Perkin Transactions 2* **1999**, *2*, 493–504.

[81] Clarkson, I.; Dickins, R.; de Sousa, A.; Williams, J.; Woods, M. *Journal of the Chemical Society, Perkin Transactions 2* **1999**, 493–504.

[82] Supkowski, R. M.; Horrocks, W. D. *Inorganic Chemistry* **1999**, *38*, 5616–5619.

[83] Butler, S. J.; Parker, D. *Chemical Society Reviews* **2013**, *42*, 1652–1666.

[84] Richarson, F. *Chemical Reviews* **1982**, *82*, 541–552.

[85] Liu, G.; Song, X.; Chan, K. W. Y.; McMahon, M. T. *NMR in Biomedicine* **2013**, *26*, 810–828.

[86] Frullano, L.; Catana, C.; Benner, T.; Sherry, A. D.; Caravan, P. *Angewandte Chemie* **2010**, *49*, 2382–2384.

[87] Harvey, P.; Blamire, A. M.; Wilson, J. I.; Finney, K.-L. N. A.; Funk, A. M.; Kanthi Senanayake, P.; Parker, D. *Chemical Society* **2013**, *4*, 4251–4258.

[88] Neubauer, A. M.; Myerson, J.; Caruthers, S. D.; Hockett, F. D.; Winter, P. M.; Chen, J.; Gaffney, P. J.; Robertson, J. D.; Lanza, G. M.; Wickline, S. A. *Magnetic Resonance in Medicine* **2008**, *60*, 1066–1072.

[89] Ruiz-Cabello, J.; Barnett, B. P.; Bottomley, P. A.; Bulte, J. W. M. *NMR in Biomedicine* **2011**, *24*, 114–129.

[90] Srinivas, M.; Boehm-Sturm, P.; Figdor, C. G.; de Vries, I. J.; Hoehn, M. *Biomaterials* **2012**, *33*, 8830–8840.

[91] Gonen, O.; Murphy-Boesch, J.; Li, C.-W.; Padavic-Shaller, K.; Negendank, W. G.; Brown, T. R. *Magnetic Resonance in Medicine* **1997**, *37*, 164–169.

[92] Knight, J. C.; Edwards, P. G.; Paisey, S. J. *RSC Advances* **2011**, *1*, 1415–1425.

[93] Rolfe, B. E.; Blakey, I.; Squires, O.; Peng, H.; Boase, N. R. B.; Alexander, C.; Parsons, P. G.; Boyle, G. M.; Whittaker, A. K.; Thurecht, K. J. *Journal of the American Chemical Society* **2014**, *136*, 2413–2419.

[94] Du, W.; Nyström, A. M.; Zhang, L.; Powell, K. T.; Li, Y.; Cheng, C.; Wickline, S. a.; Wooley, K. L. *Biomacromolecules* **2008**, *9*, 2826–2833.

[95] Tanaka, K.; Kitamura, N.; Chujo, Y. *Bioconjugate Chemistry* **2011**, *22*, 1484–1490.

[96] Matsushita, H.; Mizukami, S.; Sugihara, F.; Nakanishi, Y.; Yoshioka, Y.; Kikuchi, K. *Angewandte Chemie* **2014**, *53*, 1008–1011.

[97] Temme, S.; Grapentin, C.; Quast, C.; Jacoby, C.; Grandoch, M.; Ding, Z.; Owenier, C.; Mayenfels, F.; Fischer, J. W.; Schubert, R.; Schrader, J.; Flögel, U. *Circulation* **2015**, *131*, 1405–1414.

[98] Bo, S.; Song, C.; Li, Y.; Yu, W.; Chen, S.; Zhou, X.; Yang, Z.; Zheng, X.; Jiang, Z.-X. *The Journal of Organic Chemistry* **2015**, *80*, 6360–6366.

[99] Khan, F.; Kuprov, I.; Craggs, T. D.; Hore, P. J.; Jackson, S. E. *Journal of the American Chemical Society* **2006**, *128*, 10729–37.

[100] Kuprov, I. Chemically Induced Dynamic Nuclear Polarization of ^{19}F Nuclei. Ph.D. thesis, University of Oxford, 2005.

[101] Goldman, M. *Journal of Magnetic Resonance* **2001**, *149*, 160–187.

[102] Sanders, L. K.; Oldfield, E. *Journal of Physical Chemistry A* **2001**, *105*, 8098–8104.

[103] Harvey, P.; Kuprov, I.; Parker, D. *European Journal of Inorganic Chemistry* **2012**, *2012*, 2015–2022.

[104] Senanayake, P. K.; Kenwright, A. M.; Parker, D.; van der Hoorn, S. K. *Chemical Communications* **2007**, 2923–2925.

[105] Keliris, A.; Mamedov, I.; Hagberg, G. E.; Logothetis, N. K.; Scheffler, K.; Engelmann, J. *Contrast Media & Molecular Imaging* **2012**, *7*, 478–483.

[106] Mizukami, S.; Takikawa, R.; Sugihara, F.; Hori, Y.; Tochio, H.; Wälchli, M.; Shirakawa, M.; Kikuchi, K. *Journal of the American Chemical Society* **2008**, *130*, 794–795.

[107] Harvey, P.; Chalmers, K. H.; De Luca, E.; Mishra, A.; Parker, D. *Chemistry–A European Journal* **2012**, *18*, 8748–8757.

[108] Terreno, E.; Botta, M.; Boniforte, P.; Bracco, C.; Milone, L.; Mondino, B.; Uggeri, F.; Aime, S. *Chemistry–A European Journal* **2005**, *11*, 5531–5537.

[109] Tanaka, K.; Kitamura, N.; Takahashi, Y.; Chujo, Y. *Bioorganic & Medicinal Chemistry* **2009**, *17*, 3818–3823.

[110] Plaunt, A. J.; Clear, K. J.; Smith, B. D. *Chemical Communications* **2014**, *50*, 10499–10501.

[111] Helm, L. *Future Medicinal Chemistry* **2010**, *2*, 385–396.

[112] Kuda-Wedagedara, A. N. W.; Allen, M. J. *Analyst* **2014**, *139*, 4401–4410.

[113] Gale, E. M.; Kenton, N.; Caravan, P. *Chemical Communications* **2013**, *49*, 8060–8062.

[114] Regueiro-Figueroa, M.; Bensenane, B.; Ruscsák, E.; Esteban-Gómez, D.; Charbonnière, L. J.; Tircsó, G.; Tóth, I.; de Blas, A.; Rodríguez-Blas, T.; Platas-Iglesias, C. *Inorganic Chemistry* **2011**, *50*, 4125–4141.

[115] Kim, W. D.; Kiefer, E.; Maton, F.; Mcmillan, K.; Muller, R. N.; Sherry, A. D. *Inorganic Chemistry* **1995**, *34*, 2233–2243.

[116] Polasek, M.; Caravan, P. *Inorganic Chemistry* **2013**, *52*, 4084–4096.

[117] Carniato, F.; Tei, L.; Arrais, A.; Marchese, L.; Botta, M. *Chemistry–A European Journal* **2013**, *19*, 1421–1428.

[118] Rieter, W.; Kim, J.; Taylor, K.; An, H.; Lin, W.; Tarrant, T.; Lin, W. *Angewandte Chemie* **2007**, *119*, 3754–3756.

[119] Davis, J. J.; Huang, W.-Y.; Davies, G.-L. *Journal of Materials Chemistry* **2012**, *22*, 22848–22850.

[120] Laurent, S.; Elst, L. V.; Henoumont, C.; Muller, R. N. *Contrast Media and Molecular Imaging* **2010**, *5*, 305–308.

[121] Stöber, W.; Fink, A.; Bohn, E. *Journal of Colloid and Interface Science* **1968**, *26*, 62–69.

[122] Huang, W.-Y.; Davies, G.-L.; Davis, J. J. *Chemical Communications* **2013**, *49*, 60–62.

[123] MacKenzie, K. J. D.; Smith, M. E. *Multinuclear Solid-State NMR of Inorganic Materials. Pergamon Materials Series*, 1st ed.; Elsevier Science Ltd, 2002; p 727.

[124] Parida, S. K.; Dash, S.; Patel, S.; Mishra, B. K. *Advances in Colloid and Interface Science* **2006**, *121*, 77–110.

[125] Mindt, T. L.; Müller, C.; Stuker, F.; Salazar, J.-F.; Hohn, A.; Mueggler, T.; Rudin, M.; Schibli, R. *Bioconjugate Chemistry* **2009**, *20*, 1940–1949.

[126] Csajbók, É.; Bányai, I.; Vander Elst, L.; Muller, R. N.; Zhou, W.; Peters, J. A. *Chemistry–A European Journal* **2005**, *11*, 4799–4807.

[127] Jin, Y.; Lohstreter, S.; Pierce, D. T.; Parisien, J.; Wu, M.; Iii, C. H.; Zhao, J. X. *Chemistry of Materials* **2008**, 4411–4419.

[128] Rampazzo, E.; Brasola, E.; Marcuz, S.; Mancin, F.; Tecilla, P.; Tonellato, U. *Journal of Materials Chemistry* **2005**, *15*, 2687–2696.

[129] Andre, A. P.; Mäcke, H. R.; Merbach, A. E. *JBIC Journal of Biological Inorganic Chemistry* **1999**, *4*, 341–347.

[130] Parker, D. *Chemical Society Reviews* **2004**, *33*, 156–165.

[131] Aime, S.; Delli Castelli, D.; Terreno, E. *Angewandte Chemie* **2002**, *41*, 4334–4336.

[132] Carniato, F.; Tei, L.; Cossi, M.; Marchese, L.; Botta, M. *Chemistry–A European Journal* **2010**, *16*, 10727–10734.

[133] Skår, H.; Seland, J. G.; Liang, Y.; Frøystein, N. Å.; Törnroos, K. W.; Anwander, R. *European Journal of Inorganic Chemistry* **2013**, *2013*, 5969–5979.

[134] Zhang, W.; Peters, J. A.; Mayer, F.; Helm, L.; Djanashvili, K. *The Journal of Physical Chemistry C* **2014**, *119*, 5080–5089.

[135] Guckenberger, R.; Heim, M.; Cevc, G.; Knapp, H. F.; Wiegräbe, W.; Hillebrand, A. *Science* **1994**, *266*, 1538–1540.

[136] Sulpizi, M.; Gaigeot, M.; Sprik, M. *Journal of Chemical Theory and Computation* **2012**, *8*, 1037–1047.

[137] Franke, M. E.; Simon, U. *ChemPhysChem* **2004**, *5*, 465–472.

[138] Meinhold, R.; Bibby, D. *Zeolites* **1990**, *10*, 74–84.

[139] Marschall, R.; Tölle, P.; Cavalcanti, W. L.; Wilhelm, M.; Köhler, C.; Frauenheim, T.; Wark, M. *Journal of Physical Chemistry C* **2009**, *113*.

[140] Mikhailenko, S.; Desplantier-Giscard, D.; Danumah, C.; Kaliaguine, S. *Microporous and Mesoporous Materials* **2002**, *52*, 29–37.

[141] Izawa, K.; Yamamoto, T.; Masuda, H.; Nishio, E.; Connor, C. J. O. *Colloid and Polymer Science* **2002**, *280*, 135–145.

[142] Perrin, D. D.; Dempsey, B.; Serjeant, E. *pKa Prediction for Organic Acids and Bases*, 1st ed.; Springer, 1981; p 145.

[143] Manzanoa, M.; Ainaa, V.; Arean, C.; Balas, F.; Cauda, V.; Colilla, M.; Delgado, M.; Vallet-Regi, M. *Chemical Engineering Journal* **2008**, *137*, 30–37.

[144] Kruk, M.; Jaroniec, M. *Chemistry of Materials* **1999**, *11*, 492–500.

[145] Kruk, M.; Jaroniec, M.; Kim, J. M.; Ryoo, R. *Langmuir* **1999**, *15*, 5279–5284.

[146] Spiess, H. W. *eMagRes* **2012**, *1*, 109–126.

[147] Graf, R.; Heuer, A.; Spiess, H. W. *Physical Review Letters* **1998**, *80*, 5738–5741.

[148] Buntkowsky, G.; Breitzke, H.; Adamczyk, A.; Roelofs, F.; Emmler, T.; Gedat, E.; Grünberg, B.; Xu, Y.; Limbach, H.; Shenderovich, I.; Vyalikhzb, A.; Findenegg, G. *Physical Chemistry Chemical Physics* **2007**, *9*, 4843–4853.

[149] Trebosc, J.; Wiench, J. W.; Huh, S.; Lin, V. S. *Journal of American Chemical Society* **2005**, *127*, 3057–3068.

[150] Ye, G.; Janzen, N.; Goward, G. R. *Macromolecules* **2006**, *39*, 3283–3290.

[151] Agmon, N. *Chemical Physics Letters* **1995**, *244*, 456–462.

[152] Hassanali, A.; Prakash, M. K.; Eshet, H.; Parrinello, M. *Proceedings of the National Academy of Sciences* **2011**, *108*, 20410–20415.

[153] Supkowski, R. M.; Horrocks, W. D. *Inorganica Chimica Acta* **2002**, *340*, 44–48.

[154] Ali, M. M.; Woods, M.; Caravan, P.; Opina, A. L.; Spiller, M.; Fettinger, J.; Sherry, A. D. *Chemistry–A European Journal* **2008**, *14*, 7250–7258.

[155] Wei, L.; Hu, N.; Zhang, Y. *Materials* **2010**, *3*, 4066–4079.

[156] Sun, J.-T.; Hong, C.-Y.; Pan, C.-Y. *Journal of Physical Chemistry C* **2010**, *114*, 12481–12486.

[157] Wang, C.; Nakamura, S. *Journal of Polymer Science Part A: Polymer Chemistry* **1995**, *33*, 2027–2031.

[158] Pyun, J.; Jia, S.; Kowalewski, T.; Patterson, G. D.; Matyjaszewski, K. *Macromolecules* **2003**, *36*, 5094–5104.

[159] Tang, W.; Kwak, Y.; Braunecker, W.; Tsarevsky, N. V.; Coote, M. L.; Matyjaszewski, K. *Journal of American Chemical Society* **2008**, *130*, 10702–10713.

[160] Zhang, K.; Chen, H.; Chen, X.; Chen, Z.; Cui, Z.; Yang, B. *Macromolecular Materials and Engineering* **2003**, *288*, 380–385.

[161] Lee, A. S.; Gast, A. P.; Bütün, V.; Armes, S. P. *Macromolecules* **1999**, *32*, 4302–4310.

[162] Glasoe, P. K.; Long, F. *The Journal of Physical Chemistry* **1960**, *64*, 188–190.

[163] Verbaan, F.; Oussoren, C.; van Dam, I.; Takakura, Y.; Hashida, M.; Crommelin, D.; Hennink, W.; Storm, G. *International Journal of Pharmaceutics* **2001**, *214*, 99–101.

[164] Roy, I.; Ohulchanskyy, T. Y.; Bharali, D. J.; Pudavar, H. E.; Mistretta, R. A.; Kaur, N.; Prasad, P. N. *Proceedings of the National Academy of Sciences of the United States of America* **2005**, *102*, 279–284.

[165] Huang, W.-Y.; Davies, G.-L.; Davis, J. J. *Chemistry–A European Journal* **2013**, *19*, 17891–17898.

[166] Manders, E. M. M.; Verbeek, F.; Aten, J. *Journal of Microscopy* **1993**, *169*, 375–382.

[167] Kankaanpää, P.; Paavolainen, L.; Tiitta, S.; Karjalainen, M.; Päivärinne, J.; Nieminen, J.; Marjomäki, V.; Heino, J.; White, D. J. *Nature Methods* **2012**, *9*, 683–689.

[168] Holland, G.; Bottomley, P. A.; Hinshaw, W. *Journal of Magnetic Resonance (1969)* **1977**, *28*, 133–136.

[169] Krafft, M. P.; Riess, J. G. *Biochimie* **1998**, *80*, 489–514.

[170] Jacquemain, D.; Grayer Wolf, S.; Leveiller, F.; Lahav, M.; Leiserowitz, L.; Deutsch, M.; Kjaer, K.; Als-Nielsen, J. *Journal of American Chemical Society* **1990**, *112*, 7724–7736.

[171] Hsu, S. L.; Reynolds, N.; Bohan, S. P.; Strauss, H. L.; Snyder, R. G. *Macromolecules* **1990**, *23*, 4565–4575.

[172] Bernett, M. K.; Zisman, W. A. *Journal of Physical Chemistry* **1963**, *67*, 1534–1540.

[173] Peng, H.; Blakey, I.; Dargaville, B.; Rasoul, F.; Rose, S.; Whittaker, A. K. *Biomacromolecules* **2009**, *10*, 374–381.

[174] Oishi, M.; Sumitani, S.; Bronich, T. K.; Kabanov, A. V.; Boska, M. D.; Nagasaki, Y. *Chemistry Letters* **2009**, *38*, 128–129.

[175] Hu, L.; Zhang, L.; Chen, J.; Lanza, G. M.; Wickline, S. A. *Journal of Magnetic Resonance Imaging* **2011**, *34*, 653–661.

[176] Ma, K.; Werner-Zwanziger, U.; Zwanziger, J.; Wiesner, U. *Chemistry of Materials* **2013**, *25*, 677–691.

[177] Liang, Z.; Fadhel, B.; Schneider, C. J.; Chaffee, A. L. *Microporous and Mesoporous Materials* **2008**, *11*, 536–543.

[178] Hoet, J. New catalysts for the enantioselective addition of diorganozinc compounds to aldehydes and imines. Ph.D. thesis, UCL, 2005.

[179] Diou, O.; Tsapis, N.; Giraudeau, C.; Valette, J.; Gueutin, C.; Bourasset, F.; Zanna, S.; Vauthier, C.; Fattal, E. *Biomaterials* **2012**, *33*, 5593–5602.

[180] Janjic, J. M.; Srinivas, M.; Kadayakkara, D. K. K.; Ahrens, E. T. *Journal of the American Chemical Society* **2008**, *130*, 275–290.

[181] Jiang, Z.; Liu, X.; Jeong, E.; Yu, Y. *Angewandte Chemie* **2009**, *121*, 4849–4852.

[182] Chin, L. S.; Lim, M.; Hung, T. T.; Marquis, C. P.; Amal, R. *RSC Advances* **2014**, *4*, 13052–13060.

[183] Zhong-Xing, J.; Xin, L.; Eun-Kee, J.; Yu, Y. B. *Angewandte Chemie* **2009**, *48*, 4755–4758.

[184] Hu, Y.; Atukorale, P. U.; Lu, J. J.; Moon, J. J.; Um, S. H.; Cho, E. C.; Wang, Y.; Chen, J.; Irvine, D. J. *Biomacromolecules* **2009**, *10*, 756–765.

[185] Shen, W.; Wang, L. M.; Tian, H. *Journal of Fluorine Chemistry* **2008**, *129*, 267–273.

[186] Nielsen, A. B.; Frydenvang, K.; Liljefors, T.; Buur, A.; Larsen, C. *European Journal of Pharmaceutical Sciences* **2005**, *24*, 85–93.

[187] Matsumoto, M.; Kishikawa, R.; Kurosaki, T.; Nakagawa, H.; Ichikawa, N.; Hamamoto, T.; To, H.; Kitahara, T.; Sasaki, H. *International Journal of Pharmaceutics* **2008**, *363*, 58–65.

[188] Tomalia, D. A.; Reyna, L. A.; Svenson, S. *Biochemical Society Transactions* **2007**, *35*, 61–67.

[189] Placidi, P.; Natrajan, L. S.; Sykes, D.; Kenwright, A. M.; Faulkner, S. *Helvetica Chimica Acta* **2009**, *92*, 2427–2438.

[190] Davies, G.-L.; Brown, A.; Blackburn, O.; Tropiano, M.; Faulkner, S.; Beer, P. D.; Davis, J. J. *Chemical Communications* **2015**, *51*, 2918–2920.

[191] Tropiano, M.; Blackburn, O. A.; Tilney, J. a.; Hill, L. R.; Placidi, M. P.; Aarons, R. J.; Sykes, D.; Jones, M. W.; Kenwright, A. M.; Snaith, J. S.; Sorensen, T. J.; Faulkner, S. *Chemistry–A European Journal* **2013**, *19*, 16566–16571.

[192] Bergna, H. E.; Roberts, W. O. *Colloidal Silica: Fundamentals and Applications*; CRC Press, 2005; Vol. 131; p 944.

[193] Barrett, E.; Joyner, L.; Halenda, P. *Journal of American Chemical Society* **1951**, *73*, 373–380.

[194] Brunauer, S.; Emmett, P.; Teller, E. *Journal of American Chemical Society* **1938**, *60*, 309–319.

[195] Corsi, D. M.; Platas-Iglesias, C.; Van Bekkum, H.; Peters, J. A. *Magnetic Resonance in Chemistry* **2001**, *39*, 723–726.

[196] Feike, M.; Demco, D.; Graf, R.; Gottwald, J.; Hafner, S.; Spiess, H. *Journal of Magnetic Resonance A* **1996**, *122*, 214–221.

[197] Von Werne, T.; Patten, T. E. *Journal of the American Chemical Society* **1999**, *121*, 7409–7410.

[198] Barge, A.; Cravotto, G.; Gianolio, E.; Fedeli, F. *Contrast Media and Molecular Imaging* **2006**, *1*, 184–188.

[199] Han, J.; Burgess, K. *Chemical Reviews* **2009**, *110*, 2709–2728.

[200] Vijayakrishna, K.; Jewrajka, S. K.; Ruiz, A.; Marcilla, R.; Pomposo, J. A.; Mecerreyes, D.; Taton, D.; Gnanou, Y. *Macromolecules* **2008**, *41*, 6299–6308.

[201] Acik, M.; Dreyer, D. R.; Bielawski, C. W.; Chabal, Y. J. *The Journal of Physical Chemistry C* **2012**, *116*, 7867–7873.

[202] Das, D.; Dasgupta, A.; Das, P. K. *Tetrahedron Letters* **2007**, *48*, 5635–5639.

[203] Lazarus, R. A.; Benkovic, S. J. *Journal of the American Chemical Society* **1979**, *101*, 4300–4312.

[204] Sen, T.; Bruce, I. J. *Scientific Reports* **2012**, *2*, 564.